**The University of Sheffield**

Department of Civil & Structural Engineering

# The Tensile Membrane Action of Non-orthogonal Composite Slabs at Elevated Temperatures

By

Yuan Tian

A thesis submitted in partial fulfilment of the requirements for the degree of Doctor of Philosophy

June 2014

# Acknowledgement

The author special thanks to Professor Ian Burgess for his guidance, support and supervising me throughout my research project. His continuous awareness and encouragement over the whole period of my study was crucial to the completion of this thesis. The financial support provided by TATA Steel Ltd. and the University of Sheffield is also greatly appreciated.

The author would like to thank the colleagues and friends in the Structural Fire Engineering Research Group, who provided great help on my research topic and great opportunities to acquire knowledge in different fields. I am also very grateful to my mother and my friends for their endurance and encouragement during the course of my PhD.

# Declaration

I certify that this thesis submitted for the degree of Doctor of Philosophy is the result of my own research, except where specific reference has been made to the work of others. No portion of the work presented in this thesis has been submitted for another degree or qualification to this, or any other university or institution.

Yuan Tian

# Abstract

In order to generalize the applicability of nonlinear numerical investigation of the structural behavior of slab panels at high deflections, which utilizes tensile membrane action in the slabs, the meshing of such floor systems cannot be restricted to orthogonal grids. A separate but related issue is that nonlinear numerical modelling of internal slab panels with continuity across their edges has shown that the way in which their boundary conditions are defined can have a considerable influence on their predicted membrane forces in various situations. This research investigates the behaviour of the membrane forces in orthogonal and non-orthogonal composite slabs at elevated temperatures by means of numerical modelling. With different continuity conditions at slab panel edges, the effects of various boundary conditions on the tensile membrane action of non-orthogonal slabs at high deflections are identified. In order to achieve this end, a penalty function method is first developed which allows boundary conditions to be defined in terms of relationships between different degrees of freedom in the system's global coordinates, as opposed to the conventional binary "free or restrained" choice for individual degrees of freedom. This allows boundary conditions either to be defined with respect to axes inclined to the global system, or to link displacements at different nodes. This easily defines suitable boundary conditions for non-orthogonal slabs, and also allows the continuity of internal panels to be realistically modelled.

In terms of simplified design methods, it is often possible to divide internal floor areas of a building into rectangular or square panels, but the problem of slabs at or near the edges of non-orthogonal buildings still exists. This thesis attempts to begin to extend these methods to non-orthogonal slabs by determining the optimal small-deflection yield-line failure patterns for quadrilateral slabs of different geometries. Simplified design methods assume that the enhancement of capacity due to tensile membrane action increases continuously with vertical deflection. However, as slab deflection increases, through-depth cracks which may or may not coincide with the yield lines can occur, and these cause progressive reduction of the enhancement of load capacity. Optimizing assumed yield-line patterns by using a plastic work balance method, the research establishes and validates two existing yield-line patterns for trapezoidal slabs. Further studies to determine the precise yield-line patterns of trapezoidal slabs are made by gradually changing of the geometrical parameters.

A new plastic energy method which includes the internal work dissipation during rebar extension has been extended to triangular slabs. The post-yield-line behaviour of such slabs has been demonstrated. This research validates and compares the enhancement factor performance from the new plastic energy method to the existing simplified design method. An investigation of the influence of different reinforcement meshes and geometry on the enhancement of load-carrying capacity of isosceles triangular slabs has been carried out.

# Table of contents

# List of figures

## Figures in Appendix

# List of tables

# Glossary of notation

| | |
|---|---|
| $A_S$ | cross-sectional area of reinforcement (*m*$^2$) |
| $E$ | modulus of elasticity of steel for normal temperature design (*MPa*) |
| $E_\theta$ | slope of the linear elastic range (Young's modulus) of steel at temperature $\theta$ (*MPa*) |
| $E_s$ | design value of modulus of elasticity of reinforcing steel (*MPa*) |
| $F_p$ | yielded bar force per unit width of slab (*N/m*) |
| $D$: | internal work (*N/m*) |
| $K$ | ratio of yield force in the reinforcing steel in the short span to the yield force in the reinforcing steel in the long span |
| $L$ | longer span of rectangular slab (*mm*) |
| $M$ | resistance moment of the slab per unit width |
| $M_{1,m}$ | moment about the support due to membrane forces for the element 1 |
| $M_{2,m}$ | moment about the support due to membrane forces for the element 2 |
| $P$ | load-bearing capacity for a given deflection (*N/m*$^2$) |
| $P_0$ | initial yield-line load-bearing capacity (*N/m*$^2$) |
| $P_{ft,0}$ | initial bearing capacity of the slab (*N/m*$^2$) |
| $S$ | distance between rebar and the edge of the slab along the crack (*mm*) |
| $T_0$ | yield force in reinforcing steel per unit width in the long span (*kN/m*) |
| $T_1$ | top temperature of the slab ( ℃) |
| $T_2$ | bottom temperature of the slab ( ℃) |
| $X$ | orthogonal projection of $S$ in *X*-direction (*mm*) |
| $Y$ | orthogonal projection of $S$ in *Y*-direction (*mm*) |
| $a$ | aspect ratio of the slab |
| $b$ | parameter defining the magnitude of the membrane force |
| $d$ | spacing between two rebars in long or short span (*mm*) |
| $d_1$ | effective depth of the reinforcement in the shorter span of the slab (*mm*) |
| $d_2$ | effective depth of the reinforcement in the longer span of the slab (*mm*) |
| $e$ | overall enhancement factor due to membrane forces |
| $e_1$ | net enhancement factor due to membrane forces for element 1 |
| $e_2$ | net enhancement factor due to membrane forces for element 2 |
| $e_{1b}$ | enhancement factor of bending resistance due to membrane forces for element 1 |

| | |
|---|---|
| $e_{2b}$ | enhancement factor of bending resistance due to membrane forces for element 2 |
| $e_{1m}$ | enhancement factor above the yield-line load due to membrane forces for element 1 |
| $e_{2m}$ | enhancement factor above the yield-line load due to membrane forces for element 2 |
| $f_{ck,t}(\theta)$ | compressive strength of concrete at temperature $\theta$ ($MPa$) |
| $f_{p,\theta}$ | proportional limit of steel at temperature $\theta$ ($MPa$) |
| $f_y$ | yield strength of steel at 20 ℃ ($MPa$) |
| $f_{y,\theta}$ | effective yield strength of steel at temperature $\theta$ ($MPa$) |
| $h$ | thickness of the slab ($mm$) |
| $k$ | parameter defining the magnitude of the membrane force |
| $k_{c,t}(\theta)$ | reduction factor for the characteristic tensile strength of concrete at temperature $\theta$ |
| $k_{E,\theta}$ | reduction factor for the slope of the linear elastic range of steel at temperature $\theta$ |
| $k_{p,\theta}$ | reduction factor for the proportional limit of steel at temperature $\theta$ |
| $k_{y,\theta}$ | reduction factor for effective yield strength of steel at temperature $\theta$ |
| $l$ | shorter span of rectangular slab ($mm$) |
| $n$ | parameter defining the intersection of the yield-lines |
| $r$ | length ratio for triangular or trapezoidal slab |
| $w$ | vertical displacement ($mm$) |
| $w_e$ | vertical displacement caused by mechanical strain in the reinforcement ($mm$) |
| $w_\theta$ | vertical displacement due to the thermal curvature ($mm$) |
| $w_m$ | maximum allowable deflection of the slab ($mm$) |
| $\Delta_A$ | displacement in x-direction between edges of facets 1 and 2 ($mm$) |
| $\Delta'_A$ | displacement in y-direction between edges of facets 1 and 2 ($mm$) |
| $\Delta l$ | thermal expansion ($mm$) |
| $\Delta_{lim}$ | maximum extension for rebar ($mm$) |
| $\alpha$ | coefficient of thermal expansion |
| $\gamma$ | angle defining the yield-line pattern formed by the element 2 |
| $\delta$ | vertical displacement of the loads on each region ($mm$) |
| $\varepsilon$ | average strain in the tensile part of the steel – mesh reinforcement – concrete |
| $\varepsilon_{c1,\theta}$ | strain of concrete at maximum compressive strength at temperature $\theta$ |
| $\varepsilon_{cu1,\theta}$ | ultimate strain of concrete in compressoin at temperature $\theta$ |

| | |
|---|---|
| $\varepsilon_{P,\theta}$ | strain in the proportional limit at temperature $\theta$ |
| $\varepsilon_{t,\theta}$ | limiting strain for yield strength of steel at temperature $\theta$ |
| $\varepsilon_u$ | fracture ductility strain of a mesh |
| $\varepsilon_{u,\theta}$ | ultimate strain of steel a temperature $\theta$ |
| $\varepsilon_{y,\theta}$ | yield strain of steel at temperature $\theta$ |
| $\mu$ | average depth of reinforcement for the new plastic method (*mm*) |
| $\sigma_{c,\theta}$ | compressive stress of concrete at temperature $\theta$ (*MPa*) |
| $\sigma_{s,\theta}$ | steel stress at temperature $\theta$ (*MPa*) |
| $\xi$ | angle of rotation between both element ($\alpha$ or $\beta$) |
| $\eta$ | angle of element rotation against his edge ($\theta$ or $\phi$) |

# Chapter 1 Introduction

In the past two decades, the design of composite structures to resist the effects of fire has been greatly developed. Performance based approaches are gradually replacing the traditionally-used prescriptive method for structural fire safety design. These traditional methods are based on the results from standard fire tests on single structural elements and ignore the interactions which occur between structural elements in real buildings under fire situations. As a result, the traditional methods requiring the application of passive fire protection to all exposed steelwork as protection against elevated temperatures have generally been proved to be over-conservative. With the generation of observations from real structural fire tests, and advanced understanding of the influence of composite floor systems on overall structural stability at elevated temperatures, considerable reductions in passive protection costs, while maintaining equivalent or higher levels of safety, have been made possible.

## 1.1 Background

In the presence of sufficient oxygen and combustible material, relatively small ignition sources can generate fire easily. For a natural fire, the development is divided into four phases: ignition, growth, heating and cooling. The ignition phase is when the combustible material starts to burn locally. Then the fire gradually spreads over the combustible materials during the growth phase, until the average temperature is about 600 ℃. Then the fire starts to grow rapidly, and develops the rapid heating phase (called flashover) where everything in the compartment is heating up. When the combustible material is consumed slowly, or there is not enough oxygen, it enters the cooling phase, which terminates when the material or oxygen has gone completely. In most cases, a fire happens accidentally and unpredictably. It is impossible to prevent fires from happening, so that the aim of fire safety engineering is to ensure that the whole structure is capable of maintaining its stability and integrity for at least the period the occupants require to exit the building safely, and also to minimize the economic loss of property and contents.

For the steel and composite structural elements which are commonly used in building construction, fire is certainly one of the biggest problem the designer faces. Due to their high strength-to-weight ratio, structural steel elements can cross longer spans and also have a lower requirement for foundations. These benefits make steel one of the most popular structural materials in multi-storey building construction in the UK. However, there is one obvious disadvantage to steel; its high thermal conductivity, which means that the temperature of steel grows rapidly when it is heated by a fire environment. When the temperature of steel has increased sufficiently, it loses its strength and stiffness very quickly, which suggests that the structural elements will no longer be capable of supporting their applied loads. Therefore, in order to ensure that structural elements retain appropriate strength and stiffness to survive during a given fire resistance period, it is necessary to apply passive protection materials to keep them below their limiting temperatures over that period. Even so, the cost of these protective materials can be very high, and the industry is investing in developing economic protection materials and updating design methods to reduce the expense.

## 1.2 Structural fire engineering

With the target of protecting life and property, structural fire engineering includes developing design methods for structural members to achieve appropriate fire resistance, and also to analyse the behaviour of structural members under fire situations. The available design codes such as BS5950 Part 8 (2003) and Eurocode 3 Part 1.2 (CEN 1995) contain some limitations, because their development is based on previous tests on isolated structural members, and neglects the interaction between them and other members. From the observations in a series of fire tests carried out by the Building Research Establishment on an 8-storey steel-framed building at the Cardington Laboratory, the traditional design method based on the behaviour of isolated members in fire was shown to be over-conservative. The interactions between the structural members showed the existence of an inherent fire resistance which somehow improved the load carrying capacity of the whole structure. This has persuaded a growing number of designers to adopt the performance-based design method, which is a rational fire engineering approach to provide fire safety as required, by taking account of the actual behaviour of the three-dimensional structure in fire. If the interactions are considered in determining the fire protection by using a performance-based design method, it can never practically be based on using results from large-scale tests, because the cost is extremely high. Therefore, it is becoming increasingly important to allow the performance-based design method to be based on numerical modelling which can accurately illustrate the behaviour of structures in fire situations.

Using the results from numerical modelling of the behaviour of structures in fire, the performance-based approach has been made possible, and is a considerable improvement on the previous design methods. However, there are still some limitations on numerical modelling based on the finite element method. The first step in numerical modelling is to build up a model which is divided into a mesh of elements located according to the 3D global coordinates. After input of the properties of the materials, applied loads, structural elements etc., it is necessary to define movement constraints on specific nodes dependent on the locations of the supports, which are also known as boundary conditions.

For the structural elements which are simulated parallel to the global axes and without continuity, the boundary conditions can be set as fixed or free to move in any of the global coordinate directions. However, for those elements not parallel to any global axis or with continuity, these simple constraints are not enough to model the actual supports accurately. This situation is quite common, as with the development of modern architecture, many buildings are designed with non-orthogonal floor layouts, which means that at least one edge of any floor slab is aligned in a direction that is not parallel to any global axis. To ensure the accuracy of analysis results, the problem of defining boundary conditions has to be resolved.

## 1.3 Research aims

The finite element program *Vulcan* has been developed by the Structural Fire Engineering Research Group at the University of Sheffield for three-dimensional analysis of the behaviour of structures at elevated temperatures. The main objective of this research is based on the *Vulcan* code, to create a practical structural fire engineering analysis tool which is able to analyse models with non-orthogonal meshes. In other words, update the program with the new function of defining the boundary conditions of any model in localized coordinates. Once the problem of restraining the boundary conditions has been resolved, the membrane actions of non-orthogonal slabs can be analysed, and the final target of extending the simplified design method for rectangular slabs to non-orthogonal ones can be developed.

The main threads of this research include:

- By applying penalty function methods to the original structural stiffness matrix, the ability of the program *Vulcan* can be improved to restrain the nodal movements on structural elements in any direction. Further studies can be done on the behaviour of composite floor systems with non-orthogonal slab panels and continuous edges.

- Simpler modelling can be done assuming the collapse mechanisms of triangular and trapezoidal slabs, based on yield-line patterns, by applying work equations to confirm the locations of yield line intersections in triangular and trapezoidal slabs. Parametric studies can be done on the influence of change of geometry on trapezoidal and triangular slabs, and developing the relationships between geometric parameters and the locations of yield line intersections.

- Research on the previously developed simplified design method for rectangular composite slabs in fire includes considering the enhancement of tensile membrane action due to large deflection. An initial objective was to extend this method to triangular and trapezoidal slabs at elevated temperature and to determine the distribution of membrane force. In fact there were found to be limitations and uncertainties in extending the simplified design method into triangular and trapezoidal slabs.

## 1.4 Outline of this thesis

The main body of this thesis consists of seven chapters. Each chapter includes a brief introductory paragraph at the beginning, giving an overview of the chief contents in the particular chapter. At the end of each chapter, a concluding section summarizes the crucial findings.

### Chapter 2: Literature review

The chapter provides relevant observations from previous fire tests and research works relating to structural fire engineering and the tensile membrane action of composite slabs at elevated temperature. This includes not only fundamental knowledge about steel and composite structure in fire and design methods, but also the development of the BRE-Bailey method which simply models the enhancement of load capacity which derives from tensile membrane action occurring when the slab attains large deflections as part of a design tool for fire resistance of composite slabs.

**Chapter 3: Penalty function method and relative constraints**

In this chapter, a brief introduction to the penalty function method has been provided and some simple examples illustrate the details of application of the penalty function method to structural finite-element-based stiffness analysis. In the latter section of this chapter, a validation study on the influence of nodal movement constraints, represented by the penalty function method is demonstrated in both rectangular and irregular shapes of slab. In addition, the effect on membrane action has been compared between rectangular slabs with and without nodal displacement restrained.

**Chapter 4: Numerical modelling and validation**

This chapter shows the research on the behaviour of triangular and trapezoidal slabs at elevated temperatures by using the non-linear analysis program *Vulcan* with the penalty function method applied. The study has investigated triangular slab panels at different locations within a floor layout. The effects on tensile membrane action due to different boundary conditions have been studied. On the other hand, analysis of rectangular slab panels with continuous edges is also illustrated. It is a very common situation that the behaviour of rectangular or square slab panels with different boundary conditions needs to be analysed individually instead of a whole floor system. After applying the penalty function method, this demand can be satisfied.

**Chapter 5: Simplified design method for non-orthogonal slabs**

In this chapter, the calculation for load capacity or fire resistance enhancement by tensile membrane action in triangular slabs has been attempted. However, in the process of building up equilibrium equations, the limitation of the previous method’s assumptions for rectangular slabs has been pointed out as not suitable for triangular slabs. In order to extend the simplified design method to trapezoidal slabs, the locations of yield line intersections have to be found. Hence, two main yield-line patterns have been assumed, optimized and validated. Since the locations of yield line intersections are dependent on the trapezoidal geometry, the change-over between these two yield-line patterns has been investigated by performing a geometric parametric study. As there is little research work that has been done to date, some fresh views about yield-line pattern transformation due to geometry change have been developed, but further research is needed on the process of extending the simplified design method into trapezoidal slabs.

**Chapter 6: New internal work method for capacity enhancement**

This chapter explains a new method to calculate the internal work dissipation, based on different assumed collapse mechanisms, recently reported by Burgess (2013). A comparison of enhancement factors between this method and BRE-Bailey method has been carried out and extended into triangular slabs. A parametric study on the influence on enhancement factors from geometry change has been carried out. The results from this method at ambient temperature have made good sense, but its performance at elevated temperature needs further research in future.

**Chapter 7: Conclusion and further study**

This chapter presents the findings and conclusions of this research, recommendations on the limitations and unsolved problems for future work.

# Chapter 2 Literature Review

In this chapter, relevant fundamental knowledge and the development of structural fire engineering are reviewed. As one of the most important factors affecting the behaviour of structural elements at elevated temperatures, the properties of steel are reviewed and summarized. The behaviour of reinforced concrete slabs at elevated temperature are described on the basis of previous researches, together with the development of simplified design methods, including the load bearing capacity enhancement of slabs due to tensile membrane action.

Between 1995 and 2003 a series of fire tests (Kirby, 1998) were conducted at the Building Research Establishment (BRE) Large Building Test Facility at Cardington. Before the Cardington Fire tests, in the early 1990s the behaviour of composite slabs had been brought to attention in a number of fire accidents (Abu, 2009). In the post-accident investigations, it was observed that the integrity of composite slabs was generally maintained, although the steel deck was observed to have separated from the concrete slab. It was suspected that the existing prescriptive methods for selection of fire protection were over-conservative. Because of this uncertainty about the traditional methods and a shortage of observations from real building fires, the Cardington fire tests were set up in a specially-designed 8-storey steel-framed composite-floored building. The results of Cardington tests (Kirby, 1998) generally confirmed the over-conservativeness of the previous method, and indicated that tensile membrane action needed to be considered in design methodologies.

## 2.1 Material properties at elevated temperature

### 2.1.1 Steel properties at elevated temperature

For steel and reinforced concrete composite structures, the mechanical properties of steel at elevated temperature is one of the most important aspects which influence their structural behaviour in fire. As a thermally conductive material, steel has a fairly low resistance to heat (Purkiss, 1996). Steel starts to lose its strength dramatically at about 400°C, and this continues to decline until about 800°C at an almost constant rate. Above this temperature, the strength of steel continues to decrease, but at a slower rate, until its melting point is reached at about 1500°C.

The stress-strain behaviour of steel at elevated temperatures is definitely different from that at ambient temperature, because of the lack of a yield plateau and the fact that the slope of the stress-strain curve remains positive during most of the plastic range. From British Steel data (Kirby and Preston, 1988) about a series of test on isolated steel members, it was apparent that the stress-strain behaviour of steel at elevated temperatures is dependent on the rate of heating because of the influence from the creep at temperature over 450°C. The clearly defined yield plateau at 20°C is replaced by a gradual increase of strength with strain at elevated temperatures. As the strength of steel is one of the most important parameters in structural fire design, however, this makes it quite difficult to define the strength of steel at elevated temperatures. Instead of fixing a unique limiting strain value for yield strength at elevated temperature (such as 0.2% at 20°C), the design codes BS5950 and Eurocode 3 employ different values of limiting strain to evaluate the reduction factors. BS 5950 Part 8 (BSI 1990) adopts a strain limit of 1.5% for beams and 0.5% for columns, whereas Eurocode 3 Part 1.2 (CEN 2005a) adopts 2.0% as a “yield” strain for all member types. The steel grades 43A and 50B were until recently the UK grades most commonly used in construction; the equivalent steel grades defined by the Eurocodes are S275 and S355 respectively. According to the equations provided by Eurocode 3 Part 1.2 (CEN 2005a), the stress-strain curves are standardised in the form shown in Figure 2.1.

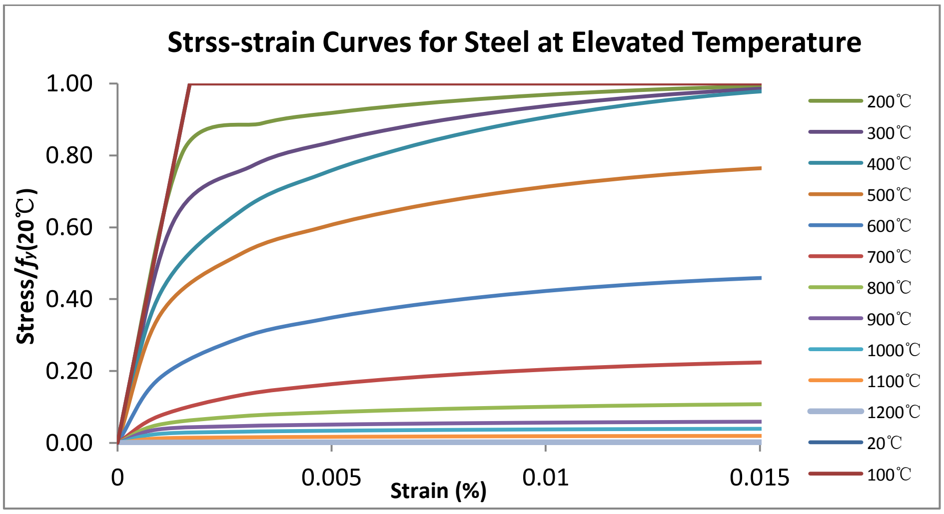

**Fig. 2.1 Stress-strain curves for steel at elevated temperatures**

| Steel Temperature $\theta_a$ | Reduction factors at temperature $\theta_a$ relative to the value of $f_y$ or $E_a$ at 20 ℃ | | |
|---|---|---|---|
| | Reduction factor (relative to $f_y$) for effective yield strength $k_{y,\theta} = f_{y,\theta} / f_y$ | Reduction factor (relative to $fy$) for proportional limit $k_{p,\theta} = f_{p,\theta} / f_y$ | Reduction factor (relative to $Ea$) for the slope of the linear elastic range $k_{E,\theta} = E_{a,\theta} / E_a$ |
| 20 ℃ | 1.000 | 1.000 | 1.000 |
| 100 ℃ | 1.000 | 1.000 | 1.000 |
| 200 ℃ | 1.000 | 0.807 | 0.900 |
| 300 ℃ | 1.000 | 0.613 | 0.800 |
| 400 ℃ | 1.000 | 0.420 | 0.700 |
| 500 ℃ | 0.780 | 0.360 | 0.600 |
| 600 ℃ | 0.470 | 0.180 | 0.310 |
| 700 ℃ | 0.230 | 0.075 | 0.130 |
| 800 ℃ | 0.110 | 0.050 | 0.090 |
| 900 ℃ | 0.060 | 0,.0375 | 0.0675 |
| 1000 ℃ | 0.040 | 0.0250 | 0.0450 |
| 1100 ℃ | 0.020 | 0.0125 | 0.0225 |
| 1200 ℃ | 0.000 | 0.0000 | 0.0000 |
| **NOTE**: For intermediate values of the steel temperature, linear interpolation may be used. | | | |

**Table. 2.1 Reduction factors for stress-strain relationship of carbon steel at elevated temperatures (Eurocode 3 Part 1.2 (CEN 2005a) Table 3.1)**

in which,

$k_{y,\theta}$ is the reduction factor for effective yield strength of steel (2% strain) at relevant elevated temperature,

$k_{p,\theta}$ is the reduction factor for proportional limit,

$k_{E,\theta}$ is the reduction factor for the linear elastic range (Young’s Modulus).

In the table provided by Eurocode 3 Part 1.2 (CEN 2005a), temperature increments are given from ambient temperature (20 ℃) to elevated temperature in 100 ℃ steps. The proportional limit and Young’s modulus are assumed decrease from about 200 ℃, while the effective yield strength is assumed start to drop from 400 ℃, but more rapidly than the other two parameters. The reduction factors for yield strength, proportional limit and elastic modulus taken from Eurocode 3 are shown in Figure 2.2 below,

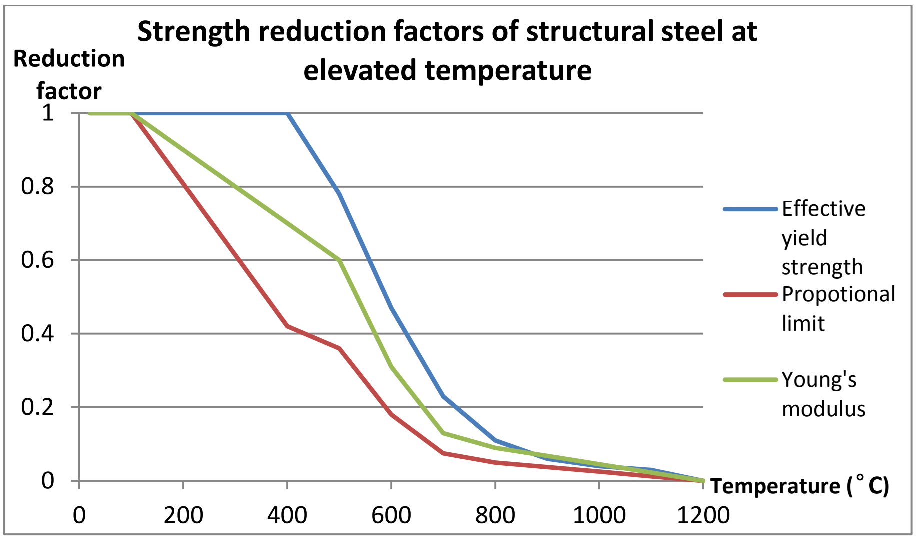

**Fig. 2.2 Strength reduction factors of structural steel at elevated temperature**

For reinforcing steel, Eurocode 4 Part 1.2 (CEN, 2005b) suggests, the strength and deformation properties of reinforcing steels at elevated temperatures may be obtained using the same mathematical model as for structural steel, the three main parameters given in Table 2.2 may be used for hot-rolled reinforcing steel. For cold-rolled reinforcing steel the values of the three main parameters are given in Eurocode 4 Part 1.2 (CEN, 2005b) Table 3.4, and also in Eurocode 2 Part 1.2 (CEN 2004) Table 3.2a.

### 2.1.2 Concrete properties at elevated temperature

Concrete also loses its stiffness and strength at high temperature as well. An important aspect is water, which exists in normal form as liquid, and turns into steam and evaporates when it is heated to over 100 ℃. This phenomenon also happens in concrete, in which a great proportion of free water exists. When the temperature exceeds 300 ℃, siliceous concrete starts to lose its strength because of the different thermal expansion of aggregates and cement matrix. Depending on the type of aggregates, the properties of concrete are different in compression and tension. According to Eurocode 2 Part 1.2

(CEN, 2004), when concrete under compression, the form of the stress-strain relationship at elevated temperature is presented in Figure 2.3.

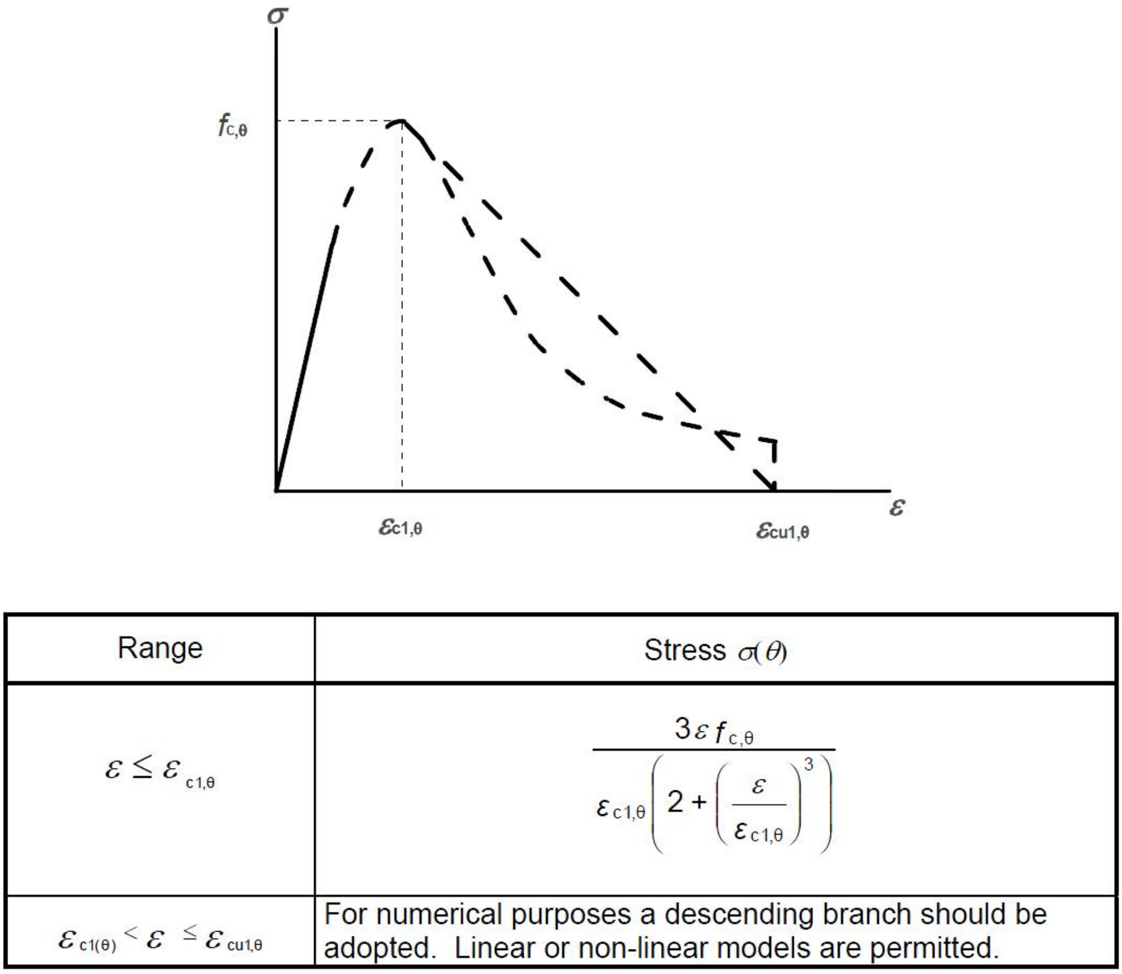

| Range | Stress $\sigma(\theta)$ |
|---|---|
| $\varepsilon \le \varepsilon_{c1,\theta}$ | $\dfrac{3\varepsilon f_{c,\theta}}{\varepsilon_{c1,\theta}\left(2+\left(\dfrac{\varepsilon}{\varepsilon_{c1,\theta}}\right)^3\right)}$ |
| $\varepsilon_{c1(\theta)} < \varepsilon \le \varepsilon_{cu1,\theta}$ | For numerical purposes a descending branch should be adopted. Linear or non-linear models are permitted. |

**Fig. 2.3 Stress-strain relationships of concrete under compression at elevated temperatures (Eurocode 2 Part 1.2 (CEN, 2004))**

For concrete under compression, the stress-strain relationships given in Fig. 2.3 are defined by three parameters: the compressive strength $f_{c,\theta}$ and the corresponding strain $\varepsilon_{c1,\theta}$ define ultimate conditions. Values for $\varepsilon_{cu1,\theta}$ , which define the range of the descending branch, are taken from the table provided in Eurocode 2 Part 1.2 (CEN, 2004). The values of both of the strains $\varepsilon_{c1,\theta}$ and $\varepsilon_{cu1,\theta}$ are temperature-dependent. For the tensile strength of concrete at elevated temperature, Eurocode 2 Part 1.2 suggests it should be ignored for conservativeness. However, if the tensile strength needs to be taken into account, a simplified reduction of the characteristic tensile strength of concrete by the coefficient $k_{c,t}(\theta)$can be adopted as,

$$f_{ck,t}(\theta) = k_{c,t}(\theta) \cdot f_{ck} \tag{2.1}$$

The reduction factor $k_{c,t}(\theta)$ is defined as follows:

- For $20°\text{C} \leq \theta_c \leq 100°\text{C}$:

$$k_{c,t}(\theta) = 1.0 \tag{2.2}$$

- For $100°C < \theta_c \leq 600°C$:

$$k_{c,t}(\theta) = 1.0 - 1.0\,(\theta - 100)/500 \tag{2.3}$$

Generally, concrete provides the greatest fire resistance properties of any common building material. This excellent fire resistance is due to the properties of concrete's constituent materials (i.e. cement and aggregates). When these materials chemically combine, this creates a material which is essentially inert and has low thermal conductivity (50 times lower than steel), which means that its interior heats very slowly in fire, causing a slow degradation of strength with increase of the outside temperature. This low thermal conductivity and strength loss enable concrete to provide very effective inherent fire resistance.

## 2.2 Review of yield-line theory and virtual work method

### 2.2.1 Introduction

The yield-line theory, which was initiated by Ingerslev (1923) and greatly extended and improved by Johansen (1962), is a method for the limit analysis of reinforced concrete slabs. The theory have been great enhanced and extended by many authors such as Jones and Wood (1967), Sawczuk and Jaeger (1963), Park and Gamble (1980), Kemp (1965), Morley (1966), and Kwiecinski (1965). Described by Prager (1955), the yield line theory is recognized as a simple and quick method to determine the upper bound of the small-deflection plastic failure loads of slabs. As an upper bound approach, the plastic load capacity of the slab is estimated by assuming a failure mechanism which is compatible with its specific boundary conditions. In the yield line theory, the moments across the plastic hinge lines are equal to the moments of resistance of the reinforced concrete sections, and by applying the energy balance principle to generate equations of equilibrium, by equating the work done by external loads to the work dissipated across yield lines, the load capacity can be determined. Being an upper bound approach, the yield line method provides ultimate loads which are either correct or too high. However, the advantages of yield line design are easy to observe:

1. Firstly, applying the yield line method makes slab design quick and simple. For reinforced concrete slabs, using linear elastic analysis makes it very complicated to determine the shear forces and moments in each direction due to the applied load, and for irregular shapes of slab this becomes even more difficult. In the latter case numerical analysis is nearly always necessary for adequate solution. However, when using the yield line method, manual calculation can be done easily; computational approaches are not necessary, but the designer requires experience to recognize a probable collapse mechanism.
2. Secondly, the linear elastic method can only predict when the first yield appears, whereas the yield line method gives the ultimate capacity which dictates what makes a slab collapse and helps the engineer to appreciate its ultimate behaviour.
3. Finally, the yield line method is much easier to implement in different geometric shapes of slab than is linear elastic analysis. No matter how complex the slab shape or applied load profile, it is always possible to obtain a reasonable value of the ultimate load.

The disadvantages of yield line design also need to be considered. A critical factor in using this method is that it requires familiarity with the probability of a slab failure mechanism. This demands a certain amount of design experience to be applied with confidence and accurate judgement. As mentioned above, the yield line method is easy for hand calculation, because it treats complex slabs in a simple way and is an independent method of analysis and verification. However, as it concerns ultimate limit state behaviour, it does not provide guidance on slab behaviour in a serviceability limit state.

### 2.2.2 Fundamental concepts and rules of yield line theory

In the yield line theory, the slab is postulated to collapse at a certain ultimate loading through generating a series of cracks in the reinforced concrete slab, across which reinforcing bars have yielded and plastic rotation occurs. At these locations the reinforcing bars are all assumed to have yielded, and the moment in each bar direction reaches the moment of resistance; these discrete cracks, which are named yield lines, constitute plastic hinge lines. The yield lines divide the slab into several rigid regions ("facets") which are assumed to remain plane throughout the collapse process. When the collapse mechanism has formed, the plastic deformations across the yield lines are much larger than any elastic deformations of the slab facets between the yield lines (Park and Gamble, 1980), so that the rigid perfectly-plastic assumption is reasonable. Since the yield lines are the hinges about which rotation occurs between two adjacent slab segments, and since they form the intersections between inclined flat plates as the slab deflects, they must be straight lines. According to the geometry of the deformed slab, for compatibility of deformation the yield lines must intersect at common points of adjacent regions. Another rule for yield lines is that the axes of rotation of the facets generally lie along the lines of support and pass over any columns; also the yield lines must end at a slab edge. As described above, the yield lines develop into a mechanism form which is called yield line pattern.

As mentioned by Park and Gamble (1980), the regions of the slab between the yield lines are not investigated to guarantee that the moments do not exceed the ultimate moments of resistance of the sections, but the ultimate moments of resistance between the lines of plastic hinges will be exceeded only if an inappropriate collapse mechanism is applied. Therefore, selecting the correct yield line pattern for a given slab and its load arrangement becomes the primary task when applying yield line analysis. As described by Wood (1961), for rectangular slabs with isotropic reinforcement the mode of collapse has to be bisymmetric, and the central yield line must be parallel to two edges because the corresponding axes of rotation can never meet. In general, for a yield line pattern normally originating from the positions of the axes of rotation, such as the supported slab edges, has yield lines which pass through the intersections of the axes of rotation at the slab corners. However, there still many possible yield line patterns which can be assumed for a given slab, although they all obey these general rules. For each assumed yield line pattern, the ultimate collapse load can be found by using the plastic work balance or equilibrium method. The correct yield line pattern is the one which gives the lowest collapse load.

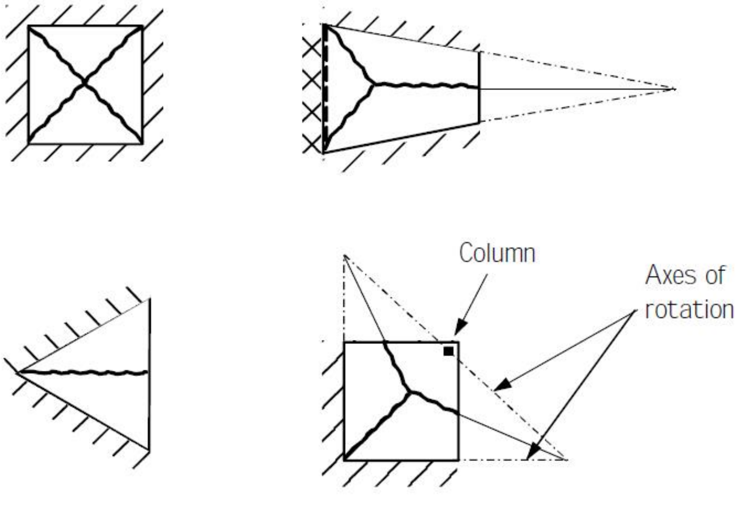

**Fig. 2.4 Typical simple yield line patterns (Kennedy and Goodchild, 2003)**

### 2.2.3 Virtual work method

The plastic work balance method of analysis is the most common and simplest way of applying yield line theory; it is also considered the quickest way to analyse a slab by hand calculation. The primary principle of the method is that the external work done by displacement of the loads must balance with internal work absorbed by rotation under fully plastic moments at the yield lines. In fact, the virtual work balance can be expressed as,

$$\sum (P \times \delta)_{for\ all\ regions} = \sum (M \times l \times \theta)_{for\ all\ regions} \tag{2.4}$$

In which,

$P$ = applied load(s) on a particular region of slab;

$\delta$ = the vertical displacement of the load(s) $P$ on each region;

$M$ = the ultimate moment of resistance of slab per unit width;

$l$ = the length of yield line or projected length on the axis of rotation for the region;

$\theta$ = the angles of rotation of the regions about the yield lines.

In the work balance equation (2.4), the vertical displacement $\delta$ is calculated as a proportion of the maximum deflection $\delta_{max}$ occurring at a point located on the yield line pattern. For the purpose of convenience, the maximum deflection always is given a value of unity during the calculation, because it cancels out with the fraction of $\delta_{max}$ on the other side of the equation. The value of $M$ is given by Park and Paulay (1975) as,

$$M = A_s f_y (d - 0.59 A_s \frac{f_y}{f_c' b}) \tag{2.5}$$

where $A_s$ is the area of tension steel reinforcement per unit width, $f_y$ is the yield strength of the reinforcement, $d$ is the distance from compression concrete edge to the centroid of the tension steel, $b$ is the width of concrete in compression. The angle of rotation $\theta$ of a region is assumed to be vanishingly small, so that it can be expressed as $\delta_{max}$/length, in which the length is the perpendicular distance between the point of maximum deflection and the axis of rotation of that region.

For a given slab with given geometry and reinforcement details, all these parameters can be defined. As consequence, the collapse load $P$ can be found as the solution of Equation 2.4. Thus, for a given slab, it is possible that different collapse mechanisms are postulated, and after comparing the collapse loads for each of them the lowest should be selected as the best model of the correct yield line pattern for the slab.

## 2.3 Review of behaviour of steel-Framed buildings at elevated temperature

### 2.3.1 Introduction

In the ambient temperature condition, the load-carrying capacity of a composite floor system is assessed on the basis of the supporting composite beams and flexural strength of the composite slab. The flexural strength of the composite slab is generally dependent on the steel profile deck and concrete, and the contribution from mesh is ignored. Current fire design methods follow a similar approach, except that the simplified analytical design method for composite slabs in fire ignores any contribution from the steel deck (Bailey and Moore, 2000b). The reason for neglecting the effect of the steel deck follows the observations from earlier accidental fires, such as Broadgate

(1991a) and Basingstoke (1991b) both of which gave evidence of the separation of steel deck and concrete, due both to the free water in concrete turning into steam and being released at high temperature, and to differential thermal expansion between the steel deck and the concrete surface. Hence, the flexural strength of slab at elevated temperature only depends on the reinforcement mesh and concrete. For the whole floor system, the structural components that are assumed to make a contribution to the load carrying capacity in fire conditions are reinforcement mesh, concrete and composite steel beams. However, according to the design code, the strengths of these components are reduced significantly within the fire resistance regime.

### 2.3.2 Broadgate Phase 8 fire, London

In 1990, a fire took place in an uncompleted 14-storey composite steel-framed office block in the Broadgate development in London. The floor system consisted of arrays of composite beams forming a composite slab which was designed to have 90 minutes' fire resistance. At the time of the fire, the sprinkler system and other active measures were not ready to use, and the fire protection for steel beams was unfinished because the building was still under construction. After the fire, an investigation indicated that the temperature of the exposed steel beams did not exceed 600℃ although the fire temperatures were estimated to be more than 1000℃ (SCI, 1991). Even with a maximum permanent vertical deflection of 600mm, the composite slab still maintained its integrity, with observations indicating only some reinforcement failure and debonding of the steel profiled decking from the concrete. The composite beams also deflected between 82 mm and 270 mm; however, there was no observation of structural collapse. Beams which suffered higher deflections were found to exhibit local buckling of the bottom flange and web near their supports. In addition, the steel columns without protection were found to be deformed so that they shortened by about 100 mm. All of the behaviours were considered to have been induced by the restraint to the thermal expansion of these components by adjacent structure which remained much cooler (Newman *et al.*, 2000; 2006).

### 2.3.3 Churchill Plaza building, Basingstoke

In 1991, a fire accident occurred in the Mercantile Credit Insurance Building, Churchill Plaza, Basingstoke. This was a 12-storey building constructed in 1988 with passive board protection to columns and spray protection to the steel downstands of composite floor beams. The bottom face of the composite slab was left unprotected and the building was designed for 90 minutes' fire resistance.

The fire started on the eighth floor and then spread to the tenth floor very quickly, because of the failure of glazing. Fortunately, the fire protection materials performed well, so that there was no permanent deformation to the structural steel frame. Similarly to the Broadgate fire, debonding between the steel decking and the concrete was observed. After the fire, a load test was carried out on the most seriously affected area; however, the slab was observed to have sufficient load-carrying capacity, and was ready to be reused with no structural repair needed.

### 2.3.4 Cardington fire tests

Between 1995 and 2003, a series of fire tests was carried out on an 8-storey steel-framed building at the Building Research Establishment's Cardington Laboratory in the UK. The aim of these tests was to investigate the behaviour of a real building under mainly natural fire situations, and to gather experimental data which could be used to validate the results from numerical analysis of structures in fire.

The composite structural design of the building met the UK national design codes BS 5950 (BSI, 1990a; 1990b) and was verified for compatibility with Eurocodes 3 and 4 (CEN, 1992; CEN, 1994). The whole building's footprint was 21m x 45m, and the overall height was 33m. The floor system consisted of a 0.9mm thick PMF CF70 steel decking with downstand steel beams, with shear studs welded through the trapezoidal steel deck onto both primary and secondary beams in order to ensure composite action. The slab cast onto the decking was of light-weight Grade 35 concrete with 130 mm maximum thickness and A142 (142mm$^2$/m in both directions) anti-crack reinforcement mesh. Two overall views of the building are shown in Figure 2.5 below.

**Fig. 2.5 Cardington fire test building (Foster *et al.*, 2007)**

As described by Kirby (1998), in these tests three main beam sections (305 x 48kg/m UB, 356 x 51kg/m UB and 610 x 101kg/m UB) and three column sections (305 x 198kg/m UC, 305 x 118kg/m UC and 254 x 89kg/m UC) were selected. The design imposed load was 2.5kN/m$^2$ on each floor, except for the roof which was supposed to support a plant room with 7.5kN/m$^2$ loading. Apart from the fifth floor, all other loads were imposed using sand bags each weighing 11kN, uniformly distributed throughout the whole building to simulate typical office loading.

The first six fire tests took place between January 1995 and July 1996. These tests included:

1. Restrained beam;
2. A plane frame;
3. Two corner compartments;
4. A large compartment and an office fire demonstration test.

Another test was carried out in 2003 in order to collect more experimental data on the behaviour of beam-to-beam and beam-to-column connections. This test has also gave the opportunity to verify the suitability of specialized numerical modelling software (Foster *et al.*, 2007). The first 6 tests occurred on various floors; the location of each test is shown in Figures 2.6 and 2.7 below.

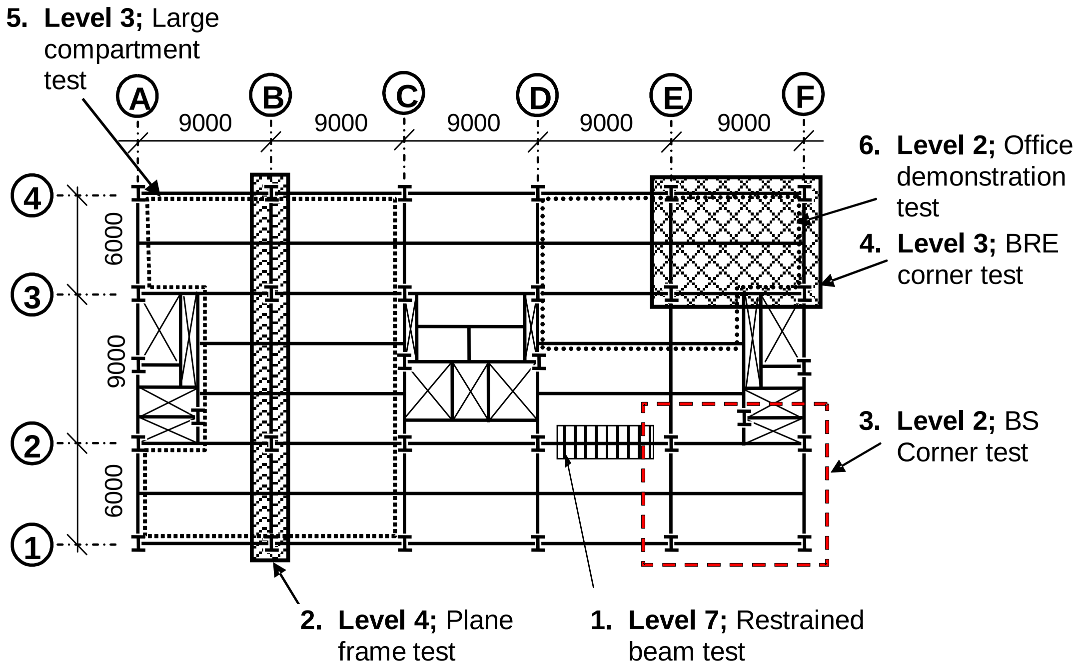

**Fig. 2.6 Locations of first 6 fire tests at Cardington (Foster *et al.*, 2007)**

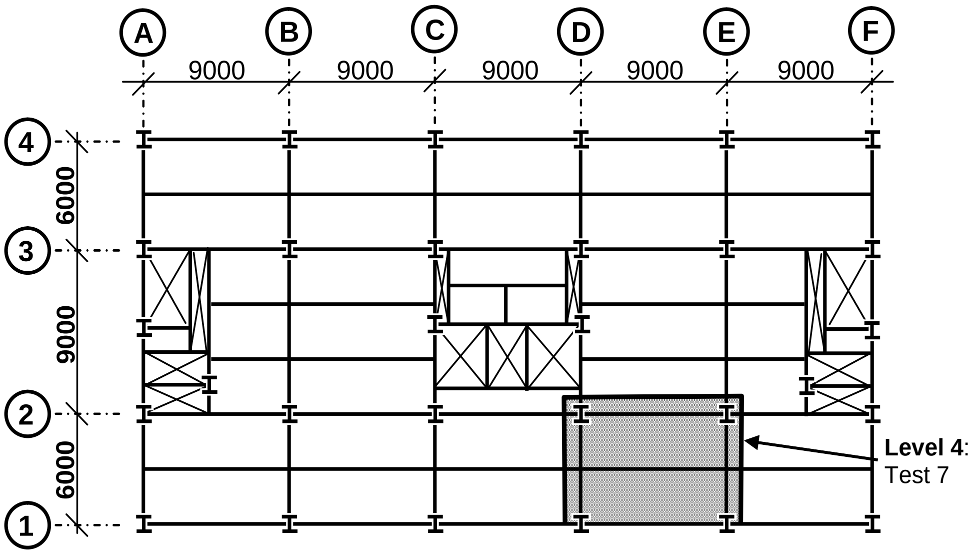

**Fig. 2.7 Location of the seventh test at Cardington (Foster *et al.*, 2007)**

### 2.3.5 Observations from fire accidents and Cardington fire tests

In the Broadgate fire it had been shown that, although some debonding between steel deck and concrete was observed, the composite slab could still maintain its integrity. Moreover, when some structural components had lost their load-carrying capacity in fire, the composite slab with supporting perimeter beams and adjacent structure staying in a cooler condition, made a considerable contribution to the global structural stability. The reason for this effect is the composite slab performing as a highly-deflected membrane which can distribute the loads from the weakened area to the supporting edges, together with the restraints to thermal expansion provided by the surrounding cooler members.

The observations from Churchill Plaza indicated that the conventional design for exposed steelwork protection is over-conservative. The post-fire load test on the most damaged area of the slab gave evidence that extra load carrying capacity exists (SCI and CTICM, 2009).

Observations from the Cardington fire tests once again showed that the traditional fire protection design methods for composite floor systems are very conservative. These traditional design methods suggest either protecting all the steel beams and columns or using the limiting temperature method provided in BS 5950 (BSI, 1990a; 1990b) or the similar Critical Temperature method from Eurocode 3 Part 1-2 (CEN 2005a). According to Bailey and Moore (2000c), in the former method, the ‘Yellow Book’ (ASFP, 1992) is normally used to decide the level of fire protection needed, and it is assumed that the steel member is fully loaded (subject to the normal ULS safety factors) at ambient temperature, which is a highly conservative assumption for loading which coincides with a fire event. However, the conventional design methods obviously ignore the real load-path mechanisms when the composite floor system suffers the large vertical deflections which commonly occur during a fire.

## 2.4 Tensile membrane action

During the late 1960s, a considerable number of theoretical and experimental research papers (Park, 1964a and 1964b; Kemp, 1967; Wood, 1961; Sawczuk, 1965; Hayes, 1968) were published on the performance of reinforced concrete slab floors when large vertical displacements take place. These works indicated that slabs at large vertical deflection are capable of carrying greater loads than those given by the original (small-deflection) yield line theory, because tensile membrane action occurs within the slab whether or not there was horizontal restraint at the slab edges. As mentioned by Bailey (2004), for a given vertical displacement a floor slab with horizontal restraint to movement around its perimeter will have a greater load-carrying capacity compared to an equivalent horizontally unrestrained floor slab. For a slab without horizontal restraint at its boundaries, a ring of compressive membrane force can be seen to be generated within the slab and around its edges, and this provides the horizontal restraint to a field of tensile membrane forces in the slab's central area, as shown in Figure 2.8.

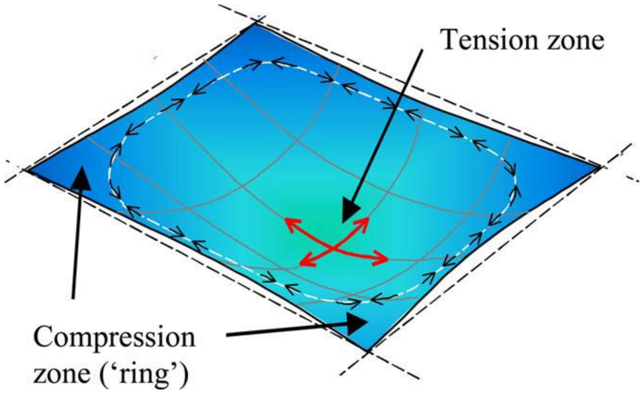

**Fig. 2.8 Membrane action of a floor slab with no horizontal restraint around its perimeter (Bailey, 2004)**

However, the essential condition for the supporting compressive ring to be created is that the vertical displacements at the slab perimeter must remain small as the load increases (Foster *et al.*, 2004). The reason for this requirement was explained by Bailey (2004). If the perimeter beams are able to collapse at the same load as the internal beams, with central plastic hinges forming, a collapse mechanism consisting of a single yield line passing through the whole arrangement of composite beams which forms the slab will make the floor effectively fold along this yield line. Therefore, tensile membrane action can never happen because run-away deflection occurs.

Even though the previous research illustrated some perceptions of the behaviour of slabs at large vertical displacement, no practical context was identified in which tensile membrane action, so the methods generated were not able to be applied in practice. However, the observations from the Cardington fire tests have clearly indicated both that the existing design models for composite floor behaviour at elevated temperature are over-conservative, and that their deflections can become very large; thus the behaviour of concrete slabs at large deflection once again became worthy of attention. Following the results obtained from the Cardington tests, many researchers have simulated these fire tests using experiments (Bailey, *et al.*, 1999; 2000a) and by finite element modelling (Elghazouli, *et al.*, 2000; Gillie, *et al.*, 2002; Huang, *et al.*, 2002; 2003a; 2003b; O'Connor, *et al.*, 2003). After much validation of finite element software, it is now possible to predict the extent and advantage of tensile membrane action of composite floor systems in fire. At the same time, two simplified analytical methods have been developed, by Bailey (2000b; 2001a; 2001b; 2003; 2004) and by Cameron and Usmani (2005a; 2005b). In Bailey's method (often referred to as the Bailey-BRE Method), he assumes that the slab has no horizontal restraint at its edges, so that the membrane action comprises tensile membrane force in the slab's central area surrounded by a ring of compressive membrane force. On the other hand, in Cameron and Usmani's method, it is assumed that the tensile membrane forces developed in the slab can only be balanced by the provision of anchorage along the slab edges, since most of the slab's bending capacity is lost at high temperatures. However, from the small-scale tests and modelling by Foster (2004; 2006) and Abu (2009), it has been shown that thermal gradients acting alone through the depth of the slab can cause significant amounts of tensile membrane stress in axially-unrestrained simply-supported slabs. Contrary to the suggestion made by Cameron and Usmani (2005a; 2005b), it is not essential to provide horizontal edge restraint to sustain this load-carrying mechanism at elevated temperatures. Some other researchers have also developed simplified design methods to determine the capacity of composite slabs in fire including consideration of tensile membrane action (Clifton, 2001; Omer *et al.*, 2006; Li *et al.*, 2007). The Steel Construction Institute (SCI) has adopted the Bailey-BRE method in its design guidance on evaluating the load-carrying capacity of composite slabs in fire (Newman *et al.*, 2000; 2006).

## 2.5 Developments of the Bailey-BRE method

The observations from the Cardington fire tests on composite floor systems showed that the increase in slab load-carrying capacity was due to the development of tensile membrane action in the slab's central area with its perimeter vertically supported. This conclusion concurs with that of the early research studies (Wood, 1961; Park, 1964; Taylor, 1965; Sawczuk and Winnicki, 1965; Kemp, 1967; Hayes, 1968) on tensile membrane action at ambient temperature. Bailey and Moore (2000a; 2000b) initially developed the design method by Hayes (1968) for composite slabs at elevated temperature. In 2000, a 9.5m x 6.5m composite slab test at ambient temperature (Bailey, 2000) was carried out at BRE Garston. In this test, a transverse tension crack penetrating the full slab thickness was eventually observed across the middle of the long span of the slab. At this stage the failure load was 4.81kN/m$^2$ and the vertical deflections were over 650mm. On investigating the test results, tensile membrane action was observed and the eventual failure load was almost twice the load-carrying capacity calculated using the conventional yield-line theory.

In early investigations about membrane action at ambient temperature (Wood, 1961; Hayes, 1968), it had been concluded that when the slab was subjected to an increasing vertical displacement the initial yield-line pattern still remained. This was also observed in the BRE Garston ambient temperature test. This corresponded well with the consistent observations from previous experimental investigations (Bailey, 2000) that a large full depth tensile crack occurs across the slab shorter span at the centre of the longer span. The previous research by Sawczuk and Winnicki (1965) had shown that two possible failure modes exist, as shown in Figure 2.9.

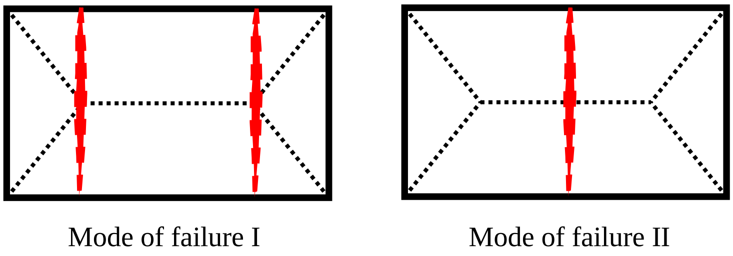
Mode of failure I

Mode of failure II

**Fig. 2.9 Two modes of slab failure mechanism by Sawczuk and Winnicki (Bailey, 2001a)**

The failure mode I (two transverse cracks located at the intersections of yield-lines along the shorter span) was considered the more critical. According to the observations from the BRE Garston test and test results from other investigation, an update of the simple design method took both modes of failure into account (Bailey, 2001a). The fundamental design strategy, illustrated in Figure 2.10, for using the simple design method is that a composite floor is divided into an array of rectangular or square horizontally unrestrained composite slab panels with unprotected internal beams, but with protected beams supporting their edges.

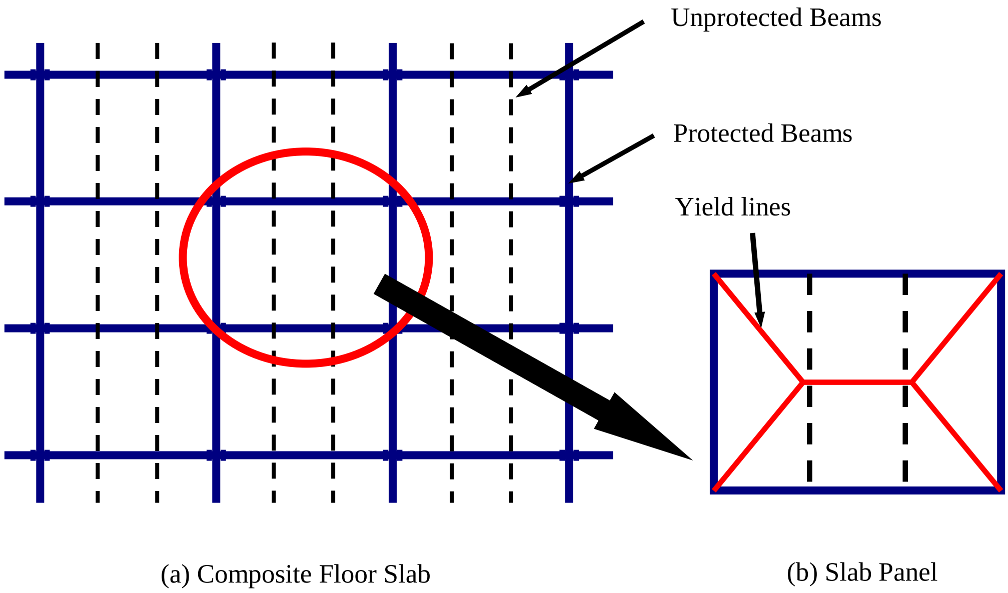

(a) Composite Floor Slab

(b) Slab Panel

**Fig. 2.10 Floor plate division and Schematic of Bailey-BRE Method (Abu, 2009)**

The calculation procedure used by Bailey and Moore (2000b) is almost identical to the previous calculation procedure initiated by Hayes (1968). This method also based on rigid-perfectly plastic yield-line theory, but subjecting the slab to large deflections, and assessing the enhancement of its load-carrying capacity due to tensile membrane action above the traditional small-deflection yield-line load capacity.

However, for the first few years after the simplified design method was developed, there was only one failure mechanism considered in original Bailey-BRE method, which is a full-depth tension crack at the middle of the slab's longer span, aligned across its shorter span (Bailey, 2000; 2001a; 2003; 2004), shown as mode of failure II in Figure 2.9. In 2007, the design method was reviewed and the failure mode was been updated to include not only tensile fracture of reinforcement across the shorter span but also compressive crushing of the concrete slab at its corners (Bailey and Toh, 2007). In this version of the design method, the derivation was also updated to account for the failure mode incorporating two tension cracks from the intersections of the yield lines. The in-plane stress assumption along the yield lines and the central crack is as shown in Figure 2.11.

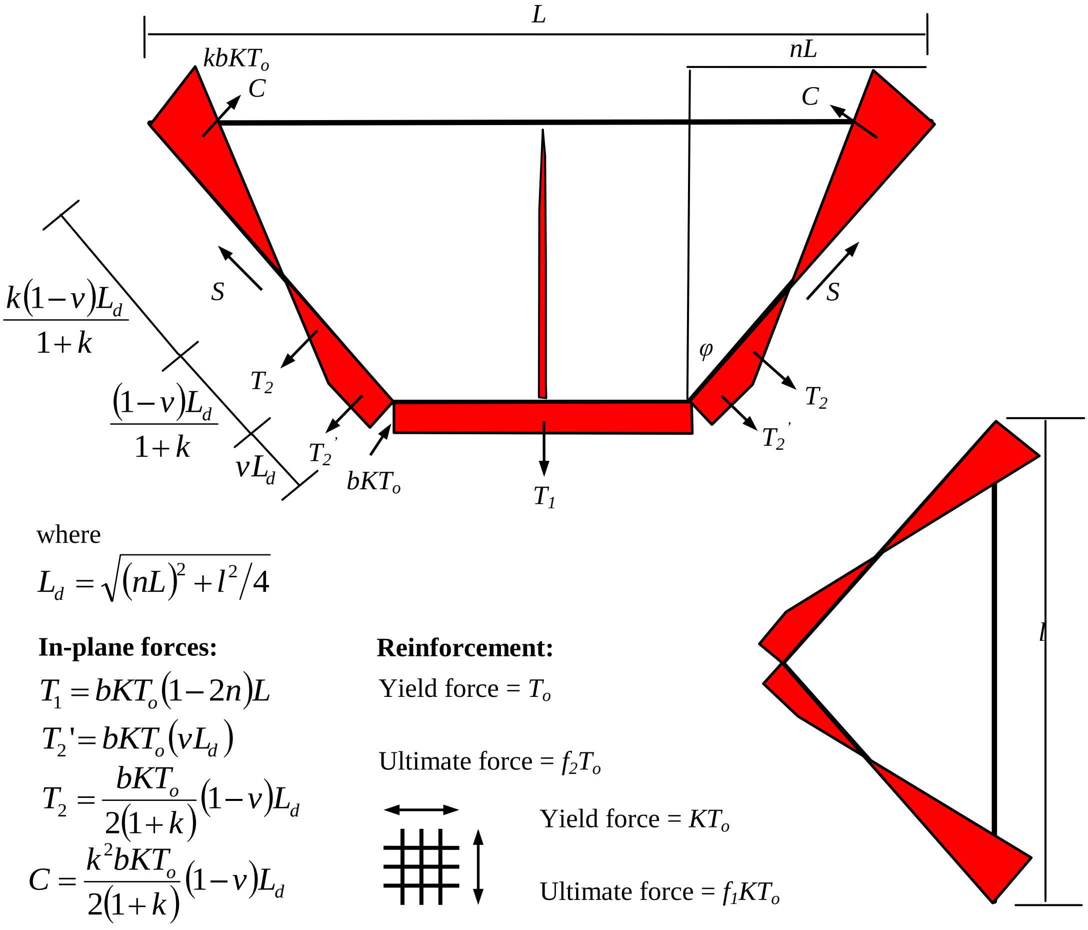

**Fig. 2.11 In-plane stress distribution of updated BRE-Bailey design method (Bailey and Toh, 2007)**

For the updated design method, the modifications included trapezoidal tensile stress blocks instead of a linear stress distribution along the diagonal yield lines. However, the method still neglected any contribution from the tensile strength of concrete to the load capacity, in order to remain conservative. It is assumed that, in reality, the passive fire protection applied to the perimeter beams will keep them at a low enough temperature to control their deflections sufficiently to provide effective vertical support to the slab edges. The load carrying capacity of a composite slab after a given time in fire can be calculated from Equation 2.6.

$$w_{p\theta} = e\left(\frac{Internal\ work\ done\ by\ the\ composite\ slab\ in\ bending}{External\ work\ done\ by\ the\ floor\ per\ unit\ load}\right) + \frac{Internal\ work\ done\ by\ the\ beams\ in\ bending}{External\ work\ done\ by\ the\ floor\ per\ unit\ load} \tag{2.6}$$

In which,

$w_{p,\theta}$ is the load carrying capacity of composite slab at a given time;

$e$ is the enhancement factor calculated by the design method (Bailey and Toh, 2007)

As initially announced by Hayes (1968), the overall enhancement factor $e$ is calculated as,

$$e = e_1 - \frac{e_1 - e_2}{1 + 2\mu a^2} \tag{2.7}$$

in which, $\mu$ is the ratio of the yield moment capacity of the slab in orthogonal directions, and $a$ is the aspect ratio. In the Equation 2.7, when the aspect ratio is equal to 1, and the reinforcement ratio is same in both directions, which the coefficient of orthotropy $\mu$ is equal to 1, $e_1$ and $e_2$ is identical, therefore, the overall enhancement $e$ equals to either one of them. However, if the coefficient $\mu$ is not equal to 1, this equation can not tell if the longer or shorter span dominating the overall enhancement factor. According to Hayes (1968), normally, the value of $e_1$ and $e_2$ is not same and the difference is explained by the effects of vertical shear or in-plane shear. Obviously, this explanation is not enough to resolve the problem caused by the variety of orthotropy.

Prediction of the maximum allowable vertical displacement at the fire limit state is based on the appearance of the central through-depth tension crack. This attempts to combine deflection due to thermal bowing of the slab and mechanical strain in the slab reinforcement, as shown in Equation 2.7. The limitation of deflection due to mechanical strain in reinforcement is 'shorter span/30'. The full derivation, with amendments for both isotropic and orthotropic reinforcement, can be found in the references by Bailey (2000; 2001a; 2001b; 2003; 2004) and by Bailey and Toh (2007).

$$\Delta_\theta = \frac{\alpha(T_2 - T_1)l^2}{19.2h} + \sqrt{\left(\frac{0.5f_{sy}}{E_s}\right) \times \frac{3L^2}{8}} \tag{2.8}$$

in which,

$\alpha$ is the coefficient of thermal expansion of the concrete slab;

$T_2$ and $T_1$ are the bottom and top surface temperatures of the slab;

$L$ and $l$ are the longer and shorter spans of the slab;

$h$ is the effective thickness of the slab;

$f_{sy}$ and $E_s$ are reinforcement strength and Young's modulus.

As mentioned in above, this equation to estimate the maximum allowable deflection includes two sections, thermal effects and mechanical strains in the reinforcement.

*Thermal effects*

When considering the thermal effects, it assumes the slab to be unrestrained with four edges simply supported, also the temperature distribution through the slab is assumed to be linear (Vassart and Zhao, 2013). Announced by Bailey (2001b), for design purposes, the value of ($T_2 - T_1$) for composite slabs can be taken as 770 ℃ for up to 90 minutes fire resistance and 900 ℃ for 2 hours fire resistance.

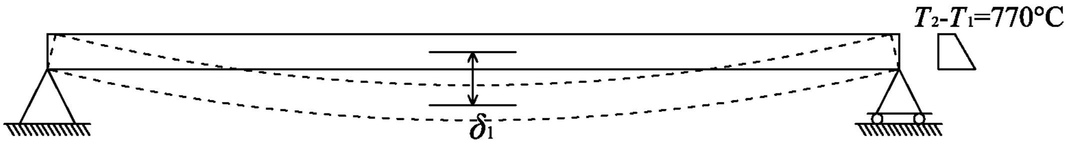

**Fig. 2.12 Slab deflection due to thermal effects**

As illustrated in Fig.2.12, the vertical displacement $\delta_1$ represents the deflection induced by thermal effects as the composite slab definitely will experience thermal curvature when subject to fire condition. The deflection is given by,

$$\delta_1 = \frac{\alpha(T_2 - T_1)l^2}{8h} \tag{2.9}$$

where,

$\alpha$ is the coefficient of thermal expansion

$l$ is the length of the slab shorter span

$h$ is the thickness of the slab

Because the Equation 2.8 is initially based on a one-way spanning slab with assumed linear temperature distribution through the depth, for four edges simply supported slab, a reduction factor of 2.0 is applied at first. However, after comparison to the results from Cardington tests, Bailey and Moore (2000a) had increased the ‘safety factor’ from 2.0 to 2.4, for the purpose of ensuring the deflection limit is conservative. Therefore, the vertical deflection due to thermal effects becomes as,

$$\delta_1 = \frac{\alpha(T_2 - T_1)l^2}{19.2h} \tag{2.10}$$

*Mechanical strains in reinforcement*

In calculating the mechanical strains in reinforcement, it was assumed that the deflected shape of the slab due to transverse loading is parabolic, and the strain in the reinforcement is the same value along the slab length (Bailey and Moore, 2000a). In order to make this assumption which takes transverse loading into account, the slab has to be pin supported as,

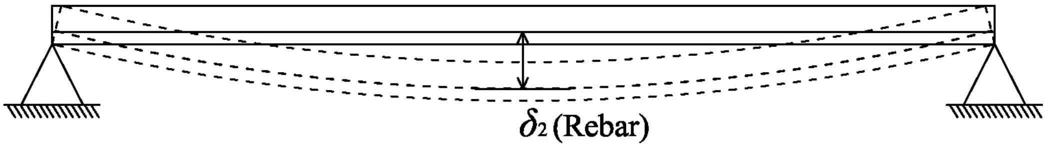

**Fig. 2.13 Slab deflection due to mechanical strains in reinforcement**

and the displacement is given by,

$$\delta_2 = \sqrt{\left(\frac{0.5f_{sy}}{E_s}\right)\frac{3L^2}{8}} \tag{2.11}$$

where,

$E_s$ is the elastic modulus of the reinforcement at room temperature

$f_{sy}$ is the yield strength of the reinforcement at room temperature

$L$ is the length of slab longer span at zero displacement

When calculating the slab deflection considering the membrane forces, the total slab deflection is evaluated by combining the components due to thermal effects and strain in reinforcement, which is,

$$\delta = \delta_1 + \delta_2 \tag{2.12}$$

in which,

$$\delta_2 \leq \frac{l}{30} \tag{2.13}$$

However, as we look into these two components which are combined together, in fact, the two equations are concluded from two situations with different types of support. In the first equation, it assumes the slab is simply supported on all edges, which implies that there is no transverse force existed in the system. But when it calculating the deflection due to strains in the reinforcement, it assumes the deflection shape of the slab is due to transverse loading. In this case, the deflection due to thermal effects and strains in the reinforcement cannot be just simply added up but need further investigations.

## 2.6 Extension and validation of BRE-Bailey method

The original Bailey-BRE method has been extended to include the effects of continuity and additional reinforcement which may sometimes be placed in the slab ribs, by Clifton (2001). In his method, the capacity of the unprotected beams at high temperature was also considered in the yield-line calculation.  This method checks the individual components of a slab panel, such as protected beams and columns. Following Clifton’s method, Bailey (2004) investigated the contribution of the unprotected beams in catenary action to the load carrying capacity, and concluded that it is usually negligible.

Usmani and Cameron (2004) also developed a 3-step design method to calculate the load capacity of horizontally restrained composite slabs at elevated temperatures. The origin of this method was from the results of numerical and analytical research following the Cardington tests, and proposed that the main factor which governed the behaviour of composite slabs at elevated temperatures was thermal strain. It asserted that the deflected shape due to thermal bowing is the main aspect of behaviour which leads to tensile membrane action. It also assumed that the bending resistance of a composite slab can be ignored when it is subject to large displacements, such as in the fire condition. The temperature distribution through the slab thickness is predicted for a given fire situation, and the change of slab shape and membrane stress and strain due to the thermal condition are determined. The energy balance method is then adopted to determine the maximum collapse load of the slab.

Since the cost of carrying out full-scale composite slab tests in fire is extremely high, some analysis programs based on the finite element method have been developed in order to simulate the behaviour of composite slabs under fire conditions. These programs include *Vulcan* (Bailey, 1995; Najjar and Burgess 1996; Huang, *et al.* 1999; 2000; 2004a; 2004b) developed at the University of Sheffield to analyse steel and concrete structures; ADAPTIC, developed at Imperial College in London; SAFIR, from the University of Liège in Belgium, and ABAQUS which is a general-purpose finite element program. These finite element programs have been employed by many researchers to verify the results from experiments, and can show tensile membrane action at elevated temperatures. From comparison of results using *Vulcan*, Huang, *et al.* (2004a) indicated that both the simplified design method and *Vulcan* output confirm that the existence of tensile membrane action in concrete slabs greatly influences the integrity of composite floor systems at large deflections. The paper also concludes that the Bailey-BRE method tends to predict larger load capacity enhancements caused by tensile membrane action than the modelling using *Vulcan* analysis; this means that the Bailey-BRE method may predict greater fire resistance finite element modelling can justify (Huang, *et al.* 2004a).

Foster (2006) conducted a series of experiments on small-scale slabs to verify the tensile membrane action behaviour of concrete slabs at ambient and elevated temperatures. The test results were generally in accordance with the Bailey-BRE method at ambient temperature (Foster *et al.*, 2004). However, at elevated temperatures, it indicated that the transverse crack across the shorter span could be observed before the yield line pattern was seen to form, as the material strength decreased dramatically. The appearance of the transverse crack was unexpected, but occurred without any sign of structural failure. From these tests, it was also observed that slabs showed higher capacity when using reinforcement with low bonding to the concrete (Foster, 2006).

Since the development of Bailey-BRE design method, many researchers have carried out extensive work. Bailey and Toh (2007a; 2007b) performed a series of experiments on small-scale concrete slabs at ambient and elevated temperatures. The experiments showed that the mild steel reinforcement was crucial to the appearance of tensile membrane action, since the collapse of the slab can be avoided when it is subject to large deflections. In the tests, two modes of failure were observed at ambient temperature: with lower reinforcement ratios applied; tensile fracture of reinforcement occurring across the middle of the slab, and (with higher reinforcement ratios) compressive crushing happening at the slab corners. The simplified design method was updated, although compressive crushing was not observed in the elevated temperature tests (Bailey and Toh, 2007a; 2007b).

In spite of some discrepancies between the Bailey-BRE method and other investigations, tensile membrane action is absolutely a potentially useful tool to develop a performance-based fire engineering design method. However, in the Bailey-BRE method, the initial step is to divide the composite floor system into rectangular or square slab panels. This is the major limitation to analysing non-orthogonal slab panels. The research outlined in this thesis will therefore search for solutions for floor slabs which can not be divided into orthogonal shapes, and to extend simplified models to be applicable for non-orthogonal slab panels.

## 2.7 Summary

In this chapter, the material properties and key properties of steel and concrete that influence their structural behaviour in fire conditions have been reviewed. Relevant current design processes and research in structural fire engineering have also been summarized. Previous tests have indicated that the phenomenon of tensile membrane action exists, and that prescriptive standards for composite floor design are over-conservative. The traditional fire resistance test procedure is not accurate or appropriate in determining the structural behaviour, because the behaviour of isolated elements under test differs from that of members in whole structures.

As the foundation of the manual calculation method of tensile membrane action, the yield-line theory and the work balance method have been reviewed. Since yield-line theory is an upper-bound method, for slabs of any geometry the correct load bearing capacity can only be determined by assuming the correct yield-line pattern. In other words, if a comprehensive set of different yield-line patterns are assumed the minimum load capacity obtained from the set using the work-balance method determines the correct yield-line pattern.

The development of performance-based design methods within fire safety engineering has been described. The previous investigations and researches into tensile membrane action and the development of the BRE-Bailey method have been summarized. Earlier research into tensile membrane action at ambient temperature, based on yield-line theory for slabs at small deflections, has been developed by several researchers into the high-temperature stage. Although the BRE-Bailey method has been widely adopted, there are still some shortcomings which are currently unexplained.

# Chapter 3 Penalty function method and relative constraints

## 3.1 Introduction of penalty function method

Most optimization problems attempt to provide solutions within a set of defined constraints. The set of solutions which are obtained as the final result of an evolutionary search must necessarily be feasible; that is, they must satisfy all constraints (Smith and Coit, 1995). Several methods exist to take into account the constraint relationships. The penalty function method is one of these ways, using a series of unconstrained problems to replace a problem with constraints. Each unconstrained problem is formed by adding a term which is called a penalty function to the objective function. The penalty functions each consist of a penalty parameter multiplied by the equation of one of the constraints. The measure of violation of a constraint is non-zero when the constraints are violated and is zero when constraints are not violated. Generally, two basic types of penalty functions exist: exterior penalty functions, which penalize unfeasible solutions, and interior penalty functions, which penalize feasible solutions.

The advantages of the penalty function method are that the size of the system matrix is preserved, and multiple constraints can be handled, whether they act on a single node or many nodes. Imposing a constraint using a penalty function means that the equation of constraint is multiplied by a parameter (called penalty parameter) which is defined by the user, and the result is then added to the whole system of equations (Askes and Ilanko, 2006). However, the main limitation of the penalty function method can not be neglected. In practice, the difficulty of selecting a suitable value of the penalty parameter is the most significant shortcoming of the method. If the penalty parameter is assigned too small a value, implementation of constraints cannot be absolutely achieved, but if an over large value is given to the penalty parameter, the tolerance during nonlinear solution will affect the final results. Exact answers would be generated if the penalty parameter were able to approach infinity. Obviously this is not feasible in practical computational solution processes, so the penalty parameter is normally set as a very large number, which is positive in order to ensure positive-definiteness of the resulting system of equations (Bathe 1996; Hughes 2000; Zienkiewicz and Taylor 2000). However, if the value of the penalty parameter is set too large, this will destroy the conditioning of the matrix, which means that solution of the system of equilibrium equations becomes impossible.

## 3.2 Aims and objective of using penalty functions method

As modern architecture develops, numerical investigations on structural behaviour which utilize tensile membrane action can not restrict themselves to rectangular meshing. Although simplified methods can divide the internal floor areas of a building into rectangular or square panels, the problem of slabs at non-orthogonal edges of buildings still exists. The edge slab panel ABCD, shown in Fig. 3.1, can not logically be divided into rectangular or square panels, and so although membrane action can be analysed, this requires the boundary conditions to be reset. In this case, as the three internal edges are not orthogonal to each other, not all boundary conditions at these edges can be set in terms of simple freedom or restraint of degrees of freedom aligned parallel to the global coordinates.

Generally, when the edges of a slab are parallel to one or other of the global coordinate axes, the boundary conditions are easily set as restraint or freedom of the degrees of freedom at nodes, since each of these degrees of freedom represents a movement along or about these axes. However, if the edges are not set parallel these axes, it is impossible to define the boundary conditions based on the global coordinate axis directions, because the movements of the edges which require to be constrained are not along or perpendicular to these axes, but are aligned to the local coordinate system. In order to resolve this problem, the penalty function method needs to be applied, so that the movements of edge nodes which need to be constrained can be determined as relationships between global degrees of freedom, rather than as simple restraint or freedom of these degrees of freedom.

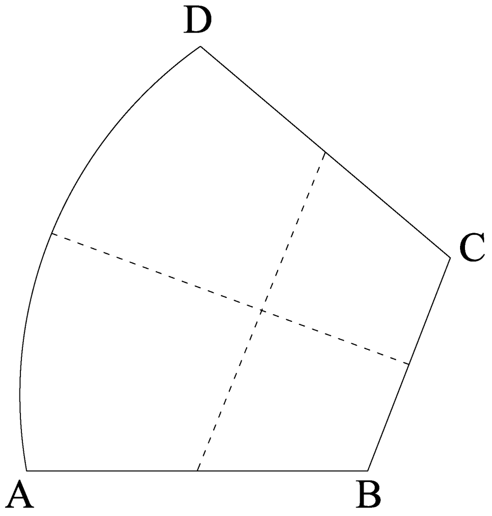

**Fig. 3.1 Typical slab panel at edge of a modern building**

In addition to imposing logical boundary conditions for non-rectangular slabs, the continuity boundary conditions can be resolved for sub-panels of large slab areas by applying the penalty function method.

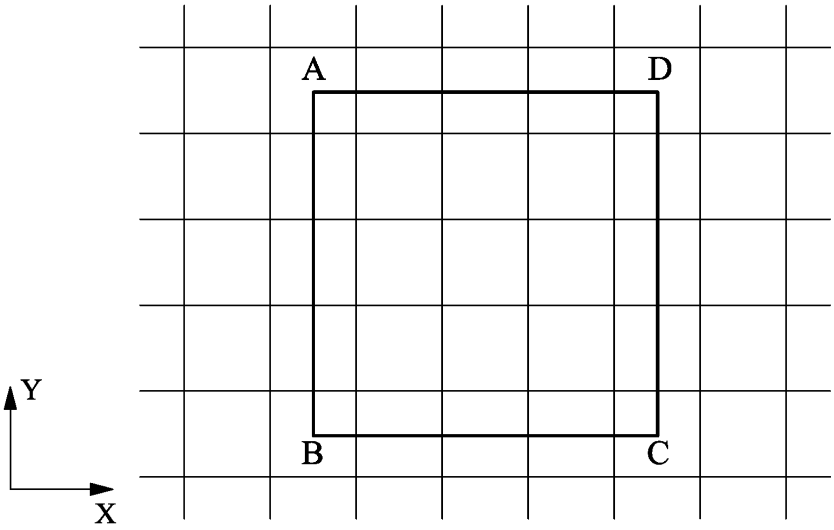

**Fig. 3.2 Slab analysis of a sub-panel with continuity boundary modelling**

In some cases, it is necessary to analyse the performance of slab elements for a specific area of a whole floor panel. When defining the boundary conditions of this area, it is often unreasonable to set up restraints as simple on/off switches on the global degrees of freedom. Obviously, as shown in Fig. 3.2 above, the boundaries of the area for analysis are not outer edges of the floor panel, and so the degrees of freedom at nodes on the boundaries AB, BC, CD and AD can not logically be set as restrained or free to move, because the movements of nodes on these boundaries must be compatible with those of the adjacent slab panels. Their movements may exist in absolute terms but not be totally free to do so. In order to keep the transverse movements compatible with adjacent slabs which are assumed to behave identically, the transverse nodal displacements of the separating boundaries can be set to be identical when these edges move, so that the edges moves as straight lines transverse to their alignment. This process can be modelled by using the penalty function method to set the relationship between the relevant degrees of freedom at adjacent nodes in pairs to have identical displacements.

## 3.3 Application of penalty function method

In order to impose the penalty functions onto a structural analysis, the process involves 4 steps, as follows:

In a linear analysis (which is an incremental analysis under a Newton-Raphson solution process), from Hooke's law the deformation in any degree of freedom is directly related to the generalized forces applied to it. Therefore, a system of linear equations can be written as,

$$\boldsymbol{K} \cdot \boldsymbol{u} = \boldsymbol{f}$$

Here ***K*** is the global stiffness matrix which represents the aggregated force-deformation relationships for the model. Each stiffness is related to the nature of the deformation in each degree of freedom. Generally, each stiffness will be a function of the Young's modulus ***E***, and a sectional parameter (the area of the element ***A***, or the second moment of area ***I.*** As ***u*** is the vector of amplitudes of the degrees of freedom of the nodal, such as the displacements and rotations at all the nodes, and there are 6 degrees of freedom at each node, which are the displacements in the *X*, *Y* and *Z* directions and the rotations about these 3 directions. The vector ***f*** represents the external forces acting on the degrees of freedom. In the calculation procedure, ***K*** is a symmetric matrix of the form $\begin{bmatrix} k_{11} & k_{12} & k_{13} & \cdots \\ k_{21} & k_{22} & k_{23} & \cdots \\ k_{31} & k_{32} & k_{33} & \cdots \\ \vdots & \vdots & \vdots & \ddots \end{bmatrix}$, in which $k_{12}=k_{21}$, $k_{13}=k_{31}$, $k_{23}=k_{32}$ ….And ***u*** is a column vector of d.o.f. of the form $\begin{Bmatrix} u_{1x} \\ u_{1y} \\ u_{1z} \\ \theta_{1xy} \\ \vdots \end{Bmatrix}$, in which $u_{1x}$, $u_{1y}$ and $u_{1z}$ are the orthogonal in-plane and transverse panel displacements and rotations about each axis at Node 1, respectively, and the $\boldsymbol{f}$ is a column vector of external forces corresponding to each degree of freedom at the node, of the form $\begin{Bmatrix} f_{1x} \\ f_{1y} \\ f_{1z} \\ f_{2x} \\ f_{2y} \\ f_{2z} \\ \vdots \end{Bmatrix}$.

After the stiffness matrix and the linear equations have been set up, it is necessary to impose the relative boundary conditions. This involves setting up the penalty parameter matrix $\boldsymbol{\alpha}$ . In most cases, $\boldsymbol{\alpha}$ is a diagonal matrix with components $\alpha_i$, of the form $\begin{bmatrix} \alpha_i & \cdots & 0 \\ \vdots & \ddots & \vdots \\ 0 & \cdots & \alpha_i \end{bmatrix}$. Before imposing the $\boldsymbol{\alpha}$ matrix**,** it is necessary to set up the matrix representing the constraint conditions. In order to find this matrix of constraints, it is necessary to write the constraint equations representing the physical boundary conditions provided. The components of the matrix of constraints are the coefficients of the equation. After that we can impose $\boldsymbol{\alpha}$ into the process by multiplying the matrix of constraints [C], the diagonal matrix of the penalty parameter $[\boldsymbol{\alpha}]$, and the transposed matrix of constraints $[\mathrm{C}]^T$:

$$[\mathrm{C}]\,[\alpha]\,[\mathrm{C}]^T$$

The next step is to add this to the stiffness matrix:

$$[K]+[\mathrm{C}]\,[\alpha]\,[\mathrm{C}]^T$$

This new matrix will replace the original stiffness matrix $[K]$, so that the stiffness equation becomes,

$$([K]+[\mathrm{C}]\,[\alpha]\,[\mathrm{C}]^T)\cdot\{u\}=\{F\} \tag{3.1}$$

Solving this new equation, answers which contain the penalty parameter $\boldsymbol{\alpha}$ are found. These solutions can also be checked against the answers from the original linear equation, by setting the $\boldsymbol{\alpha}$ value to infinity.

## 3.4 Examples of application of penalty functions

### 3.4.1 Cantilever with axial force

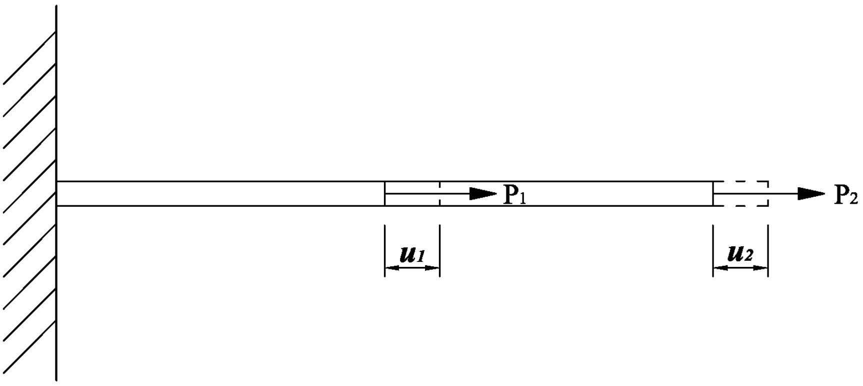

**Fig. 3.3 Cantilever with axial force**

The node movement is constrained to $u1 = u2$. The calculation procedure is as follows:

Constraint equation:

$$u1 - u2 = 0 \tag{3.2}$$

Matrix of constraint: [C] =$[1 \quad -1]$

$[C]^T = \begin{bmatrix} 1 \\ -1 \end{bmatrix}$

By using physical balance analysis, the equilibrium equations can be written as:

$$2ku_1 - ku_2 = P_1 \tag{3.3}$$

$$-ku_1 + ku_2 = P_2 \tag{3.4}$$

The stiffness matrix of the unconstrained system is:

$$\begin{bmatrix} 2k & -k \\ -k & k \end{bmatrix}$$

The penalty function is imposed:

$$\left(\begin{bmatrix} 2k & -k \\ -k & k \end{bmatrix} + \begin{bmatrix} 1 \\ -1 \end{bmatrix} [\alpha][1 \quad -1]\right) \begin{Bmatrix} u_1 \\ u_2 \end{Bmatrix} = \begin{Bmatrix} P_1 \\ P_2 \end{Bmatrix}$$

(3.5)

The solutions are then:

$$u_1 = \frac{P_1 + P_2}{k}$$

(3.6)

$$u_2 = \frac{(k+\alpha)P_1 + (2k+\alpha)P_2}{k(k+\alpha)}$$

(3.7)

As $\alpha$ becomes very large, $u_2$ tends towards $\frac{P_1+P_2}{k} = u_1$, which is in accordance with the constraint conditions. As $\alpha$ approaches 0, the constraint is in the process of vanishing, and the solutions will be same as those from the unconstrained system.

### 3.4.2 Cantilever with vertical loads

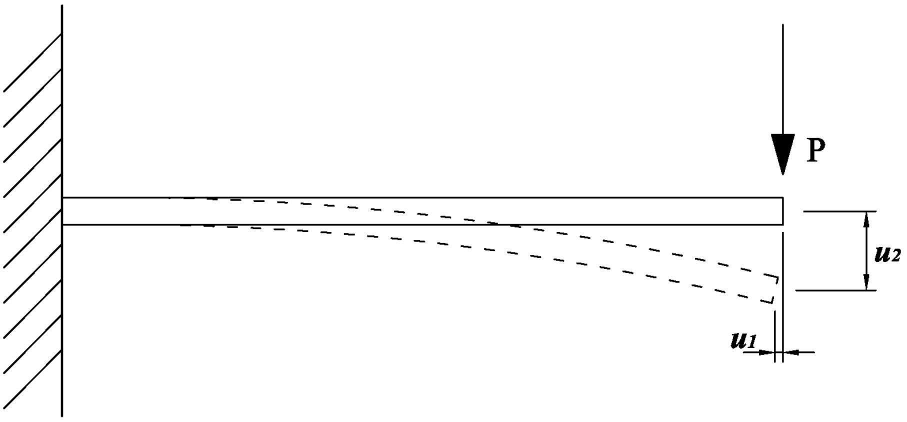

**Fig. 3.4 Cantilever with vertical point load at its end**

The relationship between the displacements in the *X* and *Y* directions is constrained to be $u_1 = u_2 \tan\theta$. We can simply assume the boundary condition and the subsequent process as:

Constraint:

$$u_1 - u_2 \tan\theta = 0$$

(3.8)

$$[\mathrm{C}] = [1 \quad -tan\,\theta]$$

(3.9)

$$[\mathrm{C}]^T = \begin{bmatrix} 1 \\ -\,tan\,\theta \end{bmatrix}$$

The stiffness matrix: $\begin{bmatrix} k_1 & 0 \\ 0 & k_2 \end{bmatrix}$

(where $k_1 = \frac{EA}{l}$ and $k_2 = \frac{3EI}{l^3}$ for a uniform elastic section)

Unconstrained stiffness equations: $\begin{bmatrix} k_1 & 0 \\ 0 & k_2 \end{bmatrix} \begin{Bmatrix} u_1 \\ u_2 \end{Bmatrix} = \begin{Bmatrix} 0 \\ P \end{Bmatrix}$

Penalty function imposed:

$$[\mathrm{C}]^T \alpha [\mathrm{C}] = \begin{bmatrix} 1 & -\,tan\,\theta \\ -tan\theta & tan^2\theta \end{bmatrix} [\alpha]$$

$$= \begin{bmatrix} \alpha & -\,\alpha tan\,\theta \\ -\alpha tan\theta & \alpha tan^2\theta \end{bmatrix}$$

(3.10)

The stiffness equations with constraints:

$$\begin{bmatrix} k_1 + \alpha & -\alpha tan\theta \\ -\alpha tan\theta & k_2 + \alpha tan^2\theta \end{bmatrix} \begin{Bmatrix} u_1 \\ u_2 \end{Bmatrix} = \begin{Bmatrix} 0 \\ P \end{Bmatrix}$$

(3.11)

The solution is found as,

$$u_1 = \frac{P\alpha.tan\theta}{k_1 k_2 + \alpha(k_1 tan^2\theta + k_2)}$$

(3.12)

When $\alpha$ approaches infinity,

$$u_1 = \frac{Ptan\theta}{k_1 tan^2\theta + k_2}$$

The second root is,

$$u_2 = \frac{P(k_1 + \alpha)}{k_1 k_2 + \alpha(k_1 tan^2\theta + k_2)} \tag{3.13}$$

As $\alpha$ approaches infinity,

$$u_2 = \frac{P}{k_1 tan^2\theta + k_2}$$

It can be seen that $u_1 = u_2\, tan\,\theta$, which satisfies the constraint assumed. If $\alpha$ approaches 0, the solutions tend to $u_1 = 0, u_2 = \frac{P}{k_2}$, which correspond to the solutions for the system without constraints.

### 3.4.3 Continuous beam with vertical loads

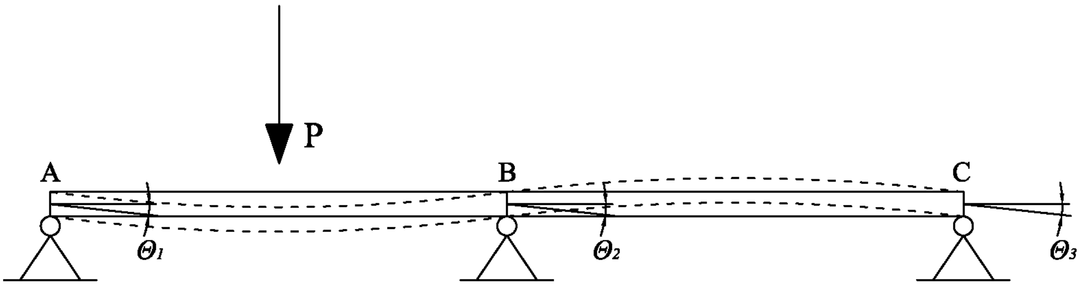

**Fig. 3.5 Continuous beam with point load within one span**

By using the Slope-deflection Method, for a central point load *P*,

$$M_{AB}^F = +\frac{Pl}{8}$$

$$M_{BA}^F = -\frac{Pl}{8}$$

and,

$$M_{AB} - M_{AB}^F = \frac{2EI}{l}(2\theta_1 + \theta_2) \tag{3.14}$$

$$M_{BA} - M_{BA}^{F} = \frac{2EI}{l}(\theta_1 + 2\theta_2)$$

(3.15)

In this same way, we can write the equations for the span BC:

$$M_{BC} - M_{BC}^{F} = \frac{2EI}{l}(2\theta_2 + \theta_3)$$

$$M_{CB} - M_{CB}^{F} = \frac{2EI}{l}(\theta_2 + 2\theta_3)$$

(3.16)

Eliminating the internal moments,

$$\frac{2EI}{l}(2\theta_A + \theta_B) = \frac{Fl}{8}$$

(3.17)

$$\frac{2EI}{l}(\theta_A + 4\theta_B + \theta_C) = -\frac{Fl}{8}$$

(3.18)

$$\frac{2EI}{l}(\theta_B + 2\theta_C) = 0$$

(3.19)

In matrix form, the stiffness equations can be represented as,

$$\frac{2EI}{l}\begin{bmatrix} 2 & 1 & 0 \\ 1 & 4 & 1 \\ 0 & 1 & 2 \end{bmatrix} \begin{Bmatrix} \theta_1 \\ \theta_2 \\ \theta_3 \end{Bmatrix} = \frac{Fl}{8}\begin{bmatrix} -1 \\ 1 \\ 0 \end{bmatrix}$$

(3.20)

We now impose an additional constraint $\theta_3 = 0$

As there are 3 degrees of freedom which need to be considered, and the constraint is $\theta_3 = 0$, the coefficients of $\theta_1$ and $\theta_2$ are 0, so that,

$$[\mathrm{C}] = [0 \;\; 0 \;\; 1]$$

$$[\mathrm{C}]^T = \begin{bmatrix} 0 \\ 0 \\ 1 \end{bmatrix}$$

$$[\mathrm{C}]^T \alpha [\mathrm{C}] = \begin{bmatrix} 0 \\ 0 \\ 1 \end{bmatrix} \alpha [0 \;\; 0 \;\; 1] = \begin{bmatrix} 0 & 0 & 0 \\ 0 & 0 & 0 \\ 0 & 0 & \alpha \end{bmatrix}$$

(3.21)

Now imposing the penalty function:

$$[K] + [\mathrm{C}]^T \alpha [\mathrm{C}] = \begin{bmatrix} \frac{4EI}{l} & \frac{2EI}{l} & 0 \\ \frac{2EI}{l} & \frac{8EI}{l} & \frac{2EI}{l} \\ 0 & \frac{2EI}{l} & \frac{4EI}{l} + \alpha \end{bmatrix}$$

(3.22)

$$\begin{bmatrix} \frac{4EI}{l} & \frac{2EI}{l} & 0 \\ \frac{2EI}{l} & \frac{8EI}{l} & \frac{2EI}{l} \\ 0 & \frac{2EI}{l} & \frac{4EI}{l} + \alpha \end{bmatrix} \begin{Bmatrix} \theta_1 \\ \theta_2 \\ \theta_3 \end{Bmatrix} = \frac{Fl}{8} \begin{bmatrix} 1 \\ -1 \\ 0 \end{bmatrix}$$

(3.23)

$$\begin{cases} \frac{4EI}{l}\theta_A + \frac{2EI}{l}\theta_B = \frac{Fl}{8} \\ \frac{2EI}{l}\theta_A + \frac{8EI}{l}\theta_B + \frac{2EI}{l}\theta_C = -\frac{Fl}{8} \\ \frac{2EI}{l}\theta_B + \left(\frac{4EI}{l} + \alpha\right)\theta_C = 0 \end{cases}$$

(3.24)

Solving the equations,

$$\theta_A = \frac{Fl^2(52\alpha l + 18EI)}{16EI(7\alpha l + 24EI)}$$

(3.25)

$$\theta_B = -\frac{3Fl^2(\alpha l + 4EI)}{16(7\alpha l + 24EI)}$$

(3.26)

$$\theta_C = \frac{3Fl^2}{192EI + 56\alpha l} \tag{3.27}$$

As $\alpha$ becomes large, $\theta_C$ approaches 0, which corresponds to the constraint imposed. For the other degrees of freedom, $\theta_A$ approaches $\frac{13Fl^2}{28EI}$, and $\theta_B$ approaches $-\frac{3Fl^2}{112EI}$.

## 3.5 Validation of penalty function method in *Vulcan*

### 3.5.1 Orthogonal composite slab with applied constraints

As a first step in applying constraints using the penalty function method, a comparison between an orthogonal slab with specific independent boundary conditions and relative boundary conditions is made. The purpose of this comparison is to determine the extent to which relative boundary constraints influence tensile membrane action in comparison to the usual fixed/free displacements.

A slab panel of dimensions 7.5m x 9.0m, with its composite beams designed for a 60-minute fire resistance period was chosen. The slab panel is designed as an array of composite secondary beams 7.5m long, at 3m spacing, of which those not directly connected to columns are supported by 9.0m primary beams. The sample orthogonal slab is modelled with 30 elements (*1.5m* × *1.5m* each) with properties:

**Material properties:**

- Normal weight concrete (Siliceous aggregate), with compressive strength 45*MPa* at ambient temperature;
- Yield strength of reinforcing steel at ambient temperature: 265*MPa*;
- Young’s modulus of reinforcing steel at ambient temperature: 200*GPa*;

**Slab properties:**

- The thickness of the flat slab analysed is 100*mm*; since this is actually a ribbed slab it is given equivalent stiffness coefficients in its two principal directions which are appropriate to a trapezoidal lower edge giving a maximum physical depth of 130mm and a minimum depth of 70mm;
- The flat slab is divided into 13 layers;

- The fourth and fifth layers from the bottom of the slab are uniaxial steel reinforcement layers;

**Load properties:**

| **Permanent Loads** | *kN/m*$^2$ | **Imposed Loads** | *kN/m*$^2$ |
|---|---|---|---|
| Concrete Slab self-weight | 2.40 | Variable load | 3.5 |
| Steel Beam self-weight | 0.20 | Partitions, ceilings/services | 1.7 |
| Reinforcement Mesh | 0.03 | | |

**Table. 3.1 Slab panel design loading**

According to SCI P-288 (Newman *et al.*, 2006) and the design load given in Table 3.1, a reinforcement mesh size of A193 (193mm$^2$/m in each direction) was selected.

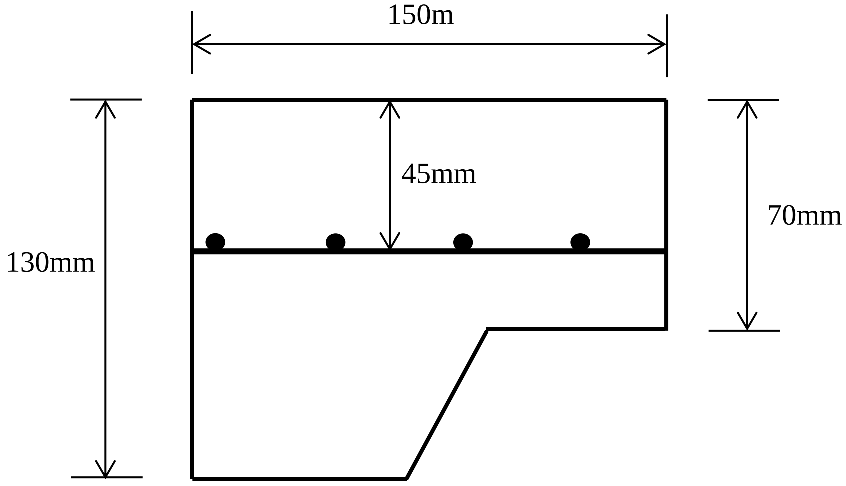

**Fig. 3.6 Concrete slab physical cross-section with trapezoidal decking profile**

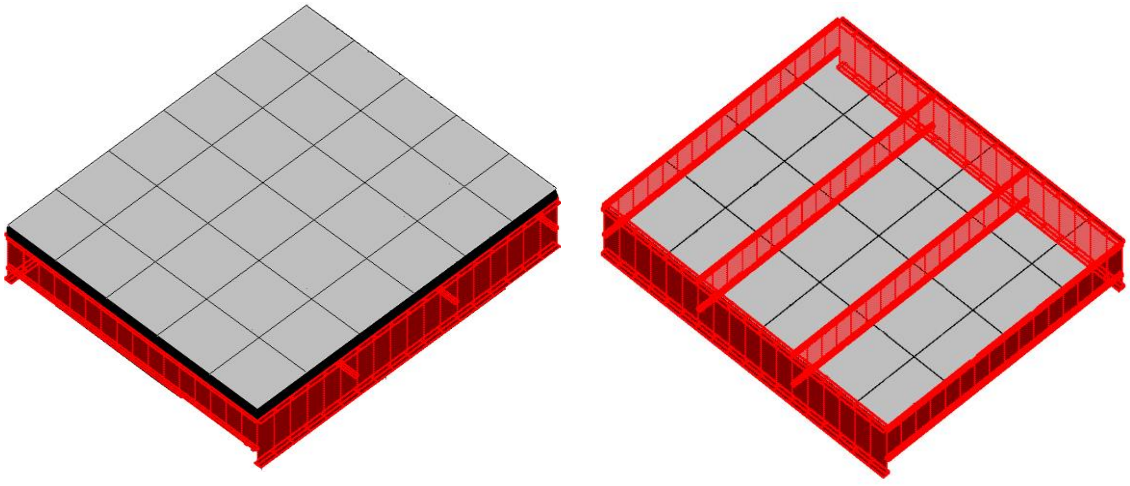

**(a): Slab panel top face** **(b): Slab panel bottom face**

**Fig. 3.7 The 9.0m x 7.5m slab panel analysed in *Vulcan***

Ambient- and elevated-temperature design of the floor beams was carried out using Eurocode 4 Part 1-1 (CEN, 2005a) and Eurocode 4 Part 1-2 (CEN, 2005b), assuming full composite action between the beams and the slab. The design resulted in the choice of 356x127x33UB and 533x210x82UB as secondary and primary beams respectively. The finite element analyses were performed with *Vulcan* (Najjar and Burgess 1996, Huang, *et al.*, 1999; 2000; 2004). Because the physical cross-section of the slab panel is different in the two principal directions, an equivalent solid slab of 100mm thickness (the average physical depth of the composite slab) is used. The distribution of temperature through the 13 layers was carried out by the program FPRCBC-T (Huang *et al.*, 1996) subjected to the ISO834 standard temperature-time curve.

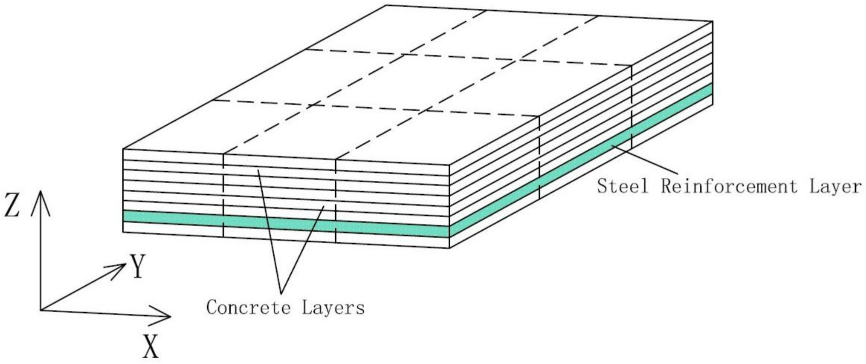

**Fig. 3.8 Division and layers of reinforced concrete slab**

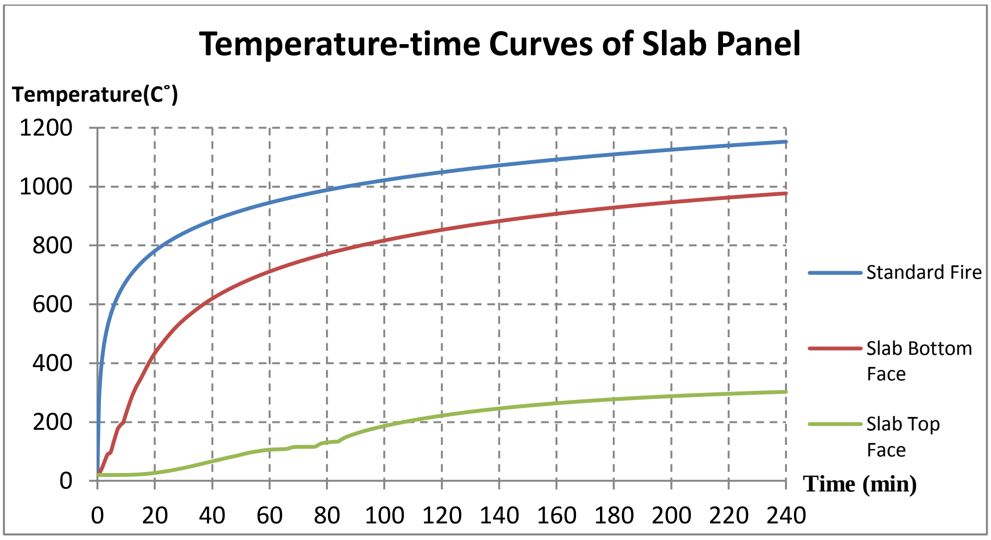

**Fig. 3.9 Temperature-time curves; standard fire, top and bottom faces of slab panel**

In order to display how the penalty function approach works, the node numbers on one of the slab's short-span edges are assigned as shown in Fig. 3.10 below. Because the aim of this test is to verify the influence of the movement of the edge of a slab which is geometrically symmetric, only the left edge node numbers are shown.

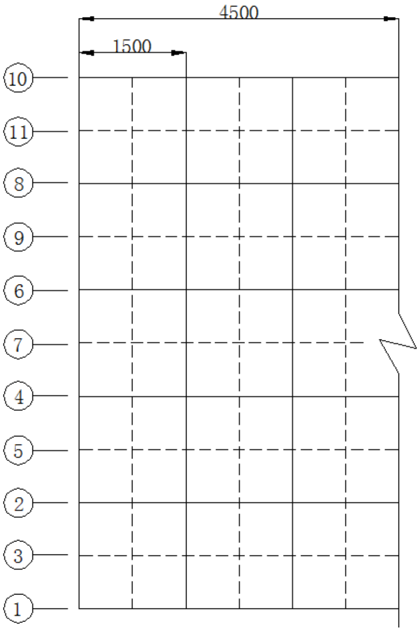

**Fig. 3.10 Geometry and layout of the slab sample**

When using *Vulcan* to process the calculation procedure, the most significant task was in amending *Vulcan* to add the constraint matrix, which is read from the input file, onto the original stiffness matrix. Before analysis it is necessary to define the values of the coefficients which represent the relationships between pairs of d.o.f. and the positions of these two d.o.f., in the <RELATIVE CONSTRAINTS> block in the *Vulcan* input file. In the <RELATIVE CONSTRAINTS> block, the user defines two or more groups of data to describe the relationships as shown below:

$$a_1 \quad i_1 \quad e_1, \quad a_2 \quad i_2 \quad e_2, \quad a_3 \quad i_3 \quad e_3 \ldots\ldots$$

in which,

$a$ is the node number which needs relative boundary restraint applied to it,

$i$ is the $i^{th}$ degree of freedom, needing be restrained,

$e$ is the coefficient needed to define the relationship.

In order to illustrate the influence of relative constraints, two models with simple vertical support on all edges have been employed. In the model with normal boundary conditions, all four edges are vertically supported but free to move in the *X* and *Y* directions. On the other hand, in the model with relative constraints, the four edges are also vertically supported, but the two edges along the short span are equipped with a pre-defined boundary condition constraining the *X*-direction movements of nodes on those edges to be equal to each other, which aims to make the edge move as a straight line.

After the geometrically nonlinear analysis, the horizontal displacements of one edge of the slab above are shown in Figs. 3-11 to 3-13.

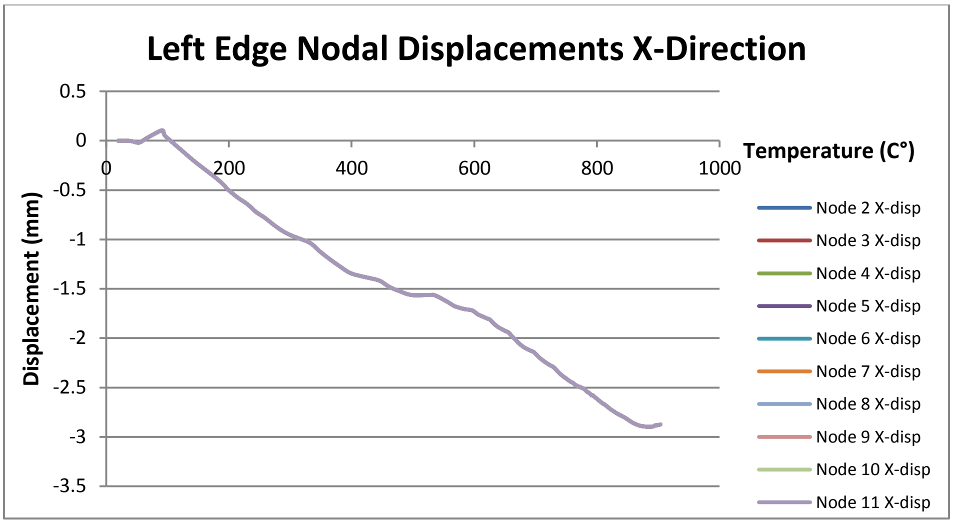

**Fig. 3.11 *X*-direction displacements of left edge with relative constraint**

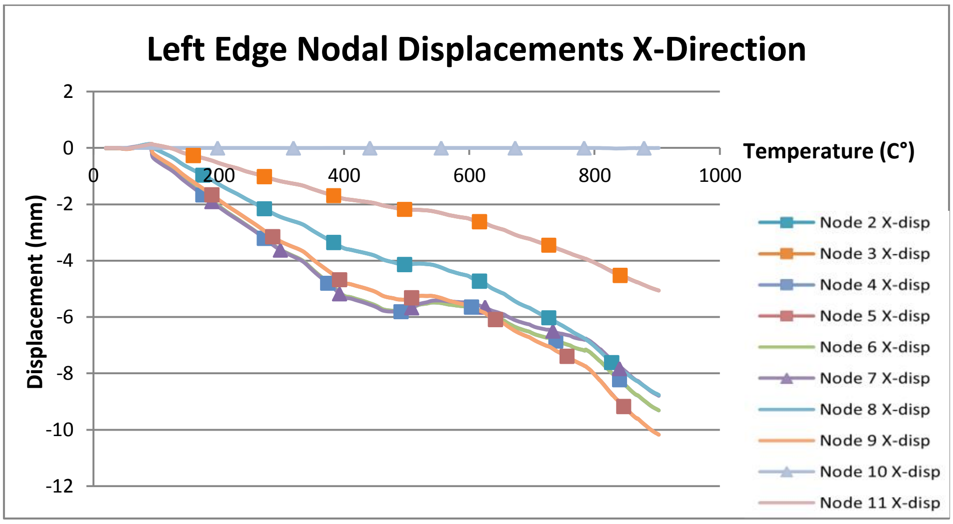

**Fig. 3.12 *X*-direction displacements of left edge without constraint**

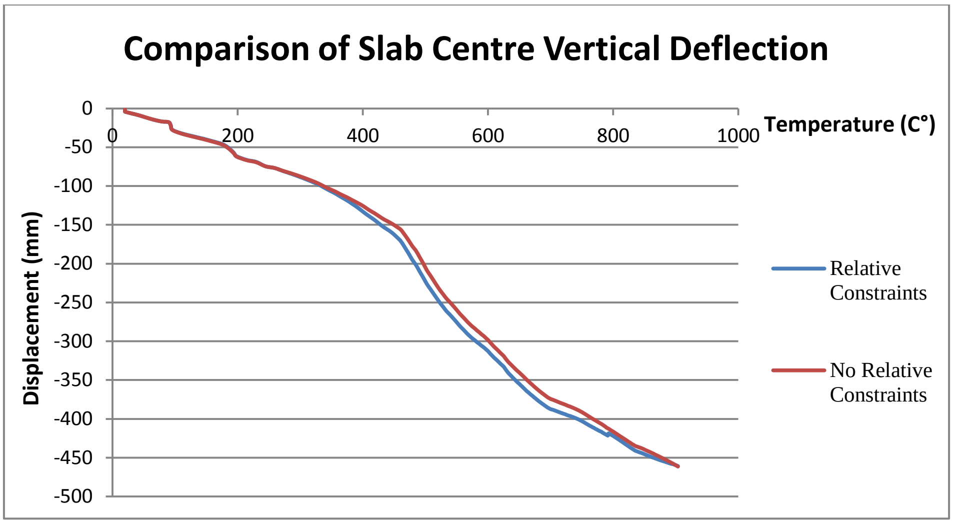

**Fig. 3.13 Comparison of vertical displacements of slab centre**

From Figs. 3.11 and 3.12 above, clearly the horizontal displacements differ with and without the relative constraints. In Fig. 3.12, the displacement curves of the nodes without constraints differ from one another, which mean that the slab edges curve. However, with the displacements pre-set to be equal using the penalty function method, all the nodal displacements are identical, as shown in Fig.3.11. In fact, if the slab edge is at the edge of a floor the constrained displacement curves shown in these figures are not the natural movements of the nodes for an isolated slab, because they have been forced to obey the "equal to other nodes" relationship, which we can see has been very successfully imposed during the whole analysis process. In contrast, if the slab panel models an internal part of the floor system, in-plane curvature of the slab edge can not happen in reality. After analysis, the membrane force distribution for a slab without relative edge constraints is shown in Fig. 3.14 and that for the slab with edges forced to remain straight in Fig. 3.15.

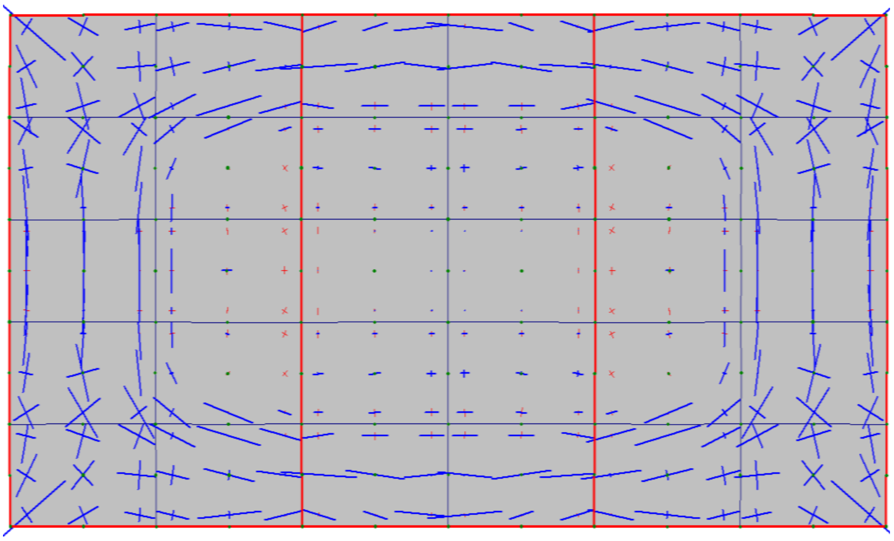

**Fig. 3.14 Membrane Action with no constraints applied at slab bottom 900.3°C**

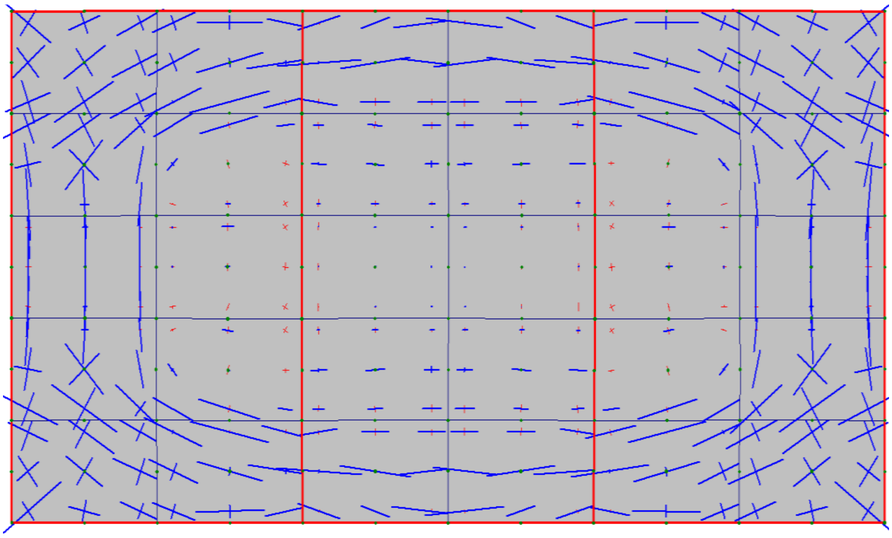

**Fig. 3.15 Membrane Action with constraints applied at slab bottom 900.3°C**

It can be seen that the membrane forces in these two examples are quite similar over most of the area of the slab. This is because they have the same geometry, and all edges have vertical support; the vertical displacements at the centres of the slabs are very close to each other overall, which means that the membrane action will be similar in the two cases. From about 400°C to 800°C the difference between the curves is more pronounced; the vertical displacement of the slab with constraints is a little larger than that without constraints. Hence, the area of tensile membrane force in the centre of the slab with constraints is the bigger of the two.

As shown in the simple calculations illustrating the penalty function method, when the penalty parameter $\boldsymbol{\alpha}$ approaches infinity (in *Vulcan* this is represented by a very large positive number), the solutions are subject to the set constraints. On the other hand, when the penalty parameter $\boldsymbol{\alpha}$ is 0, the results are the same as those of the unconstrained problem. To verify this, two slab models of the same size and properties are now used as above, but one is run in *Vulcan* with no recourse to the penalty function method, whereas the other uses the penalty function method but sets the penalty parameter to 0. It can be seen that the two deflection-temperature curves in Fig. 3.16 match exactly.

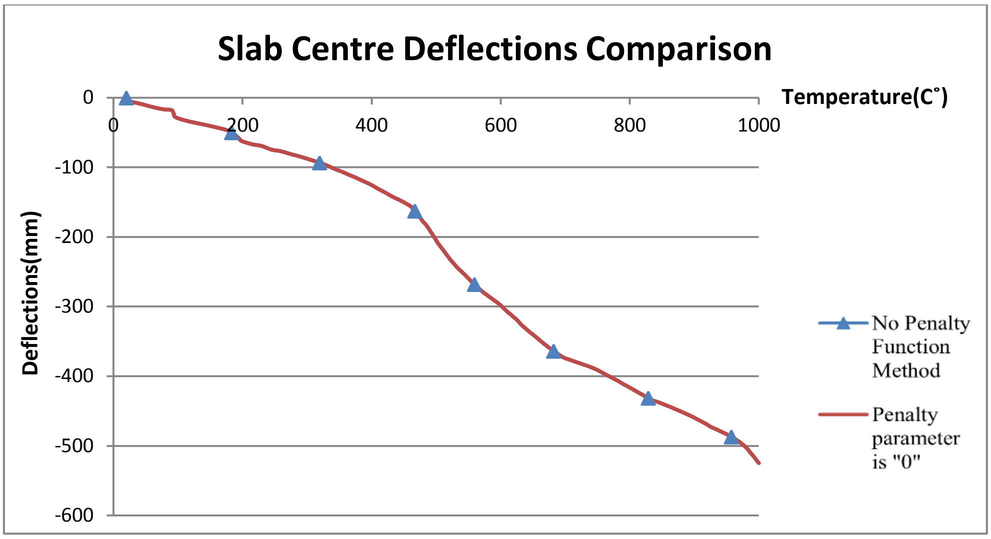

**Fig. 3.16 Comparison of slab centre deflections**

### 3.5.2 The non-orthogonal composite slab with applied constraints

The penalty function method is now applied to a non-orthogonal slab to verify its functionality further. In this example, the material properties are kept identical to those of the orthogonal slab, but its geometry is amended in order to model a part of a floor layout with irregular geometry, as shown in Fig. 3.17 below. As we are concerned with an individual slab panel, as in Fig. 3.18, it can be seen that there are four edges of the slab panel which are not parallel to the axis of any degree of freedom. The current *Vulcan* can only set each degree of freedom as fixed or free in terms of this global coordinate system.

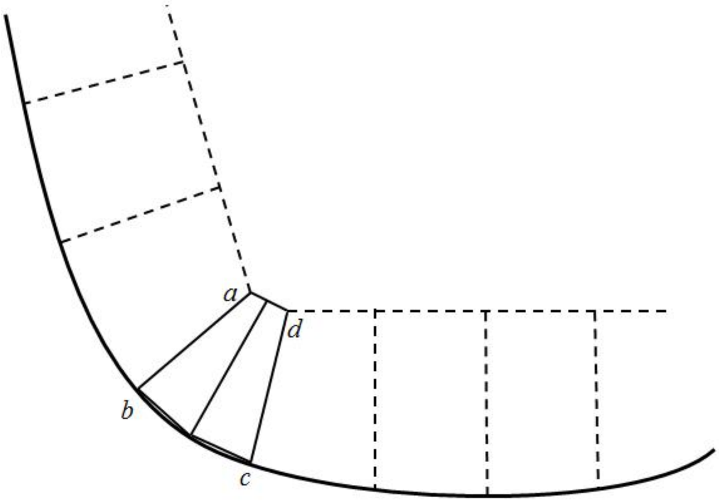

**Fig. 3.17 Typical irregular slab panel located at the edge of a floor layout**

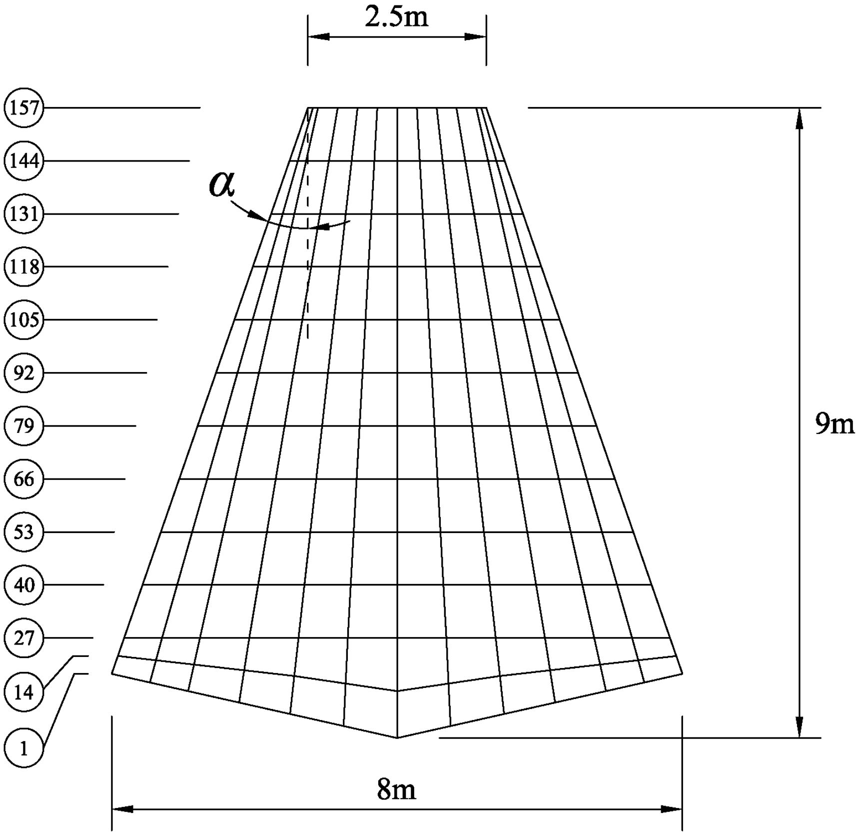

**Fig. 3.18 Geometry and layout of the non-orthogonal slab example**

Obviously, nodes on the left and right edges can not be either fixed or free in the *X* or *Y* directions. If we consider the bottom of the slab panel as the edge of the floor layout, its nodes can be free to move. At high temperature, the left and right edges of the slab can be constrained to move inward together because they must remain as straight lines; therefore it can be assumed that the slope between any pair of nodes on these edges has to remain the same. To reach this goal, the relative boundary conditions can be set by using the penalty function method, as

$$D_{x157} - D_{x144} = D_{x144} - D_{x131}$$

$$D_{y157} - D_{y144} = D_{y144} - D_{y131}$$

(3.28)

and so on for the rest of the nodes on the left edge of the slab panel. On the right edge, the same restraints have also been adopted. As there is symmetry of the slab panel geometry, only the left edge is illustrated here. Since this case aims to model a part of the slab panel extracted from a floor plate with irregular geometry, the boundary conditions are set with the top and bottom edges defined with fire protection but the with side edges left unprotected.

After the analysis in *Vulcan*, the nodal displacements on the left edge of the slab panel at 550°C have been listed in the table below. To verify the results, it is simple to put the nodal displacements into an Excel spreadsheet, together with the relative constraint equation 3.28. It can be determined whether the results satisfy the equation by checking if all the difference is identical.

| Node Number | Nodal Displacement (mm) | | Constraint Equation Results | |
|---|---|---|---|---|
| | *X*- | *Y*- | *X*- | *Y*- |
| 1 | -1.4409 | 25.5755 | $D_{xi} - D_{x(i-13)}$ | $D_{yi} - D_{y(i-13)}$ |
| 14 | -2.221 | 24.1689 | -0.7801 | -1.4066 |
| 27 | -3.0012 | 22.7622 | -0.7802 | -1.4067 |
| 40 | -3.7812 | 21.3552 | -0.78 | -1.407 |
| 53 | -4.5613 | 19.9481 | -0.7801 | -1.4071 |
| 66 | -5.3412 | 18.5408 | -0.7799 | -1.4073 |
| 79 | -6.1211 | 17.1334 | -0.7799 | -1.4074 |
| 92 | -6.901 | 15.7259 | -0.7799 | -1.4075 |
| 105 | -7.6807 | 14.3182 | -0.7797 | -1.4077 |
| 118 | -8.4604 | 12.9105 | -0.7797 | -1.4077 |
| 131 | -9.24 | 11.5026 | -0.7796 | -1.4079 |
| 144 | -10.0195 | 10.0948 | -0.7795 | -1.4078 |
| 157 | -10.7989 | 8.6869 | -0.7794 | -1.4079 |

**Table. 3.2 The displacement of each node on left edge and constraint equation results**

It can be seen that the nodal displacements in the *X* and *Y* directions vary with pre-defined constraints. However, from the constraint equation results, it can be observed that all the results are very close to each other, which means that the constraint equation works perfectly after applying the penalty functions. Moreover, the aim of keeping the edge of the slab panel in a straight line during temperature increase has been achieved. On the other hand, an identical model has been set up with no relative constraints applied, leaving the slab edges to move freely. After gathering the displacements from both models, the movements of slab left edge are illustrated in Fig. 3.19.

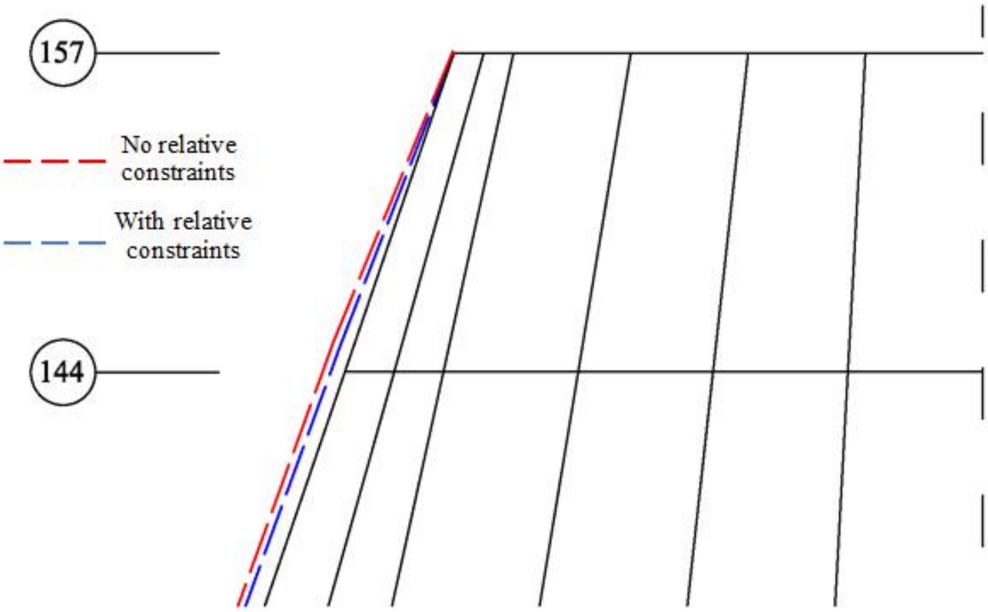

**Fig. 3.19 Comparison of slab left edge movements of slab lower face at 550°C**

In the figure above, it can be seen that the slab edge movement with relative constraints applied (represented as the blue dashed line) has stayed straight, but the movement without relative constraints (represented as the red dashed line) shows a curvature, although it appears very close to the blue dashed line. It is known that with adjacent slab panels, the movement of the slab edge must be kept very close to a straight line, so that the penalty function has successfully helped to make the results correspond to reality.

Forcing the movements of slab edges to stay in a straight line also makes the overall behaviour of slab edges to be different from that with free movements. With pre-defined relative boundary conditions, the beams beneath the slab side edges acquire smaller vertical deflections than those with free movement. Because an edge with relative constraint conditions is forced to remain in a straight line, this generates inward internal forces which prevent the edge from expanding into a curve. At the same time, the internal forces also contribute to decreasing the vertical displacement. In the figures below, the nodal vertical deflections at the slab left edge have been illustrated.

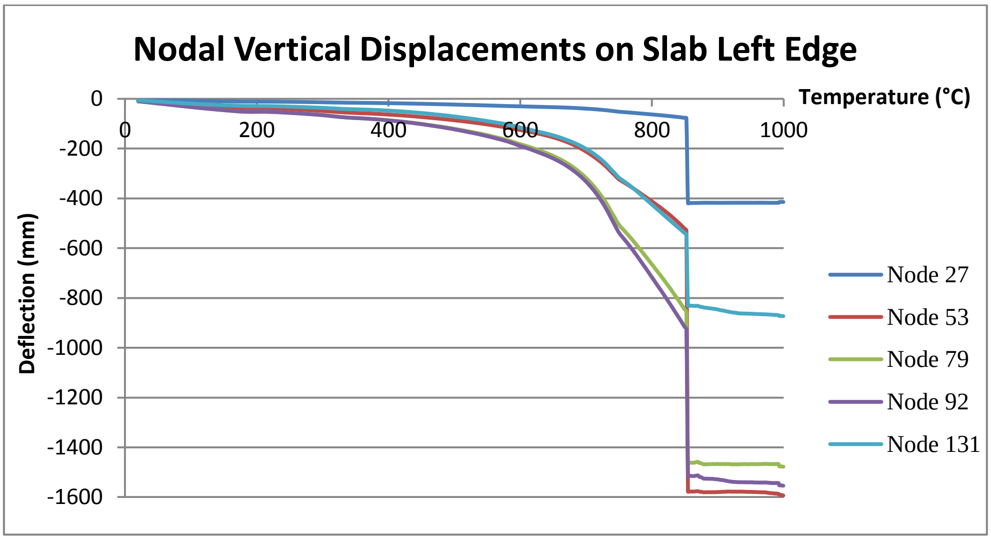

**Fig. 3.20 Slab left edge vertical deflections with relative constraints**

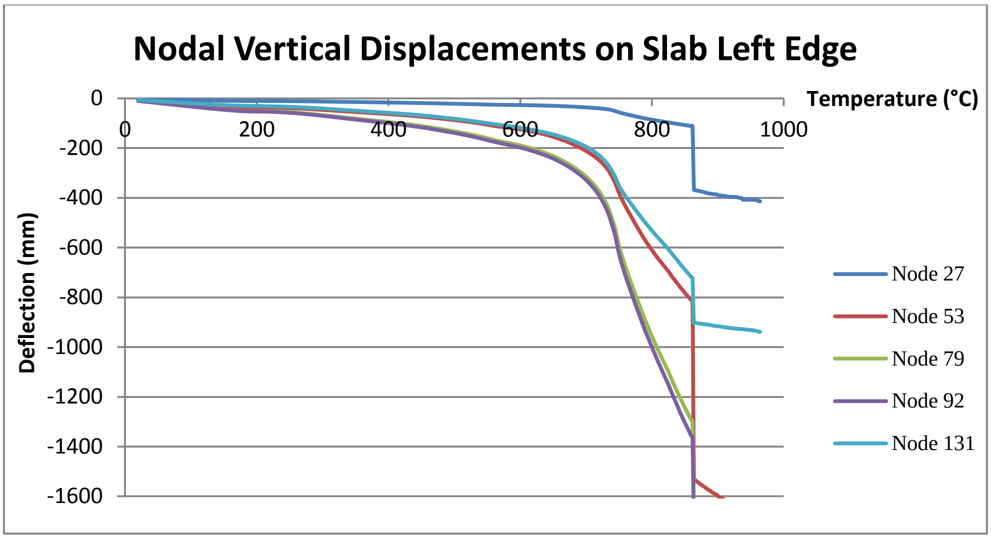

**Fig. 3.21 Slab left edge vertical deflections with free movement**

The vertical deflections of the slab edges also affect its central deflection. Since the beams under the slab side edges are unprotected, as temperatures increase the steel loses its stiffness rapidly. Normally, above 800 ℃ the stiffness of steel is at a very low level, and a plastic hinge can form at the beam’s mid-span, leading to a “folding” collapse mechanism. In both figures above, the vertical straight lines at the end of each curve represent the collapse of the beam; all of these occur at around 850 ℃. According to the nodal vertical deflections on the slab edges it can be predicted that the slab central deflection of the model with relative constraints should be smaller than that with free movement.

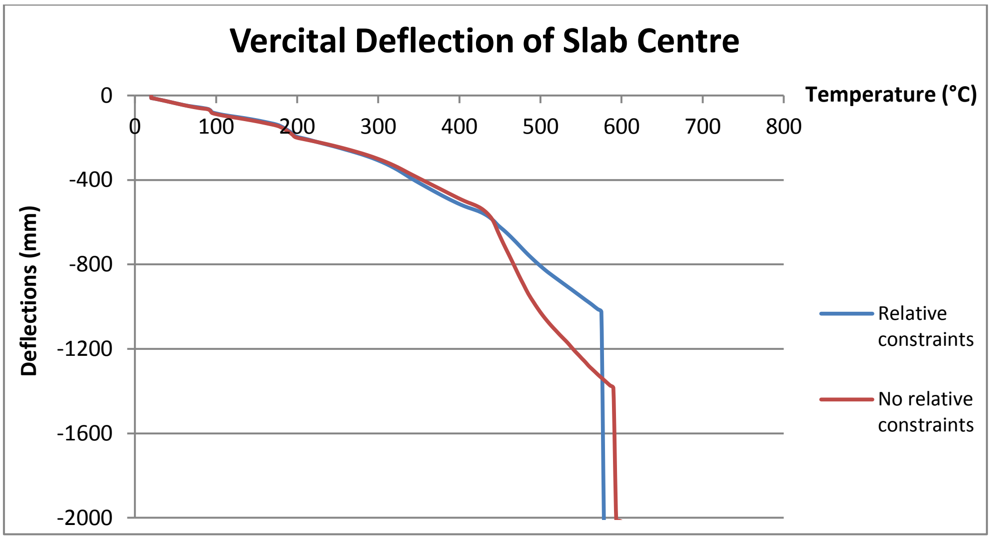

**Fig. 3.22 Vertical deflection of slab centre**

In Fig. 3.22 it is shown that, due to the vertical displacement of the unprotected beams, the slab with free edge movements has larger central vertical displacement above about 450 ℃. It can be observed from Figs. 3.20 and 3.21 that, below 750 ℃, the vertical displacements of the beam are very close to each other for the two models.

Since the slab side beams are unprotected, and so membrane action can not appear in either model, a comparison of membrane forces is not made here.

## 3.6 Summary and discussion

In order to analyse tensile membrane action in non-orthogonal slabs at elevated temperatures, in the context of existing finite element programs the essential modification to be made is to re-define the statement of boundary conditions. In rectangular or square geometries, as successive edges of the slab are perpendicular to each other these edges can be aligned along the global axes when modelling takes place. Therefore, the boundary conditions of slab edges can be defined as restrained or free to move in the directions of the global axes. Under some conditions, however, in which the slab is actually continuous, displacements at adjacent edge nodes may need to be 'tied' together.

When the geometry of a slab panel is non-orthogonal, typically triangular or trapezoidal, some of its edges can not be parallel to any global axis; only one or two can be aligned parallel to an axis, while the others are angled with respect to the global axes. For this reason, the penalty function method has been employed to resolve the problem of setting appropriate nodal boundary conditions on the slab edges which are not parallel to the global axes. Although there are several methods which can resolve this problem by applying constraints to the boundary conditions, the reason for adopting the penalty function method in preference to others is because of its advantage in retaining the size and symmetry of the whole-system stiffness matrix. Since this method is part of a standard finite element solution process, retaining the size of the stiffness matrix causes little increase in memory space usage, and retaining symmetry allows the standard solution process to be used.

When applying the penalty function method in the analysis program *Vulcan*, the value of the penalty parameter $\boldsymbol{\alpha}$ is user-defined. As mentioned previously, too large a value of $\boldsymbol{\alpha}$ will destroy the conditioning of the matrix, making the arithmetic processes of matrix solution rather inaccurate, and occasionally making it impossible to find answers. Based on previous experience, 1000 times the average nodal stiffness has been used as the value of the penalty parameter within this research. It appears that this selection is appropriate, as the nodal displacements have satisfied the intended constraints in the cases examined. The penalty function method has been seen to work well in *Vulcan*, and the program is able to investigate the behaviour of non-orthogonal slabs at elevated temperatures.

# Chapter 4 Numerical modelling and validation

## 4.1 Introduction of *Vulcan* analysis program

The numerical modelling of structural elements in this study was carried out using the finite element analysis program *Vulcan,* which has been progressively developed at the University of Sheffield for some years (Bailey, 1995; Najjar and Burgess 1996; Huang, *et al.* 1999; 2000; 2004a; 2004b). For composite floor system analysis in *Vulcan*, it is assumed that the nodes of the elements representing concrete slabs and steel beams are defined as lying in a common reference plane, which is assumed to coincide with the mid-surface of the concrete slab shell element as shown in Figure 4.1.

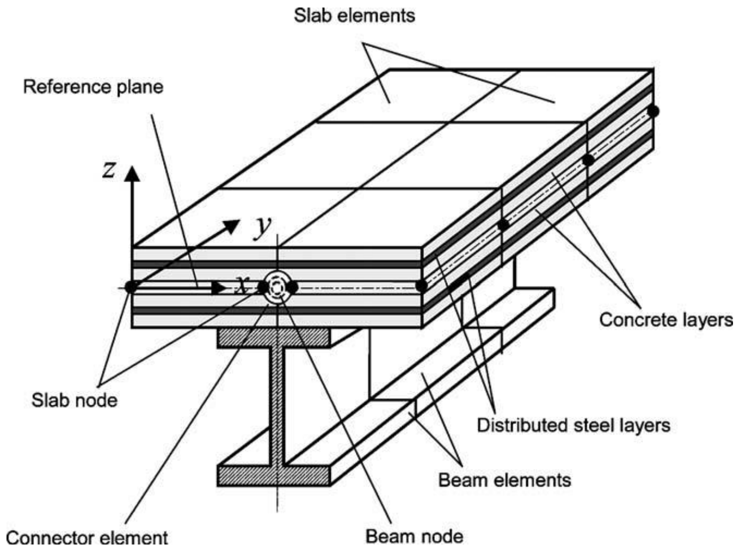

**Fig. 4.1 Division of reinforced concrete structure into beam and slab elements (Huang, Burgess *et al.* 2004b)**

In *Vulcan*, the concrete slabs are modelled as an assemblage of finite plate elements, which are of the quadrilateral nine-noded high-order isoparametric element type described by Bathe (1996). All the plate elements are divided into several layers representing concrete and reinforcement mesh. In the context of this layered approach, several assumptions had been made as follows:

1. The slab elements are considered to consist of plain concrete layers and steel reinforcement layers, without slip between them.
2. The temperatures of individual layers can differ, but must be uniform within each

layer of an element. As the original properties of each layer may be different, their stress-strain relationships can change individually.

3. The reinforcement steel bars in the orthogonal mesh directions are modelled by equivalent smeared steel layers with uniaxial stiffnesses in the directions of the reinforcing bars. As the thickness of slab is defined by the user, the cross-section of the reinforcing steel layer is equal to the total area of rebar in the appropriate direction. In addition, bond between the steel layers and the concrete surrounding them is assumed perfect.

4. The layers of concrete are each in a plane-stress state, and after the initiation of cracking the concrete is assumed to be an orthotropic material with principal axes normal and parallel to the cracking direction, and with the *X*-, *Y*-, and *Z*- axes defining the planes of orthotropy.

According to the thickness of slab, in previous research (Huang *et al.*, 1999) it is recommended that the appropriate number of layers used to analyse reinforced concrete slabs under fire condition should be 10-20. Therefore, in this study the slab panels have been divided into 13 layers to represent the temperature distributions across the reinforced concrete slab thickness.

Because of the relatively poor thermal conductivity of concrete, the temperature of the top surface of the slab is always much lower than that of the bottom surface. From a previous study (Lin *et al.*, 1989) of fire testing of reinforced concrete slabs, the temperature of top surface was about 13.5% of the bottom surface, which means that even when the temperature of the bottom surface of slab had reached 1200°C, the top surface of slab was only at about 180°C. In *Vulcan*, there are five options to represent temperature distribution assumptions; user input, uniform distribution, linear distribution, bilinear distribution and tri-linear distribution. In this study the temperature distribution was defined by user input. The temperature of each layer was determined at any time using a finite element thermal analysis program, FPRCBC-T (Huang *et al.*, 1996) which was developed to evaluate the temperature distribution history of reinforced concrete structural member cross-sections. With the fire temperature-time curve entered as data, the program can predict of the temperature of any point within the structural element by finite element calculation.

## 4.2 Convergence test and sensitive study

In order to assure the accuracy of results, it is essential to define an appropriate element mesh density in any analysis software based on the finite element method. The advantage in terms of accuracy comes from smaller divisions (a more dense mesh), but this has the disadvantage that it will take longer to process the analysis. For the purpose of determining an appropriate balance point in *Vulcan*, it is necessary to find the most efficient density of elements.

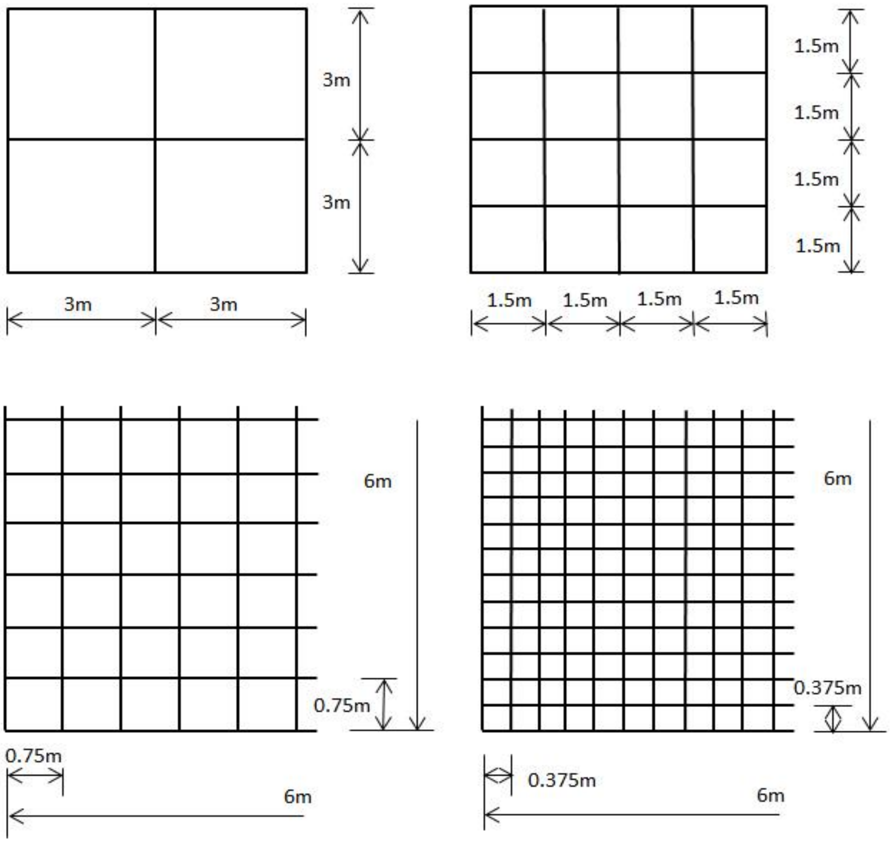

**Fig. 4.2 Four different slab panels with identical overall dimensions**

In this convergence test, a slab of the same dimensions (6m x 6m) has been meshed in four different ways with square elements of side length 3m, 1.5m, 0.75m and 0.375m, as shown in Figure 4.2. All four panels have same dimensions, cross-section, boundary conditions and temperature environment. In the simulations, the logic indicates that, as the element length decreases, the results should gain in accuracy but the runtimes should be longer. In reality, an optimum size will give sufficiently accurate results in a sufficiently short runtime.

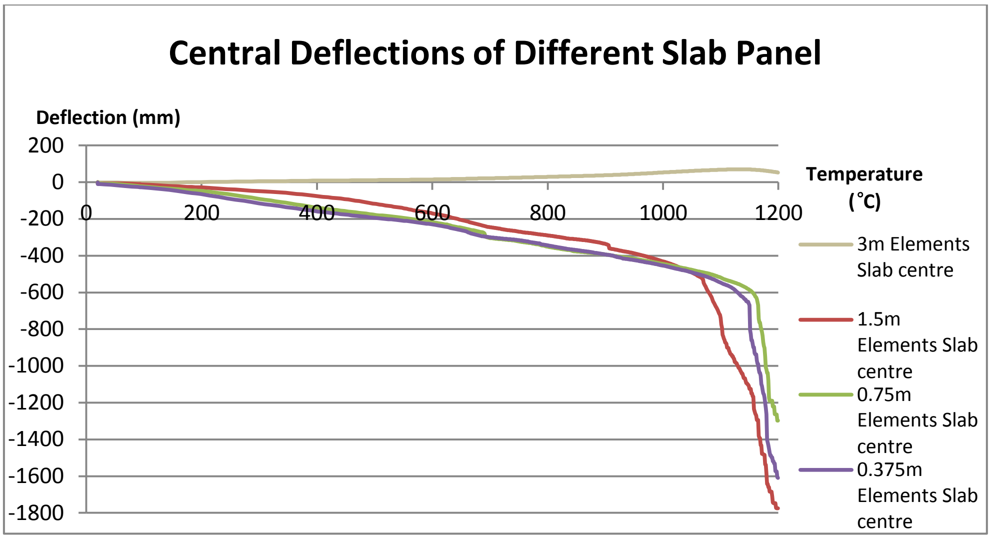

**Fig. 4.3 Central deflections of 4 different slab panel divisions with same area**

As shown in Figure 4.3 above, apart from the first (3m element length) case, the results are similar in terms of slab centre deflection. For the two finest (0.75m and 0.375m element length) cases, the curves are almost identical. Comparing the results of the 1.5m and 0.75m cases, the differences between are in the range of millimetres before runaway happens. Considering the runtime cost and the convenience of meshing slab panels, the recommended range of element dimension is 1 – 1.5 m, which should give accurate enough results and an efficient runtime.

## 4.3 The behaviour of triangular slabs

Once the appropriate dimensions of elements have been verified for non-orthogonal slabs at elevated temperatures, it is necessary to apply *Vulcan*, including the penalty function procedure,. Before building up triangular slab models in *Vulcan*, it is desirable to apply a design method to the floor slab covering both ambient and elevated temperature. However, the design of non-orthogonal slabs can not exactly follow the standard methods for rectangular or square slabs, because the difference of geometry distinctly changes the properties of the slab panel. There are some assumptions which have to be made during the design process, in order to make the analysis correspond to reality, with the aim of ensuring that membrane action occurs in non-orthogonal slabs.

### 4.3.1 Behaviour of triangular slab with two continuous edges

There are various locations at which triangular slab panels typically to exist in floor layout, and these different locations also determine the constraints on the movements of the slab panel edges. The most important factor which influences the deformation of slab edges is whether there are adjacent slab panels; in other words, whether the slab panel to be analysed has continuity across its edges. When determining the boundary conditions for the nodes on slab edges, the following rules generally apply:

1. If the edge has no other slab panel directly adjacent, it is considered that the edge can move freely in the direction perpendicular to itself.
2. If there is an adjacent slab panel connected to the edge, the movement of the slab edge needs to be restrained by applying the penalty function method, so that its nodes move as a straight line.

#### 4.3.1.1 Slab panel properties and floor design

Since there is currently no established design guidance for triangular slabs, the design method chosen is that for a square slab panel of dimensions 6.0m x 6.0m with 60-minutes' fire resistance, using normal-weight concrete and a trapezoidal profiled decking, as shown in Figure 4.4. According to SCI P-288 (Newman, 2006), under the design loading defined in Table 4.1 the required minimum mesh size is A193. By using Eurocode 4 Part 1-1 (CEN, 2005a) for steel floor beam design at ambient temperature, and Eurocode 4 Part 1-2 (CEN, 2005b) for fire resistance design at elevated temperatures, the primary and secondary steel beams are selected as UB 356x171x45 and UB 305x102x28 respectively. Sufficient fire protection to provide 60 minutes' fire resistance is applied to the primary and secondary beams around the edges of the slab panel, and the intermediate secondary beams are left unprotected.

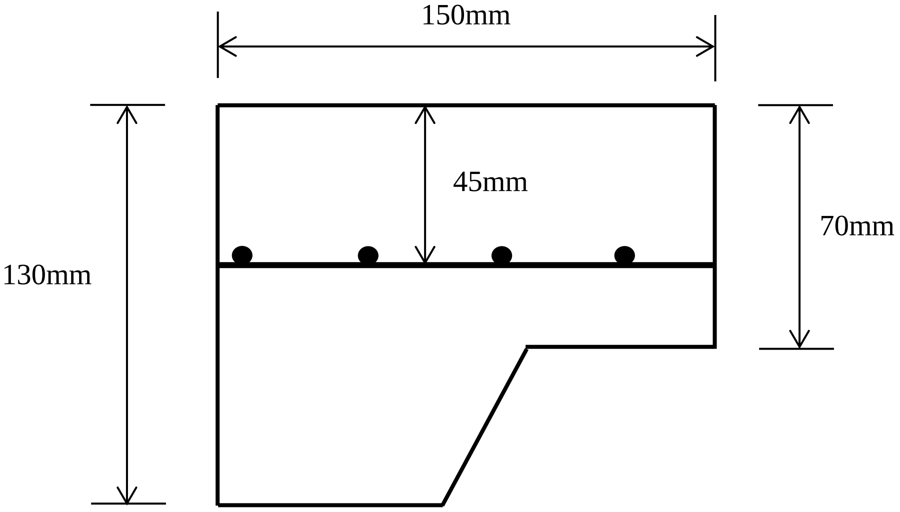

**Fig. 4.4 Reinforced concrete slab cross-section with steel decking**

| Permanent Loads | $kN/m^2$ |
|---|---|
| Concrete Slab self-weight | 2.40 |
| Steel Beam self-weight | 0.20 |
| Reinforcement Mesh | 0.03 |
| | |
| Imposed Loads | |
| Variable load | 3.5 |
| Partitions, ceilings/services | 1.7 |

**Table. 4.1 Design loads for slab panel**

As mentioned above, the design procedure for a square slab is not really adequate for a triangular slab, so there are some modifications which need to be applied to the square slab design. As is well known, a triangle has half the area of a rectangle or square with the same base length and height. Hence, the first modification is to change the geometry from a square to a triangular slab, as shown in Fig. 4.5.

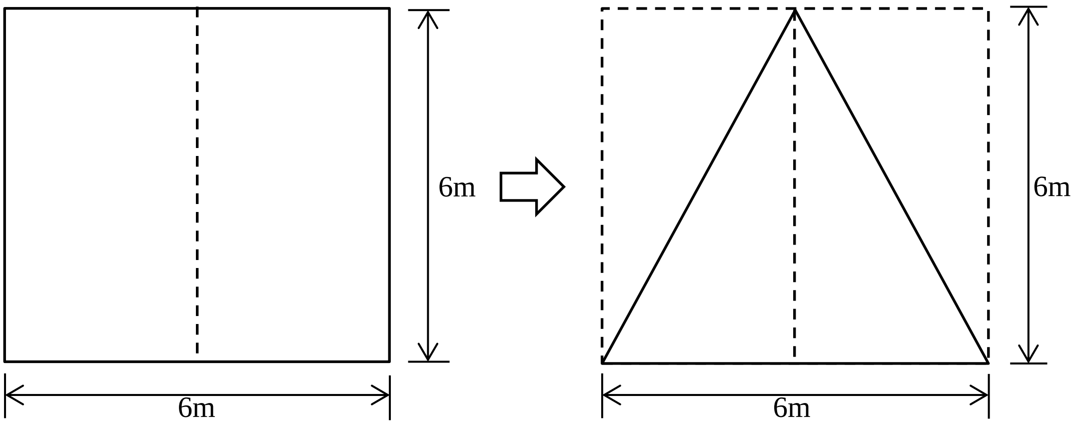

**Fig. 4.5 Change a square slab to an isosceles triangular slab**

Obviously, when considering a triangular slab which has been subdivided from a square slab, its area is just half that of the square and, since a triangle is always a more stable geometric shape than a quadrilateral, the stiffness of the triangular slab is greater than that of the original square slab. Hence, it is reasonable to reduce the section sizes of the steel beams and as well as the size of the reinforcing mesh. Although the stiffness of the panel has increased, two edges of the triangular slab have become longer than those of the original, and the performance of steel at elevated temperature must also be taken into account. It is assumed that the criterion for selecting the sizes of the steel beams in the triangular slab is that the bending moment resistance of the primary and secondary beams should be 80% of those of the original steel beams in the rectangular or square slab. Following this assumption, the beam sizes UB305x165x40 for primary beams and UB254x102x22 for secondary beams were chosen for the triangular slab. The reinforcing mesh size was decreased to A142 due to the geometry change.

### 4.3.1.2 Boundary conditions

In order to represent the slab behaviour reliably, one of the essential conditions is to ensure correct relative movements of boundary nodes, because the movements of boundary nodes affect the behaviour of the slab perimeters directly; this can also be one of the most important factors which influence the deflection of the slab centre.

For a triangular slab with two continuous edges within the floor layout of a building, only one edge may be aligned along a global axis, and the other two edges may be subject to restraint by the adjacent slab panels. The movements of slab edges are in a certain direction outward or inward relative to the slab centre, and the edges of the triangular slab should remain straight lines after the deformation occurs, as shown in Figure 4.6. This means that the movements of the slab edges are not purely free in all directions, but are subject to a defined relationship.

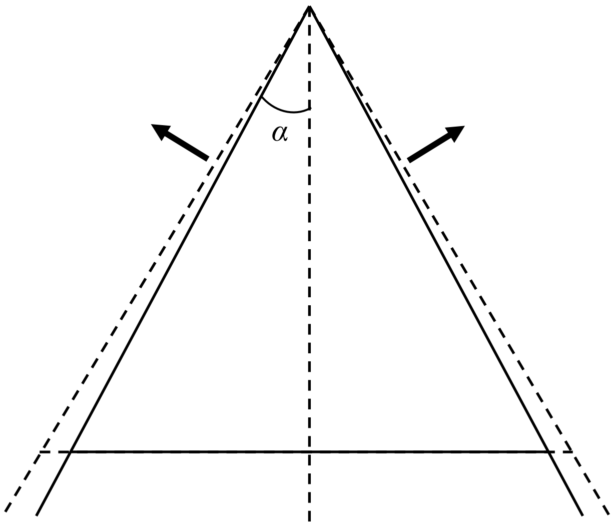

**Fig. 4.6 Movements of slab side edges with continuity**

Verification of the displacements of boundary nodes which are subject to relative constraints (where penalty functions have been applied) and comparison against those with free movements has been demonstrated in Chapter 3, and is not repeated here. The tensile membrane action of triangular slabs which are equipped with the correct boundary node movements is more the concern of this chapter. A triangular slab model with the geometry and loading shown in Fig.4.4 and Table.4.1 was selected to illustrate the results. The cross-section throughout the slab panel differs between its thickest part (through a rib) and its thinnest part (through the concrete). An equivalent solid slab with 100 mm thickness as an average-depth flat composite slab is employed. The distribution of temperature through the 13 layers into which it is divided was carried out by the program FPRCBC-T (Huang *et al.*, 1996) when its lower surface is subjected to the Standard temperature-time curve. In this model, the perimeter of the triangular slab is vertically supported as the temperature increases and the apex of the triangular slab is defined as fixed in both *X* and *Y* directions.

As mentioned above, *Vulcan* is a geometrically nonlinear finite element program which includes the influence of nonlinear material behaviour at high temperatures. In *Vulcan*, the reinforced concrete slabs are modelled as 9-noded nonlinear layered elements. Before a model analysis can be carried out, the whole slab panel needs to be divided into a mesh of 9-noded layered elements. For practical structural dimensions the lengths of elements in both the longitudinal and transverse directions need to be kept below about 1.5m. When some of the elements are triangular in shape, the three nodes on the top faces of these elements stay very close to each other in order to allow them to be considered as a single node. The finite element grid was divided as shown in Fig. 4.7.

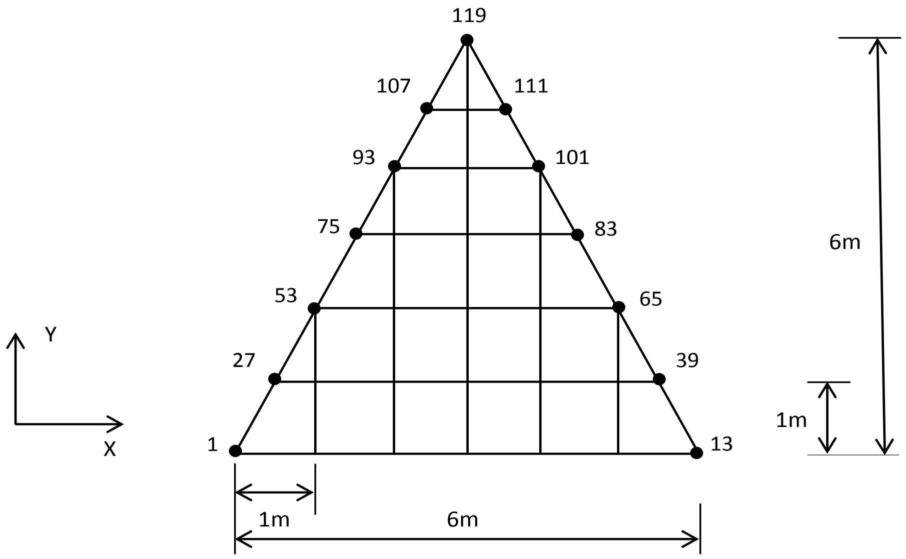

**Fig. 4.7 Grid division for triangular slab panel**

When the external loading has been applied to the slab, and as temperatures increase, the reality is that the left- and right-hand edges of the slab move outward from the slab centre but not specifically in the *X*- or *Y*-direction. Since the left and right edges are not aligned along either global axis, absolute restraints cannot be defined for any of the *X*- or *Y*-direction degrees of freedom. In reality, when the two sides of the triangular slab move, it would to make its *X*-displacements proportional to the distance from the apex since the edges have to stay straight. Therefore, according to the Figure 4.7, the restraints for the nodal movements on the left-hand edge have been set up as

$$
\begin{aligned}
&(D_{x119}cos\alpha - D_{y119}sin\alpha) - (D_{x107}cos\alpha - D_{y107}sin\alpha) \\
&\qquad = (D_{x107}cosa - D_{y107}sin\alpha) - (D_{x93}cos\alpha - D_{y93}sin\alpha)
\end{aligned}
$$

and so on for each node on the left side, with similar conditions being applied to the right-hand edge. The method of forcing this to happen is by applying penalty functions within the stiffness matrix in the way which has been explained in the previous chapter.

#### 4.3.1.3 Finite element analysis and membrane action

The location of a slab panel determines its boundary conditions. Consider an isosceles triangular slab panel with continuous boundaries in the central area of a floor, such that there are no two edges which are perpendicular to one another. Hence, only one of the three edges can be parallel to a global axis when the slab is modelled in the program. In the analytical process, an isosceles triangular slab is defined with its bottom edge parallel to the global -*X* direction, and with its other two edges defined as keeping their movements proportional by applying the penalty function method. In this case, in order to investigate membrane action occurring in this slab, the edges of the slab are fully vertically supported, as an idealisation of a protected perimeter beam.

After the finite element no-linear analysis carried out by *Vulcan*, the creation of membrane forces and distribution are shown in a series of figure with slab lower face temperature increase, as below,

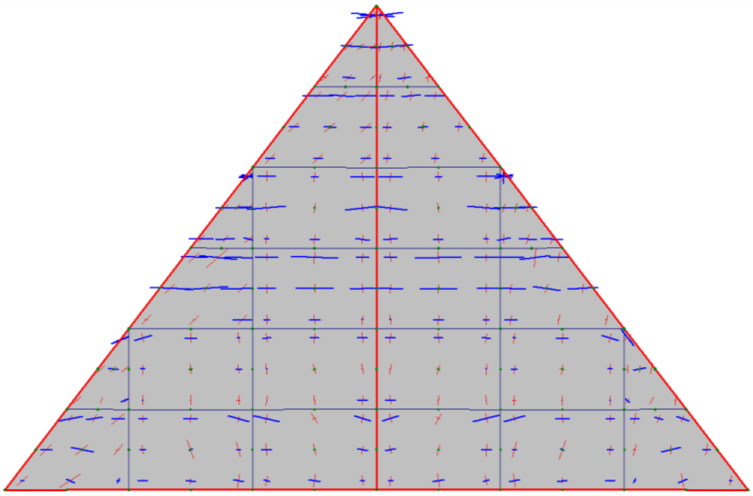

**Fig. 4.8 Membrane stress vectors at slab lower face 198°C (2D)**

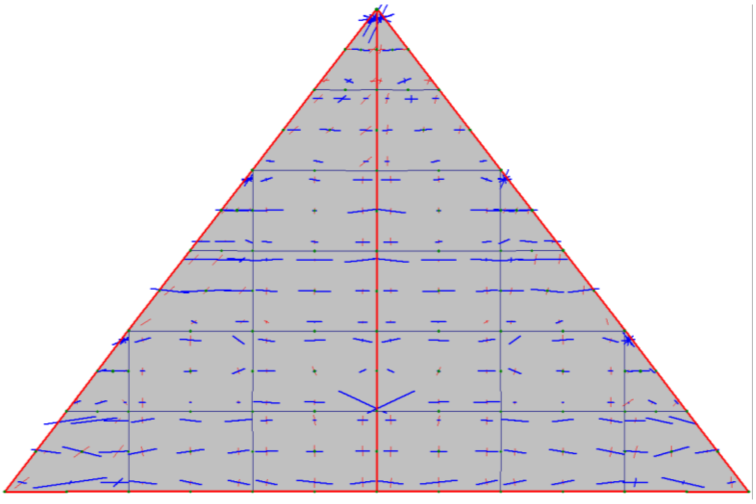

Fig. 4.9 Membrane stress vectors at slab lower face 402°C (2D)

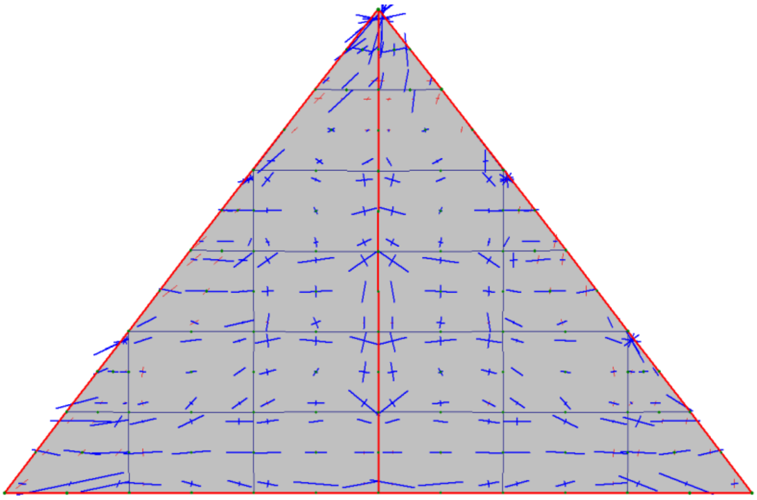

Fig. 4.10 Membrane stress vectors at slab lower face 600°C (2D)

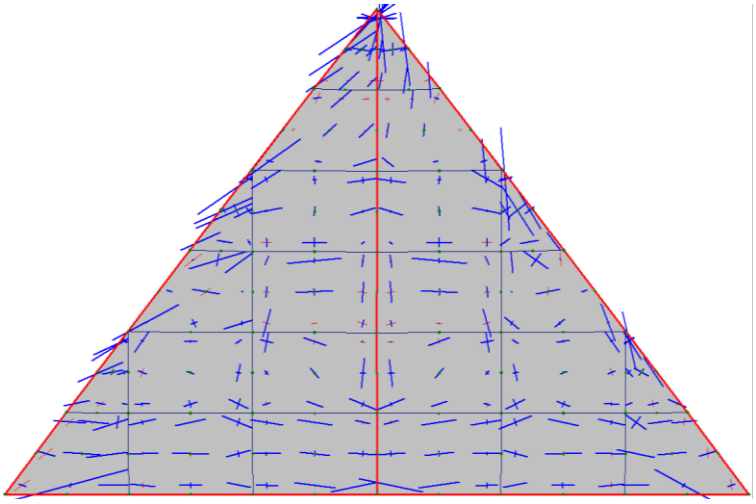

Fig. 4.11 Membrane stress vectors at slab lower face 800°C (2D)

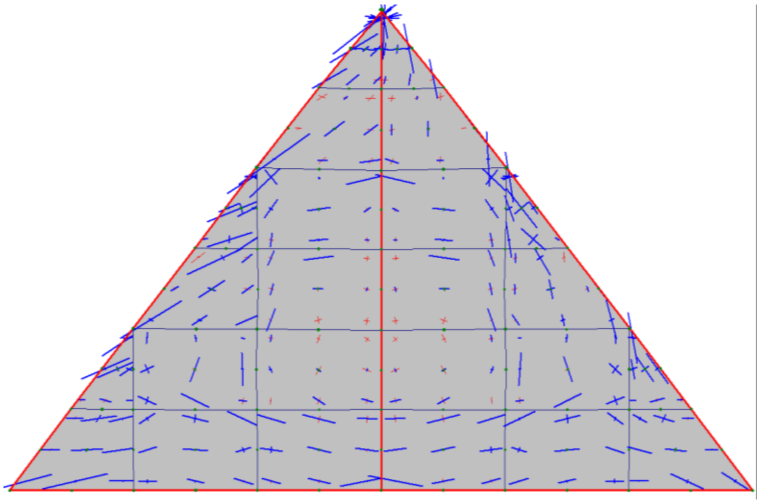

**Fig. 4.12 Membrane stress vectors at slab lower face 900°C (2D)**

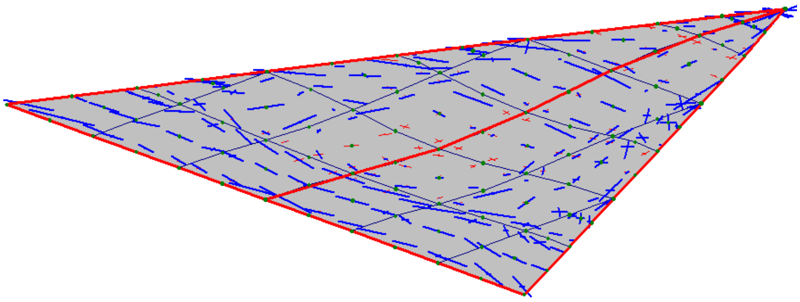

**Fig. 4.13 Membrane stress vectors at slab lower face 900°C (3D)**

When the slab at about 200°C, as the slab starts to be heated the membrane stress starts to appear because the slab attempts to expand in all directions, although these expansions are quite small. At this stage the bottom of slab had been just heated, but the top remains in a cool condition. The deflection at the centre of the slab is very small, so the thermal expansion of the bottom layer of the slab, restrained by the upper layers, causes a net compressive stress. As the temperature grows to 400°C, there are barely any tensile stresses to be seen and compressive stress dominates over most of the area of slab. At about 600°C, the compressive membrane stress becomes quite large and covers the whole slab. At 800°C, the appearance of tensile membrane stress in the central zone can be seen clearly, because the deflection of the slab centre is now large enough to cause tensile membrane action and the intermediate secondary beam has lost most of its strength. In Figs. 4.12 and 4.13, the appearance of tensile membrane force (red vectors) is obvious, and is located in the central area of the slab panel. Similar to the compressive membrane force distribution in rectangular slabs, a compressive ring is generated around the perimeter of triangular slab. However, due to the better stability of triangle than rectangular, the central vertical displacement of triangular slabs is smaller than that in rectangular slabs. Hence, the area of tensile membrane force in the triangular slab is smaller. From the performance of this triangular slab, it is easily seen that tensile membrane action occurs at a higher temperature than is usual for a rectangular slab.

### 4.3.2 Behaviour of triangular sab with one continuous edge

In the previous model, the situation of a triangular slab with two continuous edges have been simulated and analysed. In order to investigate the behaviour of triangular slab in different locations, another triangular model with exactly the same slab geometry and properties was built up. With all beams at slab perimeter protected, the only difference in this model is that the relative constraints aiming to keep the edge's movement in the $Y$ -direction in a straight line were only applied to the bottom edge which is assumed to have continuity with an adjacent slab panel, but leaves the two side edges free to move.

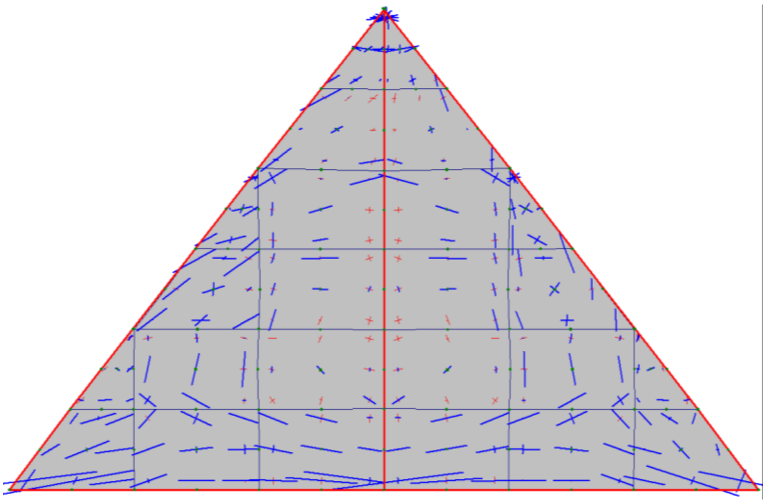

**Fig. 4.14 Membrane stress vectors at slab lower face 900°C (2D)**

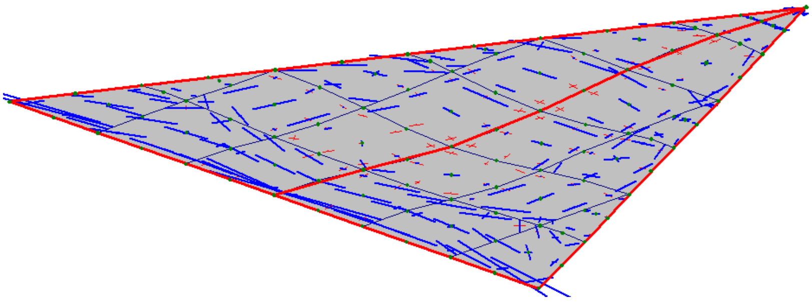

**Fig. 4.15 Membrane stress vectors at slab lower face 900°C (3D)**

Since the process of tensile membrane action generation is very similar to the previous model, only the difference between the distributions at 900°C is demonstrated here. Comparing Figs.4.12 and 4.14, the most significant distinction is that in Fig.4.14, the tensile membrane stress occupies a larger area along the axis of symmetry towards the top of slab. In the case in which two side edges have free movement, there is no adjacent slab panel which will restrain the deformation of the side edges. Therefore, the deflection of the model with no restraint on its side edges is larger than that with restraint, and this also induces the larger area of tensile membrane force in the latter case.

### 4.3.3 Behaviour of triangular slab at the edge of a building

In reality, when we consider building floor layouts with non-orthogonal slab panels, a variety of divisions of the floor layout can be used. However, for convenience of design and to standardise construction, the floor is usually divided into rectangular panels over most of its area, leaving a minority of triangular panels along the building perimeter, as shown in Figure 4.16 below.

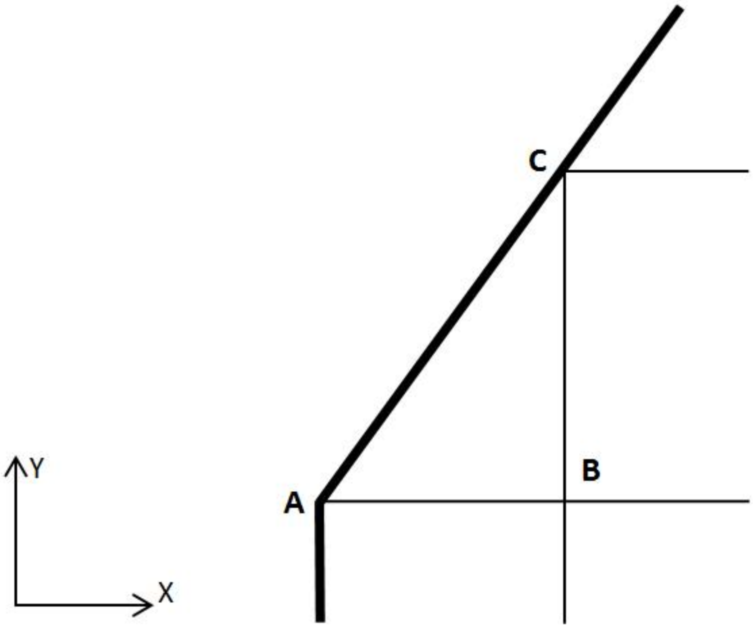

**Fig. 4.16 Typical non-orthogonal floor panel design**

### 4.3.3.1 Slab panel properties and floor design

Applying the same design process used for the previous model, both ambient- and elevated-temperature floor system designs are created for a 9.0m x 6.0m rectangular slab. The same cross-section properties, with 130mm slab thickness, trapezoidal steel decking and A252 reinforcement mesh, are specified. The sizes of primary and secondary beams are selected as UB 457x152x74 and 305x102x28 respectively. In accordance with the previous model, appropriate beam sizes for the triangular slab are assumed to need to provide 80% of the bending moment resistance of those in a rectangular slab of the same dimensions. Hence, the beam sizes for the triangular slab are UB 406x178x67 and UB 254x102x22. In addition, the reinforcement mesh is replaced by A193.

After the design for this rectangular slab panel is complete, the next process is to divide it into two triangular slabs by cutting it along a diagonal.

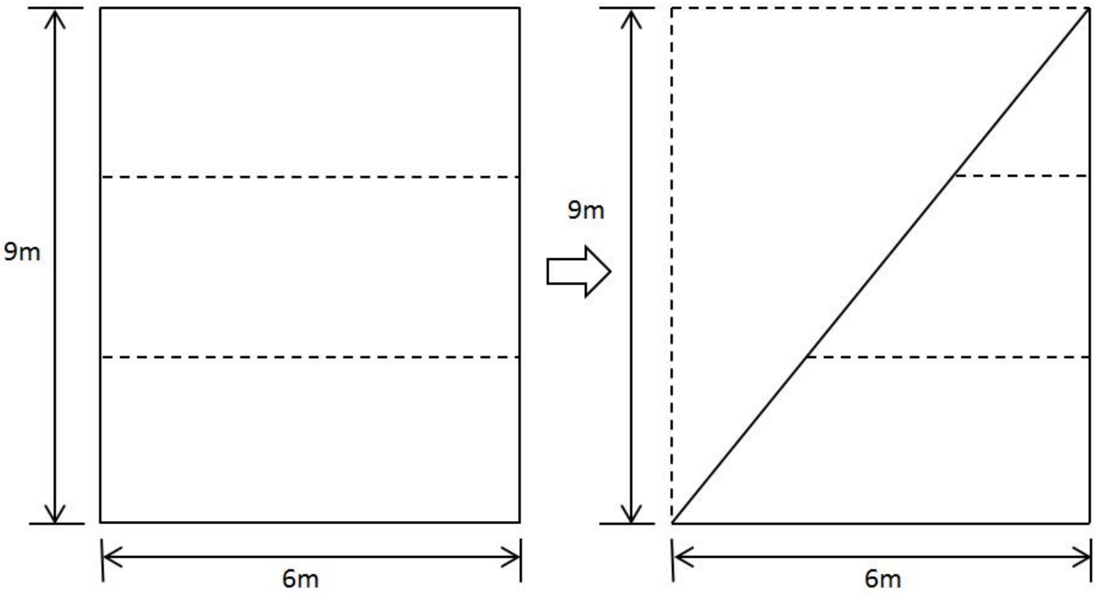

**Fig. 4.17 Division of rectangular slab to a right-triangular slab**

### 4.3.3.2 Finite element analysis and tensile membrane action

In the case shown in Figure 4.16, there are two edges AB and BC parallel to the global coordinate axes and with continuity, AC is modelled as an edge for which there is no adjacent slab panel. With the perimeter of the triangular slab vertically supported, continuity of the edge AB implies *Y*-direction displacement restraint and that of edge

BC implies *X*-direction displacement restraint. Hence, the nodal movements on AB are defined as equal to each other in the *Y*-direction, as are movements in the *X*-direction for BC. The edge AC is defined as free to move in any direction in order to simulate the situation at a perimeter edge of the floor layout.

To ensure that the tensile membrane action occurs, the essential condition is that the perimeter of a slab remains stable during the whole process of temperature increase. In this case, the beams under the slab edge are provided with 60-minutes' fire protection but the intermediate beams are left unprotected. As analysed by the finite element program *Vulcan*, the results of the model for the slab lower face at 900°C are shown in Fig. 4.18 below.

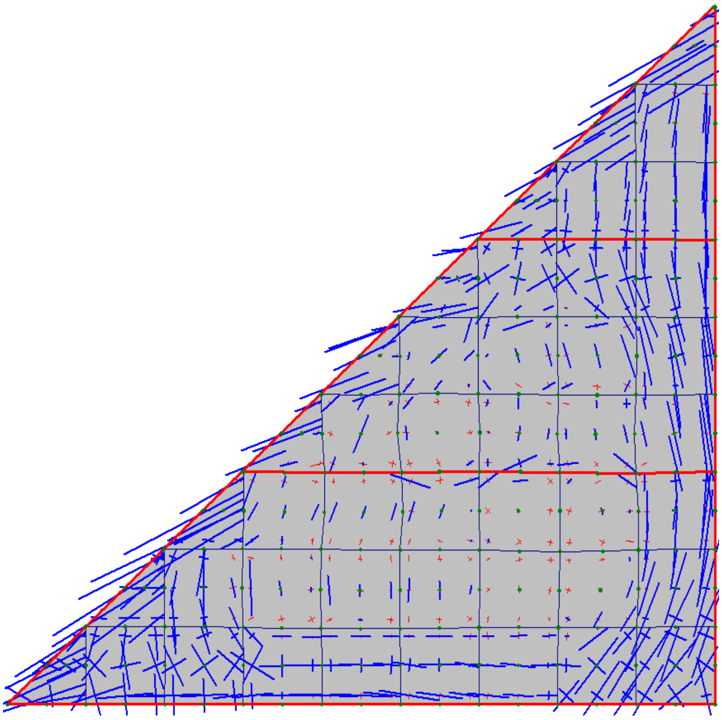

**Fig. 4.18 Membrane stress vectors at slab lower face 900°C (2D)**

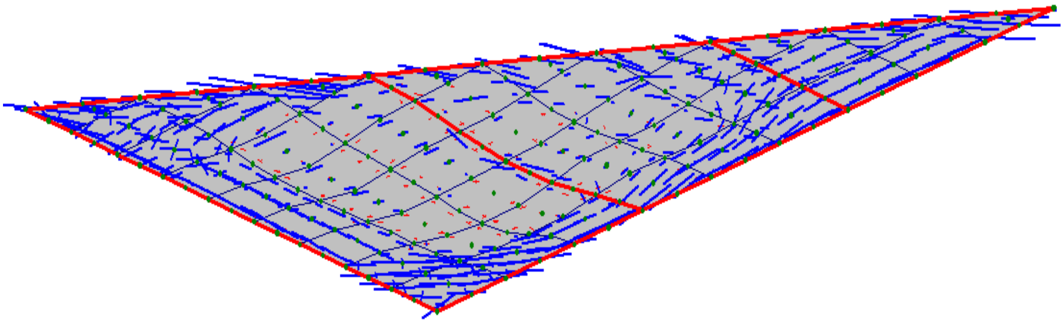

**Fig. 4.19 Membrane stress vectors at slab lower face 900°C (3D)**

From Figs. 4.18 and 4.19 it can be seen that the compressive membrane stress still forms a ring around the slab perimeter, and that the tensile membrane stress is located in lower section area of slab. The reason for this phenomenon is that, due to the reduction in the slab area and the change of geometry, the stiffness of the whole slab has been enhanced, especially for the part above the upper intermediate secondary beam, which also causes a reduction of the vertical deflection in that area. For this reason, the tensile membrane stress occurs mainly in the region below the lower intermediate secondary beam. On the other hand, the compressive membrane force keeps a fairly constant width around the slab perimeter, so that the area of tensile membrane force has shrunk.

## 4.4 Validation of trapezoidal slab behaviour

In designing a trapezoidal slab, a rational course of action is first to design a rectangular slab and then to make equal and opposite changes to the angles of two opposite edges. When following this procedure it is necessary to assess the behaviour change from a rectangular slab to a trapezoidal slab. In this study the total area of the slab is kept constant by rotating the edges about their mid-points.

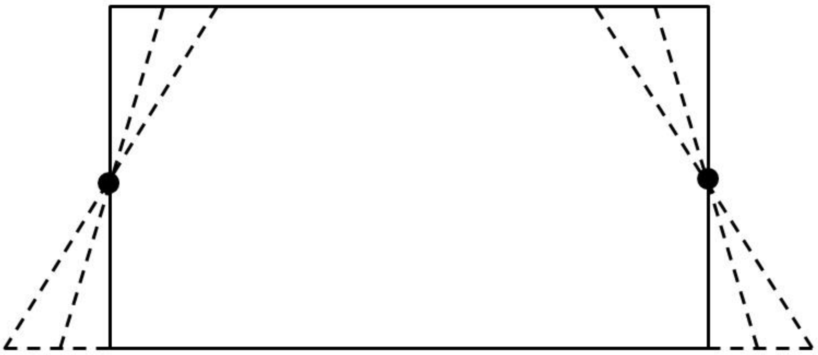

**Fig. 4.20 Transformation from rectangular slab to trapezoidal slab**

Since there is no standard design guide for trapezoidal slabs, a logical design method is to treat it as a normal rectangular slab. In contrast to representing a triangular slab as rectangular, the shape remains quadrilateral. If the angle of rotation of the two opposite edges is not excessive, it is reasonable to keep the sizes of the beams along these edges the same as for a rectangular slab. In other cases, considering the load distribution of the slab, the sizes of all beams will need to be changed, because the length of the upper primary beam is reduced while the lower primary beam is lengthened, and the lengths of all secondary beams are increased.

### 4.4.1 Slab panel properties and floor design

A composite slab panel of dimensions 7.5m x 9.0m, with protection designed for 60 minutes' fire resistance has been selected. With the same design loading defined in Table 4.1, the same cross-section properties have been adopted as in Figure 4.3, using normal-weight concrete and A193 reinforcement mesh. This model is divided into 30 elements with 1.5m x 1.5m for each; the slab contains four secondary beams as two at slab perimeter with protection and two intermediate left unprotected.

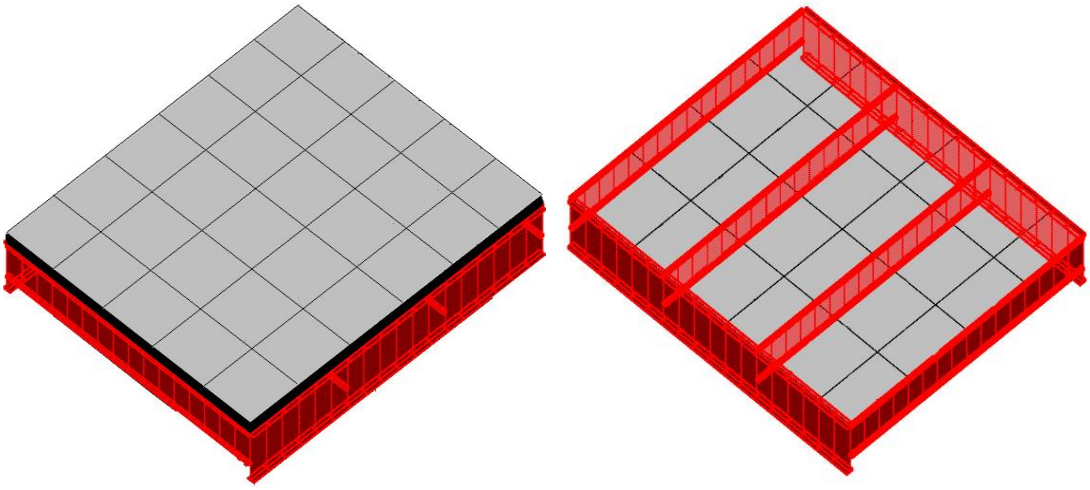

**Fig. 4.21 7.5m x 9.0m slab panel with 60 minutes' fire resistance**

Using Eurocode 4 Part 1-1 (CEN, 2005a) Eurocode 4 Part 1-2 (CEN, 2005b) for floor beam design at ambient and elevated temperatures, and assuming full composite action, the resulting selections for primary and secondary beam sections are UB 533x210x82 and UB 356x127x33 respectively.

In order to observe slab panel membrane action at elevated temperature, the primary beams and the edge secondary beams were protected, leaving the intermediate secondary beams unprotected.

After the composite rectangular slab had been designed, three cases of trapezoidal slabs were set up. Each successive trapezoidal slab model had its bottom edge length increased by 600 mm and its top edge length reduced by the same amount, so that the total area of the slab was kept constant.

| Case Num. of Models | Top Length (mm) | Bottom Length (mm) |
|---|---|---|
| 1 | 8400 | 9600 |
| 2 | 7800 | 10200 |
| 3 | 7200 | 10800 |

**Table. 4.2 Different trapezoidal slab top and bottom edge lengths**

### 4.4.2 Finite element analysis and membrane actions

To allow membrane action to occur, the rectangular slab and the three trapezoidal slab models were all considered as fully vertically supported, as an idealization of the 60-minute fire protection of the perimeter beams.

After analysis by *Vulcan*, the resulting deflections of the 4 different slab models are shown in Fig.4.22. Comparing these curves, as the geometry of slab changes from rectangular to more trapezoidal, the deflection at the slab centre starts to increase when the temperature reaches about 700°C. This is because the intermediate secondary beams in the trapezoidal slabs are longer than those in the rectangular slab, but have the same section size. The intermediate secondary beams in the trapezoidal slab definitely have larger deflections, which cause the slab centre to have higher vertical displacement.

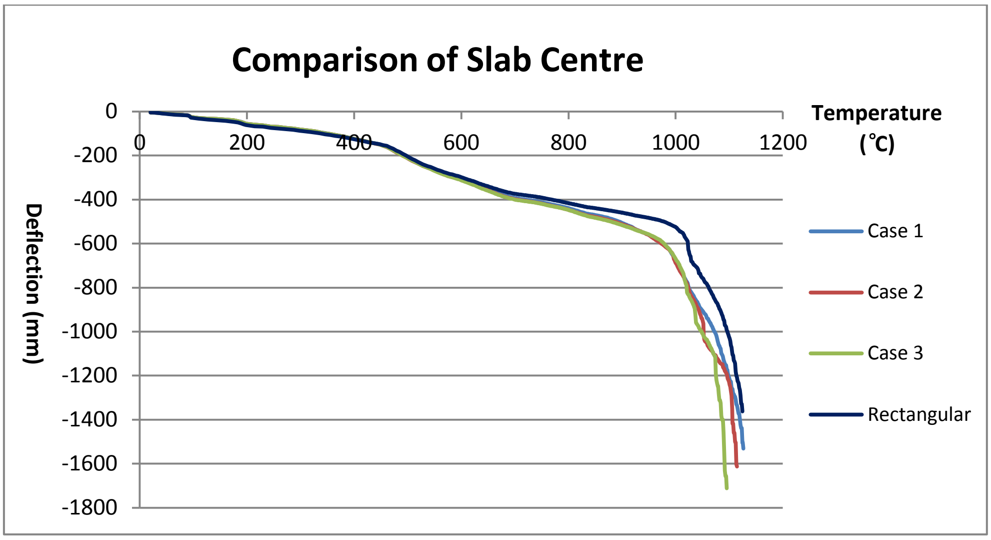

**Fig. 4.22 The slab centre deflection difference between rectangular and trapezoidal slab**

The slab centre deflections of the three models are very different at about 1100°C (slab lower face). As the ratio of top to bottom edge length reduces, the deflection of the slab centre increases.

Similar to the membrane force distribution in a rectangular slab, the membrane forces in the central area of a trapezoidal slab are tensile and this is surrounded by a compressive ring. From Fig.4.23, it can be seen that the compressive ring in the trapezoidal slab forms an approximate trapezium as well.

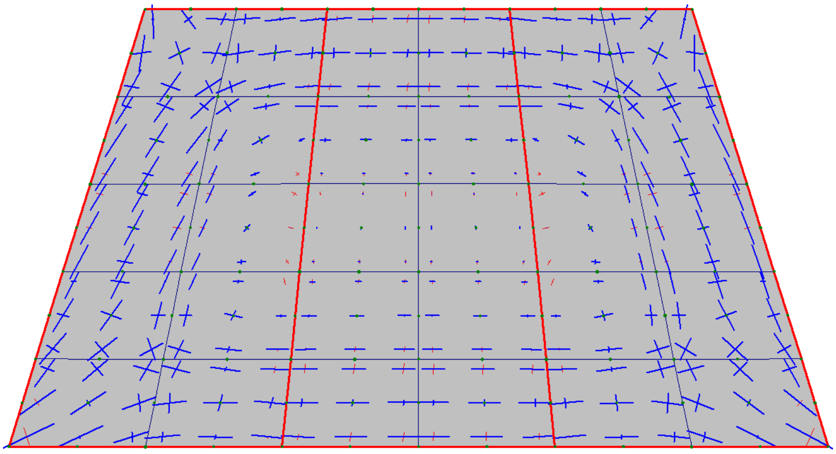

**Fig. 4.23 Membrane stress vectors at slab lower face 950°C (2D)**

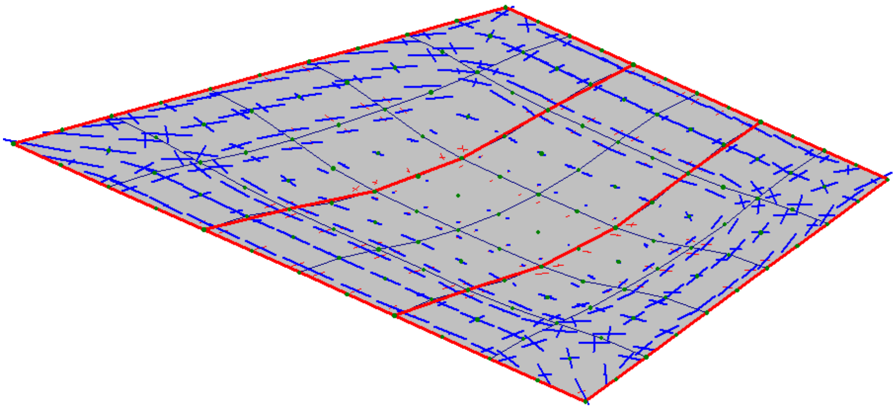

**Fig. 4.24 Membrane stress vectors at slab lower face 950°C (3D)**

## 4.5 Validation for trapezoidal continuous slab panel

In most cases, a non-orthogonal slab panel is at the edge of a building floor, which means that it is likely that there are adjacent slab panels continuous with it. In order to observe the membrane action in a continuous slab panel, the following model, shown in Fig. 4.25, was set up.

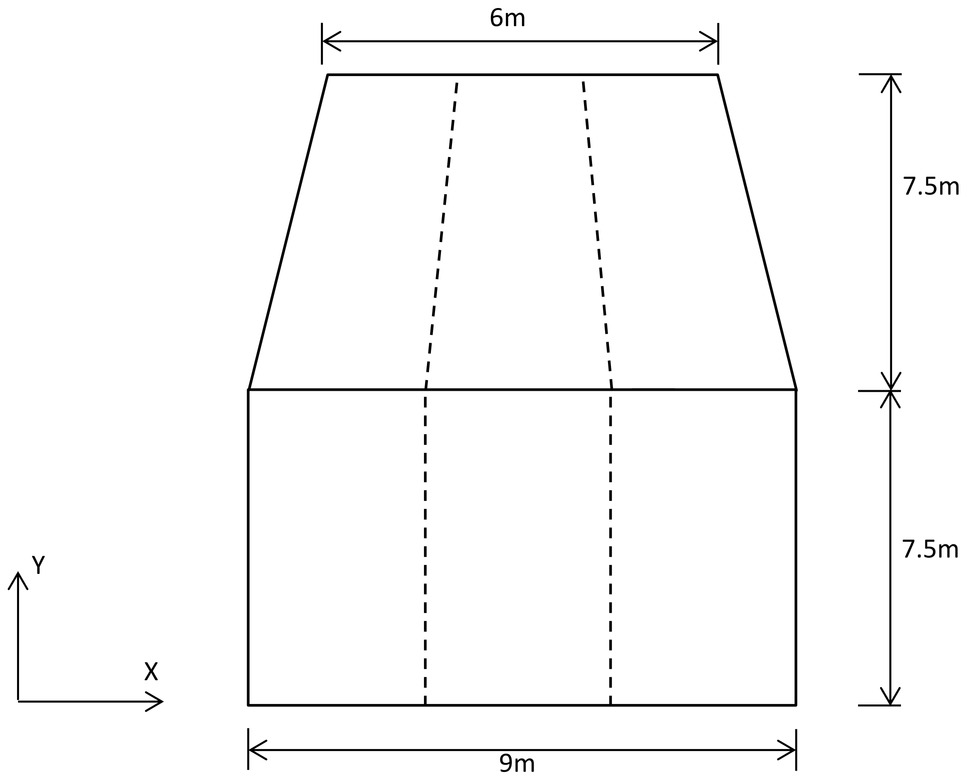

**Fig. 4.25 Layout for continuous trapezoidal slab panel**

In this model, the selection of beam sizes and slab cross-section is the same as in the previous 7.5m x 9m composite slab. The sizes of primary and secondary beams are UB 533x210x82 and UB 356x127x33, respectively. All the edge beams are protected for 60 minutes' fire resistance, but intermediate secondary beams were left unprotected. As distinct from the previous model, the intermediate primary beam in the *X* direction, between the rectangular and trapezoidal slab panels, was left unprotected, but was of the same beam size as the top and bottom primary beams.

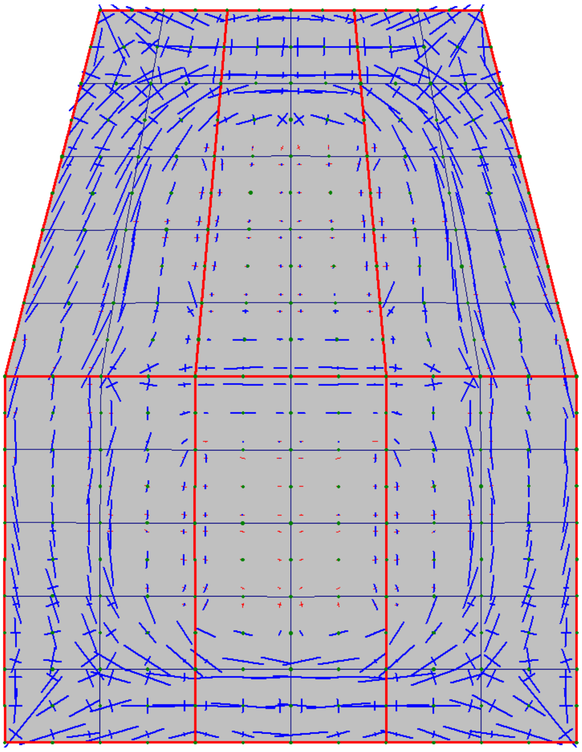

Fig. 4.26 Membrane stress vectors at slab lower face 600°C (2D)

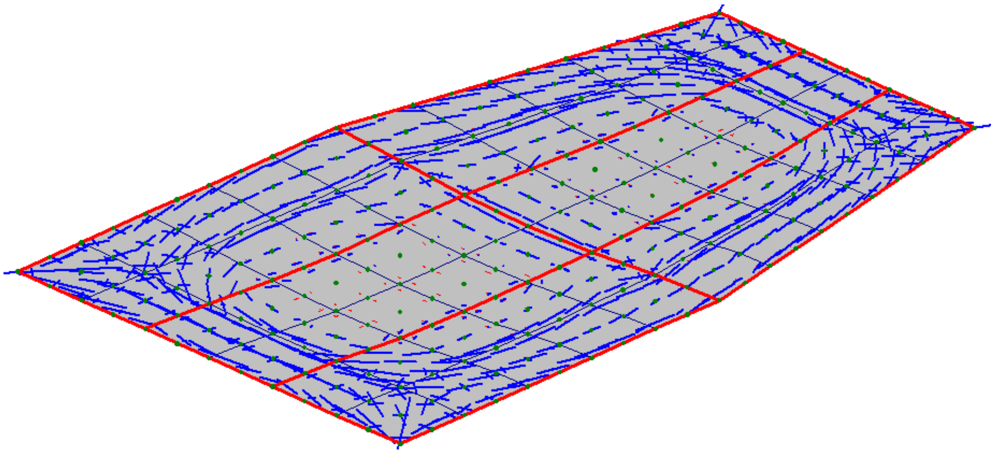

Fig. 4.27 Membrane stress vectors at slab lower face 600°C (3D)

From the figure above, the membrane action in this continuous slab panel is easy to observe. At about 600 ℃ (slab lower surface), the intermediate secondary beams have already lost most of their strength, but the central intermediate primary beam still has greater strength than the intermediate secondary beams, because of its much larger size. Therefore, the membrane action resembles that in two individual (rectangular and trapezoidal) slab panels. With compressive stresses parallel to the intermediate primary beam, the tensile stress already appears in both slab panel centres.

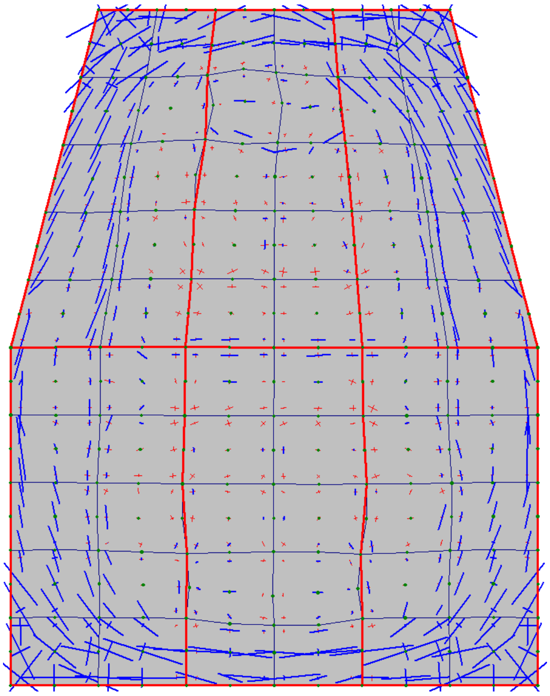

Fig. 4.28 Membrane stress vectors at slab lower face 1000°C (2D)

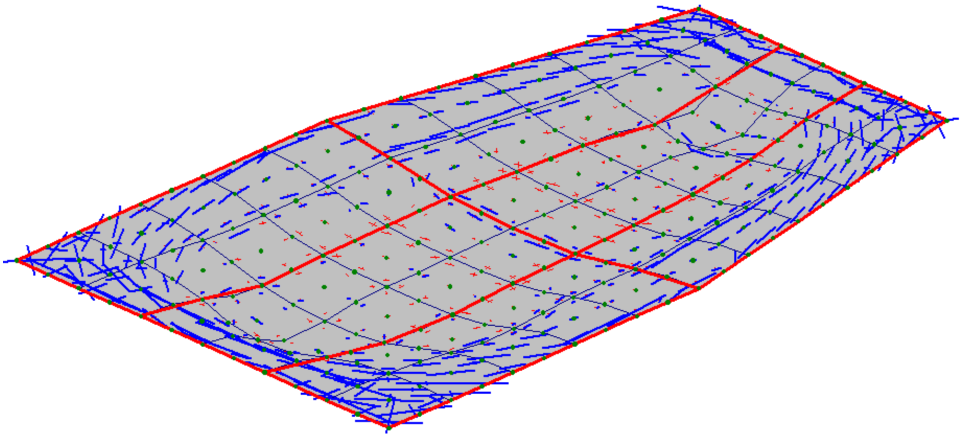

Fig. 4.29 Membrane stress vectors at slab lower face 1000°C (3D)

As the temperature increases, the intermediate primary beam keeps losing its strength and the deflection of the whole slab panel also increases. When the temperature of slab reached about 1000 ℃, the membrane action in the whole slab panel differs considerably from that at 600 ℃. Because the intermediate primary beam has lost most of its strength, the compressive stress which was previously parallel to the intermediate primary beam has almost disappeared. The tensile membrane stress has also spread to most of the slab panel's area. As a result, the individual membrane actions in the two slab panels have combined across the whole continuous panel.

From this model it can be deduced that, if the intermediate primary beam is adequately protected, the membrane action will be isolated within each of the two slab panels. This can be considered as further proof that an essential condition for membrane action to be mobilized is adequate vertical support from the beams around the perimeter of the slab panel. The change of membrane action also indicates that as the deflection of the slab central area increases, the compressive membrane stress is replaced by tensile membrane stress.

## 4.6 Tensile membrane action of rectangular slab panel with continuous edges

In practice, isolated rectangular slab panels with continuous edges often need to be analysed. Since there are four edges in a rectangular slab panel, with different locations of the panel the number of continuous edge can also differ. For a typical orthogonal building floor layout, as is shown in Fig. 4.30, the three rectangular slab panels denoted as 1, 2 and 3 are located in different positions relative to the floor perimeter, which implies differences in their boundary conditions and the existence of continuous edges.

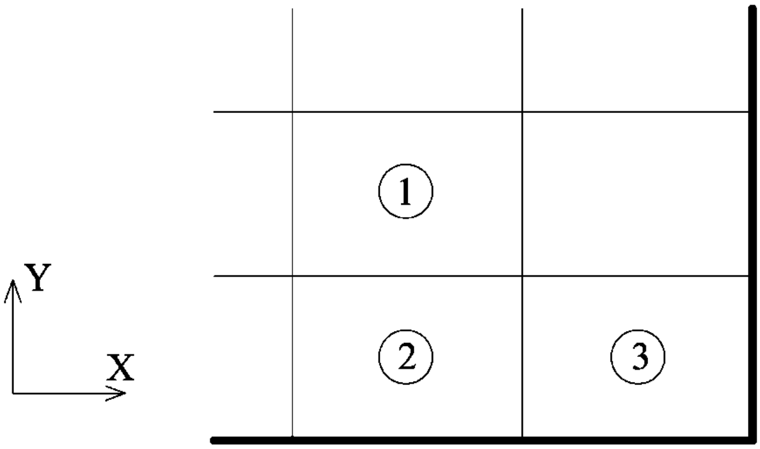

**Fig. 4.30 Typical building corner floor layout with rectangular slab panels**

In order to compare the tensile membrane action generated in these different situations of continuous edges, three isolated models have been created in *Vulcan*. The floor design and slab panel properties, together with the temperature profile, have been adopted as the same as those for the rectangular slab panel in Section 4.4.1 and Fig. 4.21. To ensure that tensile membrane action will be observed, all the edges of each slab panel are assumed to have full vertical support during the whole process of temperature increase. The finite element grid division is shown in Figure. 4.31.

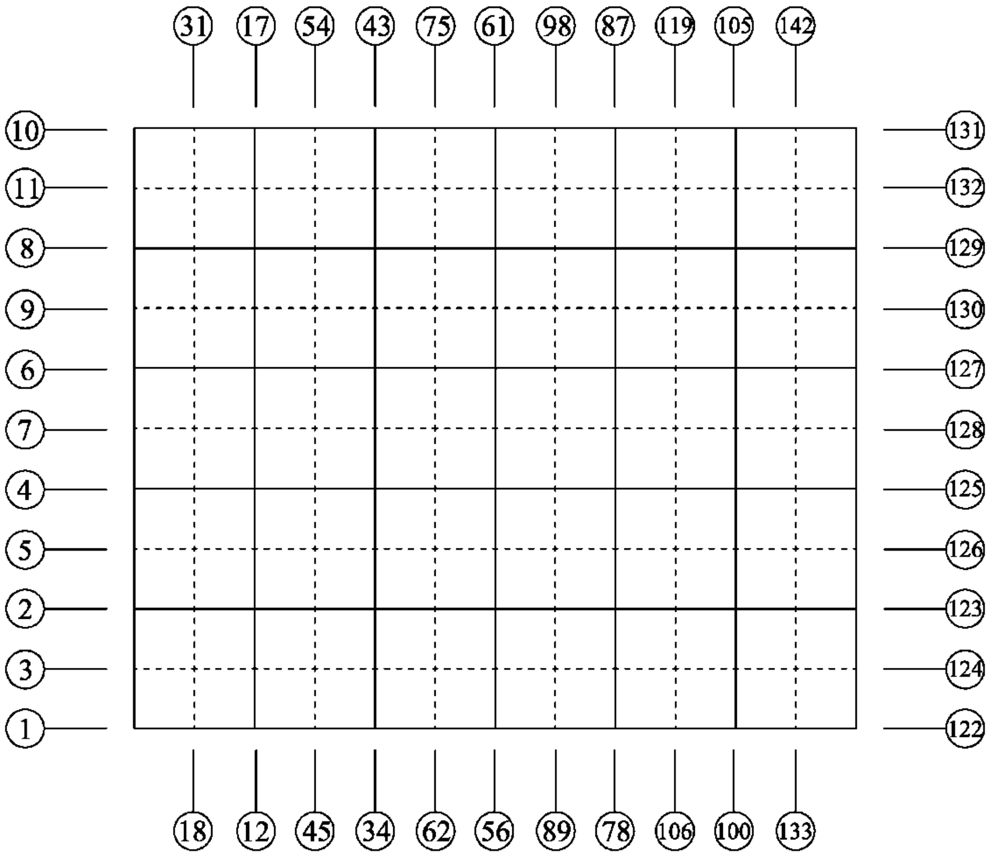

**Fig. 4.31 Finite element grid division of rectangular slab panels**

## Panel 1

This slab panel is surrounded by other slab panels, so that their interactions have to be considered; during numerical analysis all the four edges are recognized as continuous edges and therefore have to stay straight, although the nearness of the floor perimeter means that they do not have to be fixed in position. Hence, in this model, the nodal movements of the top and base edges are defined as equal in pairs in the $Y$ -direction, while the left and right edges are defined as equal in the $X$-direction. After non-linear analysis by *Vulcan*, the displacements of the slab edges at the lower face at 600°C are shown in Tables 4.3 and 4.4 below.

| Left Edge in *X*- | | Right Edge in *X*- | |
|---|---|---|---|
| Node Num. | Displacement (mm) | Node Num. | Displacement (mm) |
| 1 | -1.0931 | 122 | 1.1319 |
| 2 | -1.0932 | 123 | 1.1319 |
| 3 | -1.0932 | 124 | 1.1319 |
| 4 | -1.0931 | 125 | 1.1319 |
| 5 | -1.0932 | 126 | 1.1319 |

| | | | |
|---|---|---|---|
| 6 | -1.0931 | 127 | 1.1319 |
| 7 | -1.0931 | 128 | 1.1319 |
| 8 | -1.0932 | 129 | 1.1319 |
| 9 | -1.0932 | 130 | 1.1319 |
| 10 | -1.0931 | 131 | 1.1318 |
| 11 | -1.0932 | 132 | 1.1319 |

**Table. 4.3 Left and right edge displacements of internal slab panel 1**

| Top Edge in *Y*- | | Bottom Edge in *Y*- | |
|---|---|---|---|
| Node Num. | Displacement (mm) | Node Num. | Displacement (mm) |
| 1 | 2.0995 | 10 | -2.1075 |
| 12 | 2.0994 | 17 | -2.1074 |
| 18 | 2.0995 | 31 | -2.1074 |
| 34 | 2.0992 | 43 | -2.1072 |
| 45 | 2.0993 | 54 | -2.1073 |
| 56 | 2.0991 | 61 | -2.1071 |
| 62 | 2.0992 | 75 | -2.1071 |
| 78 | 2.0992 | 87 | -2.1072 |
| 89 | 2.0991 | 98 | -2.1071 |
| 100 | 2.0994 | 105 | -2.1074 |
| 106 | 2.0993 | 119 | -2.1073 |
| 122 | 2.0995 | 131 | -2.1075 |
| 133 | 2.0995 | 142 | -2.1074 |

**Table. 4.4 Top and bottom edge displacements of internal slab panel 1**

From Tables 4.3 and 4.4, it can be observed that the left and right edges of the slab move almost the same distance along *X*- but opposite in direction. Similar behaviour can be seen in *Y*- direction for the top and bottom edges. This result effectively clarifies the boundary movements of a slab panel with continuous edges, for which the slab edges are kept in a straight line.

The membrane stress distribution is illustrated in Figure. 4.32.

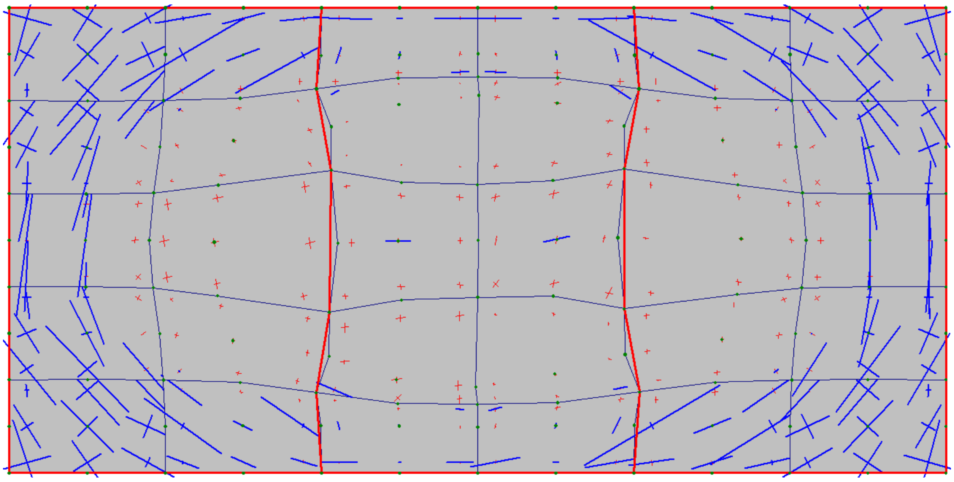

Fig. 4.32 Membrane stress vectors of internal slab panel 1 at slab lower face 600°C (2D)

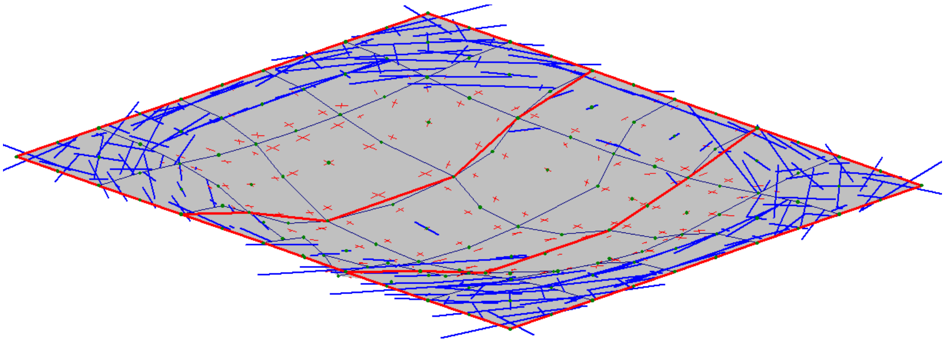

Fig. 4.33 Membrane stress vectors of internal slab panel 1 at slab lower face 600°C (3D)

From this figure it can easily be seen that, due to the symmetric relative constraints on boundary conditions, the deformations of the finite slab element are also symmetric in top and bottom part, and left and right part. This symmetry can also be found in the horizontal deformation of those two intermediate beams. With the symmetric boundary movements, both the tensile and compressive membrane stresses are almost symmetric as well.

### Panel 2

The slab Panel 2 is assumed to be located at the bottom edge of the floor layout. Therefore, apart from the bottom edge of this slab panel, the rest of the edges are defined as continuous with adjacent slab panels. The relative constraints used in Panel 1 have been applied to these three edges, but the bottom edge is left free to move in-plane. Since only one edge's boundary conditions are different from those in Panel 1, the distribution of membrane force is very similar, apart from the areas close to the edges with different conditions. The edge nodal deflections at 600°C are given below:

| Left Edge in X | | Right Edge in X | |
|---|---|---|---|
| Node Num. | Displacement (mm) | Node Num. | Displacement (mm) |
| 1 | -0.9248 | 122 | 0.9193 |
| 2 | -0.9249 | 123 | 0.9194 |
| 3 | -0.9249 | 124 | 0.9194 |
| 4 | -0.9248 | 125 | 0.9193 |
| 5 | -0.9249 | 126 | 0.9193 |
| 6 | -0.9248 | 127 | 0.9193 |
| 7 | -0.9248 | 128 | 0.9193 |
| 8 | -0.9249 | 129 | 0.9194 |
| 9 | -0.9249 | 130 | 0.9193 |
| 10 | -0.9249 | 131 | 0.9194 |
| 11 | -0.9249 | 132 | 0.9194 |

**Table. 4.5 Left and right edge displacements of edge slab panel 2**

| Top Edge in Y | | Bottom Edge in Y | |
|---|---|---|---|
| Node Num. | Displacement (mm) | Node Num. | Displacement (mm) |
| 1 | 2.7609 | 10 | 0 |
| 12 | 2.7608 | 17 | 1.9745 |
| 18 | 2.7609 | 31 | 0.5114 |
| 34 | 2.7606 | 43 | 5.4402 |
| 45 | 2.7607 | 54 | 3.8454 |
| 56 | 2.7605 | 61 | 7.1894 |
| 62 | 2.7605 | 75 | 6.8646 |
| 78 | 2.7606 | 87 | 5.5385 |
| 89 | 2.7605 | 98 | 6.8765 |
| 100 | 2.7608 | 105 | 2.0866 |
| 106 | 2.7607 | 119 | 4.003 |
| 122 | 2.7609 | 131 | 0 |
| 133 | 2.7609 | 142 | 0.5547 |

**Table. 4.6 Top and bottom edge displacements of edge slab panel 2**

In these two tables, symmetric displacements of equal magnitude in *X*- direction can be seen at the left and right edges. The top edge nodes have an identical displacement in the *Y*- direction, keeping the edge straight as expected. With a free movement boundary condition, the bottom edge shows a totally different nodal displacement pattern.

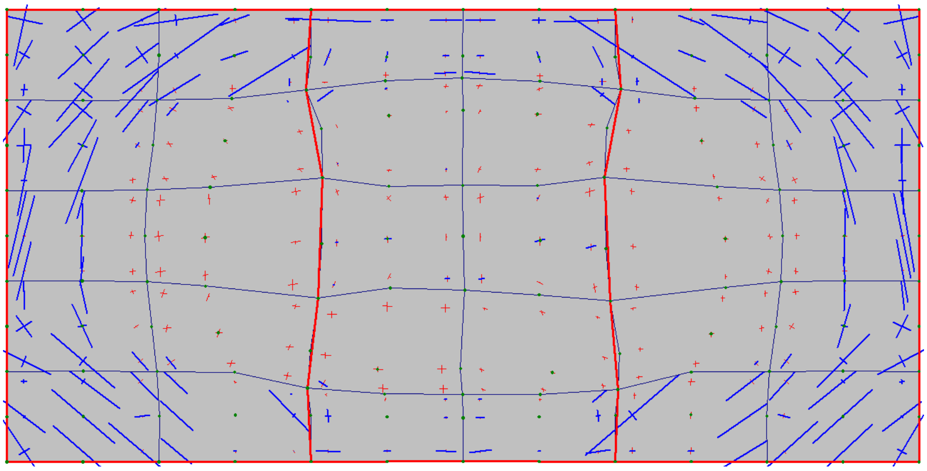

Fig. 4.34 Membrane stress vectors of edge slab Panel 2 at slab lower face 600°C (2D)

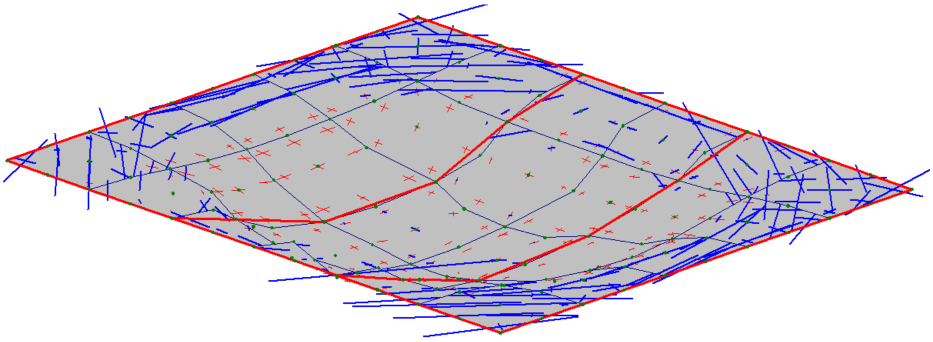

Fig. 4.35 Membrane stress vectors of edge slab Panel 2 at slab lower face 600°C (3D)

The difference in the distribution of compressive force in the lower and upper slab panel areas is easily seen. The distribution of compressive force is still almost symmetric left-to-right, and is very similar to the distribution in Panel 1. The horizontal deformation of the intermediate beams is symmetric as well. However, in the lower area next to the edge with free movement, the compressive force differs compared to the upper area.

## Panel 3

In this case, the location of this slab panel determines that there is no adjacent slab panel next to the right-hand and bottom edges. Hence, the boundary conditions on the bottom and right-hand edges are set as free to move. In contrast, the top and bottom edges with continuity have respectively been equipped with relative constraints in the *Y*- and *X*-directions. After analysis, the results for boundary displacements at the slab lower face at 600°C are listed in Tables. 4.7 and 4.8.

| Left Edge in *X*- | | Right Edge in *X*- | |
|---|---|---|---|
| Node Num. | Displacement (mm) | Node Num. | Displacement (mm) |
| 1 | -1.6571 | 122 | 0 |
| 2 | -1.6572 | 123 | 2.0145 |
| 3 | -1.6572 | 124 | 1.0987 |
| 4 | -1.6571 | 125 | -0.974 |
| 5 | -1.6571 | 126 | 0.9176 |
| 6 | -1.6571 | 127 | -2.1133 |
| 7 | -1.6571 | 128 | -2.1012 |
| 8 | -1.6571 | 129 | 0.2271 |
| 9 | -1.6571 | 130 | -0.8567 |
| 10 | -1.6571 | 131 | 0.1809 |
| 11 | -1.6571 | 132 | 0.818 |

**Table. 4.7 Left and right edge displacements of corner slab panel 3**

| Top Edge in *Y*- | | Bottom Edge in *Y*- | |
|---|---|---|---|
| Node Num. | Displacement (mm) | Node Num. | Displacement (mm) |
| 1 | 2.4606 | 10 | 0 |
| 12 | 2.4605 | 17 | 2.0222 |
| 18 | 2.4606 | 31 | 0.5225 |
| 34 | 2.4603 | 43 | 5.4608 |
| 45 | 2.4604 | 54 | 3.9164 |
| 56 | 2.4602 | 61 | 7.0949 |
| 62 | 2.4602 | 75 | 6.7946 |
| 78 | 2.4603 | 87 | 5.6077 |
| 89 | 2.4602 | 98 | 6.8243 |
| 100 | 2.4604 | 105 | 2.3844 |
| 106 | 2.4603 | 119 | 4.1963 |
| 122 | 2.4606 | 131 | 0 |
| 133 | 2.4605 | 142 | 0.7835 |

**Table. 4.8 Top and bottom edge displacements of corner slab panel 3**

With relative constraints applied, the left and top edges have the same displacements. On the other hand, the right and bottom edges, which are defined with free movement, have nodal displacements which are totally different from each other. From the nodal displacements at the free edges, it can be seen that the values are irregular and erratic which induced that the shape of the free edges becomes as an strange curve with many turning points.

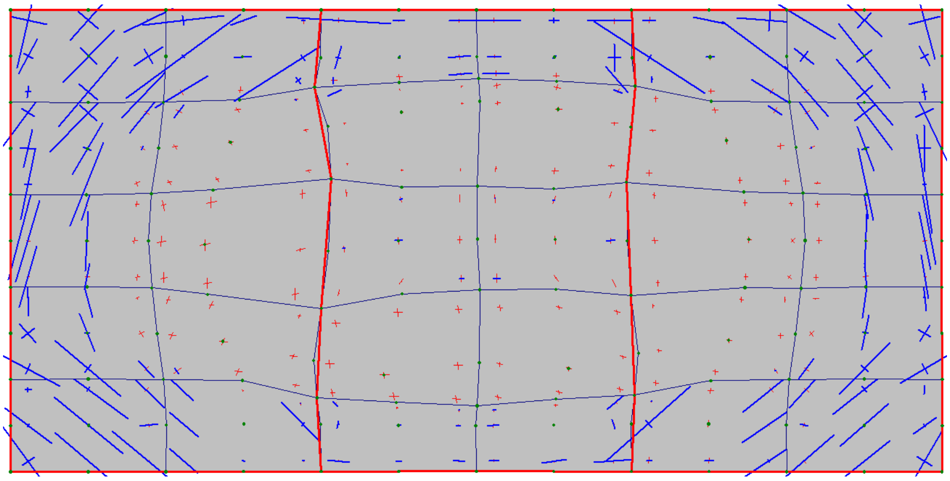

Fig. 4.36 Membrane stress vectors of corner slab Panel 3 at slab lower face 600°C (2D)

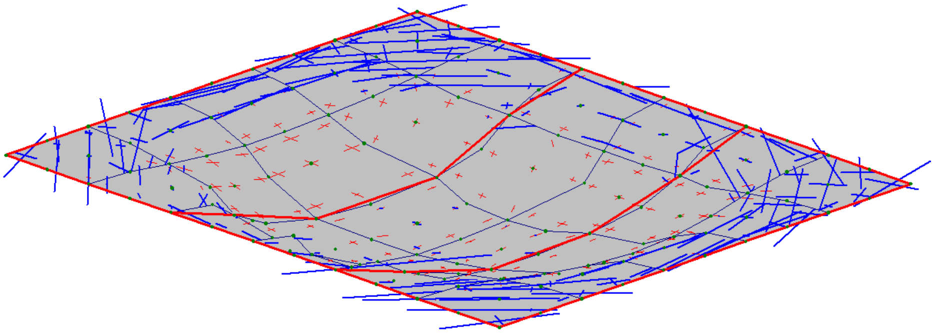

Fig. 4.37 Membrane stress vectors of corner slab Panel 3 at slab lower face 600°C (3D)

With free movement across the bottom edge, the distribution of compressive membrane force in the area near the bottom edge is exactly the same as in Panel 2, in which the bottom edge is also free to move. In the upper section of the slab panel, as all three models have assumed top edge continuity, the distribution of compressive membrane force is very similar in all three models. The most significant difference observed in this case is that the deformation of intermediate beams is no longer symmetric. Since the left edge is defined with continuity, it can be seen that the left intermediate beam has a larger horizontal deformation than the right one. Similarly, the slab elements in the left section of the slab have larger deformation than those in right section.

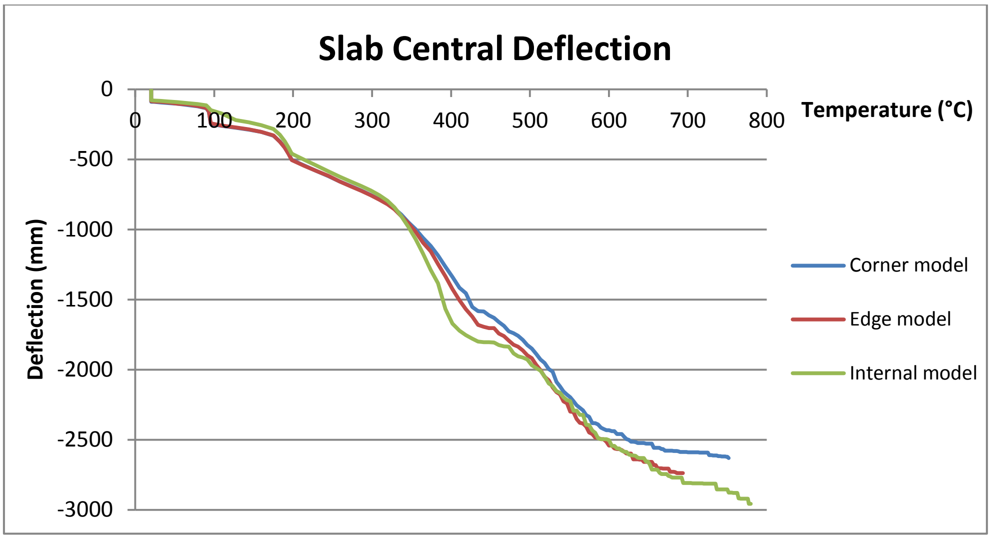

Fig. 4.38 Comparison of slab central deflections in 3 cases

In Fig. 4.38 it is shown that in the first 300°C the difference in slab central deflection in these 3 models is not very obvious, the internal model has a smaller vertical displacement. From 350°C to 400°C, and compared to other two models the internal slab panel model has a larger rate of deflection increase. This temperature is about when membrane action occurs, as it can be seen that the model which simulates the internal slab panel with four continuous edges has the largest vertical deflection. In other words, the tensile membrane force in the internal model is larger than in the other two cases. From the results, it has been found that the structural failure temperature of the edge model is 693.7°C, which is the earliest, followed by the corner model about 751.8 ℃, the internal model with all continuous edges persists to 780.8°C which is the longest.

By comparing the vertical deflections of the left and right intermediate beams in Figs. 4.39 and 40, it can be observed that, in the edge and corner models, the curve is exactly same before the structural failure temperature. However, before about 700°C, the internal model has a smaller vertical deflection than other two models. This is because, in the edge and corner models, the bottom edge of the slab panel is defined as free to move, but the bottom edge of the internal model is set with relative constraints. Therefore, it can be concluded that, for the beam at slab perimeter which supports intermediate secondary beams, the continuity of the edge will reduce the deflection of the intermediate secondary beam.

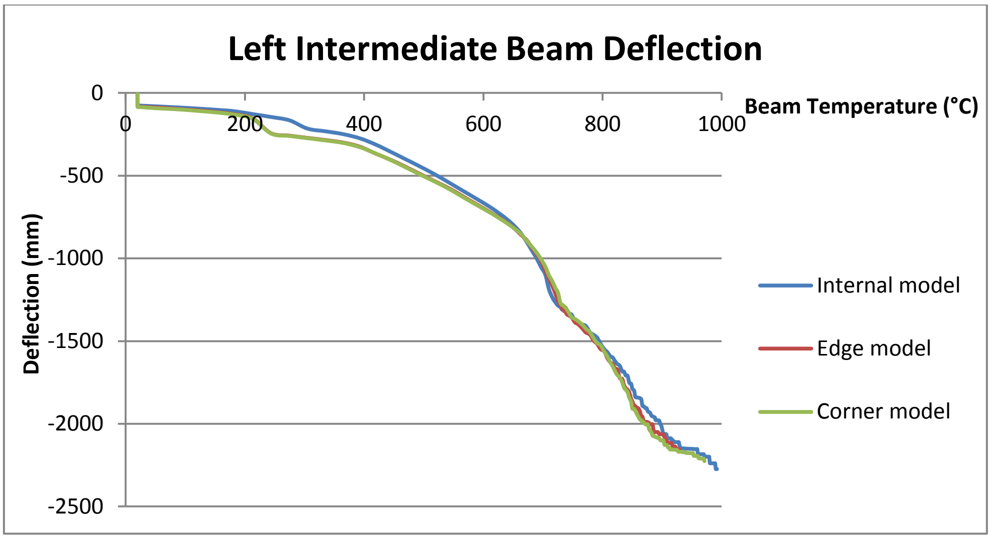

**Fig. 4.39 Vertical deflection of left intermediate beam**

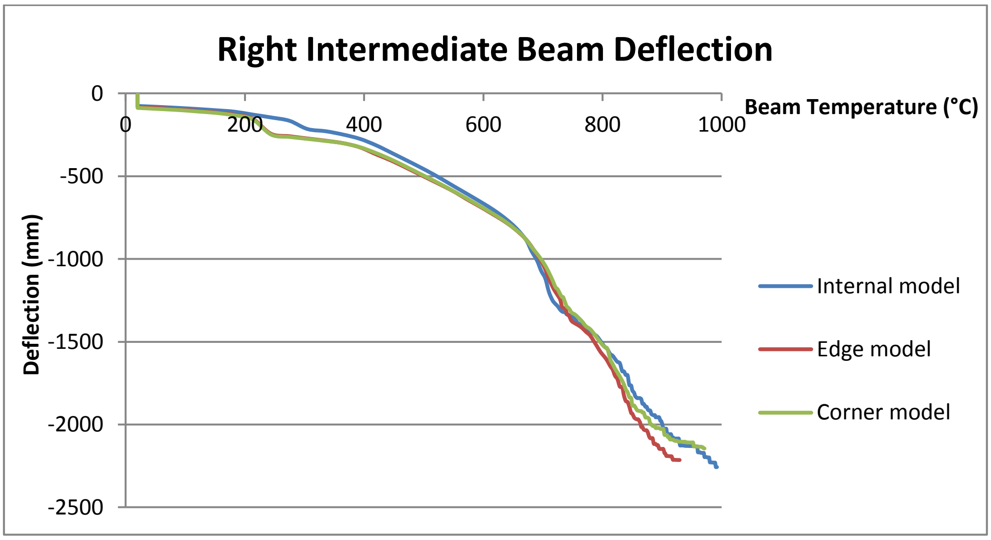

**Fig. 4.40 Vertical deflection of right intermediate beam**

## 4.7 Summary and discussion

Different buildings with different floor layouts provide various types of slab panel sub-division, when it is necessary to model single isolated panels rather than a complete floor. One of the most important factors in obtaining accurate results when using finite element analysis on these isolated panel models is to ensure the accuracy of movement of each element. For FEM analysis, the density of elements is one of the most important basic components which can directly affect the accuracy of results. As a general rule, a model which has been divided more finely will be more accurate than a coarser one. However, it is impossible to continuously reduce the dimensions of elements, as higher numbers of elements cause longer calculation times. Therefore, it is advisable to find a compromise which provides accurate enough results in an acceptable time.

As *Vulcan* is a node-based finite element program, the displacement of each node plays a key role in representing the whole structural behaviour. The nodes on boundaries determine the movements of the slab perimeter. Different locations on the slab panel are assigned different boundary conditions, although perimeter beams to slab panels are often considered as providing continuous vertical support in order to allow the membrane actions to happen. Restraints to horizontal movement are dependent on whether there are other adjacent slab panels which are not explicitly modelled.

The global axes used in most FE programs are *X, Y* and *Z,* which are orthogonal. If a structure has been divided into an orthogonal grid, which is parallel to the global axes, it is simple to impose restraints in a model. However if a slab panel is not orthogonal, the penalty function method needs to be applied to solve the problem of restraining the movements of boundaries.

Once the movements of boundary nodes have been adequately represented, the membrane action of a non-orthogonal slab panel can be observed from geometrically nonlinear numerical modelling. From all the models simulated in this chapter, it can be concluded that for non-orthogonal slab panels the distributions of membrane force are very similar to those found in orthogonal slab panels, having compressive force around their perimeter and tensile force located within the central area. However, the zone of tensile membrane action has been observed to be smaller in triangular slabs compared to rectangular slabs. This is because the geometrical characteristics of a triangle strengthen the stiffness of the slab, causing smaller central vertical displacement. Therefore, as the distribution of membrane forces has been confirmed, the extension of the basic method to the non-orthogonal case can be achieved with more accurate fire limit state design for non-orthogonal composite slabs. When applying this method to investigate rectangular slab panels in various locations, the results have also successfully shown the differences in the distribution of membrane forces. This again shows the contribution made by this study, and that it will definitely help, both in further research into slab membrane action under different boundary conditions, and also in fire-resistant design of composite slab panels in various locations.

# Chapter 5 Tensile membrane action of non-orthogonal slabs

## 5.1 Introduction of yield-line pattern of triangular slabs

According to the initial investigation of membrane action of a reinforced concrete slab, the distribution of tensile and compressive stress relates to the small-deflection yield-line pattern of slabs. Based on the yield-line theory and also the possible stress distributions, an equilibrium method was established (Hayes, 1968). With some modifications and improvements, an advanced version of this was developed (Bailey and Toh, 2007) as a simplified design method for tensile membrane action of composite slabs in fire; this is generally known as the Colin Bailey Design Method.

In order to extend simplified design into non-orthogonal slabs, the primary aim is to determine the appropriate yield-line patterns for these particular slabs. From previous experimental research, it has been apparent that the yield-line pattern of a reinforced concrete slab also represents its collapse mechanism for higher deflections. The yield-line pattern is also affected by the boundary conditions of slab edge support. For an isosceles triangular slab with simple support at its edges, the yield-line pattern can easily be found.

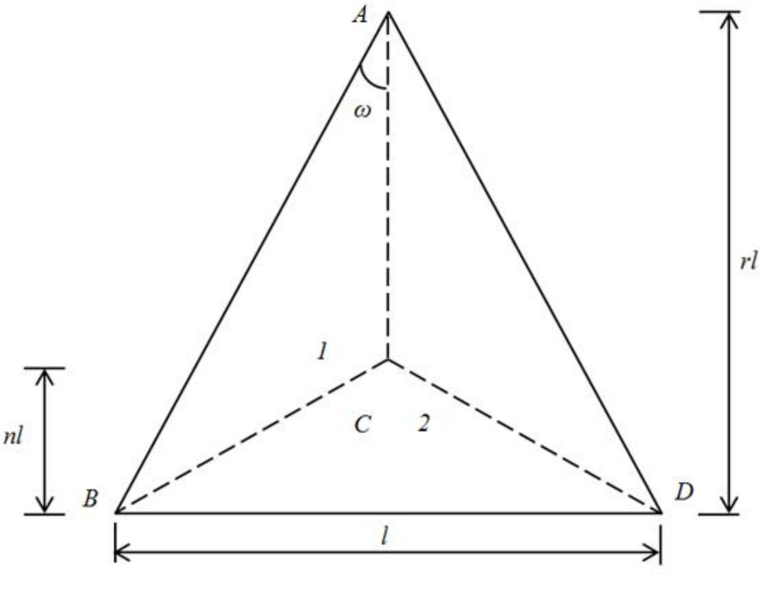

**Fig. 5.1 Yield-line pattern for triangular slab with simple supports**

It is assumed that the in-plane stress distributions of a triangular slab are based on the optimized yield-line pattern which is defined by the factor *n* (Fig.5.1). Therefore, the first problem which needs to be solved is to find the optimized value of $n$, which is related to the exact geometry of the triangular slab.

For the purpose of finding the optimized value of $n$, the energy equations are employed,

$$\delta = nl \cdot \theta \tag{5.1}$$

$$\delta = (r - n)l \sin \omega \cdot \varphi \tag{5.2}$$

$$\theta = \left(\frac{r - n}{n}\right) \varphi \sin \omega \tag{5.3}$$

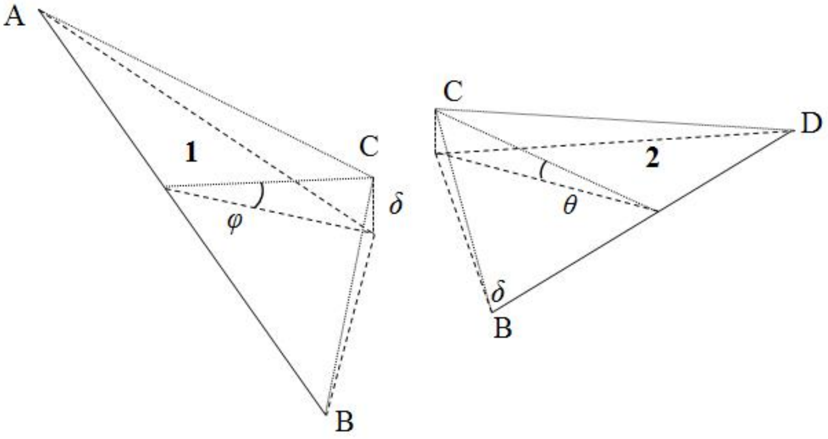

**Fig. 5.2 Triangular slab central deflection and rotation about slab edges**

$\delta$ is the vertical displacement at the yield-line intersection point C in the direction of perpendicular to the slab panel, $\theta$ is the rotation of element 2 about base edge BD, $\varphi$ is the rotation of element 1 about edge AB.

The loss of external energy due to movement of the loads can be described as,

$$E = \frac{\delta}{3} \cdot \frac{rl^2}{2} \cdot P \tag{5.4}$$

in which $P$ is the uniformly distributed load intensity on the slab panel.

On the other hand, the internal dissipation of energy can be described as,

$$W = \delta\left[M_{py}\left(\frac{2r}{r-n}\right)\cot\omega + M_{px}\left(\frac{1}{n}+\frac{1}{r-n}\right)\right] \tag{5.5}$$

in which $M_{px}$ and $M_{py}$ are the plastic moments of resistance in the $X$ and $Y$ directions respectively. When the slab is isotropic, $M_{px} = M_{py}$.

When we equate $E$ to $W$,

$$P = \frac{6}{l^2(r-n)}\left(2M_{py}\cdot cot\,\omega + \frac{M_{px}}{n}\right) \tag{5.6}$$

If $M_{px} = M_{py}$,

$$P = \frac{6M_p}{l^2(r-n)}\left(2\,cot\,\omega + \frac{1}{n}\right) \tag{5.7}$$

Differentiating the equation above with respect to n, and setting the derivative equal to 0, it is possible to find the value of $n$ which forms a yield-line pattern for minimum $P$.

$$\frac{dP}{dn} = 0$$

Giving, for $M_{px} = M_{py}$,

$$n = \frac{-1+\sqrt{1+2r\,cot\,\omega}}{2\,cot\,\omega} \tag{5.8}$$

So that, as $cot\,\omega = 2r$

in general,

$$P = \frac{6}{l^2(r-n)}\left(4rM_{py} + \frac{M_{px}}{n}\right) \tag{5.9}$$

When $M_{px} = M_{py}$

$$P = \frac{6M_p}{l^2(r-n)}\left(2\cot\omega + \frac{1}{n}\right) \tag{5.10}$$

and in general,

$$n = \frac{-M_{px} + \sqrt{{M_{px}}^2 + 4r^2 M_{px} M_{py}}}{4rM_{py}} \tag{5.11}$$

when $M_{px} = M_{py}$,

$$n = \frac{-1 + \sqrt{1 + 4r^2}}{4r} \tag{5.12}$$

where $r$ is the ratio of the triangle height to the base-side length.

## 5.2 Membrane action of triangular slabs

As the membrane stresses in triangular slabs have been found in *Vulcan*, the distributions are similar to those in rectangular slabs. Qualitatively these can be described as a field of tensile membrane stress in the central area of the slab surrounded by a ring of compressive stress around the perimeter zone of the slab. According to the previously described equilibrium method and the simplified design method, it is reasonable to assume that the membrane force variation across the yield lines in a triangular slab will be linear, since the neutral axes along the yield lines will be straight lines (Hayes, 1968). The assumed distribution of in-plane membrane stress in a triangular slab is shown in Fig. 5.3.

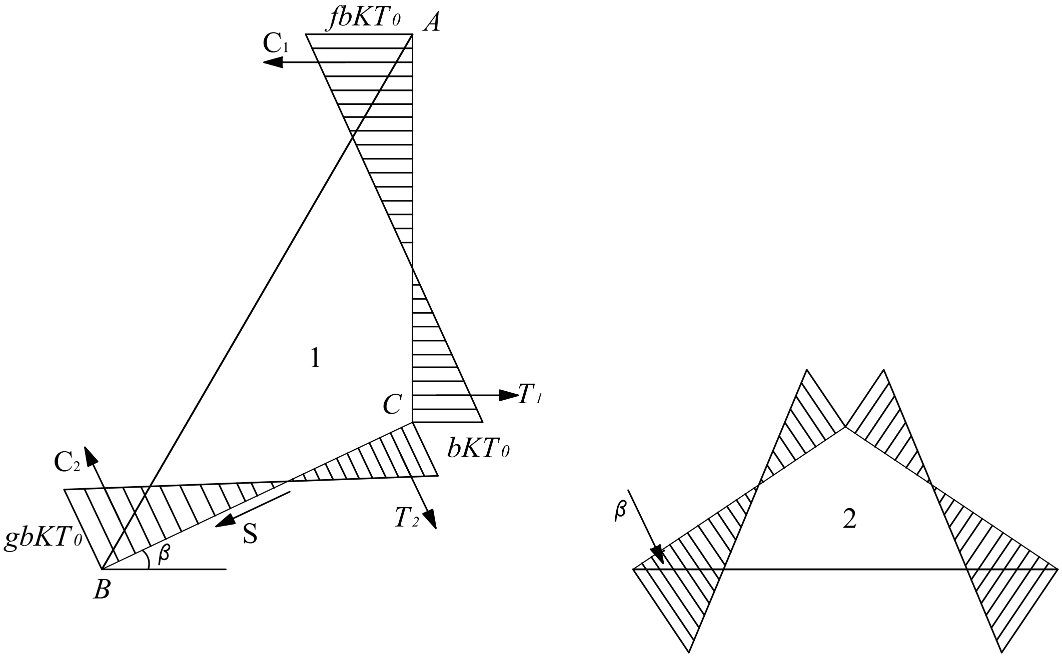

**Fig. 5.3 In-plane membrane stress distributions of triangular slab**

Where *b* is a parameter defining magnitude of the membrane force, whose value will need to be resolved. *K* is the ratio of yield force in the reinforcing steel across the two spanning directions. $KT_0$ is the yield force in the reinforcing steel per unit slab width in the direction parallel to the base of the triangle height, and $T_0$ is the yield force in reinforcing steel per unit width in the orthogonal direction.

As the apex angle is usually different from the bottom angles, the parameters *f* and *g* have been included to describe the magnitude of the membrane stress. If the slab is an equilateral triangle in shape, then *f* should have same value as *g*. The resultant tensile and compressive forces are given by the areas of the stress triangles in Figure. 5.3, as follows:

$$T_1 = \frac{bKT_0}{2}\left(\frac{1}{1+f}\right)(1-n)l$$

(5.13)

$$C_{1=}\frac{fbKT_0}{2}\left(\frac{f}{1+f}\right)(1-n)l$$

(5.14)

$$T_2 = \frac{bKT_0}{2}\left(\frac{1}{1+g}\right)\sqrt{\tan^2\alpha + n^2}\, l \tag{5.15}$$

$$C_2 = \frac{gbKT_0}{2}\left(\frac{g}{1+g}\right)\sqrt{\tan^2\alpha + n^2}\, l \tag{5.16}$$

For equilibrium of Element 1, we use the relationships

$$\mathrm{S}\sin\beta = (C_2 - T_2)\cos\beta$$

$$-\mathrm{S}\cos\beta = (C_2 - T_2)\sin\beta - (C_1 - T_1)$$

Hence,

$$(C_2 - T_2) = (C_1 - T_1)\sin\beta \tag{5.17}$$

$$\sin\beta = \frac{nl}{\sqrt{\tan^2\alpha + n^2}\, l} \tag{5.18}$$

In the previously developed simplified design method for rectangular slabs, another equilibrium equation was estimated, as described by Hayes (1968).

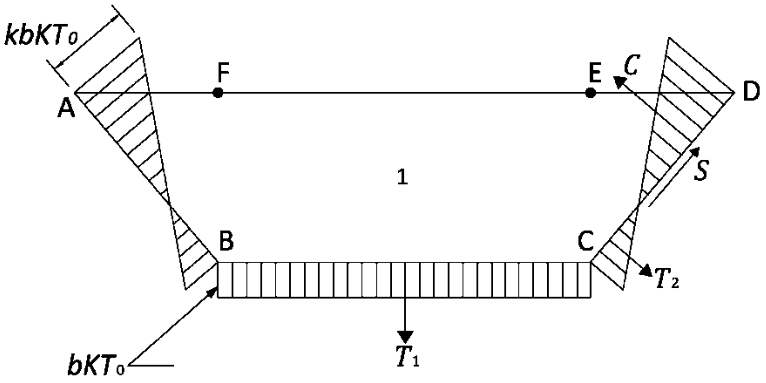

**Fig. 5.4 In-plane stress distributions for the equilibrium method (Hayes, 1968)**

According to illustration by Hayes, an upper bound to this moment may be obtained by assuming that all the reinforcement along the section is yielding and that the centroids of the compressive stress-blocks are at E and F (Fig.5.4). In his assumption of the locations of resultant forces, Hayes considered not only the compressive stresses along the yield lines, but also in other regions of Element 1. However, as the distribution of compressive stress surrounds the slab perimeter as a ring, the in-plane compressive stress is irregularly shaped between the yield line AB (or CD) and the axis of symmetry. As an approximation of the true equilibrium state, he assumed that the force resultants of each compressive stress zone pass through E and F, which are located at the same long-span coordinates as the yield line intersections B and C. This assumption has never been proved, and has no analogy in triangular slabs. This leads to insufficient equilibrium equations to find all the unknowns. Therefore, a direct extension of the Hayes design method to triangular slabs is impossible unless the assumptions made for a rectangular slab can be rationalized and proved.

## 5.3 Yield-line patterns of trapezoidal slabs and energy equations

Compared to the yield-line patterns of triangular slabs, it is more difficult to determine the yield-line patterns in trapezoidal slabs, because describing the geometry of trapezia is more complicated. Since the yield-line patterns of two-way rectangular slabs have already been optimized and are generally accepted, furthermore, small changes in two opposing sides of a rectangular slab should not make a big difference to the yield-line patterns, as shown in Figure 5.5 below.

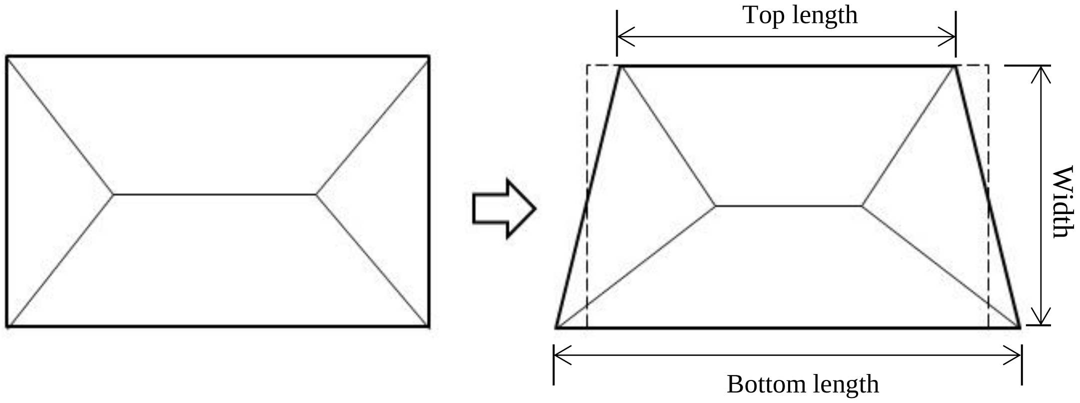

Fig. 5.5 Yield-line pattern 1 of trapezoidal slab developed from rectangular slab

Given the normal optimization of yield-line patterns of rectangular slabs, the first assumption for the yield-line pattern of a trapezoidal slab can be a similar pattern to that developed for rectangular slabs. In this pattern, the four regions rotate about the edges of the slab, and the middle yield line between two intersection points is parallel to the two parallel edges. However, changes of trapezium geometry, such as increasing the width, and also following the general rules governing the optimum yield-line pattern, the yield line between the two intersection points may be perpendicular or parallel to the two parallel sides; so the optimum yield-line pattern may either be of the type shown in Figure 5.5 or that in Figure 5.6, depending on the exact geometry and the reinforcement areas in the two directions. For rectangular slabs, the aspect ratio would be the main factor determining the direction of the central yield-line. However, in trapezoidal slabs, there cannot be just one determining factor, because more variables, such as the lengths of the top and bottom parallel sides, and the height between them.

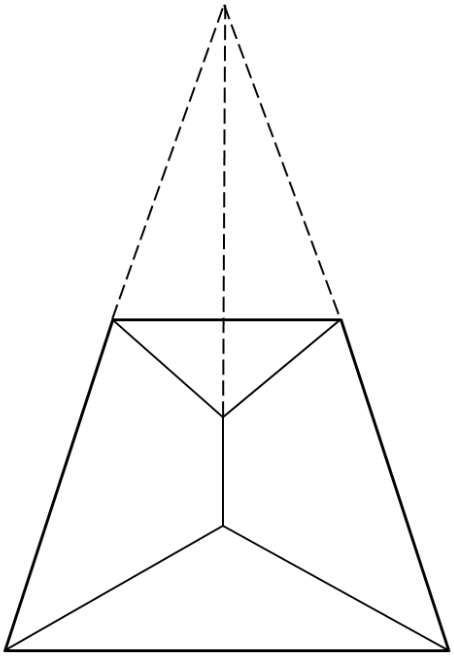

**Fig. 5.6 Assumed yield-line Pattern 2 of trapezoidal slab**

For this reason it is necessary to determine the load capacities for middle yield-lines assumed in either direction, and to investigate these by applying the energy equations with the two different yield-line patterns preset. By using the plastic energy balance method, the minimum load capacities for each of the two yield-line patterns can be found, the smaller of the two results for slabs of the same geometry being considered as the one forming the relevant yield-line pattern for the trapezoidal slab.

In general, the plastic energy balance can be described as equating the potential energy expended by the movement of the external loads (the external work) to equal the energy dissipated in yield-line rotation (the internal work). In algebraic terms:

$$\sum (P \times v)_{for\ all\ regions} = \sum (M \times l \times \theta)_{for\ all\ regions}$$

where,

*P* is the loading acting on a particular region,

$\upsilon$ is the vertical displacement corresponding to the load *P* on each region,

*M* is the plastic moment of resistance of the slab per metre of yield-line,

*l* is the length of yield-line or projected length of yield-line corresponding to *m*,

$\theta$ is the rotation at the yield-line corresponding to *M*.

Using this equation a uniform load *P* can be expressed in terms of the other variables, and by setting derivatives of *P* to zero the value of *P* can be optimized as the minimum load capacity.

### 5.3.1 Energy equations for yield-pattern 1

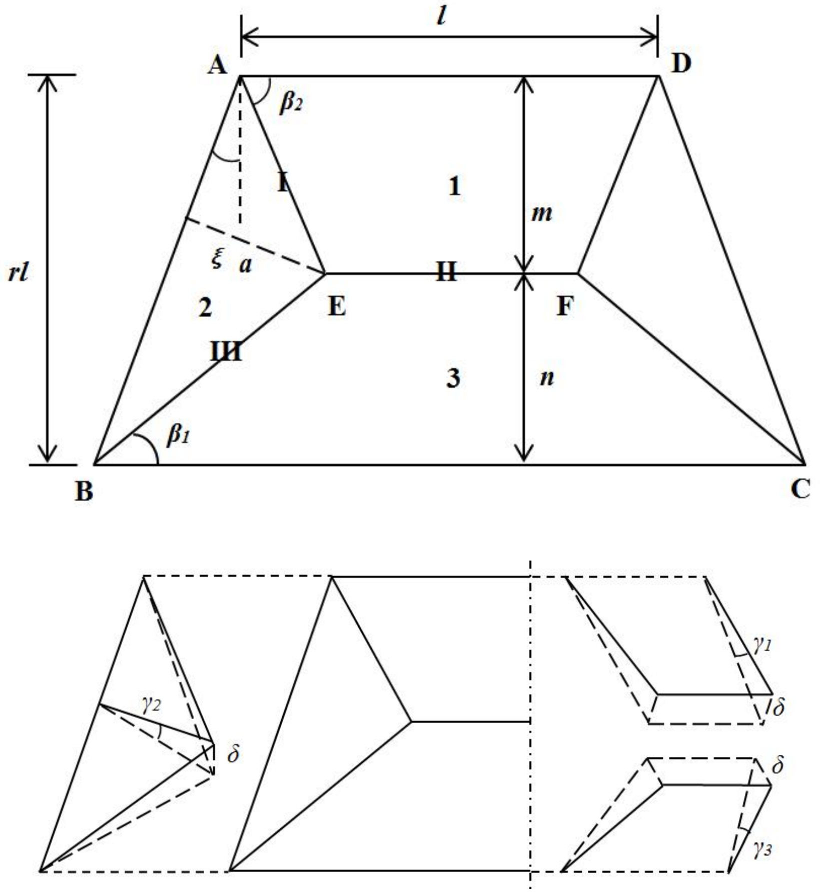

Fig. 5.7 Yield-line pattern 1 and rotations about slab edges

Firstly, the vertical displacement $\delta$ at point E can be expressed for all the regions of the slab as follows:

Element 1: $\delta = m\gamma_1$

Element 2: $\delta = a\gamma_2$

Element 3: $\delta = n\gamma_3$

From Figure 5.7 it can be seen that the rotations of Element 1 and Element 3 are about the *X* axis because the appropriate edges of the slab lay are orientated in the *X* direction. However for Element 2, the edge of the slab is not parallel to either the *X* or *Y* direction, so that the rotation is partly about the *X* axis and partly about the *Y* axis.

**Internal Work:**

For Hinge I:

About *X*: $D_x = M \cdot \frac{m}{tan\beta_2} \cdot (\gamma_1 - \gamma_2 sin\xi)$

About *Y*: $D_y = M \cdot m \cdot (\gamma_2 cos\xi)$

Therefore, for hinge I:

$$D = M \cdot \left(\frac{m}{tan\beta_2}\right) \cdot (\gamma_1 - \gamma_2 sin\xi) + M \cdot m \cdot (\gamma_2 cos\xi) \tag{5.19}$$

For hinge II:

Only about *X*:

$$D = M \cdot \left(l - \frac{2m}{tan\beta_2}\right) \cdot (\gamma_1 + \gamma_3) \tag{5.20}$$

For hinge III:

About *X*: $D_x = M \cdot \frac{n}{tan\beta_1} \cdot (\gamma_3 + \gamma_2 sin\xi)$

About *Y*: $D_y = M \cdot n \cdot \gamma_2 cos\xi$

Therefore, for hinge III:

$$D = M \cdot \left(\frac{n}{tan\beta_1}\right) \cdot (\gamma_3 + \gamma_2 sin\xi) + M \cdot n \cdot \gamma_2 cos\xi \tag{5.21}$$

As the yield-line pattern is symmetric, the total internal work dissipated is the internal work about hinges I and III multiplied by 2 plus the internal work about hinge II, so that:

Internal work:

$$= 2M \times \left(-\frac{msin\xi}{atan\beta_2} + \frac{rlcos\xi}{a} + \frac{l}{2m} + \frac{l}{2n} - \frac{m}{ntan\beta_2} + \frac{1}{tan\beta_1} + \frac{nsin\xi}{atan\beta_1}\right) \tag{5.22}$$

and,

$$a = \cos(\beta_2 - \xi) \cdot \frac{m}{sin\beta_2} \tag{5.23}$$

From the geometry shown in Figure 5.7:

$$\frac{n}{tan\beta_1} - rltan\xi = \frac{m}{tan\beta_2}$$

and,

$$n = rl - m$$

then *m* can be expressed as

$$m = \left(\frac{1 - tan\beta_1 tan\xi}{tan\beta_1 + tan\beta_2}\right) tan\beta_2 rl \tag{5.24}$$

Substituting this expression for *m* into the equation for internal work, the internal work can be expressed in terms of $\beta_1$, $\beta_2$, $\xi$ and *l* as,

$$2M \times \left[ -\frac{sin\xi cos\beta_2}{cos(\beta_2-\xi)} + \frac{cos\xi cos\beta_2}{cos(\beta_2-\xi)\cdot\left(\frac{1-tan\beta_1 tan\xi}{tan\beta_1+tan\beta_2}\right)} + \frac{1}{2rtan\beta_2\left(\frac{1-tan\beta_1 tan\xi}{tan\beta_1+tan\beta_2}\right)} \right.$$

$$+ \frac{1}{2r-2r\left(\frac{1-tan\beta_1 tan\xi}{tan\beta_1+tan\beta_2}\right)tan\beta_2} - \frac{\frac{1-tan\beta_1 tan\xi}{tan\beta_1+tan\beta_2}}{1-\left(\frac{1-tan\beta_1 tan\xi}{tan\beta_1+tan\beta_2}\right)tan\beta_2}$$

$$\left. + \frac{1}{tan\beta_1} + \frac{cos\beta_2 sin\xi - sin\beta_2 sin\xi\left(\frac{1-tan\beta_1 tan\xi}{tan\beta_1+tan\beta_2}\right)}{tan\beta_1 cos(\beta_2-\xi)\left(\frac{1-tan\beta_1 tan\xi}{tan\beta_1+tan\beta_2}\right)} \right]$$

## External Work:

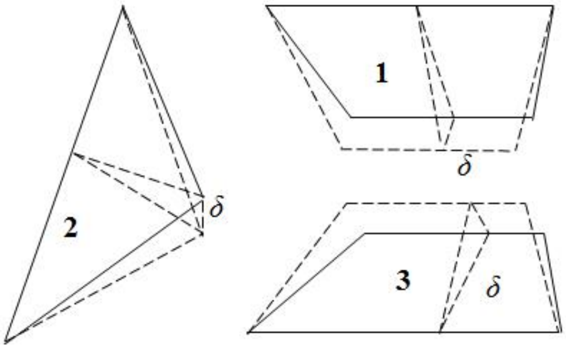

**Fig. 5.8 Deflections of different slab regions**

The vertical displacements at points E and F are both $\delta$, so that the displacement of hinge III (EF) is $\delta$. The external work is the work done by load(s) acting on each region, which gives

$$w(UDL) \times A(Area\ of\ region) \times \upsilon(Centroidal\ displacement\ of\ area)$$

For Element 2 the region is a triangle, so that the centroidal vertical displacement is $\frac{2}{3}\delta$, and for Elements 1 and 3, both regions are trapezia, which can be divided into one rectangle and two right-angled triangles. For the rectangular area, the centroidal vertical displacement is $\frac{1}{2}\delta$, and it is $\frac{1}{3}\delta$ for the two right-angled triangular areas in both trapezoidal regions. With the internal work and $\sum A \times \upsilon$ have already been sort out, then the load capacity $w$ can be expressed as,

$$w = \frac{Internal\ Work}{\sum A \times v}$$

in which

$$\sum A \times v = \frac{r^2 l^2 cos(\beta_2 - \xi)\left(\frac{1 - tan\beta_1 tan\xi}{tan\beta_1 + tan\beta_2}\right)\delta}{3cos\xi} - \frac{2}{3}\left(\frac{1 - tan\beta_1 tan\xi}{tan\beta_1 + tan\beta_2}\right)^2 tan\beta_2 r^2 l^2 \delta$$

$$+ \frac{1}{2}\left(\frac{1 - tan\beta_1 tan\xi}{tan\beta_1 + tan\beta_2}\right) tan\beta_2 r l^2 \delta$$

$$+ \frac{1}{2}\left[1 - \left(\frac{1 - tan\beta_1 tan\xi}{tan\beta_1 + tan\beta_2}\right) tan\beta_2\right] r l^2 (1 + 2r tan\xi)\delta$$

$$- \frac{2}{3tan\beta_1}\left[1 - \left(\frac{1 - tan\beta_1 tan\xi}{tan\beta_1 + tan\beta_2}\right) tan\beta_2\right]^2 r^2 l^2 \delta$$

### 5.3.2 Energy equations for yield-pattern 2

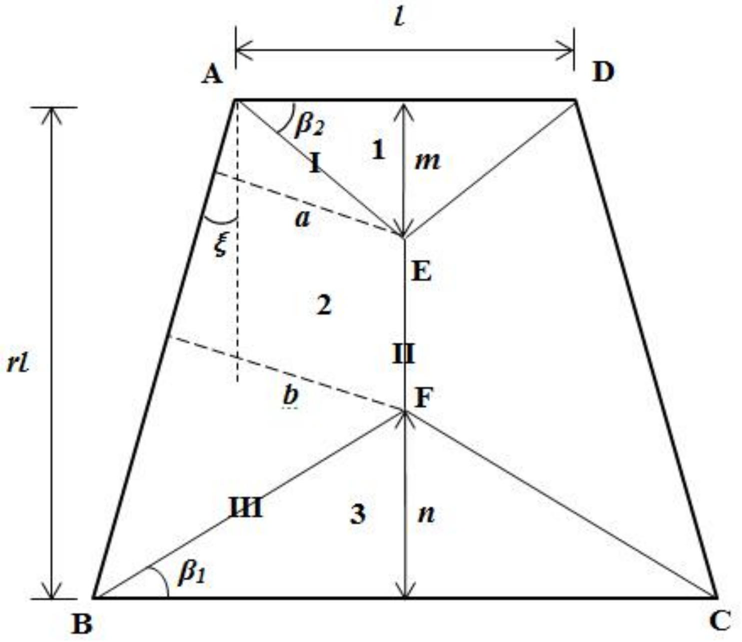

Fig. 5.9 Yield-line pattern 2 of trapezoidal slab

For this yield-line pattern case, because the distances from E and F to the edge about which Element 2 rotates are different, the vertical displacements at points E and F also differ.

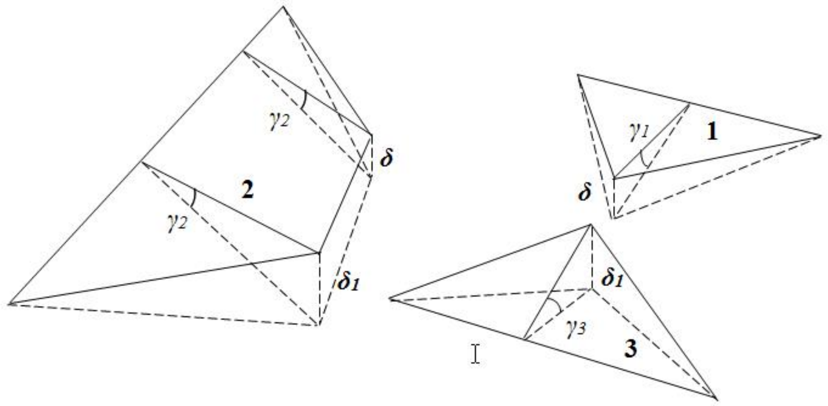

**Fig. 5.10 Deflections of different slab regions**

The relationships between deflection and rotation are as follows:

Element 1: $\delta = m\gamma_1$

Element 2: $\delta = a\gamma_2$

$\delta_1 = b\gamma_2$

Element 3: $\delta_1 = n\gamma_3$

and, $\delta_1 = \frac{b}{a}\delta$

$$m = \frac{1}{2}tan\beta_2 l$$

$$n = \frac{1}{2}tan\beta_1(1 + 2rtan\xi)l$$

$$a = \cos(\beta_2 - \xi)\frac{l}{2cos\beta_2}$$

$$b = \cos(\beta_1 + \xi)\frac{(1 + 2rtan\xi)l}{2cos\beta_1}$$

**Internal Work:**

For hinge I:

About $X$: $D_x = M \cdot \frac{m}{tan\beta_2} \cdot (\gamma_1 - \gamma_2 sin\xi)$

About $Y$: $D_y = M \cdot m \cdot (\gamma_2 cos\xi)$

Therefore, for Hinge I:

$$D = M \cdot \left(\frac{m}{tan\beta_2}\right) \cdot (\gamma_1 - \gamma_2 sin\xi) + \ M \cdot m \cdot (\gamma_2 cos\xi)$$

(5.25)

<u>For hinge II:</u>

Only about *X*:

$$D = M \cdot (l - m - n) \cdot (2\gamma_2 cos\xi)$$

(5.26)

<u>For hinge III:</u>

About *X*: $D_x = M \cdot \frac{n}{tan\beta_1} \cdot (\gamma_3 + \gamma_2 sin\xi)$

About *Y*: $D_y = M \cdot n \cdot \gamma_2 cos\xi$

Therefore, for Hinge I:

$$D = M \cdot \left(\frac{n}{tan\beta_1}\right) \cdot (\gamma_3 + \gamma_2 sin\xi) + M \cdot n \cdot \gamma_2 cos\xi$$

(5.27)

As the yield-line pattern is symmetric, the total internal work dissipated is internal work about hinge I and hinge III multiplied by 2 plus the internal work about hinge III, so that,

Total internal work

$$= 2M\left[tan(\beta_2 - \xi) + \frac{1}{tan\beta_2} + \frac{2rcos\beta_2 cos\xi}{\cos(\beta_2 - \xi)} - \frac{sin\beta_2 cos\xi}{\cos(\beta_2 - \xi)} + \frac{(1 + 2rtan\xi)cos(\beta_1 + \xi)cos\beta_2}{cos(\beta_2 - \xi)sin\beta_1} + \frac{(1 + 2rtan\xi)cos\beta_2 sin\xi}{\cos(\beta_2 - \xi)}\right]$$

**External Work:**

In Figure 5.11, the relevant out-of-plane deflections of Elements 1 and 3 are $\delta$ and $\frac{b}{a}\delta$ respectively, and both of these exist in Element 2. As Elements 1 and 3 are triangular shapes, the external work for these is much easier to calculate than that for Element 2.

Therefore, the external work calculation of Element 2 is shown here, taken in two parts, one trapezoidal and one triangular.

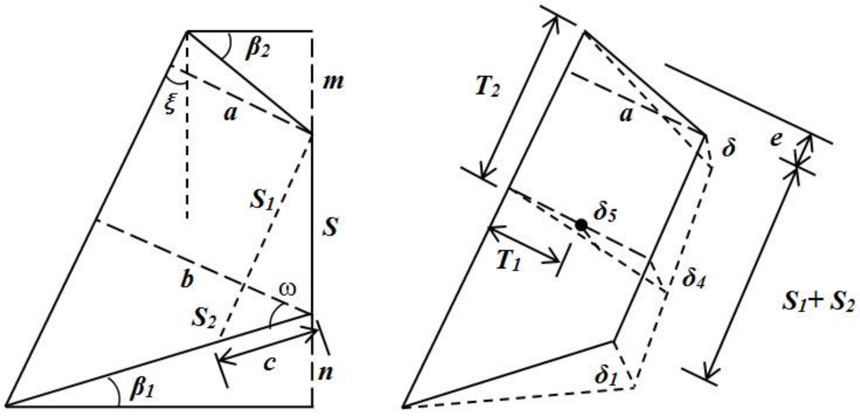

**Fig. 5.11 The external work done in trapezoid part**

From Figure 5.11 above,

$$\omega = \beta_1 + \xi$$

$$c = \frac{b-a}{\cos(\beta_1 + \xi)}$$

$$T_1 = \frac{a}{3}\left[\frac{2(S_1+S_2) + \frac{L_2 - L_1}{2sin\xi}}{S_1 + S_2 + \frac{L_2 - L_1}{2sin\xi}}\right]$$

$$e = \sqrt{\left(\frac{L_1}{2}\right)^2 + m^2 - a^2}$$

$$= \frac{L_1\sqrt{sin^2\beta_2 + cos^2(\xi - \beta_2)}}{sin\,2\beta_2}$$

$$T_2 = \frac{2(S_1+S_2)e + (S_1+S_2)^2 + e\left(\frac{L_2 - L_1}{2sin\xi}\right) + (S_1+S_2)\left(\frac{L_2 - L_1}{2sin\xi}\right) + \frac{(L_2 - L_1)^2}{4sin^2\xi}}{3\left[(S_1+S_2) + \frac{L_2 - L_1}{2sin\xi}\right]}$$

$$\delta_4 = \left(\frac{T_2 - e}{S_1 + S_2}\right)(\delta + \delta_1)$$

$$\delta_5 = \frac{T_1}{a}\delta_4$$

The external work of the trapezoidal part is $(\text{Area of Trapezium}) \times \ \delta_5$. Together with the external work of the triangular part, the total external work is,

$$
\begin{aligned}
= \left[\left(\frac{L_1}{2cos\beta_2}\right)^2 - a^2\right]^{\frac{1}{2}} \frac{aw\delta}{3} + \frac{b(ab - 2a^2 + b^2)w\delta}{3atan\xi} + \left[\left(\frac{L_2}{2cos\beta_1}\right)^2 - b^2\right]^{\frac{1}{2}} \frac{b^2 w\delta}{3a} \\
+ \frac{(L_1 ma\delta + L_2 nb\delta)w}{6a}
\end{aligned}
$$

The external work of the triangular part follows the same method as used previously and is not demonstrated here. Having derived the internal and external work, the load capacity *w* can be expressed as,

$$
\begin{aligned}
w = \Bigg[ & 2Mtan(\beta_2 - \xi) + \frac{2M}{tan\beta_2} + \frac{4Mrcos\beta_2 cos\xi}{cos(\beta_2 - \xi)} - \frac{2Msin\beta_2 cos\xi}{cos(\beta_2 - \xi)} \\
& + \frac{2Mcos\beta_2(1 + 2rtan\xi)\cos(\beta_1 + \xi)}{\cos(\beta_2 - \xi)\, sin\beta_1} + \frac{2Mcos\beta_2 sin\xi(1 + 2rtan\xi)}{\cos(\beta_2 - \xi)} \Bigg] \\
& / \Bigg[ \frac{\cos(\beta_2 - \xi)\sqrt{1 - cos^2(\beta_2 - \xi)}}{12cos^2\beta_2} + \frac{cos^2(\beta_1 + \xi)(1 + 2rtan\xi)^2}{12cos^2\beta_1 tan\xi} \\
& - \frac{cos(\beta_1 + \xi)\cos(\beta_2 - \xi)(1 + 2rtan\xi)}{6cos\beta_1 cos\beta_2 tan\xi} \\
& + \frac{cos^3(\beta_1 + \xi)cos\beta_2(1 + 2rtan\xi)^3}{12\cos(\beta_2 - \xi)cos^3\beta_1 tan\xi} \\
& + \frac{cos^2(\beta_1 + \xi)cos\beta_2(1 + 2rtan\xi)^3\sqrt{1 - cos^2(\beta_1 + \xi)}}{12cos^3\beta_1 \cos(\beta_2 - \xi)} + \frac{sin\beta_2}{12cos\beta_2} \\
& + \frac{sin\beta_1 cos\beta_2 \cos(\beta_1 + \xi)(1 + 2rtan\xi)^2}{12cos^2\beta_1 \cos(\beta_2 - \xi)} \Bigg]
\end{aligned}
$$

This equation is too complicated to optimize mathematically by setting its partial derivatives directly to zero. In consequence, the minimum value of *w* must be found iteratively case-by-case. Here this has been done using an Excel spreadsheet.

### 5.3.3 Numerical optimization of angles $\beta_1$ and $\beta_2$

Before taking the further step of looking into the trapezoidal slab's yield-line pattern, it is essential to verify the feasibility and accuracy of this numerical method. It is easy to confirm that, when the angle $\xi$ is set to 0°, the geometry of the slab becomes rectangular and, together with defining the top length *l* equal to the height *rl*, which means that *r*=1, it becomes a square slab. Because the yield-line pattern of square slabs is well known, it provides the simplest example to verify the numerical optimization of the energy equations.

The energy balance equations for the two yield-line patterns were implemented into two separate spreadsheets. The parameters which need to be set to define a slab are the top length $l$ and ratio factor $r$, together with the angle $\xi$. For the square slab test, the top length is set as 15m, so that the factor $r$ is set as 1.0 and $\xi$ as 0°to create a square slab. In both spreadsheets, the value of $\beta_1$ can be set from 0 °to 90 °, as can $\beta_2$; these vary by row and by column respectively. Every cell provides a value of $w$ for a given combination of $\beta_1$ and. In Table 5.1 the minimum values of $w$ (and the corresponding $\beta_1$) for each row which varies $\beta_2$ are shown in the tables for each of the two yield-line pattern equations.

| Yield-line Pattern 1 | |
|---|---|
| Load Capacity $w$ ($kN/m^2$) | $\beta_1$ (°) |
| 19.56304000 | 40 |
| 19.50869000 | 41 |
| 19.46676000 | 42 |
| 19.43700000 | 43 |
| 19.41922000 | 44 |
| 19.41330000 | 45 |
| 19.41922000 | 46 |
| 19.43700000 | 47 |
| 19.46677000 | 48 |
| 19.50870000 | 49 |
| 19.56305000 | 50 |

| Yield-line Pattern 2 | |
|---|---|
| Load Capacity $w$ ($kN/m^2$) | $\beta_1$ (°) |
| 19.55726000 | 40 |
| 19.50568000 | 41 |
| 19.46548000 | 42 |
| 19.43662000 | 43 |
| 19.41918000 | 44 |
| 19.41332000 | 45 |
| 19.41929000 | 46 |
| 19.43746000 | 47 |
| 19.46831000 | 48 |
| 19.51244000 | 49 |
| 19.57061000 | 50 |

**Table 5.1 Load capacity *w* from 40 °to 50 °of 15m square slab with both yield pattern equation**

In Table 5.1, only load capacities as $\beta_1$ varies from 40 ° to 50 ° are shown; clearly the lowest capacity occurs when $\beta_1$ = 45 ° in both lists. Also, at this capacity, the value for $\beta_2$ is found as 45 °. It is evident that both yield-line pattern equations provide identical correct solutions for a square slab, with $\beta_1$ and $\beta_2$ equal to 45 °.

## 5.4 Investigation of trapezoidal slab yield-line patterns

The work equations for both of the possible yield-line patterns have been carried out in terms of parameters $\beta_1$, $\beta_2$, $\xi$ and $l$. To identify the appropriate yield-line pattern for a trapezoidal slab of specified geometry, the parameters $\beta_1$, $\beta_2$ need to be optimized, with $\xi$ and $l$ pre-set. Firstly, two spreadsheets have been set up as described above, based on the energy equations for the two yield-line patterns. The requirement is then to find the minimum value of all the cells in each of the spreadsheets, and then the appropriate angles $\beta_1$ and $\beta_2$ are given with the corresponding minimum value. With identical geometry a minimum value of $w$ will exist in each. The smaller of those two values determines the appropriate yield-line pattern for the slab with that particular geometry. However, since this numerical method is only about finding the value of $\beta_1$ and $\beta_2$, validation of the length of the middle yield-line has not been included. In order to make sure that the values of $\beta_1$ and $\beta_2$ are able to make the middle yield-line exist, the following equations also have to be satisfied.

For the yield-line Pattern 1:

$$\frac{m}{tan\beta_2} \leq \frac{l}{2}$$

so that

$$\left(\frac{1 - tan\beta_1 tan\xi}{tan\beta_1 + tan\beta_2}\right) r \leq \frac{1}{2}$$

For yield-line Pattern 2:

$$rl - m - n \geq 0$$

so that

$$(tan\beta_1 + tan\beta_2 + 2tan\beta_1 tan\xi r)/r \leq 2$$

When the values of $\beta_1$ and $\beta_2$ have been identified, they have to be substituted into both of these inequalities, together with the other defining parameters, to check whether only one yield-line pattern is satisfied, or both. If both are satisfied, then the one with lower load capacity represents the appropriate yield-line pattern.

In order to find out the relationship between middle yield-line direction and trapezium geometry, a randomly selected width of 15m was set for the test slabs. Three investigations have been made:

1. Increasing the top length with fixed angle $\xi$ and width *rl*;
2. Increasing the angle $\xi$ with fixed top length and width *rl*;
3. Increasing the width *rl* with top and bottom lengths fixed.

The purpose of the first investigation is to compare the effect of top and bottom base lengths in determining the direction of the middle yield-line; the bottom base length is a function of the top length, angle $\xi$ and width *rl* as

$$L = l + 2rl\tan\xi$$

Once $rl$ and $\xi$ are fixed, the bottom base length increases with the top length. This case also investigates the effect of the ratio of (top + bottom base lengths) against width.

In the second case, the influence of bottom base length alone is considered. With width $rl$ and top length $l$ fixed, changing the angle $\xi$ changes the bottom base length accordingly.

Change of width is also tested in the third case. However, as at least two parameters are related, as the width $rl$ changes, the angle $\xi$ also has to change.

### 5.4.1 Comparison of yield-line patterns with top length increasing and $\xi$ fixed

In this case, the width of the trapezium $rl$ is set as 15m and the angle $\xi$ is fixed as 20°. The top length is controlled to increase progressively from 5m to 20m, so that the bottom base length increases from 15.2m to 30.2m. Because the angle ξ and width rl are fixed, the scale between top and bottom base length are kept.

| Ratio | Top Length (*m*) | Load Capacity ($kN/m^2$) | |
|---|---|---|---|
| *r* | *l* | Pattern 1 | Pattern 2 |
| 3 | 5 | 31.67666 | 35.8043 |
| 2.5 | 6 | 28.2279 | 32.19172 |
| 2.142857 | 7 | 25.52962 | 29.30772 |
| 1.875 | 8 | 23.31726 | 26.95486 |
| 1.666667 | 9 | 21.52369 | 25.00191 |
| 1.5 | 10 | 20.06035 | 23.35629 |
| 1.363636 | 11 | 18.83425 | 21.95318 |
| 1.25 | 12 | 17.80248 | 20.74415 |
| 1.153846 | 13 | 16.91605 | 19.69366 |
| 1.071429 | 14 | 16.15267 | 18.77297 |
| 1 | 15 | 15.48528 | 17.9611 |
| 0.9375 | 16 | 14.89968 | 17.24385 |
| 0.882353 | 17 | 14.38315 | 16.61835 |
| 0.833333 | 18 | 13.92249 | 16.06619 |
| 0.789474 | 19 | 13.50962 | 15.57339 |
| 0.75 | 20 | 13.13936 | 15.16659 |

**Table 5.2 Load capacity from two different yield-line patterns**

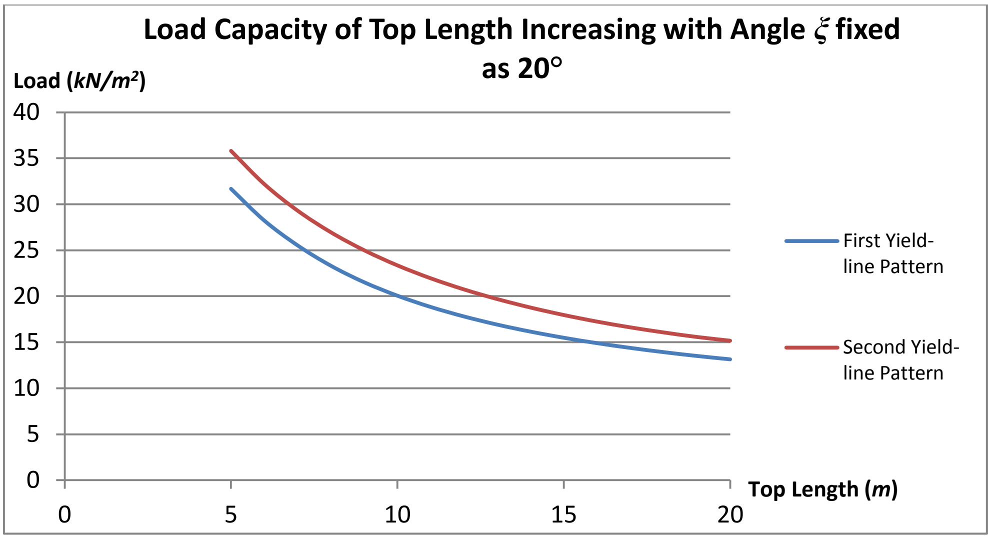

**Fig. 5.12 Load capacity comparison for two yield-line patterns**

Figure 5.12 shows the curves from the two different yield-line patterns in the respective spreadsheets. It can be seen that the curve obtained from yield-line Pattern 1 which represents the 'horizontal' middle yield-line produces a lower value of load capacity than Pattern 2, which defines the middle yield-line in the orthogonal direction. In other words, when the width of trapezoidal slab is fixed as 15m and the angle $\xi$ is fixed as 20°, there is no observed change of yield-line pattern; yield-line Pattern 1 is always preferred.

### 5.4.2 Comparison of two yield-line patterns with top length fixed and angle $\xi$ increasing

An investigation of trapezoidal cases with 15m width, top length varied from 5m to 20m and angle $\xi$ increased from 0° to 45°, the results are more complicated and sensitive. When $\xi = 0°$, which means that the geometry is rectangular, the middle yield-line should stay parallel to the longer span. Hence, when the top length is shorter than the width, yield-line Pattern 2 is optimal. When the top length approaches 15m and the geometry is square, the load capacity for both yield-line patterns should be identical. When the top length exceeds the width, yield-line Pattern 1 is optimal.

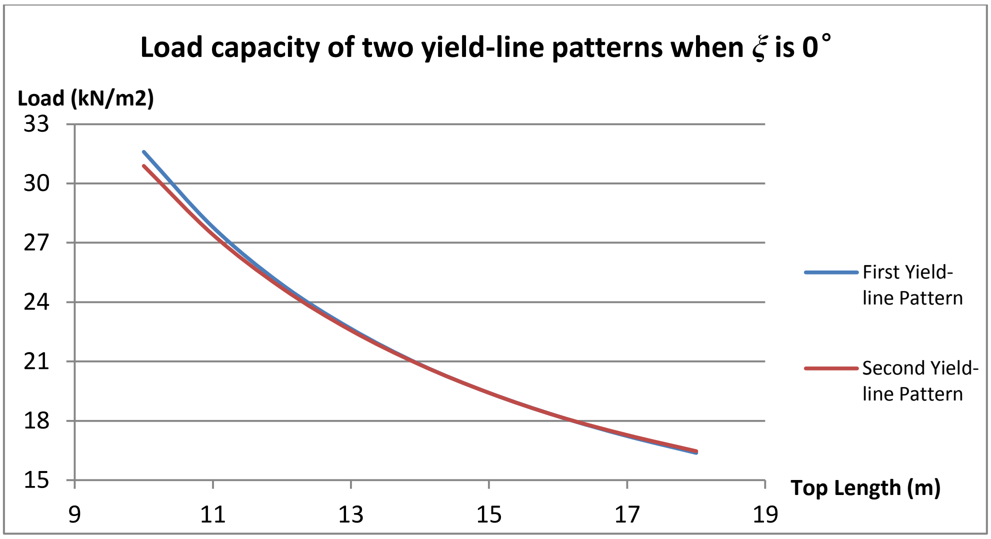

**Fig. 5.13 Load capacity of two yield-line patterns as top length increasing and ξ is 0 °**

In Figure 5.13, the prediction of the change of yield-line pattern of a rectangular slab is confirmed, although when the top length exceeds 15m the two curves are very close. However, when ξ changes from 0 ° to 1 °, the situation changes. In all the tests, for cases with top length greater than 11m, the yield-line pattern changes from 2 to 1 when ξ increases to 1 °. This is because the difference in load capacity from these two patterns is very small, especially when the top length is about the same as the width. In contrast, for cases with top length between 5m and 11m the change of yield-line pattern only occurs with ξ ≤ 10 °; the cases with ξ > 10 ° show yield-line Pattern 1 instead. Together with the results from the previous tests with ξ = 20 °, for a 15m wide trapezoidal slab with top length greater than or equal to 5m and angle ξ > 10 ° yield-line Pattern 1, with a middle yield-line in the 'horizontal' direction, will occur. For this reason, ξ is changed within the range 0-10 ° so that it is possible to observe the change of yield-line pattern.

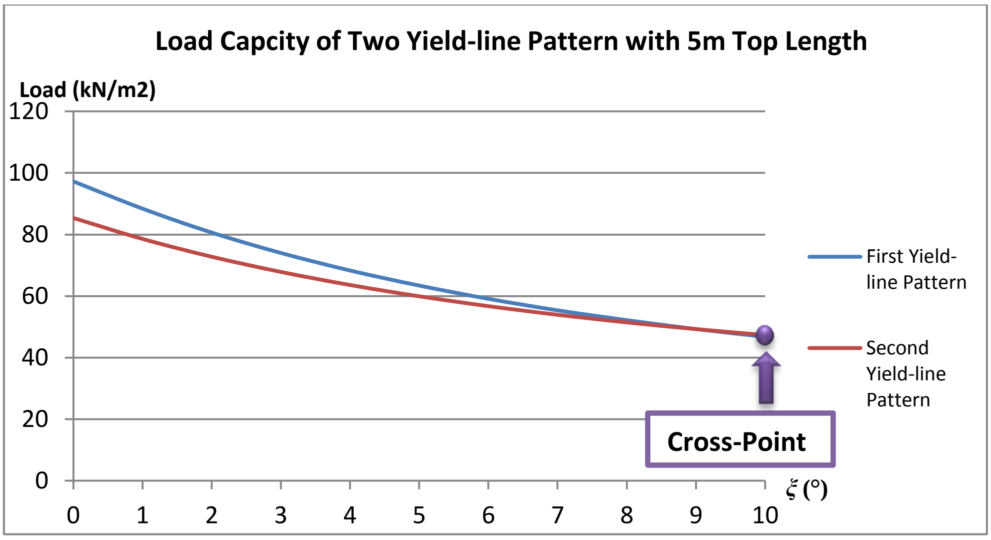

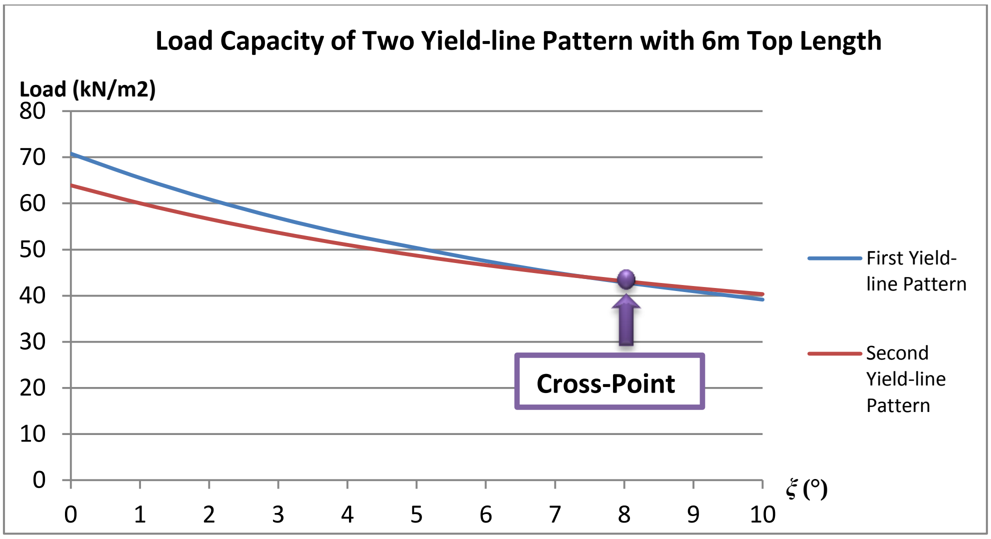
Load Capacity of Two Yield-line Pattern with 6m Top Length
Load (kN/m2)
80
70
60
50
40
30
20
10
0
0
1
2
3
4
5
6
7
8
9
10
ξ (°)
Cross-Point
First Yield-line Pattern
Second Yield-line Pattern

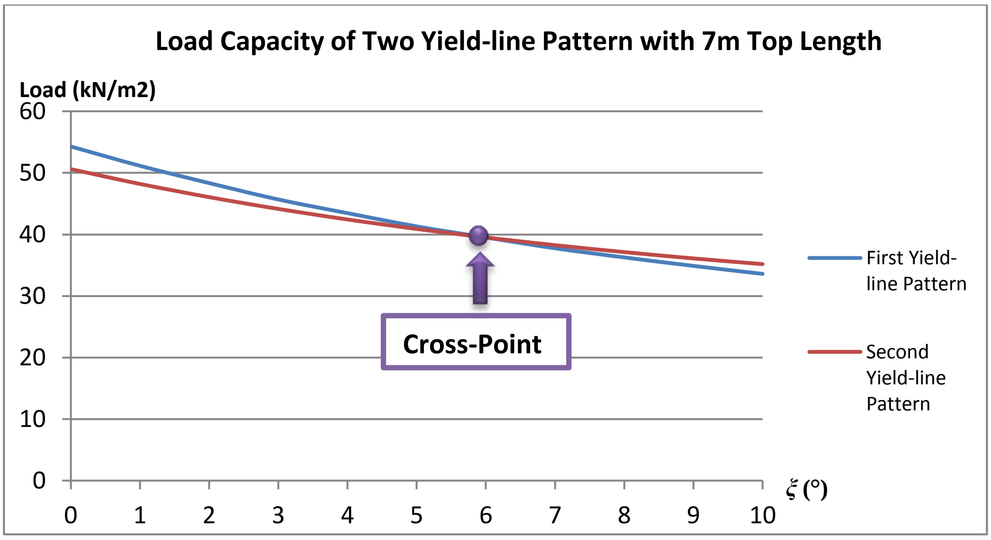
Load Capacity of Two Yield-line Pattern with 7m Top Length
Load (kN/m2)
60
50
40
30
20
10
0
0
1
2
3
4
5
6
7
8
9
10
ξ (°)
Cross-Point
First Yield-line Pattern
Second Yield-line Pattern

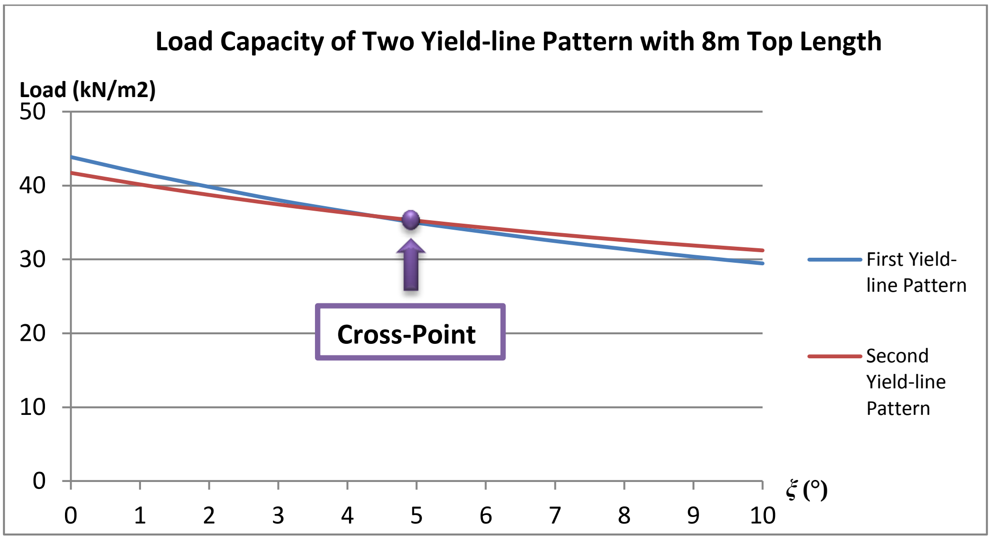
Load Capacity of Two Yield-line Pattern with 8m Top Length
Load (kN/m2)
50
40
30
20
10
0
0
1
2
3
4
5
6
7
8
9
10
ξ (°)
Cross-Point
First Yield-line Pattern
Second Yield-line Pattern

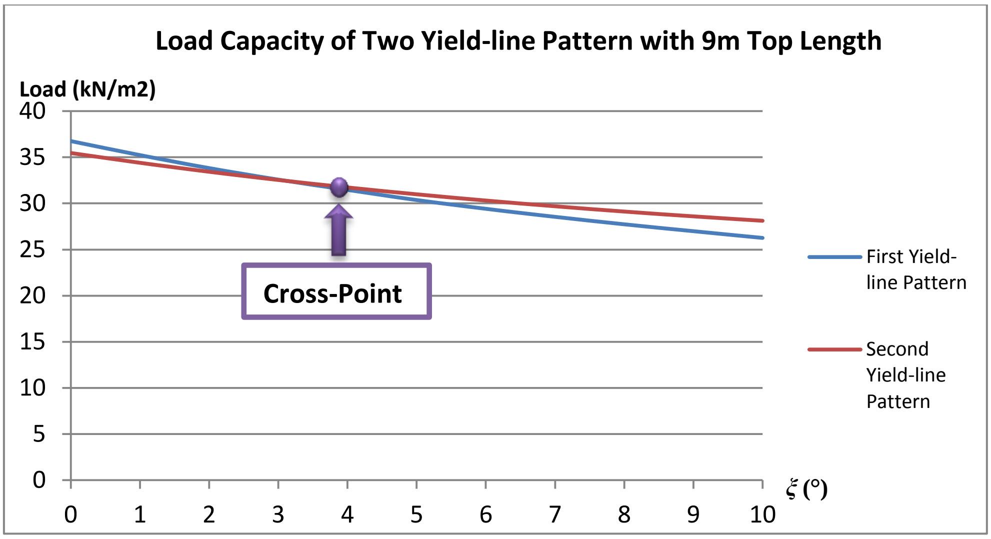

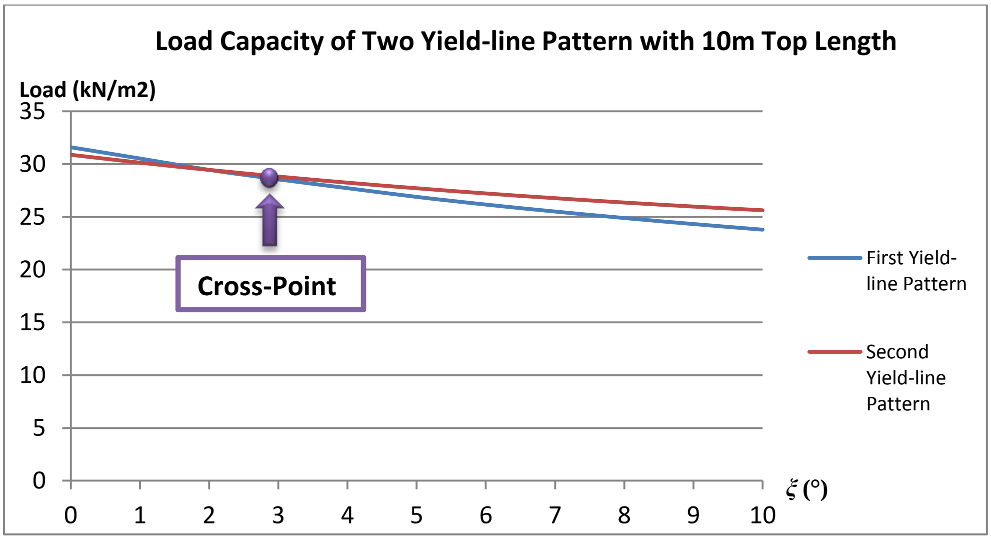

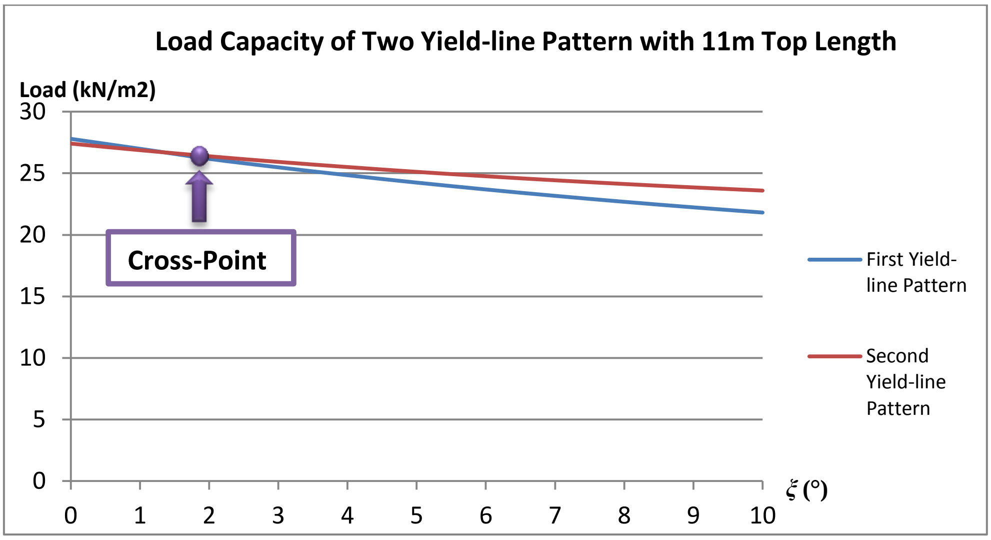

**Fig. 5.14 Load capacity comparisons with angle $\xi$ increasing**

In the series of graphs in Figure 5.14, it is easy to see that the locations of the change points in all of are related to the value of angle $\xi$. With longer top lengths, the change points occur at lower values of $\xi$. This means that at lower ratios of top:bottom lengths and for lower top lengths, there is more chance of generating yield-line Pattern 2. However, when the bottom length exceeds a specific value related to the width and angle $\xi$, the yield-line pattern will change from 2 to 1.

Since the minimum load capacity can be found, the corresponding yield-line pattern can easily be found for any case in terms of the angles $\beta_1$ and $\beta_2$. The change of yield-line pattern is clearest when top length is 8m, so this case has been chosen as an example of yield-line patterns to be shown in Figure 5.15.

For this slab, when the $\xi = 0°$, the yield-line pattern is clearly yield-line Pattern 2. As $\xi$ increases, there is no change of yield-line pattern type until $\xi = 5°$. It can be seen that the significant change of yield-line pattern occurs rather suddenly. The middle yield-line suddenly disappears instead of reducing continuously, and a common intersection point takes over in the central area. The yield-line pattern stays in this form as $\xi$ keeps increasing. When $\xi$ has increased beyond about 25°, the middle yield-line appears in the horizontal direction, forming yield-line Pattern 1.

During this process it is possible to find approximate shape definition parameter values at which the yield-line pattern changes. Firstly, the point at which the middle yield line transforms to a common intersection point is when $\xi = 5°$, or $(l + L) = 18.625m$, so that the ratio

$$\frac{(L + l)}{h} = 1.242$$

Yield-line Pattern 1 starts to occur when $\xi \approx 25°$, and $(l + L) \approx 30m$, so that the ratio

$$\frac{(L + l)}{h} \approx 2$$

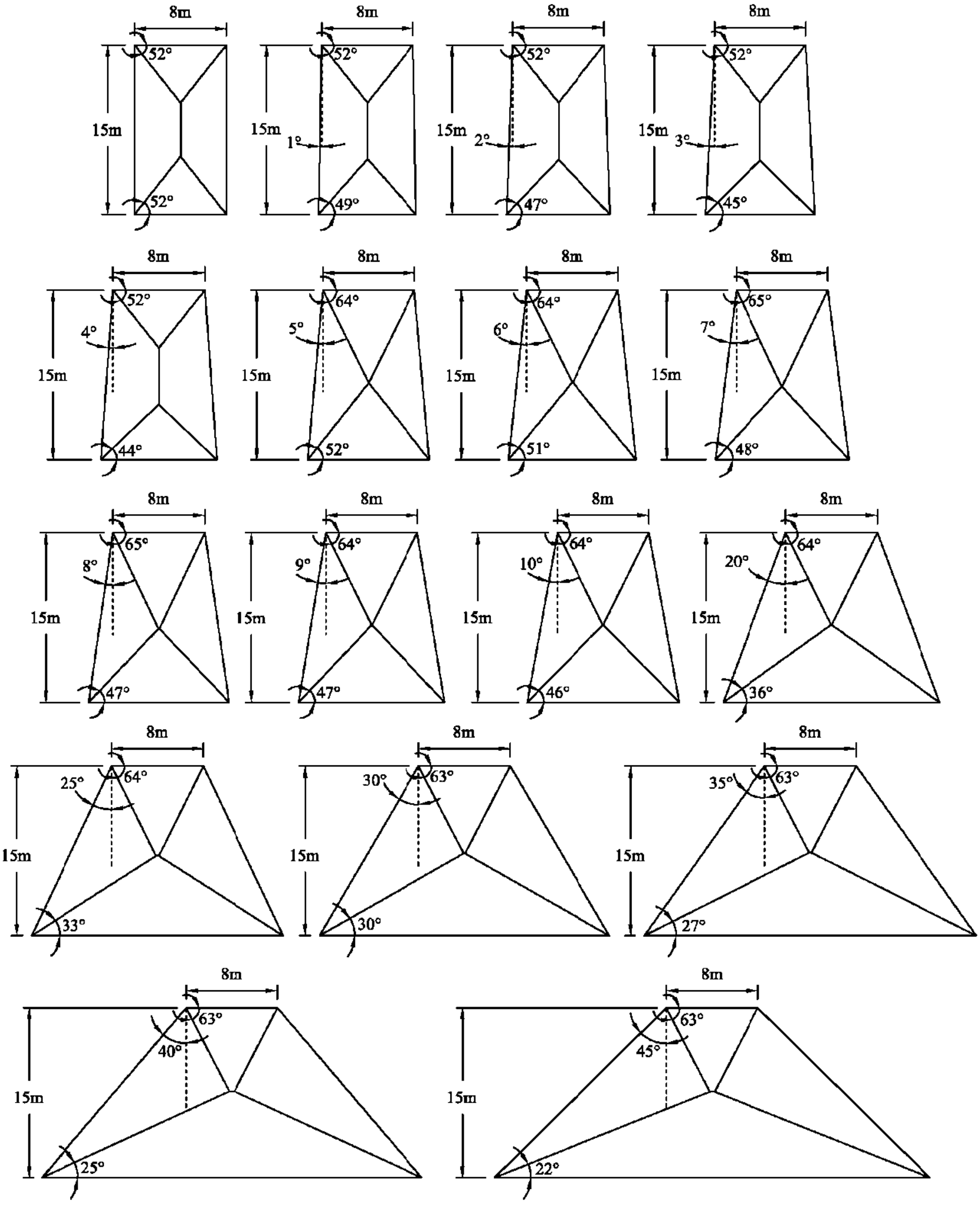

**Fig. 5.15 Yield-line patterns of 8m top length trapezoidal slab with different angle $\xi$**

It must be remembered that these ratios are specific to the other controlling shape parameter, which is the ratio $\frac{1}{r} = \frac{8}{15} = 0.533$.

### 5.4.3 Comparison of two yield-line patterns with top and bottom side lengths fixed and width *rl* increasing

In these analyses the top and bottom side lengths are set as 6m and 12m throughout, but the width is increased from 5m to 20m, so that $\xi$ reduces from 30.96° to 8.53°. The load capacities from both yield-line patterns are listed in Table 5.3 and shown graphically in the curves of Figure 5.16. As the slab height increases, the load capacities from both yield-line patterns reduce. However, the rate of reduction of yield-line Pattern 2 is greater than that of 1, so that when the height reaches 19m yield-line Pattern 2 has replaced 1 to represent the yield-line pattern occurring in the slab.

| $h$ ($m$) | $\xi$ (°) | $w$ ($kN/m^2$) | |
|---|---|---|---|
| | | Yield-line Pattern 1 | Yield-line Pattern 2 |
| 5 | 30.96375653 | 120.861 | 148.4086 |
| 6 | 26.56505118 | 93.23582 | 112.755 |
| 7 | 23.19859051 | 76.19482 | 90.60999 |
| 8 | 20.55604522 | 64.86131 | 75.8865 |
| 9 | 18.43494882 | 56.94164 | 65.545 |
| 10 | 16.69924423 | 51.19117 | 57.96566 |
| 11 | 15.2551187 | 46.89761 | 52.21169 |
| 12 | 14.03624347 | 43.60273 | 47.71982 |
| 13 | 12.99461679 | 40.93649 | 44.13329 |
| 14 | 12.09475708 | 38.82514 | 41.21451 |
| 15 | 11.30993247 | 37.08667 | 38.80223 |
| 16 | 10.61965528 | 35.63265 | 36.77338 |
| 17 | 10.0079798 | 34.4638 | 35.05077 |
| 18 | 9.462322208 | 33.37594 | 33.56963 |
| 19 | 8.972626615 | 32.49918 | 32.28688 |
| 20 | 8.53076561 | 31.72206 | 31.16123 |

**Table 5.3 Load capacity from both yield-line patterns with width increase**

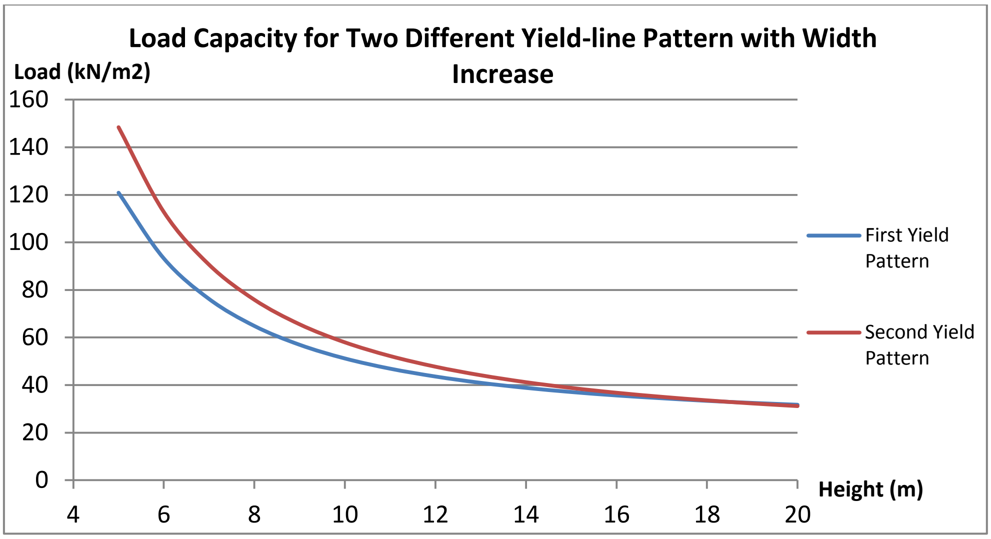

**Fig. 5.16 Load capacity comparison with height increasing**

From the data on minimum load capacity of both yield-line patterns, it is easy to find the corresponding angles $\beta_1$ and $\beta_2$. Hence, the actual yield-line pattern for the trapezoidal geometry can be sketched.

Obviously, when the width is shorter than both top and bottom base lengths, the yield-line pattern is definitely 1, with the middle yield-line parallel to the top and bottom edge lengths. With the height increasing, the length of the middle yield-line reduces until it is barely observed when the width is 9m, which is equal to $\frac{1}{2}(l+L)$. However, as the width continually rises, instead of changing to yield-line Pattern 2, the yield-line Pattern 1 maintains but with a very small distance between two intersections. When the width increases above 18m, which is equal to $(l+L)$, the yield-line pattern changes to yield-line Pattern 2. In the process of yield-line pattern transformation, the reduction of the length of the Pattern 1 middle yield-line can be considered as a continuous change, but no continuous increase of the Pattern 2 middle yield-line can be observed. On the other hand, when the slab is in yield-line Pattern 1, the middle yield-line is located almost at the centre of the width.

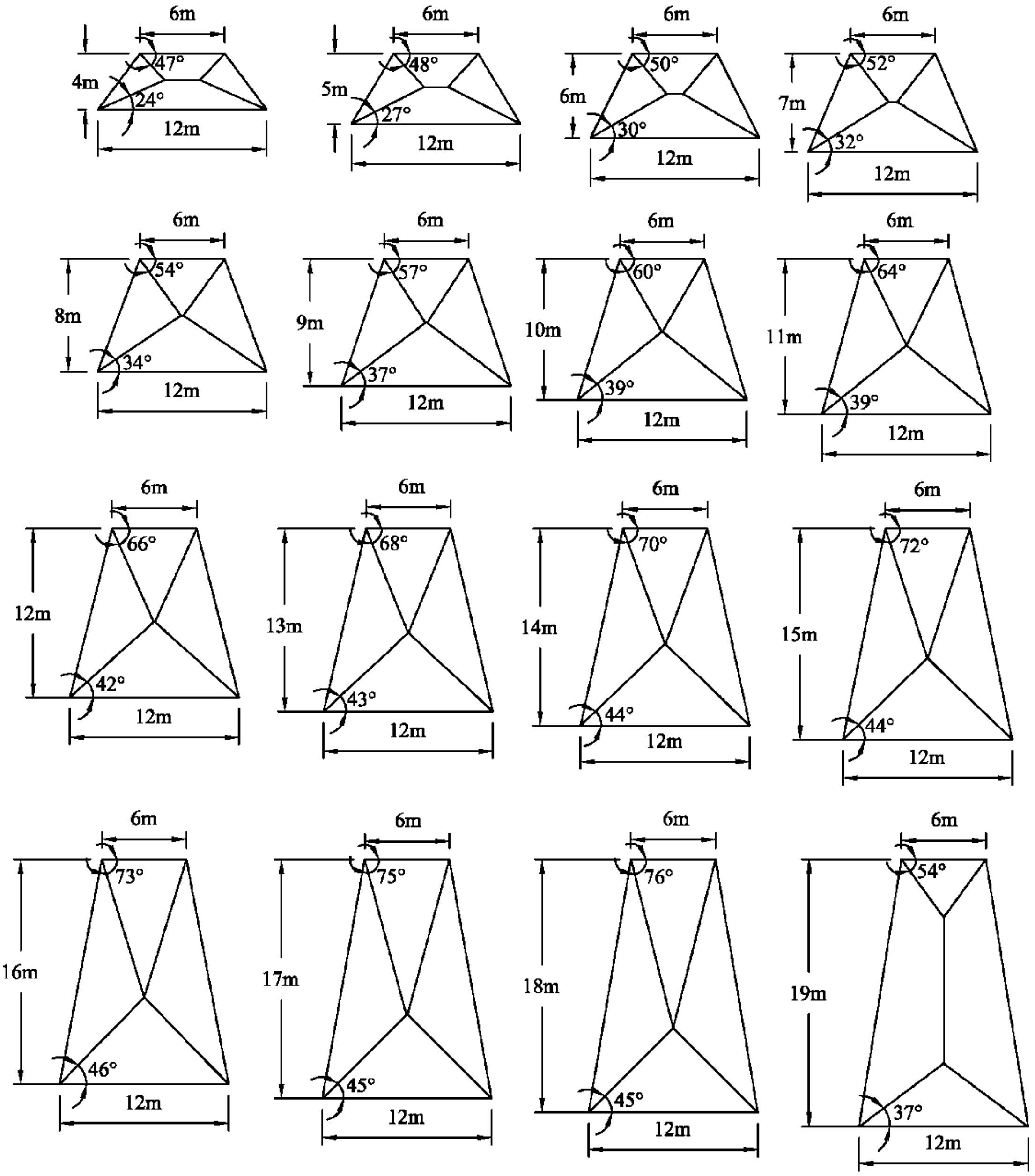

**Fig. 5.17 Transformation of the yield-line patterns as height increases.**

### 5.4.4 Investigation of change of yield-line patterns

Since the sudden change of yield-line pattern from 1 to 2 has been observed, another assumption of yield-line pattern with common intersection has been made. In this yield-line pattern, named as “Yield-line Pattern 1.5”, all four yield lines are assumed to meet at one point which located at the middle of slab.

By applying the energy equation method into Excel spreadsheet, the collapse loads which to cause this collapse mechanism can be found. In order to making comparison to the other two yield-line patterns, the continuous changes of trapezoidal slab geometry have been selected as in Fig. 5.15 and 5.17.

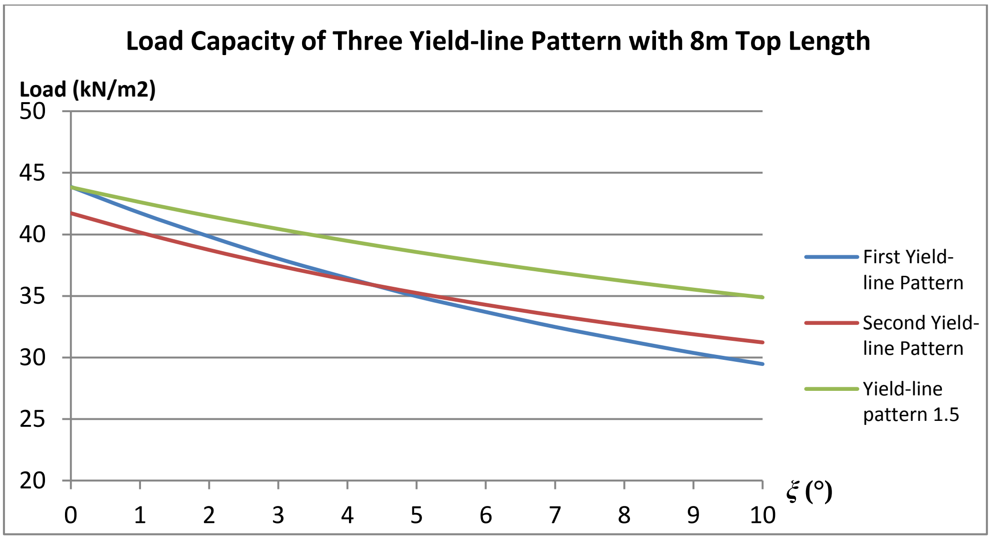

**Fig. 5.18 Comparison of load capacity for three yield-line patterns with 8m top length**

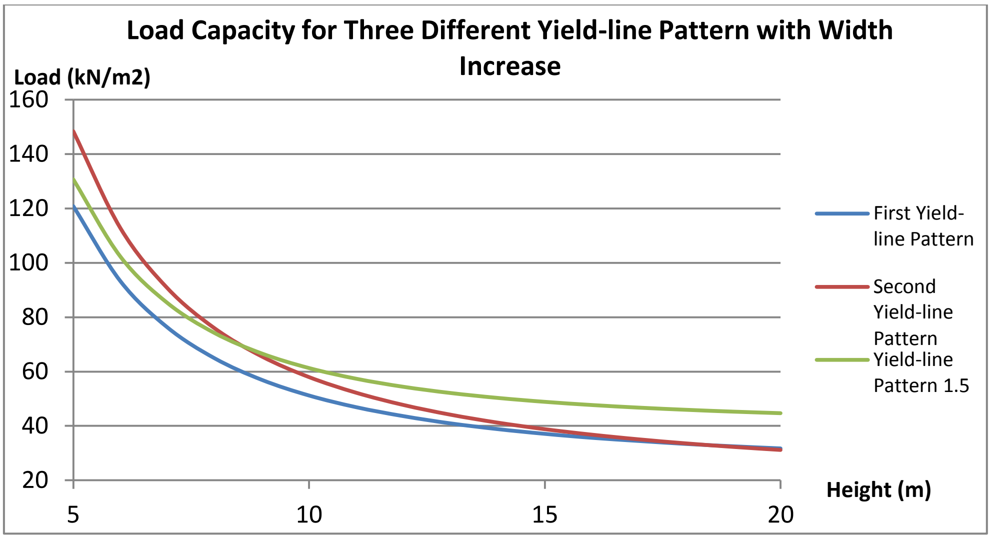

**Fig. 5.19 Comparison of load capacity for three yield-line patterns with width increase**

From both Fig. 5.18 and 5.19 above, it can be observed that, the third yield-line pattern (Yield-line Pattern 1.5) which represents all yield lines meet at one intersection is not happen during the change of angle $\xi$ and the width *rl*. Therefore, it can be conclude that from the change between Yield-line Pattern 1 and 2 is sudden, those mechanisms which are looks like with common intersection are actual still Yield-line Pattern 1 but only because the middle yield-line is very short.

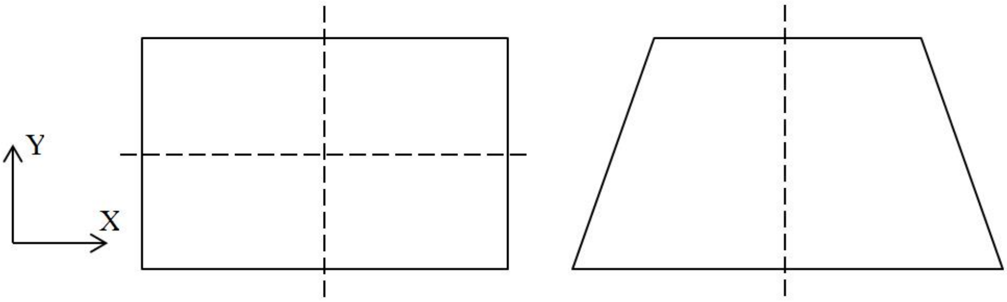

**Fig. 5.20 Comparison between rectangular and trapezoidal slab**

For a rectangular slab lay in *X*-*Y* plane, the geometry is symmetric in both *X*- and *Y*-axis as Fig. 5.20. It is well known that, if the length of longer span decreases, the middle yield line initially lay in *X* direction will decrease as well until all yield lines meet at one intersection, also the geometry of rectangle changes to square at the same time. If the decreasement continued, the middle yield line will start to grow in *Y* direction continuously. However, for a trapezoidal slab in Fig. 5.20, the symmetry of geometry is only on *X* axis, the upper and lower part of trapezoid are not symmetric. This is may be the reason why it is observed that the change of middle yield line in *X* direction is continuously, but the appearance of it in *Y* direction is sudden.

## 5.5 Summary and discussion

Throughout the development of tensile membrane action, the small-deflection yield-line pattern has been assumed to be the basis of the distribution of membrane force. In a rectangular slab, the optimal yield-line pattern has been located analytically in relation to the rectangular geometry. When extending this method to non-orthogonal slabs such as triangular and trapezoidal shapes, the first thing is also to determine the yield-line patterns. For a triangular slab, the form of yield-line pattern has been developed from previous research. However, in the original simplified method for rectangular slab membrane action, the assumption for the location of compressive stress-blocks centroid has not been proved for triangles, the simplified design method can not be extended to the triangular slab. Therefore, there is an equilibrium equation missing for three unknowns, and this also caused the problem to find the solution of membrane force enhancement for triangular slabs.

The problem in trapezoidal slabs is more complicated. One of the most important factors is the yield-line pattern of trapezoidal slab and the locations of intersections.

Two forms of yield-line pattern have been assumed from the start of this research. By applying the work balance equations, both of these yield-line patterns have been tested with trapezoidal slabs of various geometries.

Three parameters, the top length $l$, the angle of the non-parallel sides $\xi$ and width $h$ which control the geometry of a symmetric trapezium have been varied separately. As a result, when the angle $\xi$ is high (above 20°), no matter how the top length changes, yield-line Pattern 1, with middle yield-line parallel to the parallel sides, occurs. This may also be related to the width, but needs other tests changing the width and angle $\xi$ at the same time for future research. The change of bottom length and width has also been tested. From the results, the transformation of optimal yield-line patterns can be observed. As mentioned before, with a constant width the transformation of the yield-line pattern only happens when the angle $\xi$ is less than 10°. When $\xi$ increases with top length fixed, which means only the bottom length is increasing, the change from yield-line Pattern 2 to 1 is quite sudden, but in these tests the length of middle yield line as in yield-line Pattern 1 is very short until the bottom edge becomes significantly longer than the top length. The change of the yield-line in the direction of the parallel sides is more continuous. This is also revealed by the third test, in which the change of the horizontal yield-line is continuous until the length of middle yield-line becomes very short; the middle yield-line in the perpendicular direction appears fairly suddenly when the height is much greater than top and bottom base lengths. In both tests it is found that when the width is half the sum of the top and bottom base lengths the transformation between yield-line Pattern 1 and the 2 occurs but suddenly. This is dissimilar to yield-line pattern behaviour in rectangular slabs, because of the asymmetric geometry of the trapezoidal slab. This makes the transformation to yield-line Pattern 2 more difficult to summarize and needs to be verified against a wider range of cases with different geometries.

In summary, the extension of the simplified method to membrane force calculation for triangular slabs is limited due to the unproven assumption within the previous method for rectangular slabs. For trapezoidal slabs, the optimal yield-line pattern is the initial problem needing to be investigated and verified before extending the simplified membrane force calculation. Two assumed yield-line patterns have been announced and investigated, and further researches are required to examine the existence. An indication of the performance associated with these patterns has been found in these tests.

# Chapter 6 New plastic energy method for load capacity enhancement

## 6.1 Introduction of new internal work method

From previous chapters, reasons have been demonstrated why the established simplified method of calculation of capacity enhancement due to tensile membrane action cannot be extended to non-orthogonal slabs. As has been indicated in previous research papers (Bailey, 2007), the simplified method cannot properly predict the maximum allowable vertical displacement, at which actual fracture of the reinforcement or crushing of the concrete occurs. Therefore, in the BRE-Bailey method (Bailey, 2001), only a very simplified prediction of the maximum allowable vertical displacement at ambient temperature has been provided as,

$$\Delta_{20}=\sqrt{\left(\frac{0.5f_y}{E}\right)\frac{3L^2}{8}} \tag{6.1}$$

in which *E* is the Young's modulus of the reinforcement across the longer span. However, the capacity enhancement due to tensile membrane action is more complicated than is suggested by the simple view that load capacity disappears when fracture of reinforcement, or crushing of the concrete, first happens. In the process of slab collapse, the first cracking is initiated at the lower surface of the concrete slab, and occurs when the limiting tensile strain of concrete is first reached.

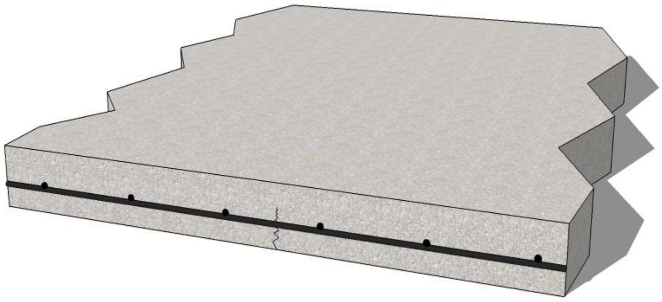

**Fig. 6.1 Crack occurring at the lower surface of concrete slab**

As deflection grows, a yield-line pattern starts to form, so that the slab elements (flat facets) rotate about each yield line. To balance the tensile force per unit width in the reinforcement mesh, a small depth of concrete at the top of the slab forms a compression block. Cracks start to open from the bottom of the slab, and the reinforcing bars are stretched by a small amount at the same time.

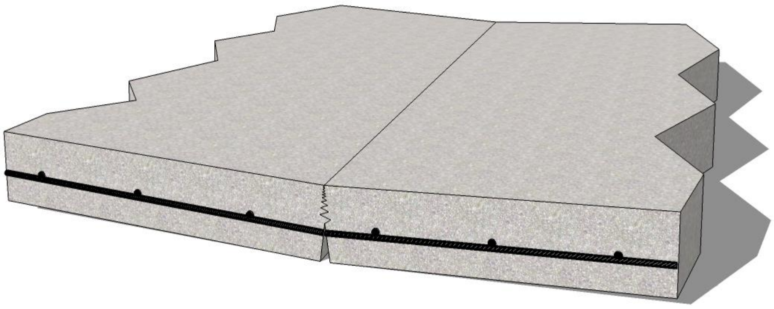

**Fig. 6.2 Crack partially open in the lower part of the concrete slab**

In the next stage, the slab elements (flat facets) continue to rotate and the crack opens fully through the whole slab thickness until the first reinforcement fracture happens. With both the in-plane and out-of-plane rotations $\xi$ and $\eta$ (Figure 6.3) caused by the loading, the vertical deflection continues to increase and reinforcing bars continue to fracture along the yield-line, until the maximum deflection is reached.

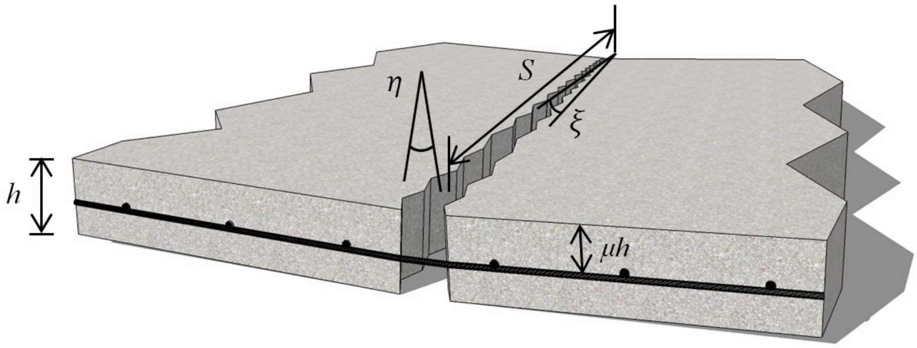

**Fig. 6.3 Crack fully open with reinforcement bars in tension**

Since the opening of cracks is a slowly progressing process, this means that the angles of in-plane rotation also increase the magnitude of the crack opening. With crack opening growing, reinforcement bars begin to fracture one by one, which means that the distance between the last fractured rebar and the slab edge reduces.

The extension of the rebar at any location between two slab elements is given by,

$$\Delta = \xi S + \eta \mu h \tag{6.2}$$

where,

$\mu$ is the average depth of reinforcement;

$h$ is the thickness of the slab;

$\eta$ is the out-of-plane element relative rotation about a yield line;

$S$ is the distance between unfractured rebar and the slab edge along the crack;

$\xi$ is the in-plane element relative rotation between two slab elements.

As the permissible extension of a bar depends on the fracture ductility strain of the steel reinforcement, the maximum extension of a rebar is given as,

$$\Delta_{lim} = \varepsilon_u \cdot d \tag{6.3}$$

where,

$\varepsilon_u$ is the fracture ductility strain of a bar.

$d$ is the spacing between two adjacent rebars in either the long or short span.

In this method, which aims to find out the capacity enhancement compared with the original capacity determined by the yield-line calculation (as well as the enhancement predicted by the existing simplified method) plastic energy/work equilibrium equations have been employed. Although the expression for the external work done by loads applied to the slab is the same as previously, the balancing internal work in the equation includes the in-plane work done in rebar extension as cracks open due to both angles of rotation. Therefore, the process by which cracks open at the rebar level needs to be considered as it controls reinforcement plastic extension and fracture.

Once the angle of a yield-line crack is determined, the extension of the rebar across it can be found geometrically, which then aggregates as the internal work done. For different failure mechanisms, the angles of deformation of cracks can be different because of different crack locations. In order to demonstrate the energy work method and validate the results by comparing with original yield-line capacity and the BRE-Bailey method, four failure mechanisms of a rectangular slab have been assumed.

## 6.2 New internal work method calculate enhancement factor for rectangular slabs

In this new internal work method initially announced by Burgess (2013), four assumed collapse mechanisms have been illustrated in the reference, as shown in Fig. 6.4.

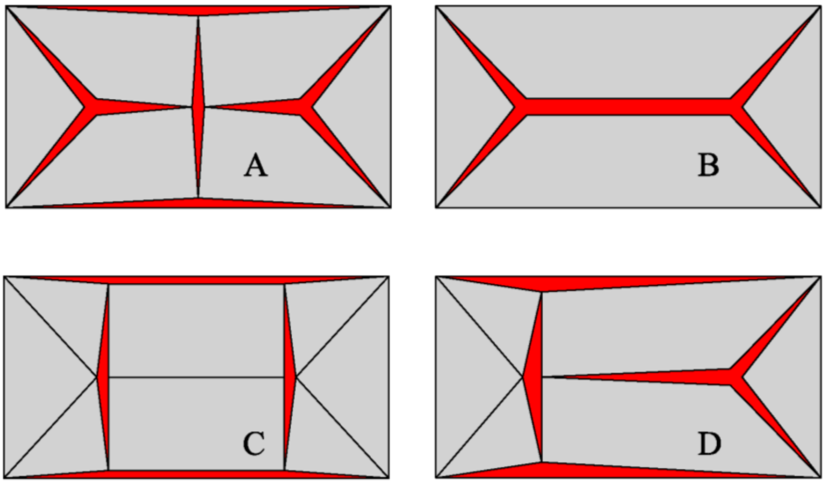

**Fig. 6.4 Four assumed collapse mechanism with crack opening**

All these four collapse mechanisms are based on the basic yield-line pattern of a rectangular slab. The locations of additional through-depth cracks are presumed to be potentially critical situations which may happen together with the initial yield-line pattern. For different locations of cracks, the equations to calculate the internal work due to the extension of reinforcement rebar differ. In general, the steps in applying this internal work calculation which assesses the energy dissipation in extension of reinforcement bars are:

1) Assume that the location of a crack opening is based on the optimum small-deflection yield-line pattern, and originates in a critical area of tensile stress, which also dictates the direction in which the crack develops;
2) According to the direction in which each crack opens, and the kinematics of the slab facets given their boundary conditions, obtain algebraic expressions for the width of opening of the cracks which represent the plastic extension of rebar;
3) With deflection increasing, the reinforcement mesh starts to 'unzip' (progressively fracture) along the crack opening until it is completely fractured along the crack. The lengths of each crack within which the reinforcement is fractured and intact can be found;

4) Calculate the internal energy dissipated at any deflection, using equations which include the specific properties of the steel reinforcing mesh, combined with the current situation in terms of intact reinforcement length.

The full derivation of the energy equations has been provided by Burgess *et al.* (2013) and is included in the Appendix of this thesis.

## 6.3 Comparison and validation of new internal work method

In the previous section, the method for calculating internal work due to the cracking opening has been illustrated, although not derived in detail. For any given deflection, the load carrying capacity can be predicted by applying the method.

To allow logical comparison, the same geometry and properties have been employed for 4 assumed rectangular slab failure mechanisms; the slab is a 9m x 6m composite slab with aspect ratio of *r*=1.5 and thickness of 120mm. It is assumed to be without continuity on any of its four edges. For the reinforcement, a conventional reinforcement mesh A142 is chosen to be positioned at the middle- thickness; the rebar sizes and spacing are shown in Table 6.1 below:

| Spacing long span | Spacing short span | Long span wire diameter | Area long span wires | Short span wires diameter | Area short span wires |
|---|---|---|---|---|---|
| (mm) | (mm) | (mm) | ($mm^2$/m) | (mm) | ($mm^2$/m) |
| 200 | 200 | 6 | 141.4 | 6 | 141.4 |

**Table. 6.1 Detailed size of reinforcement mesh A142**

For the reinforcement mesh, the yield strength of steel $f_{yk}$ has been set as 500*MPa* (*S500*) with 10% fracture ductility, and for the concrete the compressive strength has been set as 30*MPa* (C30).

The internal and external work equations have been implemented in an Excel spreadsheet, and the enhancement of capacity calculated over a range of deflection ratio $\delta/_{l}$ from 0 to 0.1, in increments of 0.0001. The capacity enhancement is plotted in Fig. 6.5.

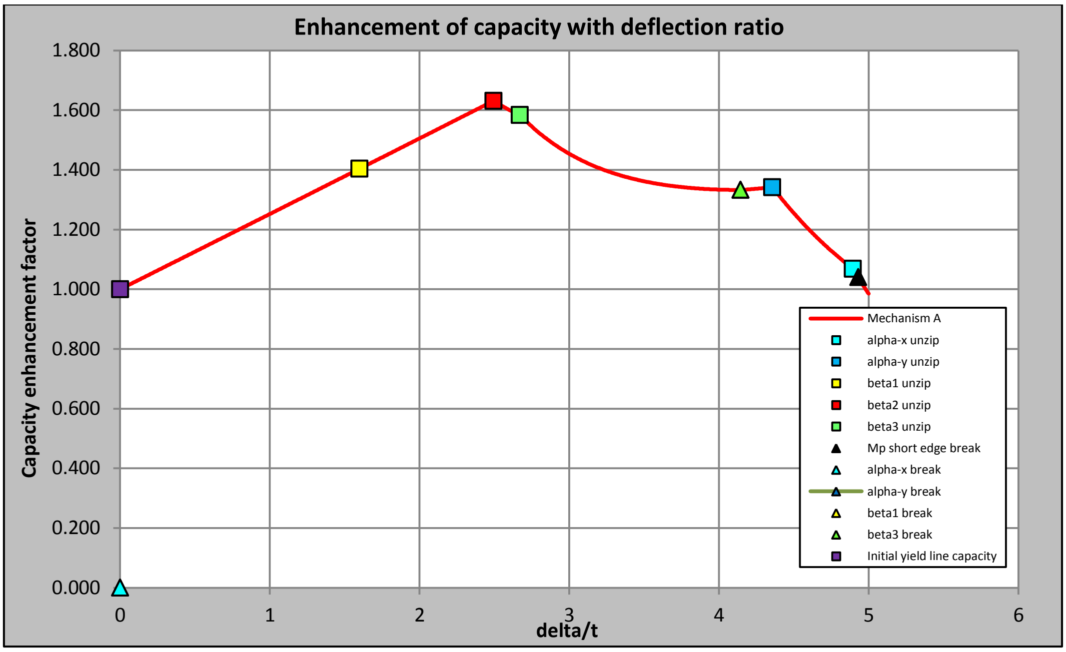

**Fig. 6.5 Enhancement factor performance of Mechanism A (Burgess *et al.*, 2013)**

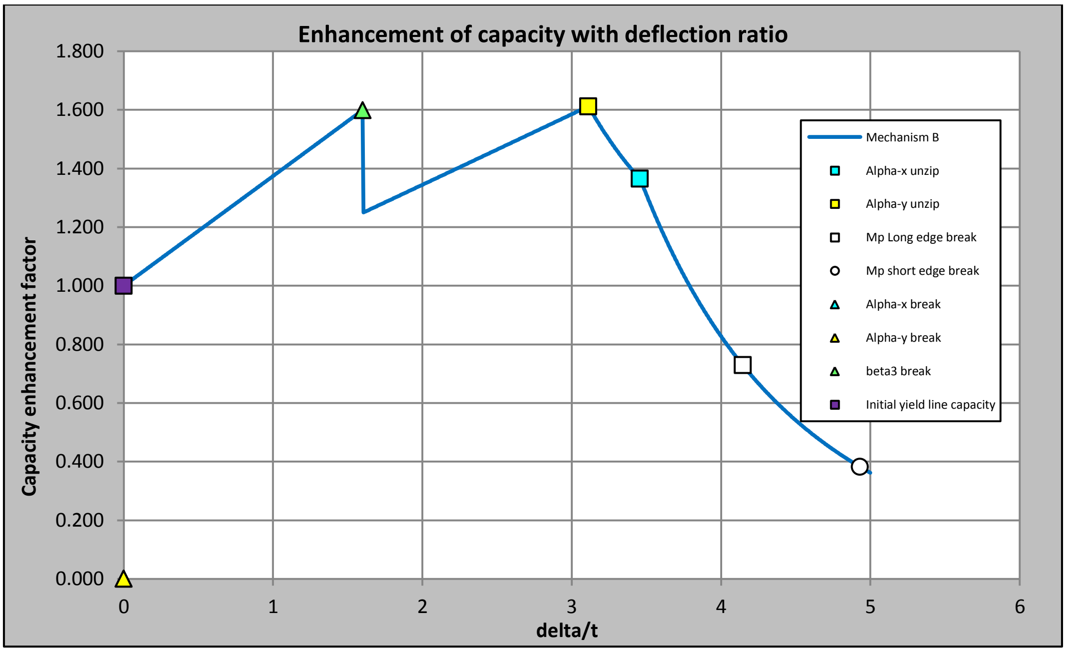

**Fig. 6.6 Enhancement factor performance of Mechanism B (Burgess *et al.*, 2013)**

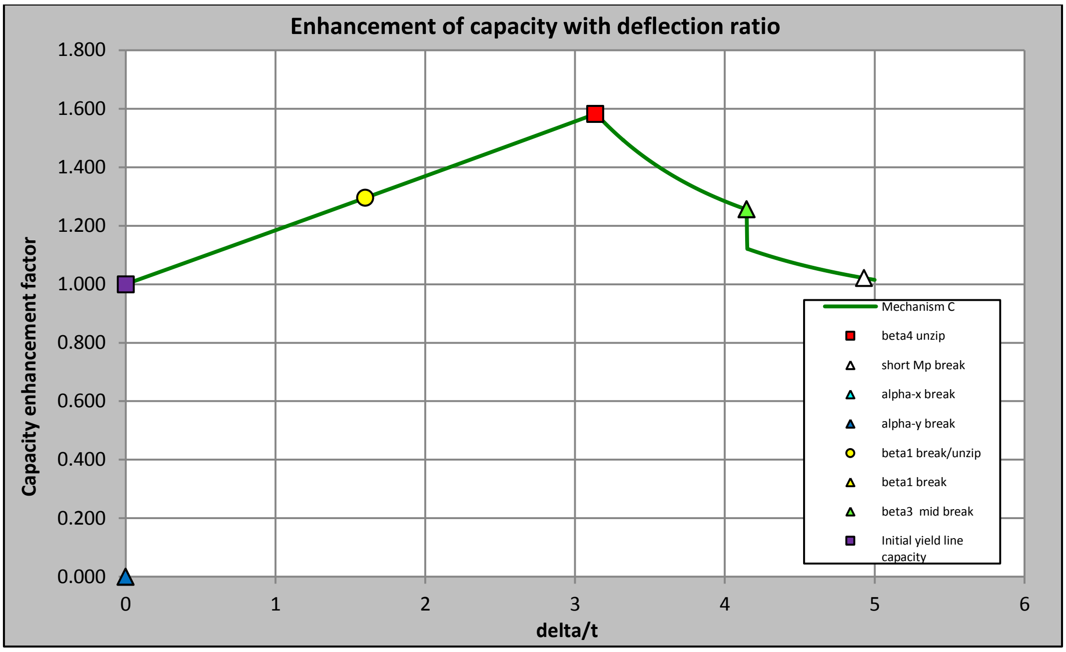

**Fig. 6.7 Enhancement factor performance of Mechanism C (Burgess *et al.*, 2013)**

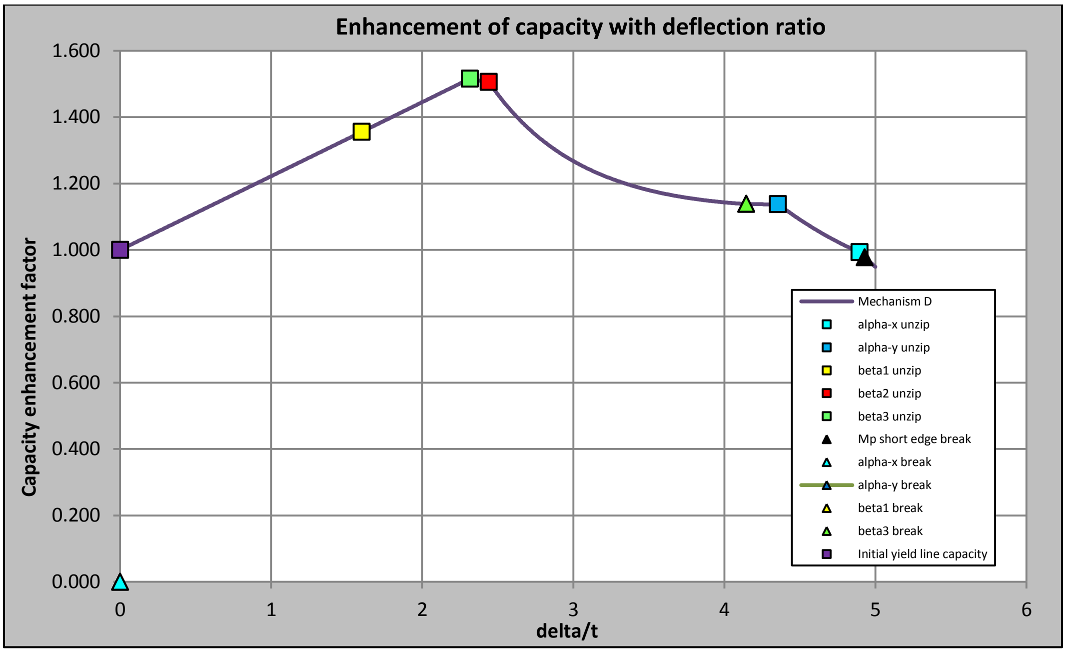

**Fig. 6.8 Enhancement factor performance of Mechanism D (Burgess *et al.*, 2013)**

After the enhancement factors have been found, comparison to the BRE limit excluding thermal expansion (red-dotted line) with maximum deflection allowable for each mechanism from the conventional methods is shown below,

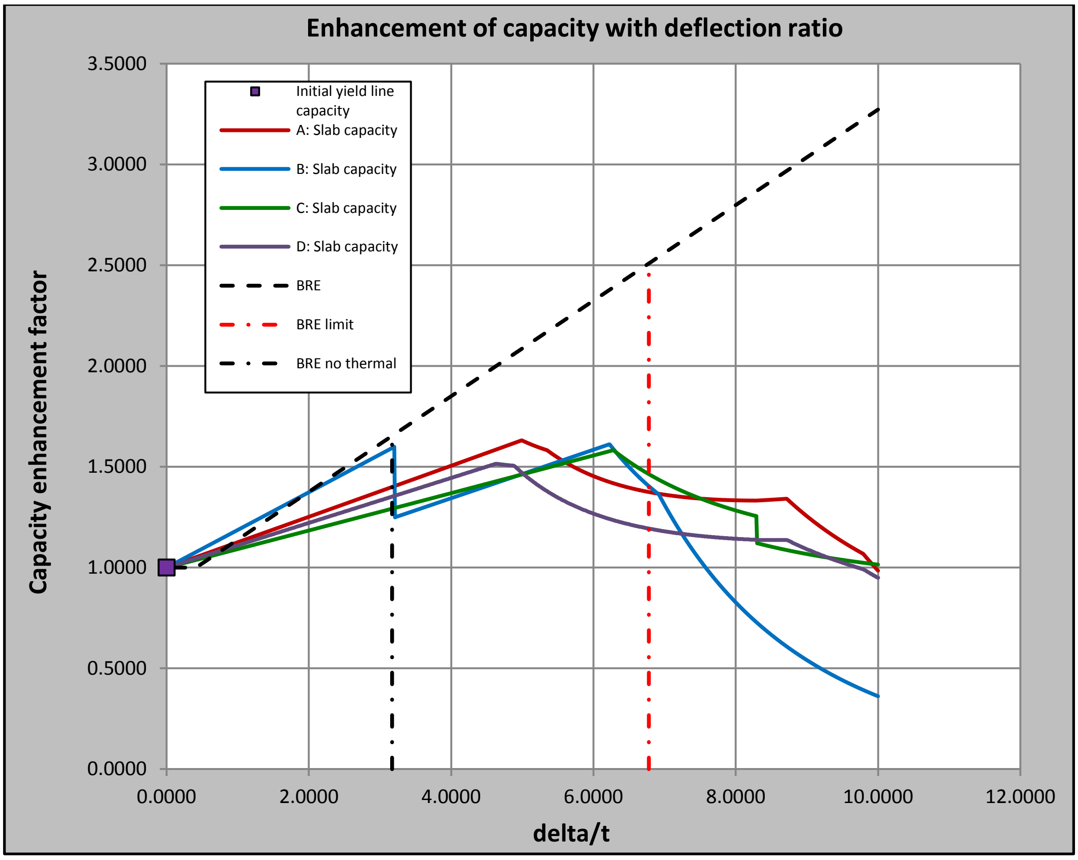

**Fig. 6.9 Combination of 4 mechanism enhancement factor and compare to BRE-Bailey method (Burgess *et al.*, 2013)**

As shown in Fig. 6.9 above, the behaviour of enhancement factor curves falls into two main phases:

1) At the beginning of first phase, all the capacity enhancement factor curves increase continuously. As we can see, the increment ratio of mechanisms A, C and D are very close to each other, as the slopes of these three curves are almost equal. The enhancement factor curve representing mechanism B exhibits a higher rate of increase than the rest of curves. However, this drops significantly when the deflection becomes sufficiently large for the rebar crossing the middle yield-line parallel to the longer span to fracture simultaneously. After this point, the curve starts to rise again up to about 1.6 times the original yield-line capacity. Apart from Mechanism B, the rest of the curves have similar performance, linearly increasing until the second phase occurs. From these 3 curves, the enhancement factor from Mechanism C is lowest as the slab initially deflects. However, this curve increases steadily until its deflection is the longest in the first phase, and its enhancement becomes higher than that of Mechanism D before the second phase happens.

2) During the second phase, steel mesh reinforcement in all the mechanisms progressively fractures along each yield-line, and the capacity enhancement factor begins to decrease until the slab entirely collapses. The fracture of reinforcement across these yield-lines takes place either as ‘unzipping’, which is shown as a continuous curve, or simultaneous fracture, which is shown as a vertical straight line. As shown in Fig. 6.9, in the second phase the enhancement factor of Mechanism B increases rapidly after the simultaneous fracture happens, and turns into the second highest before the reinforcement rebar starts to ‘unzip’. Although the curve of Mechanism B increases fastest, it loses its load carrying capacity much more quickly than other mechanism after it reaches its peak value, and becomes the lowest. For Mechanism C, the second phase happens at the highest deflection among all these curves, and it loses its load carrying capacity slowest. Mechanisms A and D have very similar curve shapes, as they do not involve any simultaneous fracture. Therefore, with only ‘unzipping’ in these two mechanisms, the two curves show smoother performance than B and C in their overall process.

It is not difficult to conclude that the results get from this energy method make more sense than the original yield-line capacity and the BRE-Bailey method its analysis of enhancement factor behaviour. The BRE-Bailey method models load carrying capacity as increasing linearly, subject only to a single deflection limit. It is inaccurate in taking amplified cracking across yield-lines into account, and can only be treated as a simplified calculation method which gives unconservative predictions. The prediction of enhancement factor which is known to be due to membrane action is definitely influenced by the crack development in the slab panel. When cracks gradually open wide, the enhancement due to membrane action reduces. In spite of the new method considering only the ambient temperature stage as far as the slab itself is concerned, the prediction of membrane action given by this energy method is reasonable and reliable. More importantly, this method can be easily adapted to non-rectangular composite slabs to find their enhancement factors due to tensile membrane action.

## 6.4 Extension of new internal work method into triangular slabs

For a typical isosceles triangular slab, the optimal yield-line pattern can be determined by applying general yield-line rules. In this research, the yield-lines are assumed to initiate from each corner of the slab and to intersect at a single point located on the slab's central axis of symmetry. With vertical deflection increasing, it is assumed that the crack opens from the yield-line intersection and then develops to the slab corners progressively.

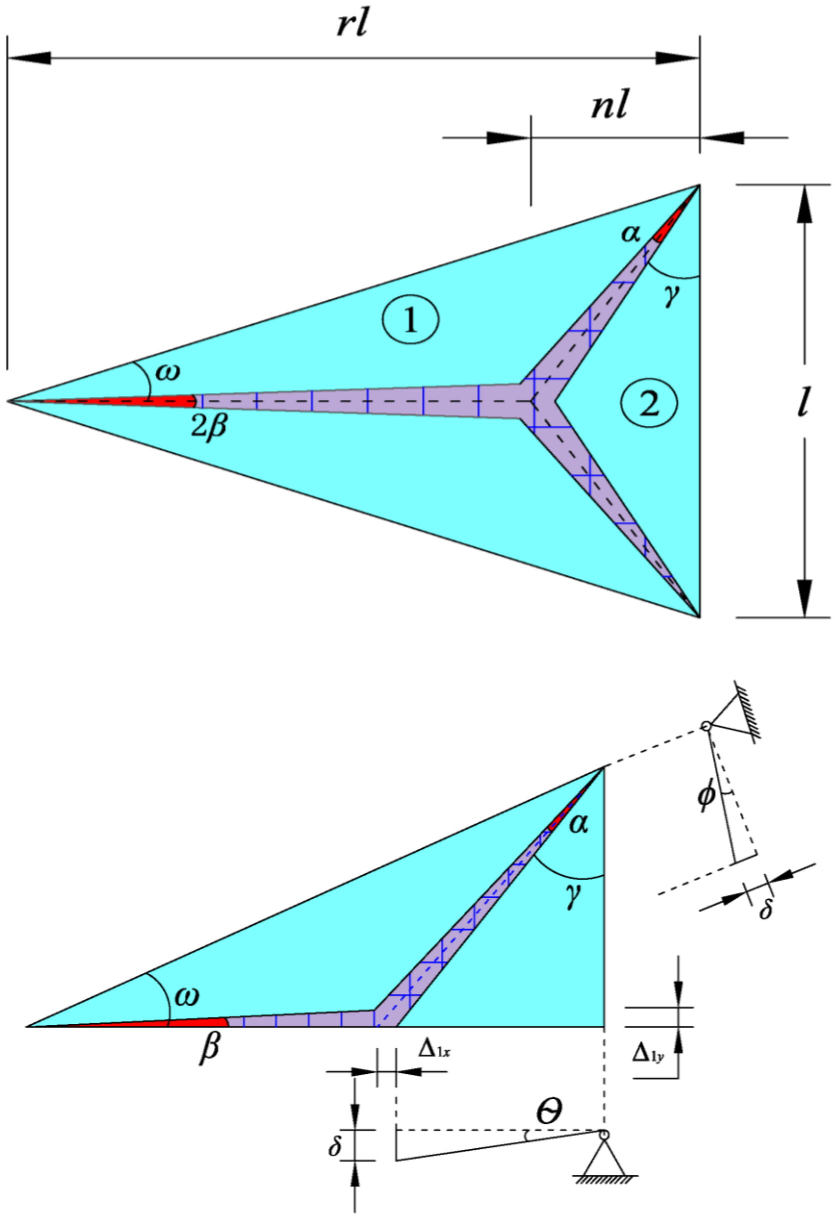

**Fig. 6.10 Assumed crack locations for isosceles triangular slab failure mechanism**

In order to compare the enhancement predicted by the plastic energy method with plastic rebar extension to the slab's original yield-line capacity, the primary task is to find the location of the yield-line intersection.

### 6.4.1 Yield-line capacity of isosceles triangular slab

Adopting the normal plastic energy balance equation which is well known as,

$$\begin{aligned} &External\ Energy\ expended\ by\ loads\ moving \\ &= Internal\ Energy\ dissipated\ by\ plastic\ extensions \end{aligned}$$

After optimizing the value of external load $P$ with respect to $n$, the location of the intersection and the load capacity provided by the yield-line mechanism can be found.

From Fig.6.10, the following relationships can be obtained:

$$\theta = \frac{\delta}{nl}$$

$$\phi = \frac{\delta}{(r-n)lsin\omega}$$

$$\omega = \arctan(\frac{1}{2r})$$

(6.4)

For the external energy due to load movement,

$$E = P\frac{l^2 r}{2}\cdot\frac{\delta}{3}$$

(6.5)

For the internal energy dissipated by rotations about the yield-lines,

$$\begin{aligned} D &= M_{py}(2\phi cos\omega)rl + M_{px}(\theta + \phi sin\omega)l \\ &= \delta\left[M_{py}\left(\frac{2r}{r-n}\right)cot\omega + M_{px}(\frac{1}{n} + \frac{1}{r-n})\right] \end{aligned}$$

(6.6)

In which, $M_{px}$ and $M_{py}$ are the moments of resistance according to the reinforcement mesh in the *X*- and *Y*- directions; if the reinforcement mesh is isotropic, then $M_{px} = M_{py}$.

From the equations above, the load capacity *P* can be expressed as,

$$P = \frac{6}{l^2(r-n)}\left(2M_{py}cos\omega + \frac{M_{px}}{n}\right) \tag{6.7}$$

If $M_{px} = M_{py} = M_p$, then

$$P = \frac{6M_p}{l^2(r-n)}\left(2cos\omega + \frac{1}{n}\right) \tag{6.8}$$

If we partially differentiate and set $\frac{d_p}{d_n} = 0$ to optimize *p*, the value of *n* is derived as,

$$n = \frac{-M_{px} + \sqrt{M_{px}^2 + 2M_{px}M_{py}rcot\omega}}{2M_{py}cot\omega} \tag{6.9}$$

If $M_{px} = M_{py} = M_p$, then

$$n = \frac{-1 + \sqrt{1 + 2rcot\omega}}{2cot\omega} \tag{6.10}$$

As $cot\omega = 2r$ so,

$$P(General) = \frac{6}{l^2} \cdot \frac{1}{(r-n)}\left(4rM_{py} + \frac{M_{px}}{n}\right) \tag{6.11}$$

$$P(Isotropic) = \frac{6}{l^2} \cdot \frac{M_p}{(r-n)}\left(4r + \frac{1}{n}\right) \tag{6.12}$$

and

$$n(General) = \frac{-M_{px} + \sqrt{M_{px}^2 + 4r^2 M_{px} M_{py}}}{4rM_{py}}$$

(6.13)

$$n(Isotropic) = \frac{1}{4r}(-1 + \sqrt{1 + 4r^2})$$

(6.14)

### 6.4.2 Capacity enhancement calculation for isosceles triangular slab

#### 6.4.2.1 Calculation of rebar extension

Using the same method as for rectangular slabs, according to the properties of the isosceles triangle, the following relationships exist:

$$\gamma = \arctan(2n)$$

$$\beta = \frac{1}{2}\phi^2 sin\omega cos\omega$$

(6.15)

$$\alpha = [n\theta^2 + (r-n)\phi^2 sin\omega]\cos^2\gamma + 2\beta(r-n)sin\gamma cos\gamma$$

(6.16)

The rebar extensions across the yield-line $\alpha$ are given as follows:

In $X$- direction:

$$\Delta_{\alpha x} = \alpha S\cos\gamma + \theta\mu h$$

so,

$$\Delta_{\alpha x} = \alpha Y + \theta\mu h \qquad (6.17)$$

In $Y$- direction:

$$\Delta_{\alpha y} = \alpha S\sin\gamma + \phi\mu h$$

so,

$$\Delta_{\alpha y} = \alpha X + \phi\mu h \qquad (6.18)$$

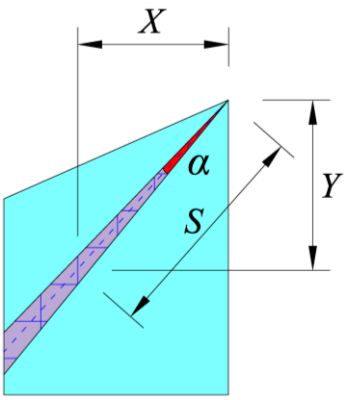

**Fig. 6.11 Rebar extension in one of two equal slab corner yield-lines**

For the yield-line $\beta$ which initiates from the corner which is on the axis of symmetry, the rebar extension in the $Y$- direction is given by,

$$\Delta_{\beta y} = 2\beta X + 2\phi\mu h \qquad (6.19)$$

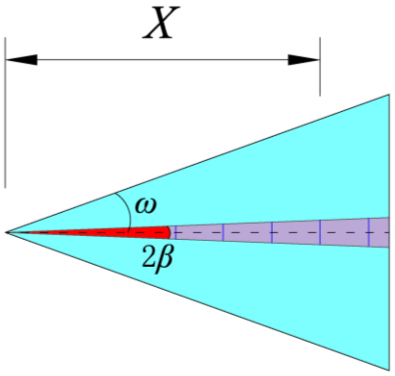

**Fig. 6.12 Rebar extension in unique slab corner yield-line**

### 6.4.2.2 Calculation of internal work

For the yield-lines $\alpha$, the internal work is given by

$$D_{\alpha x} = F_p l^2 \bar{Y}\left(\frac{\alpha}{2}\bar{Y} + (\theta + \phi sin\omega)\mu\bar{h}\right) \qquad (6.20)$$

in which, referring to Fig. 6.11,

$F_p$ is the reinforcement mesh yield force per unit length;

$l$ is the length of the triangle's bottom edge;

$\bar{Y}$ is the length of the intact yield line $\alpha$ in the $Y$- direction.

$$\bar{Y} = \frac{1}{2}\ when\ reinforcement\ is\ intact;\ \ otherwise\ \bar{Y} = \frac{\bar{v} - (\theta + \phi sin\omega)\mu\bar{h}}{\frac{\alpha}{2cos\gamma} - 2\beta(r-n)sin\gamma}$$

$$D_{\alpha y} = F_p l^2 \bar{X}_1\left(\frac{\alpha}{2}\bar{X}_1 + (\phi cos\omega)\mu\bar{h}\right) \qquad (6.21)$$

$\bar{X}_1$ is the length of the intact yield line $\alpha$ in the $X$- direction.

$$\bar{X}_1 = n\ when\ reinforcement\ is\ intact;\ otherwise\ \bar{X}_1 = \frac{\bar{v} - \phi cos\omega\mu\bar{h}}{\beta}\cdot\frac{n}{r-n}$$

For the yield-line $\beta$, the internal work is given by,

$$D_{\beta y} = F_p l^2 \bar{X}_2 \left(\beta \bar{X}_2 + (2\phi cos\omega)\mu \bar{h}\right) \tag{6.22}$$

$\bar{X}_2$ is the length of the intact yield line $\beta$ in the $X$- direction.

$$\bar{X}_2 = r - n \, when \, reinforcement \, is \, intact; \;\; otherwise \, \bar{X}_2 = \frac{\bar{v} - 2\phi cos\omega\mu\bar{h}}{\beta}$$

### 6.4.3 Validation of new internal work method for isosceles triangular slab

In the previous section, the enhancement factor curves obtained from this plastic energy method have been compared to the capacity provided by original yield-line and enhancement factors from the BRE-Bailey method. As the result is logical in its prediction of real slab behaviour, we have a good reason to trust this method when it is extended to non-orthogonal slabs.

The same calculation procedure used for rectangular slabs is applied and implemented in an Excel spreadsheet, with triangular slab geometry defined by:

Short span *l* = 6m and *r* = 1.5;

Slab depth = 100 mm;

Yield strength of steel $f_{yk}$ = 500*MPa* (*S500*) with 10% of ductility;

Concrete compressive strength = 30*MPa* (C30).

Reinforcement mesh: A142 placed at slab middle depth of 60 mm.

The curve of enhancement factor obtained from the Excel spreadsheet is shown in Fig. 6.13 below:

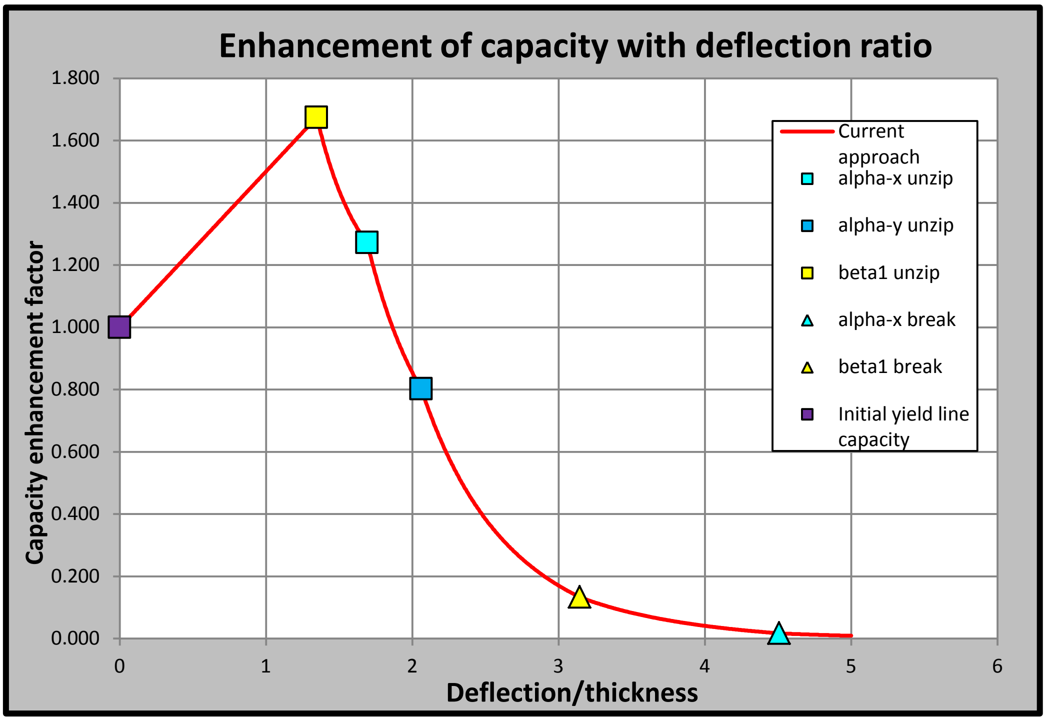

**Fig. 6.13 Enhancement factor development of triangular slab**

From Fig. 6.13, it is easy to notice that, as for rectangular slabs, this curve also has two phases. In the first phase, the enhancement of capacity is dramatically increased as slab deflection increases. In the first phase, he enhancement factor reaches its peak value at a much lower deflection ratio $(\delta / t = 1.345)$ when compared to rectangular slabs of the same aspect ratio $(\delta / t > 3)$. This is because this isosceles triangular slab is smaller in area than the rectangular slab, and also a triangle is more stable than a rectangle in geometry. After the curve has reached its peak point and cracks start to unzip along yield-line $\beta$, the enhancement factor also begins to decrease rapidly. Between every two 'unzip' commencement points the slope of curve increases. In the final stage, when the rebar across the yield-lines has completely broken, the load carrying capacity is close to zero.

### 6.4.4 Parametric study of isosceles triangular slabs

#### 6.4.4.1 Influence on load capacity for different reinforcement meshes

Generally, the definition of reinforcement ratio is,

$$\frac{Total\ area\ of\ steel\ rebar\ in\ the\ cross-section}{Area\ of\ element\ cross-section}$$

For rectangular or square slabs, the area of a cross-section is a constant, and different reinforcement mesh areas in the two axis directions represent different reinforcement ratios. However, in triangular slabs, the area of a cross-section is variable along any axis direction. Therefore, the impact of reinforcement ratio on slab load carrying capacity is shown here only by applying different reinforcement mesh sizes onto one triangular slab with the geometry and properties given below:

**Geometry**: $l$ = 6m and $r$ = 1.5, in which $r$ is defined as height-to-base ratio;

**Slab thickness**: $t$ = 120mm;

**Reinforcement mesh effective depth:** 60 mm;

**Material properties**:

Strength of reinforcement rebar: 500N/mm$^2$;

Compressive strength of concrete: 30N/mm$^2$;

Steel ductility: 10%.

In the first test, four different sizes of reinforcement mesh have been applied. These are A142, A193, A252, A393. All these four models are considered with isotropic reinforcement and without discontinuous edges. The details of these reinforcement meshes are given in Table.6.2.

| Reinforcement Mesh | Spacing long span | Spacing short span | Long span wire diameter | Area long span wires | Short span wires diameter | Area short span wires |
|---|---|---|---|---|---|---|
| | (mm) | (mm) | (mm) | (mm$^2$/m) | (mm) | (mm$^2$/m) |
| A142 | 200 | 200 | 6 | 141.4 | 6 | 141.4 |
| A193 | 200 | 200 | 7 | 192.4 | 7 | 192.4 |
| A252 | 200 | 200 | 8 | 251.3 | 8 | 251.3 |
| A393 | 200 | 200 | 10 | 392.7 | 10 | 392.7 |

**Table. 6.2 Details of isotropic reinforcement meshes**

The results for different reinforcement meshes are shown in Fig.6.14.

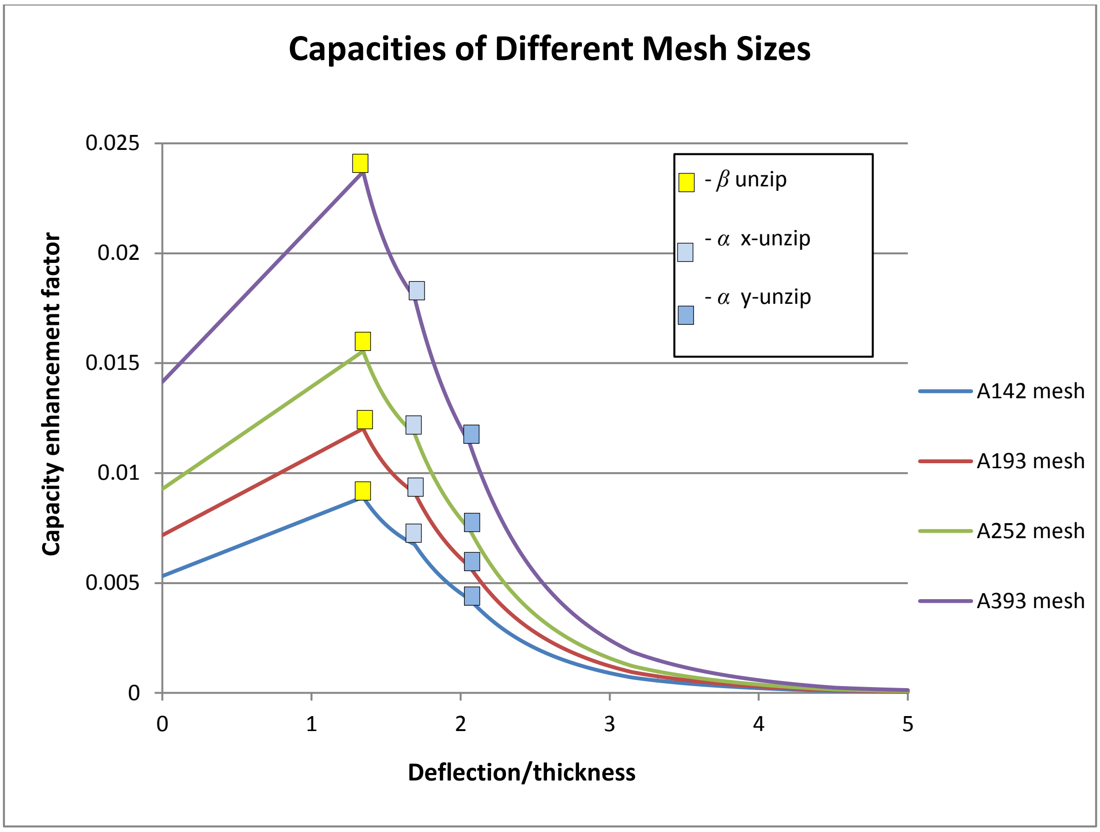

**Fig. 6.14 Capacities of different isotropic mesh sizes.**

As expected, higher reinforcement mesh size provides higher load carrying capacity, which is also a general observation from rectangular slabs. The points which represent the crack origination occur at the same proportion of the deflection-thickness ratio, because of the tensile strength of isotropic reinforcement is identical in both directions. For different isotropic reinforcement meshes, the two phases of load carrying capacity change are clearly observed, and the performance of the whole triangular slab is reasonable.

In a parallel test a triangular slab with orthotropic reinforcement meshes is investigated. With exactly the same geometry and material properties as in the example above, the only change is in applying the different orthotropic reinforcement meshes listed in Table.6.3 below.

| Reinforcement Mesh | Spacing long span | Spacing short span | Long span wire diameter | Area long span wires | Short span wires diameter | Area short span wires |
|---|---|---|---|---|---|---|
| | (mm) | (mm) | (mm) | $(mm^2/m)$ | (mm) | $(mm^2/m)$ |
| B196 (a) | 100 | 200 | 5 | 196.3 | 7 | 192.4 |
| B196 (b) | 200 | 100 | 7 | 192.4 | 5 | 196.3 |

| | | | | | | |
|---|---|---|---|---|---|---|
| B283 (a) | 100 | 200 | 6 | 282.7 | 7 | 192.4 |
| B283 (b) | 200 | 100 | 7 | 192.4 | 6 | 282.7 |
| B385 (a) | 100 | 200 | 7 | 384.8 | 7 | 192.4 |
| B385 (b) | 200 | 100 | 7 | 192.4 | 7 | 384.8 |
| B503 (a) | 100 | 200 | 8 | 502.7 | 8 | 251.3 |
| B503 (b) | 200 | 100 | 8 | 251.3 | 8 | 502.7 |

**Table. 6.3 Details of orthotropic reinforcement meshes**

In this orthotropic test, each reinforcement mesh size includes two situations. The mesh size followed by (a) has closer rebar spacing in the span parallel to the triangle height, and mesh size followed by (b) represents the opposite situation. It has been verified previously with increasing isotropic reinforcement mesh size, the load carrying capacity increases. Comparisons are made between the two situations with the same size of reinforcement mesh.

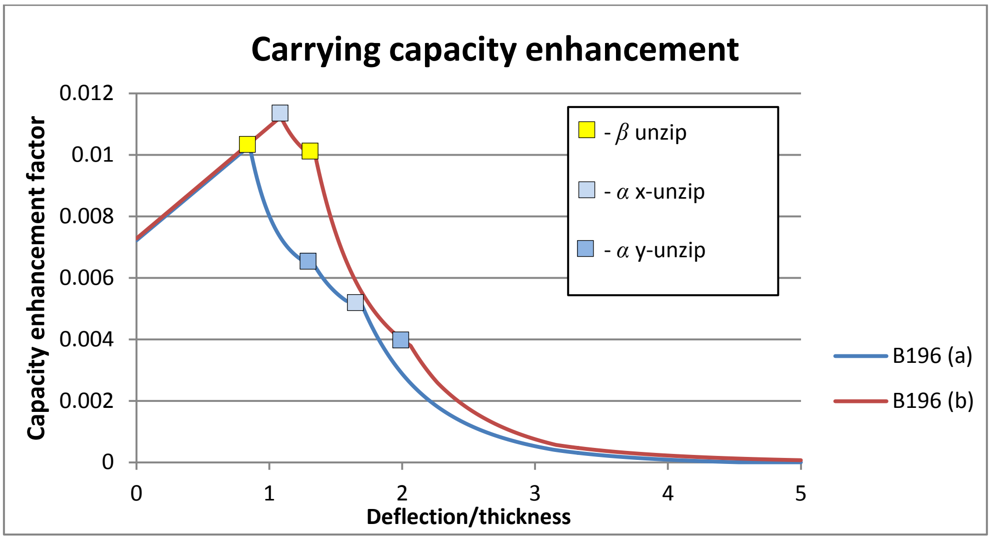

**Fig. 6.15 Comparison of load carrying capacities of orthotropic reinforcement mesh B196**

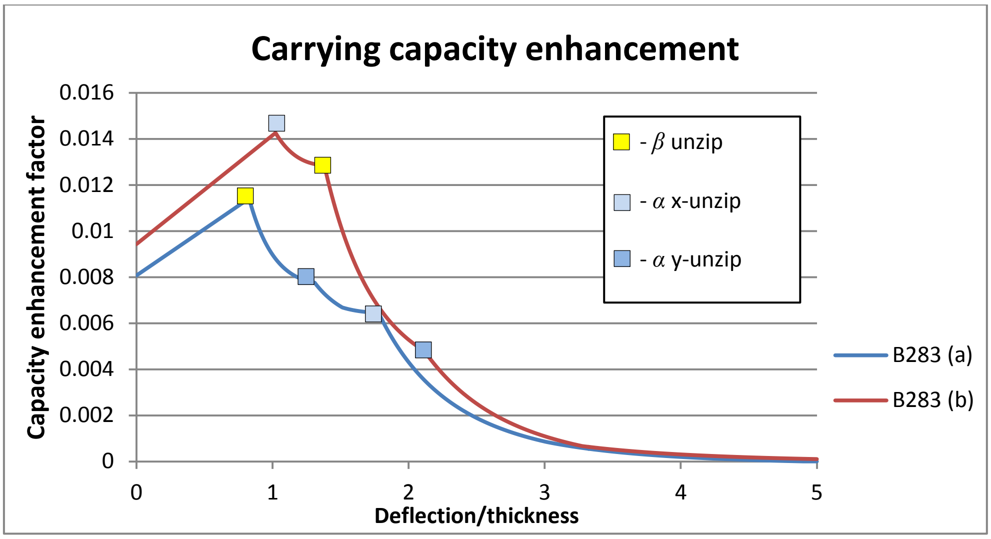

Fig. 6.16 Comparison of load carrying capacities of orthotropic reinforcement mesh B283

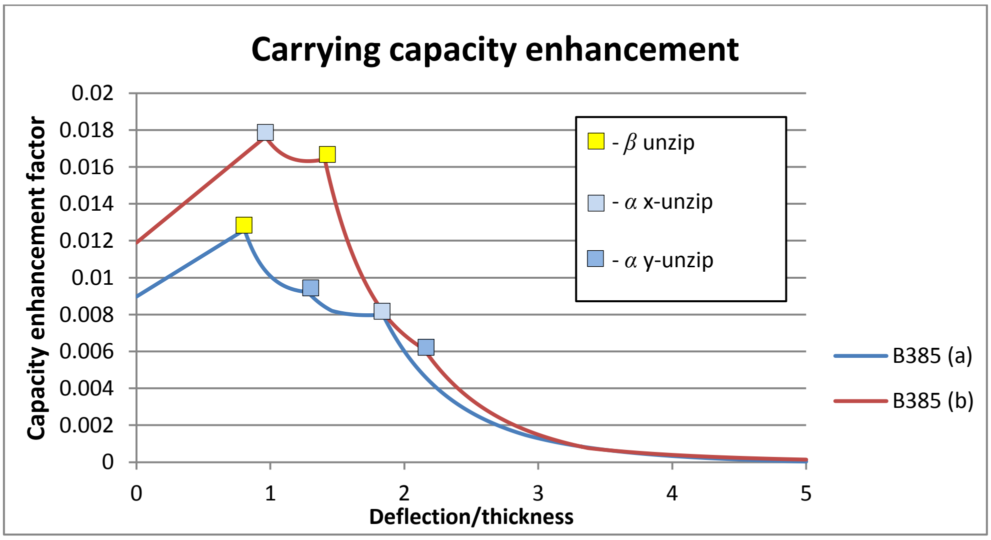

Fig. 6.17 Comparison of load carrying capacities of orthotropic reinforcement mesh B385

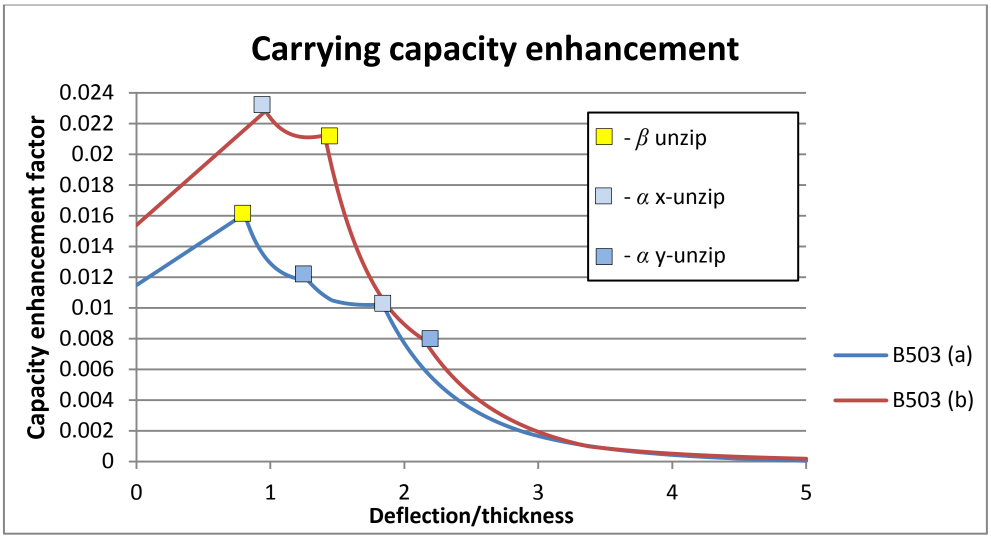

**Fig. 6.18 Comparison of load carrying capacities of orthotropic reinforcement mesh B503**

From Figs. 6.15-6.18, it can be seen that the situations (a) in which the slab has a higher reinforcement area in the 'height' span provides the lower load carrying capacity. In Fig. 6.15, for mesh B196, the enhancement of capacity for both situations is almost identical at the beginning of the deflection increase. With reinforcement size rising, the rate of capacity increase in situation (b) also becomes the higher, as shown in Figs. 6.16-6.18. However, the situation (a) in all these models shows a lower rate of decrease compared to situation (b), although with increasing the reinforcement size the difference in the capacity between the two situations becomes significant.

Since the reinforcement is orthotropic, the 'unzipping' behaviour along yield lines is quite different compared with the isotropic reinforcement cases. In all these orthotropic cases, situation (a) has a capacity drop from the point at which the crack $\beta$ starts to 'unzip' in the $Y$-direction, followed by the point where the diagonal crack $\alpha$ starts to 'unzip' in the $Y$-direction and then by $\alpha$ 'unzipping' in the $X$-direction. In situation (b), the sequence of 'unzipping' differs; firstly $\alpha$ in the $X$-direction, then crack $\beta$ and finally $\alpha$ in the $Y$-direction. This is because, in situation (a), there is shorter spacing in the $X$-direction, which means the tensile strength is greater along the $X$-direction. In other words, for situation (a) in all these cases, it is harder to open a crack in the $X$-direction than that in the $Y$-direction. Hence, in situation (a), the crack $\beta$ appears first, followed by crack $\alpha$ 'unzipping" in $Y$ and then in $X$. The behaviour of situation (b), which is totally opposite, can also be explained in this way.

### 6.4.4.2 Influence on load capacity of geometry change

The factor conventionally used in rectangular slabs to define the geometry is called ‘aspect ratio’, equivalent to the longer span divided by the shorter span. In the isosceles triangular slabs in this research, the equivalent factor used to define the geometry is the height-base ratio, which is the parameter $r$ shown in Fig. 6.10. In this analysis, the material properties have been kept the same as above; the base length $l$ is kept as 6m, and the height-base ratio $r$ is increased from 0.5 to 1.5, so that the height $rl$ varies from 3m to 9m; reinforcement mesh A142 has been selected for all these cases. The resulting enhancement factor performances are given in Fig. 6.19.

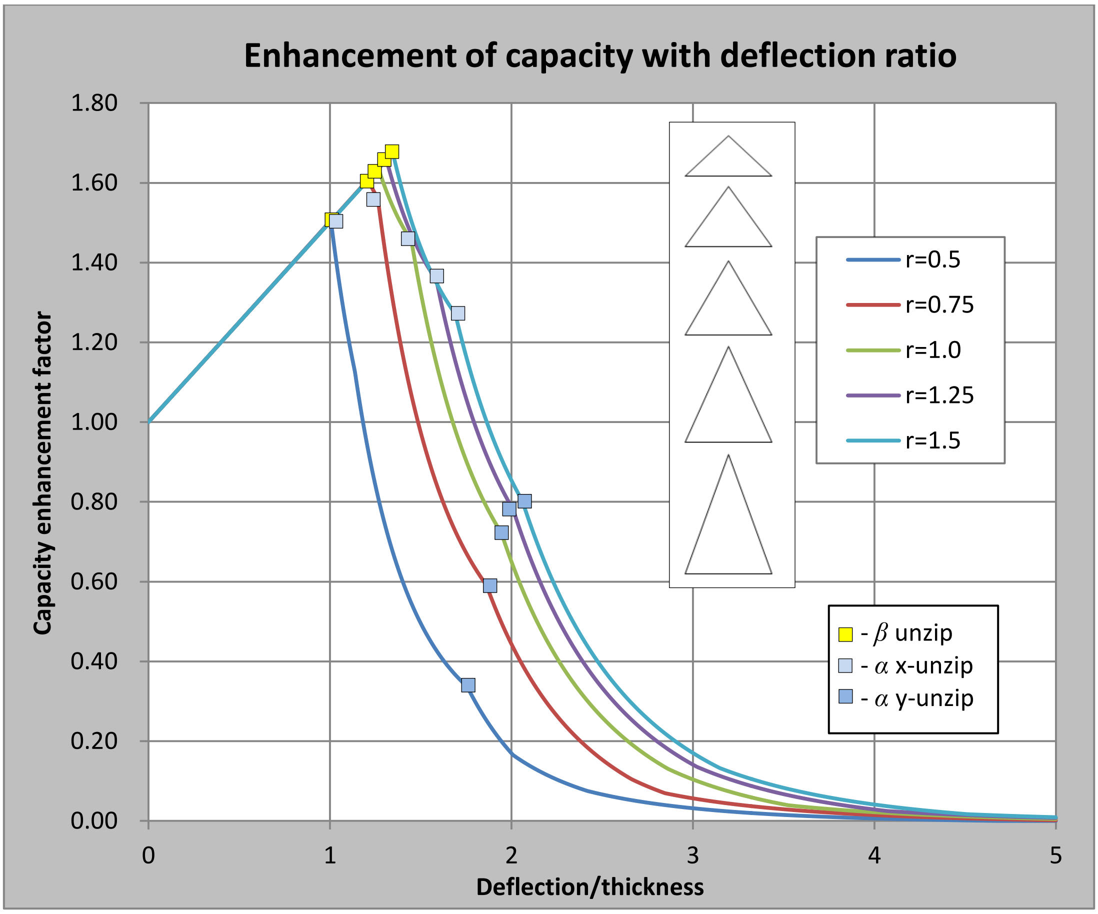

**Fig. 6.19 Enhancement factor behaviour with change of triangular geometry**

Generally, from the Fig. 6.19 above it can be concluded that, with increase of the height $rl$, the load capacity enhancement factor becomes greater. However, it can be seen that the proportion of enhancement factor increment is reduced gradually as $r$ increases. From $r$=0.5 to 0.75, the increment of enhancement factor is considerable, but for $r$=1.25 to 1.5, the difference is only about 1/6 of that from 0.5 to 0.75.

With the triangle height increasing, the appearance of crack ‘unzipping’ also differs. For lower height-base ratios, the crack $\beta$ ‘unzips’ at lower deflection-thickness ratios. Moreover, the lower height also causes earlier occurrence of the crack $\alpha$. As can be seen for $r$=0.5, the ‘unzip’ point of crack $\beta$ and $\alpha$ in the $X$-direction almost appear at the same time. However, when $r$=1.5 the ‘unzipping’ of the crack $\alpha$ in the $X$-direction occurs much later than that of crack $\beta$. In contrast, the ‘unzipping’ of crack $\alpha$ in the $Y$-direction the opposite of this. For lower height-base ratios, it takes longer for the diagonal crack $\alpha$ to start to ‘unzip’ in the $Y$-direction after it has ‘unzipped’ in the $X$-direction.

## 6.5 Summary and discussion

In general, at the serviceability stage, the behaviour of slab is elastic with maximum steel stress and deflection at the slab centre. When the load increases, a yield-line pattern starts to form at the slab corners and centre. On increasing the load further, yield-lines form in the most highly stressed locations and develop into continuous plastic hinges. These plastic hinges turn into a small-deflection mechanism forming a yield-line pattern. As the yield-lines separate the slab panel into several individual flat facets that rotate about the slab edge, cracks generate on the soffit where the tensile capacity of concrete has been exceeded along the yield-lines. As the rotation keeps increasing, the cracks continuously widen, which induces the extension of reinforcement bars and their eventual fracture. This can be considered as the post-yield-line stage behaviour of slabs in the fire situation at much greater deflections at the slab centre compared to that at ambient temperature.

In this chapter, a new plastic work balance method taking account of work done by the extension of rebar across yield-line cracks at large deflections has been illustrated. Compared to the load carrying capacity provided by the original small-deflection yield-line work equation which contains only internal work dissipated by the hinges in the yield-line rotations, the effect of tensile membrane action on capacity enhancement is clearly significant. Since the contrast is based on deflection-related results, it firmly proves the enhancement of load-carrying capacity due to tensile membrane action at large-deflections, particularly in fire situations.

Based on the original yield-line pattern, four different failure mechanisms of rectangular slab have been examined with various locations and categories of rebar fracture. Each mechanism provides its own curve of enhancement factor, which depends on the deflection at which the reinforcement crossing yield-lines starts to fracture progressively (or ‘unzip’) or to fracture simultaneously. Compared to the BRE-Bailey method, which presents an enhancement factor increasing as a straight line without considering the influence of cracks happening, the curves get from this new internal work method seem more in accordance with reality.

According to the comparisons of the results to the original yield-line capacity and the BRE-Bailey method, there can be reasonable confidence that this new internal work method can be adopted without concern about slab geometry. In fact, after applying this energy work method to a typical isosceles triangular slab, the result of enhancement factor against deflection ratio also seems convincing. The increase of enhancement factor in the early stage, when external loads act on the isosceles triangular slab, and the rapid decrease when the rebar crossing the yield-lines starts to ‘unzip’, the behaviour of the load carrying capacity is in accordance with expectation. However, since the research about non-orthogonal slabs is rare and limited, it is regrettable that there are no previously studied examples which can be used for comparison.

The new internal work method discussed in this chapter currently considers essentially ambient temperature behaviour. This is actually more relevant than it might superficially seem to be. The reinforcement layers in a composite slab are insulated by its concrete cover; according to Eurocode 4 Part 1-2 (Annex D) the rebar temperature remains below 400°C up to 60 minutes of the Standard Fire if the cover is at least 35mm. Some further study is still needed to extend this method to concrete slabs at elevated temperature, although the only variations to the method concern the reduced yield strength and fracture ductility of the rebar at elevated temperatures. Temperature prediction, at least for rebar, needs to be incorporated, either as a rigorous thermal analysis or as simplified data appropriate to particular fire curves.

# Chapter 7 Conclusions and recommendations

As the revolution in structural fire engineering gathers pace, more performance-based structural design methods have identified the existence of tensile membrane action of composite slabs under fire situation and the enhancement of fire resistance which it can cause. Tensile membrane action is considered as a primary load-carrying mechanism when a slab panel is subject to large deflection and has stiff vertical support around its full perimeter. The advantage of applying the tensile membrane action mechanism in the process of composite steel-framed building design is to reduce the cost of fire protection on a considerable number of intermediate beams, while ensuring overall structural safety. Among a number of design methods developed so far which take the influence of tensile membrane action into account, the Bailey-BRE method has been widely acknowledged and adopted. In order to use the Bailey-BRE method, the floor layout must be divided into orthogonal slab panels in rectangular or square shapes. However, as modern architecture develops in the use of more imaginative concepts, an increasing number of building floor layouts are not rectangular or square, and this induces the problem of applying the method to irregular shapes of slab panel.

The series of studies in this thesis were aimed to extend the treatment of tensile membrane action to non-orthogonal panels, and to verify such developments by using numerical modelling. The conclusions from the various studies are given in its sections, and recommendations for further study are made at the end of this chapter.

## 7.1 Conclusions

### 7.1.1 The penalty function method

In order to numerically analyse composite slabs of non-orthogonal geometry, slab panels around floor edges or corners often cannot be divided into rectangular or square shapes, but have to be considered as triangular or trapezoidal. This means that there is at least one edge of the slab panel that cannot align along a global axis. The existing analysis program *Vulcan* is only capable of applying the boundary conditions with respect to the nodal degrees of freedom as fixed or free to move with respect to each global axis. This is obviously not adequate to investigate the movements of slab panels of such irregular geometries. To resolve this shortcoming, the penalty function method has been developed and implemented into the program. The main conclusions of this section are:

- The penalty parameter, which is user-defined, determines the magnitude of the influence of the penalty function. In this research, the penalty parameter has been set as 1000 times the average stiffness and this proves to work very well;
- The degrees of freedom at any nodes can be constrained, in pairs or more, by applying penalty functions for the purpose of keeping their movements in a defined relationship with respect to any direction in the global coordinates;
- The nodal displacements on a slab panel edge can be forced to stay in a straight line when the edge is actually continuous with an adjacent panel. In other words, the continuous edges will remain straight when deformation occurs;
- Slab panels located in different areas of a floor layout can be analysed as isolated instead of modelling the whole building floor system, but considering the interaction between slab panels;
- The membrane stress vectors are shown to be compatible after application of penalty function method for various types of boundary conditions. With penalty functions applied, the movement of slab edges is different from those free from restraint, which also induces a difference in membrane stress.

### 7.1.2 Numerical modelling and validation

A series of studies on membrane action of non-orthogonal slabs at elevated temperature has been conducted. In practice, the models of non-orthogonal slabs can routinely include triangular and trapezoidal slabs. Triangular slabs of exactly the same geometry with different boundary conditions, subjected to fire, have been simulated. Also, an isolated trapezoidal slab and another with continuous edges have been analysed. The program *Vulcan*, with the penalty function method applied, has been used to analyse rectangular slab panels located in different areas of a floor layout. The following conclusions were drawn:

- The process of generation of membrane action in triangular slabs is very similar to that for rectangular slabs, but starts at higher temperatures;
- With slab vertical deflection increasing, the tensile membrane stress occurs in the central area of the triangular slab, surrounded by a compressive membrane stress;

- Compared to rectangular slabs, the area of tensile membrane stress in triangular slabs is smaller because of the different geometric characteristics. The triangle is a more stable geometry than a rectangle in terms of overall stiffness, which induced smaller deformation in triangular slabs. This is also the reason why the tensile membrane stress in a triangular slab is distributed over a smaller area and generated at higher temperatures.
- The slab edge movements can affect the tensile membrane stress significantly. With two continuous edges, the triangular slab model analysed experiences more restraint from two adjacent slab panels than that with only one continuous edge. As a result, the triangular slab panel with two continuous edges shows a smaller area of tensile membrane force compared to that with one continuous edge.
- Due to the geometric properties of a triangle, the area near the slab corners is much smaller than that in the slab centre, and therefore the stability in this area is much greater. The deformation around this area is tiny and restrains the area of tensile membrane force;
- The membrane action in trapezoidal slabs shows similar behaviour to that in rectangular slabs. The case of a trapezoidal slab with continuous edges once again proves that the essential condition for tensile membrane action to take place is that the perimeter beams have to be protected as temperatures grow.
- The boundary nodal movements of a rectangular slab panel affect the symmetry of membrane stress distribution.
- With more continuous edges, which means more restraint from adjacent slab panels, the central deflection is enlarged. In other words, the restraint from adjacent slab panels enhances the tensile membrane action with temperature growth.
- The intermediate secondary beams without protection experience smaller vertical deflections if the supporting primary beams lie along edges with continuity than those without horizontal restraint.

### 7.1.3 Tensile membrane action of non-orthogonal slabs

In the manual calculation of enhancement due to tensile membrane action developed in Hayes’ initial research and advanced in work by Bailey, the fundamental basis is the distribution of compressive and tensile membrane forces across the yield-line pattern which forms in the slabs. According to the observations from triangular and trapezoidal slab models, the distribution of compressive and tensile membrane forces has been determined. In the process of establishing and extending the Bailey-BRE method in triangular and trapezoidal slabs, the following conclusions have been reached:

- The parameters used in both the Hayes and Bailey-BRE methods are resolved in equilibrium equations, and contain an assumption that presumes the location of the centroid of the compressive stress-block is at a specific point on the rectangular slab edge. From the previous research, set out by Hayes, this assumption is only based on empirical experience and has never been proved, which leads to the conclusion that it cannot be used in triangular slabs.
- Since the assumption cannot be adopted in triangular slabs and it is not reasonable to make another similar assumption, the number of unknown parameters is more than the number of equilibrium equations. Therefore, the Bailey-BRE method is not able to be extended into triangular slabs unless a similar assumption is approved.
- Before extending the Bailey-BRE method into trapezoidal slabs, the locations of yield-line intersections have to be determined. Due to the geometry of a trapezium, two general yield-line patterns have been presumed, and the existence of both has been demonstrated by performing numerical studies.
- Establishment of a general equation to define the locations of yield-line intersections in terms of the geometric features of a trapezium has been attempted. In the process, it has been found that the transformation of the yield-line pattern corresponding to a change of trapezoidal geometry is very sensitive and discontinuous.
- Based on the knowledge about the behaviour of yield-line patterns in rectangular and square slabs, another yield-line pattern has been assumed, but has been found not to exist. This phenomenon may be due to the asymmetry of the upper and lower part of the trapezium, which induces the sudden appearance of the central yield-line in the transverse direction.

- Some rough rules linking trapezium geometry to the form of the yield-line pattern have been presented. The three parameters defining the geometry of a trapezium are the angle $\xi$ between the side and transverse directions, and the top and bottom base lengths, $l$ and $L$. When $l$ is fixed, the transformation of the yield-line pattern occurs at a specific value of angle $\xi$. With top length increasing, the transformation of the yield-line pattern happens at smaller value of angle $\xi$; when the top and bottom base lengths are fixed, the transformation of yield-line pattern when the sum of top and bottom base length is equal to the width.

### 7.1.4 New plastic energy method for load capacity enhancement

The conventional yield-line method only considers the internal work dissipation in the in-plane rotations about the yield-lines. However, after the yield-line pattern has formed the concrete in tension at the slab bottom surface starts to crack and the rebar experiences stretching. When the crack is totally open, the rebar has more significant extension until the fracture takes place. The whole behaviour can be considered both as membrane action and also as part of the internal work dissipation after the yield-line pattern forms. After validating this method and extending it to triangular slabs, parametric studies have been carried out, and the conclusions are:

- For different assumed yield-line patterns in rectangular slabs, the capacities calculated by the new internal work method are different from, and all greater than, the original yield-line capacity.
- The enhancement factor from the new internal work method increases in the first phase, when the rebar is still intact; in the second phase, the enhancement factor starts to drop after the first rebar fractures.
- As the deflection at the slab centre grows, more cracks open along the yield lines, which induces even more decrease in load capacity enhancement.
- In fact, the load capacity enhancement factor cannot keep increasing the whole time after the yield-line pattern has formed, as described in the Bailey-BRE design method. Both the crack opening and reinforcement fracture have to be considered.
- For isosceles triangular slabs, the yield-line patterns are unique. The load capacity enhancement factor performs in similar fashion to rectangular slabs.

- The performances of the load capacity enhancement factors for isotropic and orthotropic reinforcement meshes are very different, because the 'unzipping' situations of rebar along the yield lines vary.
- The geometry of an isosceles triangular slab affects the 'unzipping' of mesh rebar in terms of the deflection/depth ratio. For isosceles triangular slabs with lower height, the crack initiation from the yield-line intersection tends to happen simultaneously for all yield lines.

## 7.2 Recommendations

### 7.2.1 Slab element in finite element program

The current finite element program *Vulcan* defines a slab element as 9-noded, which needs to be improved in order to include triangular elements. Considering the stiffness and stress distribution, the best way to achieve this is to reduce the node number to 7 when analysing slabs using triangular elements, so that the stress distribution will not concentrate near to the apex.

### 7.2.2 Yield-line patterns of trapezoidal slabs

The numerical studies on two yield-line patterns in trapezoidal slabs with different geometries have shown that switching between them is very sensitive. The geometric parameters which determine the yield-line pattern and intersection need further investigation. The influences of these geometric parameters can be investigated by a larger amount of parametric studies over a wider range of parameters, such as increase top and bottom base length with width fixed in a various range of width; keep top base length and slope angle, increase the width. Summarize the results from these tests and in this thesis, the interaction among the geometric parameters can be found, and also an equation determines the yield-line pattern for a given trapezoidal slab can be created. Moreover, the location of yield-line intersection will be able to be concluded.

### 7.2.3 Equilibrium equations in extending Bailey-BRE method to triangular slabs

To ensure the validity and accuracy of the Bailey-BRE method, the assumption of the compressive stress block locations needs to be verified. Once this is validated, a similar assumption can be made for triangular slabs, and the equilibrium equations will be established easily. The method to calculate the enhancement due to tensile membrane action in triangular slabs can then be developed.

### 7.2.4 Extension of new internal work method at elevated temperature

The new internal work method which takes account of the energy dissipation in reinforcement mesh extension has provided a reasonable and realistic prediction of the load carrying capacity of a slab after a yield-line pattern forms. Since this method has currently been developed for ambient temperature, it is essential to extend the method into the elevated-temperature range. This can be achieved by combining the stiffness reduction of steel at high temperature with thermal expansion, temperature distribution and the interaction with attached composite steel beams.

The procedure with penalty function method has shown satisfying results in numerical modelling of behaviour of non-orthogonal composite slabs at elevated temperature. Using advantages of this tool, it is capable to find out the load carrying capacity of slab in any geometry with temperature grows up. Also, it can be an efficient tool to verify the results find from manual and computational calculation. It can be predicted that this procedure will play a great role in performance-based analytical design for non-orthogonal composite slabs in future.

# References

Abu, A. K. (2009), *Behaviour of Composite Floor Systems in Fire*, PhD Thesis, University of Sheffield, Sheffield, UK.

ASFP (1992), *Fire protection for structural steel in buildings* (2nd ed., revised), The Association for Specialist Fire Protection, Ascot, The Steel Construction Institute.

Askes, H. and Ilanko, S. (2006), “The use of negative penalty functions in linear systems of equations”, *Proceedings of the Royal Society A: Mathematical, Physical and Engineering Sciences*, **462**, 2965-2975.

Bailey, C. G. (1995), *Simulation of the structural behaviour of steel-framed buildings in fire*, PhD Thesis, University of Sheffield, Sheffield, UK.

Bailey, C. G., Lennon, T. and Moore, D. B. (1999), “The behaviour of full-scale steel-framed buildings subjected to compartment fires”, *The Structural Engineering*, **77**(8), 15-21.

Bailey, C. G., White, D. B. and Moore, D. B. (2000a), “The tensile membrane action of unrestrained composite slabs simulated under fire conditions”, *Engineering Structures*, **22**, 1583-1595.

Bailey, C. G. and Moore, D. B. (2000b), “The structural behaviour of steel frames with composite floorslabs subject to fire: Part 1: Theory”, *The Structural Engineer*, **78**(11), 19-27.

Bailey, C. G. and Moore, D. B. (2000c), “The structural behaviour of steel frames with composite floorslabs subject to fire: Part 2: Design”, *The Structural Engineer*, **78**(11), 28-33.

Bailey, C. G. (2000), *Design of Steel Structures with Composite Slabs at the Fire Limit State, Final Report No. 81415, prepared for DETR and SCI*, The Building Research Establishment, Garston, UK.

Bailey, C. G. (2001a), “Membrane action of unrestrained lightly reinforced concrete slabs at large displacements”, *Engineering Structures*, **23**, 470-483.

Bailey, C. G. (2001b), *Steel structures supporting composite floor slabs: design for fire, BRE digest 462*. Watford: The Building Research Establishment.

Bailey, C. G. (2003), "Efficient arrangement of reinforcement for membrane behaviour of composite floor slabs in fire conditions", *Journal of Constructional Steel Research*, **59**(7), 931-949.

Bailey, C. G. (2004), "Membrane action of slab/beam composite floor systems in fire", *Engineering Structures*, **26**, 1691-1703.

Bailey, C. G. and Toh, W. S. (2007a), "Behaviour of concrete floor slabs at ambient and elevated temperatures", *Fire Safety Journal*, **42**, 425-436.

Bailey, C. G. and Toh, W. S. (2007b), "Small-scale concrete slab tests at ambient and elevated temperatures", *Engineering Structures*, **29**, 2775-2791.

Bathe, K. J. (1996), *Finite element procedures*, Prentice-Hall, Englewood Cliffs, N. J.

Burgess, I. W., Dai, X. and Huang, S.-S. (2013), "An Alternative Simplified Model of Tensile Membrane Action of Slabs in Fire", *Applications of Structural Fire Engineering conference*, Prague, Czech Republic, 361-368.

BSI (2003), *Structural use of steelwork in building – Part 8: Code of practice for fire resistant design*, British Standards Institute, UK.

Cameron, N. J. K. and Usmani, A. S. (2005a), "New design method to determine the membrane capacity of laterally restrained composite floor slabs in fire. Part 1: Theory and method.", *The Structural Engineering*, **83**(19), 28-33.

Cameron, N. J. K. and Usmani, A. S. (2005b), "New design method to determine the membrane capacity of laterally restrained composite floor slabs in fire. Part 2: Validation.", *The Structural Engineering*, **83**(19), 34-39.

CEN (1994), *Eurocode 4: Design of Composite Steel and Concrete Structures – Part 1.2: General Rules – Structural Fire Design (Draft),* European Committee for Standardization.

CEN (1995), *Eurocode 3: Design of Steel Structures – Part 1.2: General Rules – Structural Fire Design (Draft)*, European Committee for Standardization.

CEN (2002), *Eurocode 1: Actions on Structures – Part 1.2: General actions – actions on structures exposed to fires*, European Committee for Standardization.

CEN (2004), *Eurocode 2: Design of Concrete Structures – Part 1.2: General Rules – Structural Fire Design*, European Committee for Standardization.

CEN (2005a), *Eurocode 3: Design of Steel Structures – Part 1.2: General Rules – Structural Fire Design*, European Committee for Standardization.

CEN (2005b), *Eurocode 4: Design of Composite Steel and Concrete Structures – Part 1.2: General Rules – Structural Fire Design*, European Committee for Standardization.

Clifton, C. (2001), "Design of multi-storey steel framed buildings with unprotected secondary beams or joists for dependable inelastic response in severe fires." *Steel Design and Construction Bulletin* **60**, New Zealand Heavy Engineering Research Association (HERA), 1-58.

Confidential Report (1991), *Fire damage structural survey report to Churchill Plaza, Churchill Way, Basingstoke*, Amos Broome Associates plc, UK.

Elghazouli, A. Y., Izzuddin, B. A. and Richardson, A. J. (2000), "Numerical modelling of the structural fire behaviour of composite buildings", *Fire Safety Journal*, **35**, 279-297.

Foster, S. J., Bailey, C. G., Burgess, I. W. and Plank, R. J. (2004), "Experimental behaviour of concrete floor slabs at large displacements.", *Engineering Structures* **26**, 1231-1247.

Foster, S. J. (2006), *Tensile membrane action of reinforced concrete slabs at ambient and elevated temperatures*, PhD Thesis, University of Sheffield, Sheffield, UK.

Foster, S., Chladna, M., Hsieh, C. Burgess, I and Plank, R. (2007), "Thermal and structural behaviour of a full-scale composite building subject to a severe compartment fire", *Fire Safety Journal* **42**, 183-199.

Gillie, M., Usmani, A. S. and Rotter, J. M. (2002), "A structural analysis of the Cardington British steel corner test", *Journal of Constructional Steel Research*, **58**, 427-442.

Hayes, B. (1968), "Allowing for membrane action in the plastic analysis of rectangular reinforced concrete slabs", *Magazine of Concrete Research*, **20**(65), 205-212.

Huang, Z., Platten, A. and Roberts, J. (1996), "Non-linear Finite Element Model to Predict Temperature Histories within Reinforced Concrete in Fires", *Building and Environment*, **31**(2), 109-118.

Huang, Z., Burgess, I. W. and Plank, R. J. (1999), "Nonlinear Analysis of Reinforced Concrete Slabs Subjected to Fire", *ACI Structures Journal*, **96**(1), 127-135.

Huang, Z. Burgess, I. W. and Plank, R. J. (2001), "The Influence of Tensile Membrane Action in Concrete Slabs on the Behaviour of Composite Steel-framed Buildings in Fire", *2001 Structures Congress – SEI/ASCE, Proceedings of 2001 Structures Congress*, Washington, USA.

Huang, Z., Burgess, I. W. and Plank, R. J. (2000), "Effective Stiffness Modelling of Composite Concrete Slabs in Fire", *Engineering Structures*, **22**(9), 1133-1144.

Huang, Z., Burgess, I. W. and Plank, R, J. (2002), "Modelling of six full-scale fire tests on a composite building", *The Structural Engineering*, **80**(19), 30-37.

Huang, Z., Burgess, I. W. and Plank, R, J. (2003a), "Modeling Membrane Action of Concrete Slabs in Composite Buildings in Fire. I: Theoretical Development", *Journal of Structural Engineering*, **129**(8), 1093-1102.

Huang, Z., Burgess, I. W. and Plank, R, J. (2003b), "Modeling Membrane Action of Concrete Slabs in Composite Buildings in Fire. II: Validations", *Journal of Structural Engineering*, **129**(8), 1103-1112.

Huang, Z., Burgess, I. W., Plank, R. J. and Bailey, C. G. (2004a), "Comparison of BRE simple design method for composite floor slabs in fire with non-linear FE modelling", *Fire Mater*, **28**, 127-138.

Huang, Z., Burgess, I. W. and Plank, R. J. (2004b), “Fire resistance of composite floors subject to compartment fires”, *Journal of Constructional Steel Research*, **60**(2), 339- 360.

Hughes, T. (2000), *The finite element method: Linear static and dynamic finite element analysis*, New York: Dover.

Ingerslev, A. (1923), “The Strength of Rectangular Slabs”, *J. Inst. Struct. Eng.*, **1**(1), 3-14.

Johansen, K. W. (1943), *Brudlinieteorier*, Jul. Gjellerups Forlag, Copenhagen. (*Yield Line Theory*, translated by Cement and Concrete Association, London, 1962.)

Johansen, K. W. (1968), *Pladeformier*, Polyteknisk Forlag, Copenhagen. (*Yield line formulae for slabs*, translated by Cement and Concrete Association, London, 1972.)

Kemp, K. O. (1965), “The yield criterion for orthotropically reinforced concrete slabs”, *International Journal of Mechanical Science*, **7**(11), 737-746.

Kemp, K. O. (1967), “Yield of a square reinforced concrete slab on simple supports, allowing for membrane forces”, *The Structural Engineer*, **7**(45), 235-240.

Kennedy, G. and Goodchild, C. H. (2003), *Practical Yield Line Design*, British Cement Association, Camberley, UK.

Kirby, B. R. and Preston, R. R. (1988), “High Temperature Properties of Hot-rolled, Structural Steels for Use in Fire Engineering Design Studies”, *Fire Safety Journal*, **13**, 27-37.

Kirby, B. R. (1998), *The Behaviour of a Multi-storey Steel Framed Building Subjected to Fire Attack*, British Steel plc., Swinden Technology Centre, Rotherham, UK.

Kwiecinski, M. W. (1965), “Yield criterion for initially isotropic reinforced slab”, *Magazine of Concrete Research*, **17**(51), 97 –100.

Li, G. Q., Guo, S. X. and Zhou, H. S. (2007), “Modelling of membrane action in floor slabs subjected to fire”, *Engineering Structures*, **29**, 880-887.

Lin, T. D., Zwiers, R. I., Shirley, S. T., and Burg, R. G. (1989), ‘‘Fire test of concrete slab reinforced with epoxy-coated bars’’, *ACI Structural Journal*, **86**(2), 156-162.

Morley, C. T. (1966), “On the yield criterion of an orthogonally reinforced concrete slab element”, *Journal of the Mechanics and Physics of Solids*, **14**(1), 33-47.

Najjar, S. R. and Burgess, I. W. (1996), “A Non-linear analysis for three-dimensional steel frames in fire”, *Engineering Structures*, **18**(1), 77-89.

Newman, G. M., Robinson, J. T. and Bailey, C. G. (2000), *Fire Safe Design: A New Approach to Multi-Storey Steel-Framed Buildings*, SCI Publication P288, The Steel Construction Institute, UK.

Newman, G. M., Robinson, J. T. and Bailey, C. G. (2006), *Fire Safe Design: A New Approach to Multi-Storey Steel-Framed Buildings*, Second Edition, SCI Publication P288, The Steel Construction Institute, UK.

O’Conner, M. A., Kirby, B. R. and Martin, D. M. (2003), “Behaviour of a multi-storey composite steel framed building in fire”, *The Structural Engineer*, **81**(2), 27-36.

Omer, E., Izzudin, B. A. and Elghazouli, A. Y. (2006), “Failure assessment of simply supported floor slabs under elevated temperature” *Structural Engineering International*, 1**6**(2), 148-155.

Park, R. and Gamble, W. L. (1980), *Reinforced Concrete Slabs*, New York, John Wiley and Sons.

Park, R. and Paulay, T. (1975), *Reinforced Concrete Structures*, Wiley, New York.

Park, R. (1964a), “Ultimate strength of rectangular concrete slabs under short-term uniform loading with edges restrained against lateral movement”, *Proceedings of the Institution of Civil Engineers*, **28**, 125-150.

Park, R. (1964b), “Tensile membrane behaviour of uniformly loaded rectangular reinforced concrete slabs with full restrained edges”, *Magazine of Concrete Research*, **16**(46), 39-44.

Purkiss, J. A. (1996), *Fire Safety Engineering Design of Structures*, Butterworth and Heinemann, Oxford, UK.

Prager, W. (1955), “General Theory of Limit Design”, *Proceedings of the 8th International Congress of Applied Mechanics, Istanbul 1952.* Vol. 2. University of Istanbul, Faculty of Science, 65-72.

Sawczuk, A. and Jaeger, T. (1963), *Grenztragfahigkeits-Theories Der Platten*, Berlin, Springer-Verlag.

Sawczuk, A. and Winnicki L. (1965), “Plastic behaviour of simply supported reinforced concrete plates at moderately large deflections”, *International Journal of Solids and Structures*, **1**, 97-111.

Smith, A. E. and Coit, D. W. (1995), *Penalty functions*. In: Baeck, T., Fogel,D., Michalewicz, Z. (Eds.), Handbook of Evolutionary Computation, Oxford University Press.

Steel Construction Institute (SCI) P113 (1991), *Structural fire engineering investigation of Broadgate phase 8 fire*, The Steel Construction Institute, Ascot, UK.

Steel Construction Institute (SCI) and CTICM (2009), *Fire Resistance Assessment of Partially Protected Composite Floors (FRACOF): Engineering Background*, Technical Report, CTICM, SCI, Ascot, UK.

Usmani, A. S. and Cameron, N. J. K. (2004), “Limit capacity of laterally restrained concrete floor slabs in fire.” *Cement and Concrete Composites* **26**, 127-140.

Vassart, O. and Zhao, B. (2013), Membrane Action of Composite Structures in Case of Fire, Technical Committee 3, Fire Safety, ECCS.

Wood, R. H. (1961), *Plastic and Elastic Design of Slabs and Plates*, Thames and Hudson, London, UK.

Wood, R. H. and Jones, L. L. (1967), *Yield-Line Analysis of Slabs*, Thames and Hudson, London, UK.

Zienkiewicz, O. and Taylor, R. (2000), *The finite element method. Volume 1: the basis*. London: Butterworth–Heinemann.

# Appendix A

## Application of Penalty Function Method into Vulcan Analysis Program Code

```
*********************************************************************
SUBROUTINE GET_CONS (NEQ, MINCOL, MAXCOL, CONS)
READ THE RELATIVE CONSTRAINTS FROM THE INPUT FILE AND BUILD UP
CONSTRAINT MATRIX
*********************************************************************
IMPLICIT REAL*8(A-H, O-Z)
IMPLICIT INTEGER*4(I-N)
PARAMETER (NUMNOD=1000)
DIMENSION
CONS(NUMNOD*6,NUMNOD*6),ICOL1(NUMNOD*6),ICOL2(NUMNOD*6),
*       ICOL3(NUMNOD*6),ICOL4(NUMNOD*6),ICOL5(NUMNOD*6),
*       ICOL6(NUMNOD*6)
IN=3
DO I = 1,NEQ
   DO J = 1,NEQ
    CONS(I,J) = 0.0
  ENDDO
ENDDO


DO I = 1,NEQ
```

```
ICOL1(I)=0
ICOL2(I)=0
ICOL3(I)=0
ICOL4(I)=0
ICOL5(I)=0
ICOL6(I)=0
ENDDO

IP = 1
LENGTH = 20

CALL LOCATE ('RELATIVE CONSTRAINTS        ',LENGTH)

READ(IN,*) IRNOD1,NDR1,CE1,IRNOD2,NDR2,CE2,IRNOD3,NDR3,CE3,
*     IRNOD4,NDR4,CE4,IRNOD5,NDR5,CE5,IRNOD6,NDR6,CE6

******* FIND THE POSITION OF EACH COEFFICIENT IN CONSTRAINT MATRIX ******

DO WHILE (IRNOD1.NE.0)
   N1 = (IRNOD1-1)*6 + NDR1
   N2 = (IRNOD2-1)*6 + NDR2
   N3 = (IRNOD3-1)*6 + NDR3
```

```
   N4 = (IRNOD4-1)*6 + NDR4

   N5 = (IRNOD5-1)*6 + NDR5

   N6 = (IRNOD6-1)*6 + NDR6

   ICOL1(IP)=N1

   ICOL2(IP)=N2

   ICOL3(IP)=N3

   ICOL4(IP)=N4

   ICOL5(IP)=N5

   ICOL6(IP)=N6

   CONS(IP,N1) = CE1

   CONS(IP,N2) = CE2

   CONS(IP,N3) = CE3

   CONS(IP,N4) = CE4

   CONS(IP,N5) = CE5

   CONS(IP,N6) = CE6

   IP = IP + 1

  READ(IN,*) IRNOD1,NDR1,CE1,IRNOD2,NDR2,CE2,IRNOD3,NDR3,CE3,

*                IRNOD4,NDR4,CE4,IRNOD5,NDR5,CE5,IRNOD6,NDR6,CE6

ENDDO

CALL CHECK ('RELATIVE CONSTRAINTS        ', LENGTH)


********CALCULATE THE SMALLEST COLUMN NUMBER*********
```

```
 MINCOL=ICOL1(1)

 DO I=1,IP-1

 IUU=ICOL1(I)

 IWW=ICOL2(I)

IVV=ICOL3(I)

IZZ=ICOL4(I)

ICC=ICOL5(I)

IXX=ICOL6(I)

IKK=MIN(IUU,IWW)

IPP=MIN(IVV,IZZ)

IHH=MIN(ICC,IXX)

IGG=MIN(IPP,IHH)

IF (IGG.LT.IKK) THEN

   IKK=IGG

END IF

  IF(IKK.LT.MINCOL)THEN

    MINCOL=IKK

   END IF

END DO


***********CALCULATE THE BIGGEST COLUMN NUMBER***********


MAXCOL=ICOL1(1)
```

```
DO I=1,IP

NUU=ICOL1(I)

NWW=ICOL2(I)

NVV=ICOL3(I)

NZZ=ICOL4(I)

NCC=ICOL5(I)

NXX=ICOL6(I)

NKK=MAX(NUU,NWW)

NPP=MAX(NVV,NZZ)

NHH=MAX(NCC,NXX)

NGG=MAX(NPP,NHH)

  IF (NGG.GT.NKK)  THEN

      NKK=NGG

    ENDIF

    IF(NKK.GT.MAXCOL) THEN

        MAXCOL=NKK

     ENDIF

ENDDO

RETURN

END


 *********************************************************************

 SUBROUTINE  CONSTRAINTS(CONS,NJ,MINCOL,MAXCOL,ICONSMHT,PROD)
```

```
************BULID UP THE CONSTRAINTS STIFFNESS MATRIX************


IMPLICIT REAL*8(A-H,O-Z)

IMPLICIT INTEGER*4(I-N)

INTEGER*2 LENGTH

COMMON /PROBCV/IN


PARAMETER (NUMNOD=1000)

PARAMETER (NUMMEM=1000)

DIMENSION PROD(NUMNOD*6,NUMNOD*6),NODP(9,NUMMEM),

 *     CONS(NUMNOD*6,NUMNOD*6),ALPHA(NUMNOD*6,NUMNOD*6),

 *     CONSM(NUMNOD*6,NUMNOD*6),CONST(NUMNOD*6,NUMNOD*6),

 *     IC(NUMNOD*6,NUMNOD*6),ICONSMHT(NUMNOD*6)



****************BUILD UP THE CONSTRAINTS MATRIX****************

NEQ=NJ*6

IN=3

************DEFINE THE VALUE OF PENALTY PARAMETER************

ALPH=6.5E+09

***********BUILD UP THE TRANSPOSE CONSTRAINT MATRIX***********

DO I = 1,NEQ

DO J = 1,NEQ
```

```
CONST(J,I) = CONS(I,J)
ENDDO
ENDDO
***********MULTIPLY CONSTRAINT MATRIX AND TRANSPOSED CONSTRAINT MATRIX ************
CALL MATRIXPRODUCT (CONST,NEQ,NEQ,CONS,
*                NEQ,NEQ,CONSM,NEQ,NEQ)


***************BUILD UP THE UNIT MATRIX OF 'ALPHA'****************
DO I = 1,NEQ
   DO J = 1,NEQ
        ALPHA(I,J) = 0.0
     ENDDO
ENDDO
DO I = 1,NEQ
     ALPHA(I,I) = ALPH
ENDDO


***********MULTIPLY THE PRODUCT OF CONSTRAINT MATRIX AND TRANSPOSED CONSTRAINT MATRIX WITH MATRIX ALPHA*************
CALL MATRIXPRODUCT (CONSM,NEQ,NEQ,ALPHA,
*                NEQ,NEQ,PROD,NEQ,NEQ)
```

```
****FIND THE COLUMN HEIGHT IN CONSTRAINTS MATRIX PRODUCT*****
INN=MINCOL
M=INN
DO I=MINCOL,MAXCOL
IM=ABS(M-INN)
ICONSMHT(M)=IM
M=M+1
ENDDO
RETURN
END

**********************************************************************
SUBROUTINE CONSMATRIX(NEQ,PROD,ICONSMHT,CONSTK)
**********************************************************************
```

SAVE THE CONSTRAINT MATRIX INTO AN ONE-DIMENSIONAL ARRAY LIKE THE METHOD DO WITH STIFFNISS MATRIX. THIS PROCEDURE MAKE THE CONSTRAINT MATRIX EXACTLY SAME SHAPE WITH STIFFNESS MATRIX IN ORDER TO PLUS THEM TOGETHER.

```
**********************************************************************
IMPLICIT REAL*8(A-H,O-Z)
IMPLICIT INTEGER*4(I-N)
INTEGER*4 MAXA
PARAMETER (NUMNOD=1000,NUMSKY=15000000)
DIMENSION CONSTK(NUMSKY),ICONSMHT(NUMNOD*6),
```

```
*         PROD(NUMNOD*6,NUMNOD*6)

M=1

DO J=1,NEQ

I=J

   DO N=1,ICONSMHT(J)+1

        CONSTK(M)=PROD(I,J)

        M=M+1

        I=I-1

     ENDDO

 ENDDO

RETURN

END


**********************************************************************

SUBROUTINE MATRIXPRODUCT(A, IrowsA, IcolsA, B, IrowsB, IcolsB, C, IrowsC,
IcolsC)

**********************************************************************

IMPLICIT REAL*8(A-H,O-Z)

IMPLICIT INTEGER*4(I-N)


PARAMETER (NUMNOD=1000)

DIMENSION A(NUMNOD*6,NUMNOD*6),B(NUMNOD*6,NUMNOD*6),

*              C(NUMNOD*6,NUMNOD*6)
```

```
DO I = 1, IrowsC

   DO j = 1, IColsC

      C(i,j) = 0.0

      ENDDO

ENDDO


DO i = 1, IrowsA

     DO j = 1, IcolsB

          DO k = 1, IcolsA

                    C(i,j) = C(i,j) + A(i,k)*B(k,j)

          ENDDO

      ENDDO

ENDDO


RETURN

END
```

# Appendix B

## New Plastic Energy Method for Rectangular Slab

### Failure Mechanism A

In Mechanism A, a through-depth crack forms across the slab centre, and in accordance with the typical yield-line pattern for a simply supported rectangular slab, diagonal yield-line cracks have been assumed as well. The edges of the slab move towards the centre of the slab and "relieve" the strains in the reinforcement across part of the short-span crack.

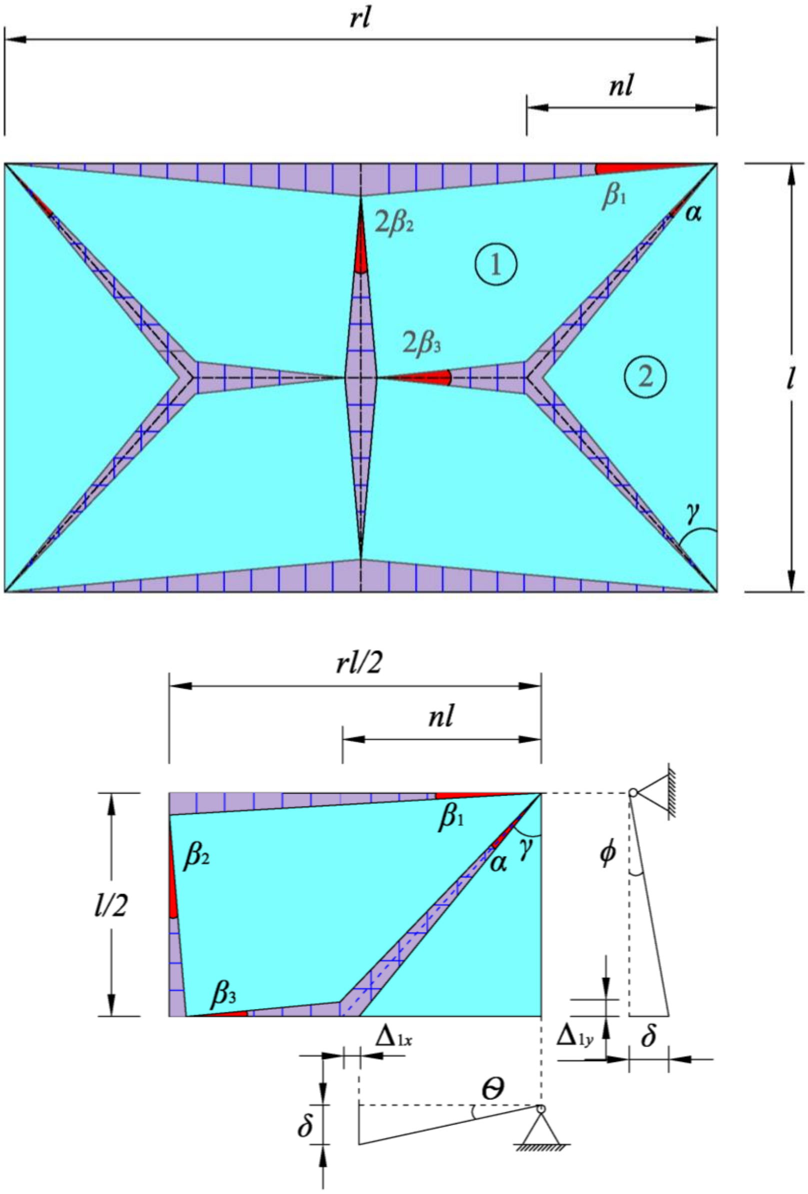

Fig. B1 Assumed crack locations for failure Mechanism A

When considering the in-plane rotation of Element 1, the behaviour of the slab element is assumed as rigid-plastic, as in yield-line theory. Therefore, the values of $\beta_1$, $\beta_2$ and $\beta_3$ are the same and represented by $\beta$. With rotation angles:

$$\theta = \frac{\delta}{nl} \; and \; \phi = \frac{2\delta}{l}$$

The angles $\alpha$ and $\beta$ of the crack openings between elements in this mechanism depend on the axis deflections during the slab separation after cracking.

In the *X*-direction:

$$\Delta_{1x} = nl - nl\cos\theta - \frac{l}{2}\beta$$

By applying the Taylor series for $\cos\theta$:

$$\cos\theta = 1 - \frac{\theta^2}{2!} + \frac{\theta^4}{4!} - \frac{\theta^6}{6!} + \cdots + (-1)^n \frac{x^{2n}}{(2n)!}$$

And,

$$\Delta_{1x} = nl\left(1 - \left(1 - \frac{\theta^2}{2}\right)\right) - \frac{l}{2}\beta$$

$$\Delta_{1x} = \frac{nl\theta^2}{2} - \frac{l}{2}\beta$$

In the *Y*-direction:

$$\Delta_{1y} = \frac{l}{2}(1 - \cos\phi\,) - nl\beta$$

By applying the Taylor series for $\cos\phi$:

$$\Delta_{1y} = \frac{l}{4}\phi^2 - nl\beta$$

Therefore, the angles $\alpha$ and $\beta$ which determines the crack opening between Elements 1 and 2 can be calculated as

$$\beta = \frac{l}{2}(1 - \cos\phi)\frac{2}{rl}$$

$$\beta = \frac{1}{r}\frac{\phi^2}{2}$$

$$\alpha = \frac{\Delta_{1x}\cos\gamma + \Delta_{1y}\sin\gamma}{\frac{l/2}{\cos\gamma}}$$

$$\alpha = \frac{2}{l}\left[\left(\frac{nl\theta^2}{2} - \frac{l}{2r}\frac{\phi^2}{2}\right)\cos^2\gamma + \left(\frac{l\phi^2}{4} - \frac{nl}{r}\frac{\phi^2}{2}\right)\sin\gamma\cos\gamma\right]$$

$$\alpha = n\theta^2\cos^2\gamma + \phi^2\left[\left(\frac{1}{2} - \frac{n}{r}\right)\sin\gamma\cos\gamma - \frac{1}{2r}\cos^2\gamma\right]$$

After taking the slab thickness into account,

$$\alpha = n\theta^2\cos^2\gamma + \frac{\phi^2}{2r}[(r-2n)\sin\gamma\cos\gamma - \cos^2\gamma]$$

in which,

$n$ is the parameter defining the location of the yield-line intersection:

$$n = \frac{1}{2r}\left(-1 + \sqrt{1+3r^2}\right)$$

$\phi$ is the rotation of slab Element 1 about edge in longer span,

$\theta$ is the rotation of slab Element 2 about edge in shorter span,

$\gamma$ is the angle between the diagonal yield-line and short span edge of Element 2,

$$\gamma = \arccos\left(\frac{1}{\sqrt{1+4n^2}}\right)$$

$r$ is the aspect ratio.

### Calculation of rebar extension

The rebar extension is obtained from the equations above. For different locations of cracks, the reinforcing bars can be stretched in their own directions by amounts depending on the crack angles to the global axes.

In -$X$ direction,

For diagonal crack $\alpha$;

In X-direction,

$$\Delta_{\alpha x} = \alpha S \cos\gamma + \theta\mu h$$

$$\Delta_{\alpha x} = \alpha Y + \theta\mu h$$

In Y-direction,

$$\Delta_{\alpha y} = \alpha S \sin\gamma + \phi\mu h$$

$$\Delta_{\alpha y} = \alpha X + \phi\mu h$$

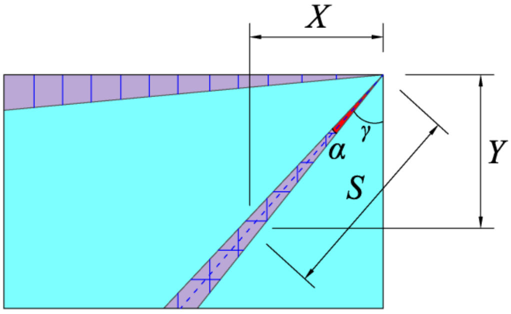

**Fig. B2 Rebar extension in diagonal crack**

For the crack at the slab edge $\beta_1$, as this only opens in the $Y$-direction and the crack is at the long edge of the slab, the rebar extension is given as,

$$\Delta_{\beta 1y} = \alpha X + \theta(1-\mu)h$$

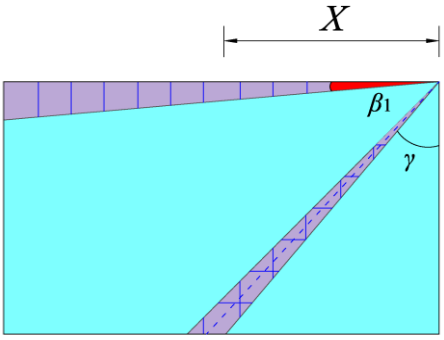

**Fig. B3 20 Rebar extension in slab edge crack**

The crack $\beta_2$ at the slab centre, which is opening on $X$ direction and caused by the in-plane rotation only, so the rebar extension is given as,

$$\Delta_{\beta 2x} = 2\beta Y$$

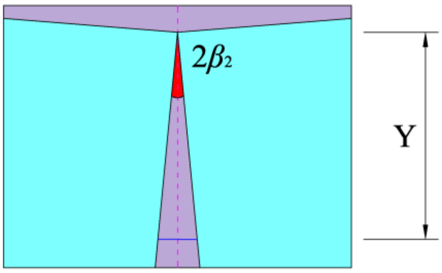

**Fig. B4 Rebar extension in slab centre crack**

For the crack $\beta_3$ in the $X$-direction along the slab central axis, the extension is

$$\Delta_{\beta 3y} = 2\beta X + 2\phi\mu h$$

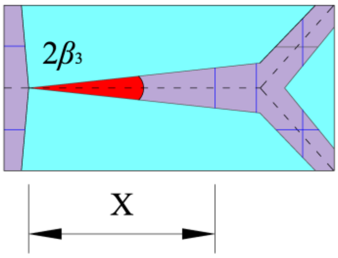

**Fig. B5 Rebar extension in slab central horizontal crack**

## Calculation of internal work

In the previous section, it has been explained that the internal work depends on the rebar extension across the yield-line, so that, the internal work due to each yield-line is given as below.

For the diagonal yield-lines $\alpha$, when the cracks initially appear the reinforcement is intact across each yield-line, so that the distances $Y = {}^{l}/_{2}$ and $X = n\, l$,

$$D_{\alpha x} = F_p \frac{l}{2}\left(\frac{\alpha l}{4} + \theta\mu h\right)$$

and,

$$D_{\alpha y} = F_p nl \left(\frac{\alpha nl}{2} + \phi\mu h\right)$$

When the cracks move into the next stage, the rebar becomes part-fractured, so the distances $Y < {}^{l}/_{2}$ and $X < n\, l$,

$$D_{\alpha x} = F_p Y \left(\frac{\alpha Y}{2} + \theta\mu h\right)$$

and,

$$D_{\alpha y} = F_p X \left(\frac{\alpha X}{2} + \phi\mu h\right)$$

in which,

$$Y = \frac{\Delta_{lim} - \theta\mu h}{\alpha}$$

$$X = \frac{\Delta_{lim} - \phi\mu h}{\alpha}$$

If we put

$$\bar{h} = \frac{h}{l} \; and \; \bar{v} = \frac{\Delta_{lim}}{l}$$

$$\bar{X} = \frac{X}{l} \; and \; \bar{Y} = \frac{Y}{l}$$

The internal work relationship can be optimized as,

$$D_{\alpha x} = F_p l^2 \bar{Y}\left(\frac{\alpha\bar{Y}}{2} + \theta\mu\bar{h}\right)$$

$$\bar{Y} = \frac{1}{2} \; when \; reinforcement \; is \; intact, otherwise \; \bar{Y} = \frac{\bar{v} - \theta\mu\bar{h}}{\alpha}$$

and,

$$D_{\alpha y} = F_p l^2 \bar{X}\left(\frac{\alpha\bar{X}}{2} + \phi\mu\bar{h}\right)$$

$$\bar{X} = n \; when \; reinforcement \; is \; intact, otherwise \; \bar{X} = \frac{\bar{v} - \phi\mu\bar{h}}{\alpha}$$

As these equations are for one diagonal yield-line, the results need to be multiplied by 4 when calculating the internal work for the whole slab.

For slab edge yield-line $\beta_3$ , by applying the same equations,

$$D_{\beta 1y} = F_p l^2 \bar{X}\left(\frac{\beta\bar{X}}{2} + \phi(1-\mu)\bar{h}\right)$$

$$\bar{X} = \frac{r}{2} when \; reinforcement \; is \; intact, otherwise \; \bar{X} = \frac{\frac{\bar{v}}{2} - \phi(1-\mu)\bar{h}}{\beta}$$

The results need to be multiplied by 4 when calculating whole-slab internal work.

For the X-direction yield-line $\beta_2$,

$$D_{\beta 2x} = F_p l^2 \bar{Y}(\beta \bar{Y})$$

$$\bar{Y} = \frac{1}{2}\ when\ reinforcement\ is\ intact, otherwise\ \bar{Y} = \frac{\bar{v}}{2\beta}$$

The results need to be multiplied by 2 when calculating whole-slab internal work.

For the Y-direction yield-line $\beta_3$,

$$D_{\beta 3y} = F_p l^2 \bar{X}\left(\beta \bar{X} + 2\phi\mu\bar{h}\right)$$

$$\bar{X} = \left(\frac{r}{2} - n\right) when\ reinforcement\ is\ intact, otherwise\ \bar{X} = \frac{\bar{v} - 2\phi\mu\bar{h}}{2\beta}$$

The results need to be multiplied by 2 when calculating whole-slab internal work.

**Failure Mechanism B**

In this assumed failure mechanism, all the cracks follow the original yield-line pattern formed in a rectangular slab with simple support at its edges, and under uniformly distributed load. The angles $\theta$ and $\phi$ are the rotations of the two elements about the slab edges, but comparing these to the rotations about the slab edges in Mechanism A, the crack $\alpha$ is the only one which opens progressively, and it is reasonable to assume that the reinforcement across the central yield-line in the long-span direction fractures simultaneously without any unzipping effect.

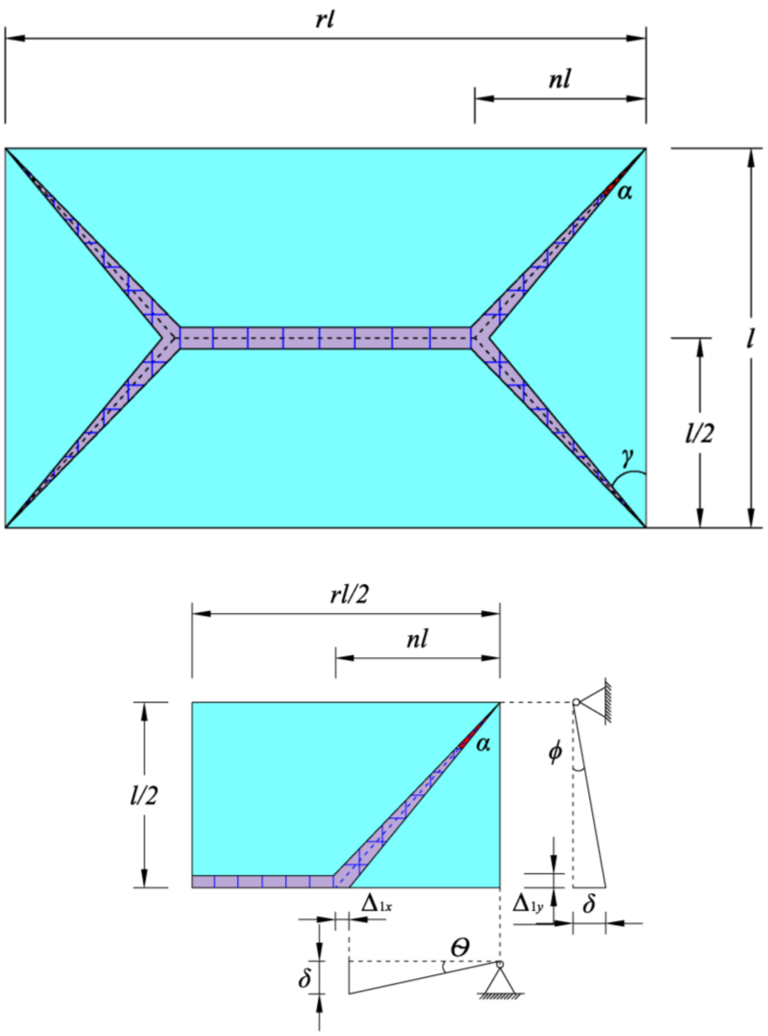

Fig. B6  Assumed crack locations for failure Mechanism B

So, $\alpha$ is given as,

$$\alpha = n\theta^2 \cos^2 \gamma + \frac{\phi^2}{2r}[(r-2n)\sin\gamma\cos\gamma]$$

## Calculation of rebar extensions

The rebar extensions across the yield-line $\alpha$ are given by,

In the X-direction:

$$\Delta_{\alpha x} = \alpha S \cos\gamma + \theta\mu h$$

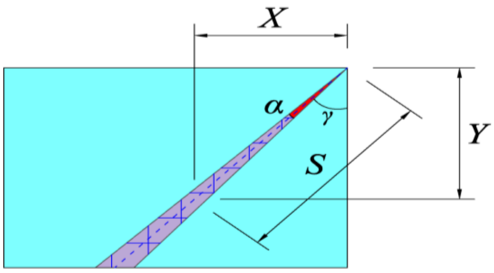

Fig. B7  Rebar extension in diagonal crack so,

$$\Delta_{\alpha x} = \alpha Y + \theta \mu h$$

In the Y-direction:

$$\Delta_{\alpha y} = \alpha S \sin \gamma + \phi \mu h$$

so,

$$\Delta_{\alpha y} = \alpha X + \phi \mu h$$

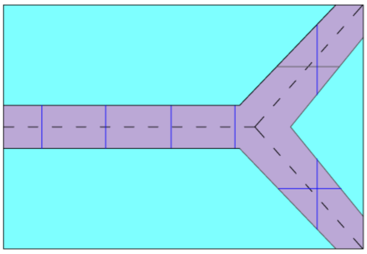

**Fig. B8 Rebar extension in slab centre crack**

For the central long-span crack, opening in the Y-direction,

$$\Delta_{\beta y} = l \frac{\phi^2}{2} + 2\phi \mu h$$

**Calculation of internal work**

Using the same calculation method as for Mechanism A, the internal work at each crack has been summarized below.

For the diagonal yield-line $\alpha$, when mesh reinforcement in the X-direction is intact over the yield-line, $Y = {}^{l}/_{2}$ so the internal work is given by,

$$D_{\alpha x} = F_p l^2 \bar{Y} \left( \frac{\alpha}{2} \bar{Y} + \theta \mu \bar{h} \right)$$

$$\bar{Y} = \frac{1}{2}\ when\ reinforcement\ \ is\ intact, otherwise\ \bar{Y} = \frac{\bar{v} - \theta \mu \bar{h}}{\alpha}$$

In the Y-direction, when mesh reinforcement is intact across the yield-line, X = n l so the internal work is given by,

$$D_{\alpha y} = F_p l^2 \bar{X} \left( \frac{\alpha}{2} \bar{X} + \phi \mu \bar{h} \right)$$

$$\bar{X} = n\ when\ reinforcement\ is\ \ intact, otherwise\ \bar{X} = \frac{\bar{v} - \phi \mu \bar{h}}{\alpha}$$

Since there are 4 diagonal cracks, the equations need to be multiplied by 4 when calculating the whole-slab internal work.

For the central long-span crack opening in the Y-direction, the internal work is given by,

$$D_{\beta y} = F_p l^2 \bar{X}\left(\frac{\phi^2}{2} + 2\phi\mu\bar{h}\right)$$

$$\bar{X} = r - 2n\ when\ reinforcement\ is\ intact, otherwise\ \bar{v} > \frac{\phi^2}{2} + 2\phi\mu\bar{h}$$

## Failure Mechanism C

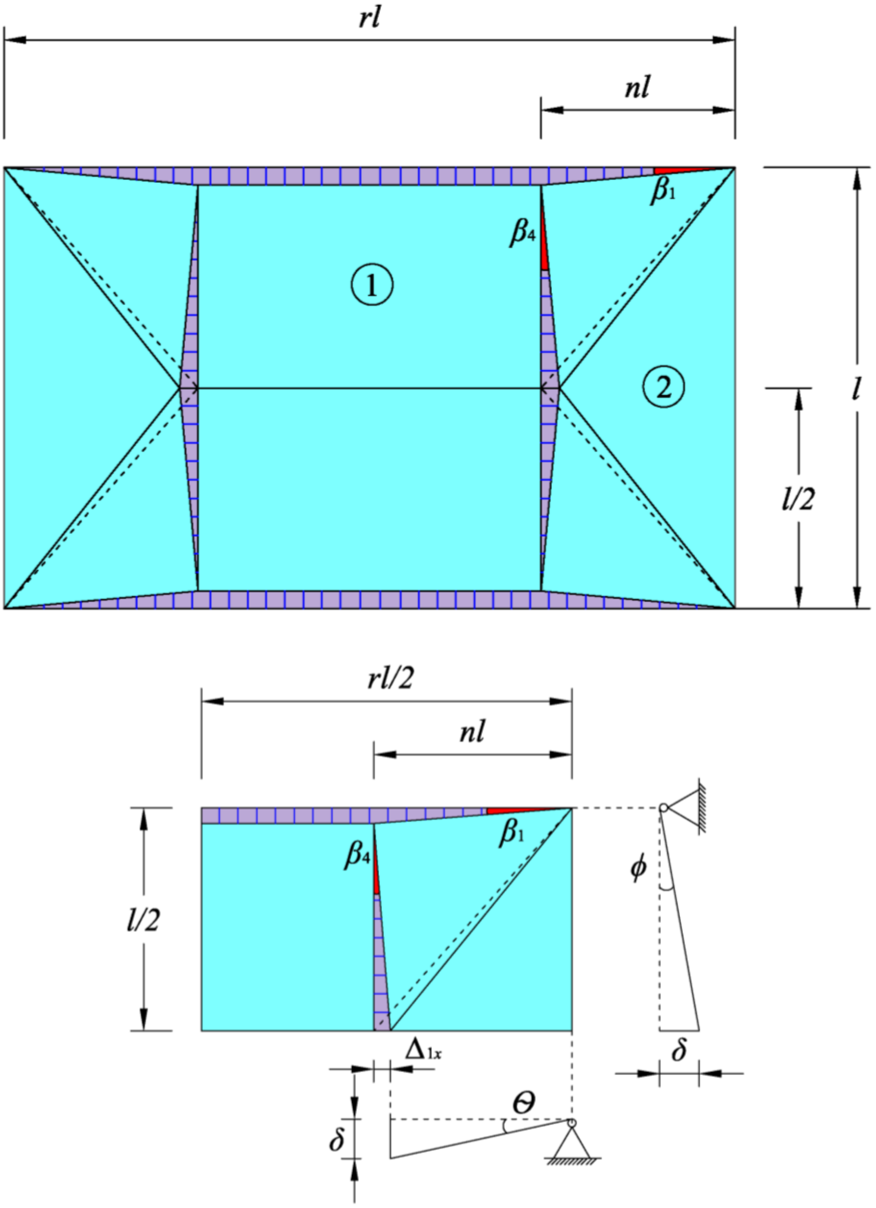

**Fig. B9 Assumed crack locations for failure Mechanism C**

In this assumed failure mechanism, the critical failure is caused by through-depth cracks opening at the yield-line intersections across the shorter span. It is assumed that the reinforcement across the diagonal yield-lines fractures simultaneously, as does the rebar across the central long-span yield-line. Only cracks $\beta_1$ and $\beta_4$ need to be investigated, which are both represented by the angle $\beta$.

$$\beta = \frac{\phi^2}{4n}$$

## Calculation of rebar extension

The rebar extension in crack $\beta_1$ is given by,

$$\Delta_{\beta 1y} = \frac{l}{2}(1 - \cos\phi) + \phi(1 - \mu)h$$

however, when $X > nl$,

$$\Delta_{\beta 1y} = l\phi\left[\frac{\phi}{4} + (1 - \mu)\frac{h}{l}\right]$$

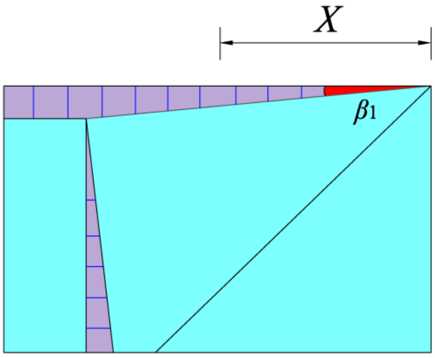

**Fig. B10 Rebar extension in the slab edge crack**

Otherwise, when $X < nl$,

$$\Delta_{\beta 1y} = \beta X + \phi(1 - \mu)h$$

For the rebar extension in $\beta_4$ is given by,

$$\Delta_{\beta 4x} = \beta Y$$

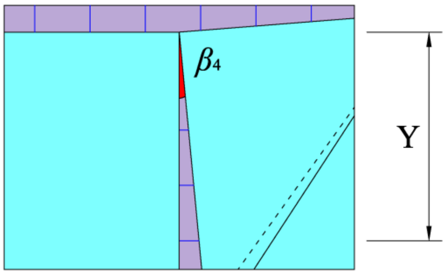

**Fig. B11 Rebar extension in crack at yield-line intersection**

**Calculation of internal work**

For the diagonal yield-line crack $\alpha$, as the reinforcement is assumed to fracture simultaneously, before fracture happens when the reinforcement is intact over the yield-line, $Y = {}^{l}/_{2}$ and $X = nl$, and the internal work is given by,

$$D_{\alpha x} = F_p l^2 \bar{Y} \theta \mu \bar{h}$$

$$\bar{Y} = \frac{1}{2}\ when\ reinforcement\ is\ intact\ with\ \bar{v} > \theta \mu \bar{h}$$

$$D_{\alpha y} = F_P l^2 \bar{X} \phi \mu \bar{h}$$

$$\bar{X} = n\ when\ reinforcement\ is\ intact\ with\ \bar{v} > \phi \mu \bar{h}$$

For the slab-edge crack $\beta_1$, the width of crack between yield-line intersections is different from that near the slab corners. In this case, $X_1$ and $X_2$ represent the distances over which rebar is still intact for slab corner zones and between the intersections respectively. The internal work is given by,

$$D_{\beta 1 y(corner)} = F_p l^2 \bar{X}_1 \left(\frac{\beta}{2}\bar{X}_1 + \phi(1-\mu)\bar{h}\right)$$

$$\bar{X}_1 = n\ when\ reinforcement\ is\ intact, otherwise\ \bar{X}_1 = \frac{\frac{\bar{v}}{2} - \phi(1-\mu)\bar{h}}{\beta}$$

$$D_{\beta 1 y(between\ intersections)} = F_p l^2 \bar{X}_2 \left(\beta \bar{X}_2 + \phi(1-\mu)\bar{h}\right)$$

$$\bar{X}_2 = r - 2n\ when\ reinforcement\ is\ intact, otherwise\ \bar{X}_2 = \frac{\frac{\bar{v}}{2} - \phi(1-\mu)\bar{h}}{\beta}$$

For the cracks located at the yield-line intersections $\beta_4$, the internal work is given by,

$$D_{\beta 4 x} = F_p l^2 \bar{Y}^2 \beta$$

$$\bar{Y} = \frac{1}{2}\ when\ reinforcement\ is\ intact, otherwise\ \bar{Y} = \frac{\bar{v}}{\beta}$$

## Failure Mechanism D

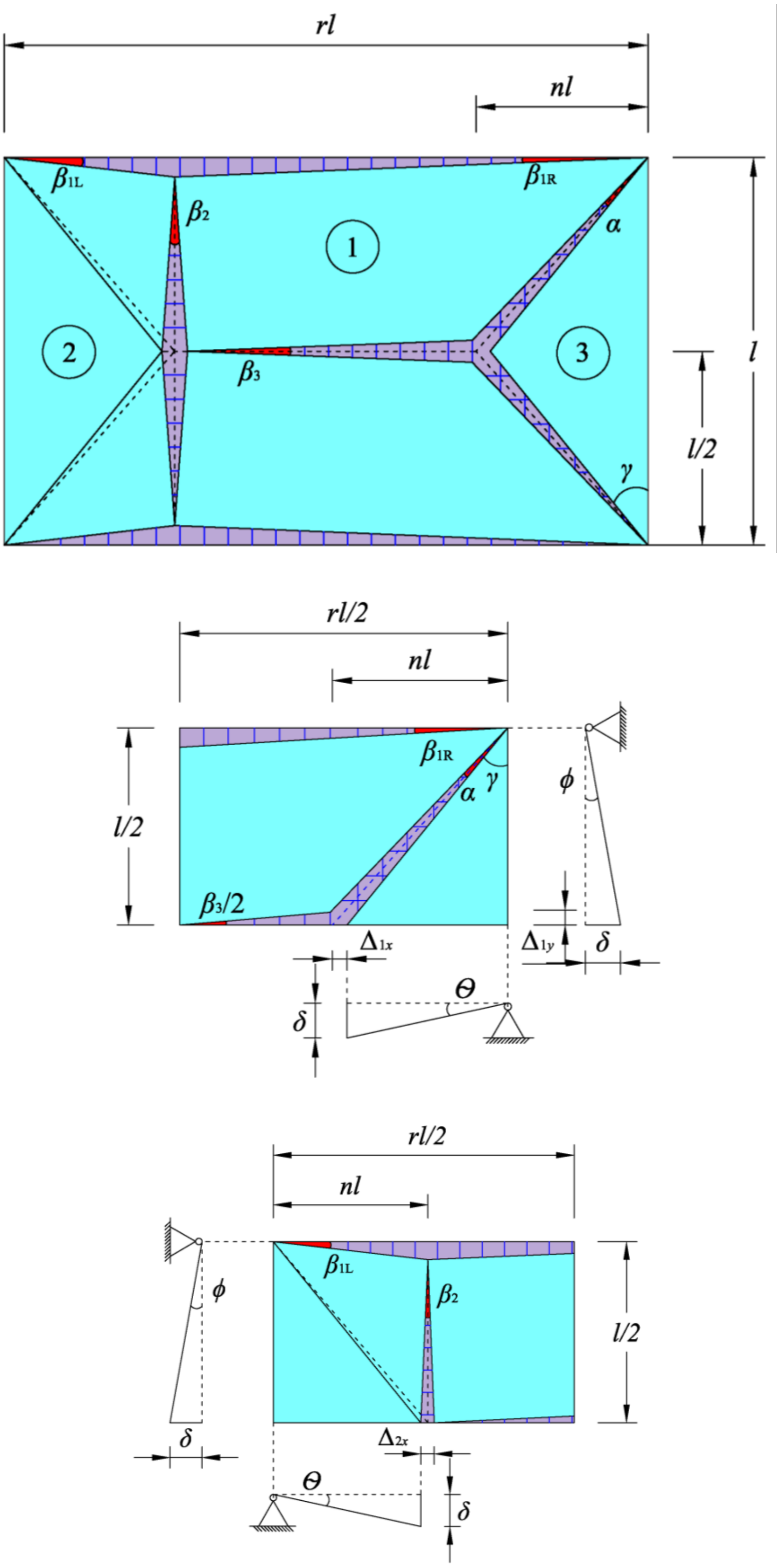

Fig. B12 Assumed crack locations for failure Mechanism D

Mechanism D is a combination of Mechanisms B and C. At one end of the slab, the crack forms at the intersection of the yield-lines like Mechanism C. At the other end, cracks formed along the diagonal yield-lines and the edges of the slab move towards the slab centre.

Applying same method used in Mechanism A to calculate the displacement caused by slab element rotation, the displacements in the *X*- and *Y*-directions are given by,

$$\Delta_{1x} = \frac{nl\theta^2}{2} - \frac{l}{2}\beta_{1R}$$

and,

$$\Delta_{1y} = \frac{l}{4}\phi^2 - nl\beta_{1R}$$

The angle $\alpha$ which controls the crack opening magnitude is given by,

$$\alpha = n\theta^2 \cos^2\gamma + \frac{\phi^2}{2(r-n)}\left[(r-2n)\sin\gamma\cos\gamma - \frac{\cos^2\gamma}{2}\right]$$

Since only one crack occurs at yield-line intersection along shorter span is assumed, the angle $\beta_{1L}$ and $\beta_{1R}$ which defines the magnitude of slab edge inward movement is different.

$$\beta_{1L} = \frac{1}{4n}\phi^2$$

and,

$$\beta_{1R} = \frac{1}{4(r-n)}\phi^2$$

Since the slab elements are considered as rigid-plastic, it can be get as,

$$\beta_2 = \beta_{1L} + \beta_{1R}$$

$$\beta_3 = 2\beta_{1R}$$

### Calculation of rebar extension

For the reinforcement extension across yield-line crack $\alpha$, the extension is calculated using the same method as for the previous mechanisms,

$$\Delta_{\alpha x} = \alpha Y + \theta \mu h$$

$$\Delta_{\alpha y} = \alpha X + \phi \mu h$$

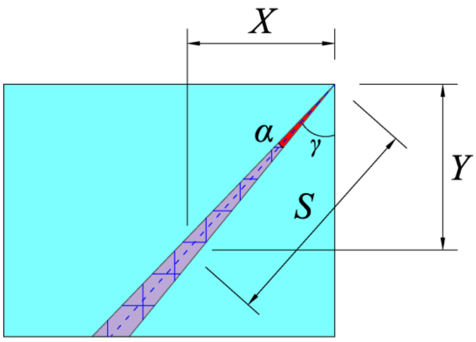

**Fig. 13 Rebar extension in diagonal crack**

For the slab edge inward movement between the slab corner and yield-line intersection, the reinforcement extension is given by,

$$\Delta_{\beta 1L\,y} = 2\beta_{L1} X + 2\phi(1-\mu)h$$

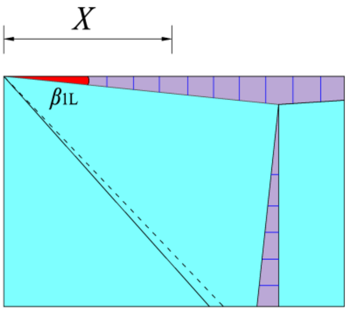

**Fig. B14 Rebar extension in slab edge inward movement $\beta_{1L}$**

For the slab edge inward movement at the end without a crack at the yield-line intersection, the rebar extension is given by,

$$\Delta_{\beta 1Ry} = 2\beta_{1R} X + 2\phi(1-\mu)h$$

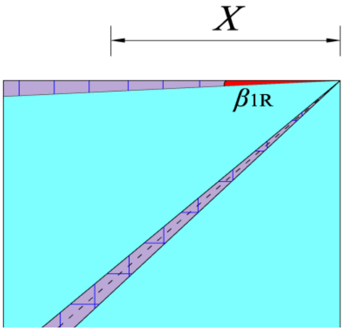

**Fig. B15 Rebar extension in slab edge inward movement $\beta_{1R}$**

For the crack located at the yield-line intersection at one end of slab, the rebar extension is given by,

$$\Delta_{\beta 2x} = (\beta_{1L} + \beta_{1R})Y$$

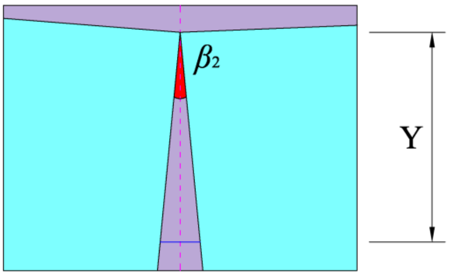

**Fig. B16 Rebar extension in yield-line intersection crack β3**

For the horizontal crack along the yield-line at the slab centre, the rebar extension is given by,

$$\Delta_{\beta 3y} = 2\beta_{1R}X + 2\phi\mu h$$

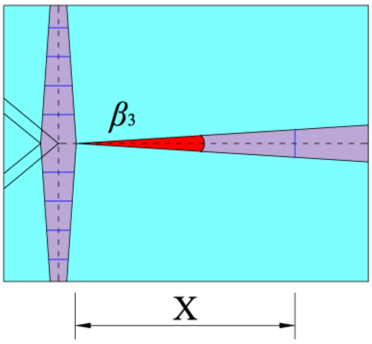

**Fig. B17 Rebar extension in horizontal yield-line crack $\beta_3$**

## Calculation of internal work

For the diagonal yield-line at one end of the slab reinforcement fracture is assumed to be simultaneous. When the rebar is intact across the yield-line, $X = nl$ and $Y = {}^{l}/_{2}$, so the internal work is given by,

$$D_{\alpha Lx} = F_p l^2 \bar{Y} \theta \mu \bar{h}$$

$$\bar{Y} = \frac{1}{2}\ when\ reinforcement\ is\ intact, otherwise\ \bar{Y} = \frac{\bar{v} - \theta\mu\bar{h}}{\alpha}$$

$$D_{\alpha Ly} = F_p l^2 \bar{X} \phi \mu \bar{h}$$

$$\bar{X} = n\ when\ reinforcement\ is\ intact, otherwise\ \bar{X} = \frac{\bar{v} - \phi\mu\bar{h}}{\alpha}$$

For the diagonal yield-line crack $\alpha$ at the other end of the slab, the internal work is given by,

$$D_{\alpha Rx} = F_p l^2 \bar{Y}\left(\frac{\alpha}{2}\bar{Y} + \theta\mu\bar{h}\right)$$

$$\bar{Y} = \frac{1}{2}\ when\ reinforcmenent\ is\ intact, otherwise\ \bar{Y} = \frac{\frac{\bar{v}}{2} - \theta\mu\bar{h}}{\alpha}$$

$$D_{\alpha Ry} = F_p l^2 \bar{X}\left(\frac{\alpha}{2}\bar{X} + \phi\mu\bar{h}\right)$$

$$\bar{X} = n\ when\ reinforcement\ is\ intact, otherwise\ \bar{X} = \frac{\frac{\bar{v}}{2} - \phi\mu\bar{h}}{\alpha}$$

For the slab-edge inward movement $\beta_1$, the internal work is given by,

$$D_{\beta 1Y} = F_p l^2 \bar{X}\left[\bar{X}_L\ \left(\frac{\beta_{1L}}{2}\bar{X}_L + \phi(1-\mu)\bar{h}\right) + \bar{X}_R\ \left(\frac{\beta_{1R}}{2}\bar{X}_R + \phi(1-\mu)\bar{h}\right)\right]$$

$$\bar{X}_L = n\ when\ reinforcement\ intact, otherwise\ \bar{X}_L = \frac{\frac{\bar{v}}{2} - \phi(1-\mu)\bar{h}}{\beta_{1L}}$$

$$\bar{X}_R = r - n\ when\ reinforcement\ intact, otherwise\ \bar{X}_R = \frac{\frac{\bar{v}}{2} - \phi(1-\mu)\bar{h}}{\beta_{1R}}$$

For the crack at the yield-line intersection across the shorter span $\beta_2$, the internal work is given by,

$$D_{\beta 2x} = F_P l^2 (\beta_{1L} + \beta_{1R})\bar{Y}^2$$

$$\bar{Y} = \frac{1}{2}\ when\ reinforcement\ is\ intact, otherwise\ \bar{Y} = \frac{\bar{v}}{\beta_{1L} + \beta_{1R}}$$

For the crack across the slab's central axis $\beta_3$, the internal work is given by,

$$D_{\beta 3y} = F_p l^2 \bar{X}\left(\beta_{1R}\bar{X} + 2\phi\mu\bar{h}\right)$$

$\bar{X} = r - 2n\ when\ reinforcement\ is\ intact, otherwise\ \bar{X} = \frac{\bar{v} - 2\phi\mu\bar{h}}{2\beta_R}$.